NUMERICAL SIMULATION OF THE DYNAMICS OF RF CAPACITIVE DISCHARGE IN CARBON DIOXIDE

Valeriy Lisovskiy*, Stanialav Dudin, Amaliya Shakhnazarian, Pavlo Platonov, Vladimir Yegorenkov

V.N. Karazin Kharkiv National University, 4 Svobody Sq., Kharkiv, 61022, Ukraine
Corresponding Author e-mail: lisovskiy@yahoo.com
Received June 12, 2024; revised July 21; accepted August 15, 2024

In this research, the one-dimensional fluid code SIGLO-rf was used to study the internal parameters of RF capacitive discharge in carbon dioxide, focusing mainly on time-averaged and spatio-temporal distributions of discharge parameters. With the help of this code, in the range of distances between electrodes $d = 0.04 – 8$ cm, RF frequencies $f = 3.89 – 67.8$ MHz, and values of carbon dioxide pressure $p = 0.1 – 9.9$ Torr, averaged over the RF period axial profiles of the density of electrons, positive and negative ions were calculated as well as potential and electric field strength. It is shown that the discharge plasma in CO_2 contains electrons, positive ions, as well as negative ions. The negative ions of atomic oxygen are formed by the dissociative attachment of electrons to CO_2 molecules. Studies of the spatio-temporal dynamics of plasma parameters (electron density, potential and electric field strength, as well as ionization and attachment rates) in RF capacitive discharge in CO_2 showed that during half of the RF period, 1 to 3 ionization bursts are usually observed. They correspond to stochastic heating in the near-electrode sheath and the formation of passive and active double layers near the sheath boundaries. The passive double layer appears in the cathode phase and maintains the discharge plasma. The active layer is formed in the anodic phase and ensures a balance of positive and negative charges escaping to the electrode during the RF period. It was found that when the conditions $pd = 2$ Torr cm and $fd = 27.12$ MHz cm are met simultaneously, during half of the RF period, 4 intense ionization peaks are observed: resulting from stochastic heating, passive, active, and additional (auxiliary) double layers. The auxiliary double layer helps bring electrons to the surface of the temporary anode and occurs near its surface inside the near-electrode sheath. Using the similarity law, the conditions for the existence of these 4 ionization peaks in a wide range of RF frequencies, carbon dioxide pressures, and distances between electrodes were verified.

Keywords: *Radio-frequency capacitive discharge; Fluid modeling; Carbon dioxide; Ionization rate; Double layers; Negative ions*
PACS: 52.80.Pi, 52.50.Qt, 52.65.Kj

INTRODUCTION

Radiofrequency capacitively coupled gas discharge has become practically irreplaceable in many plasma technologies of micro– and nanoelectronics [1–9]. These include processes of plasma etching of semiconductor materials, deposition of various coatings from the gas phase, and many others. Therefore, the properties of the RF discharge are widely studied both experimentally [10–19] and theoretically [10, 20–29]. Numerical modeling allows us to study not only the behavior of the average plasma parameter profiles (potential, electric field, ion and electron densities, etc.) over the RF period, but also to determine their dynamics under various conditions [30–39], as well as to explain experimentally observed phenomena and predict new ones.

Radiofrequency capacitive discharge in electronegative gases turned out to be especially rich in new phenomena [16, 17, 22, 40–53]. Electronegative gases are gases whose molecules capture free electrons, forming singly charged negative ions. Their presence in a sufficiently high concentration in a gas mixture significantly changes the charged particle generation and loss processes in the discharge plasma. The rate of ambipolar losses decreases [42, 44, 46], up to the transition of ambipolar diffusion to free diffusion [47]. Accordingly, this affects the time-averaged plasma potential and the flow of positive ions from the plasma to the electrodes [40, 41]. Due to the retention of negative ions in the average potential well in the RF capacitive discharge, their density increases. In this case, it can exceed the electron concentration by tens to hundreds (and sometimes thousands) times, and the plasma consists of positive and negative ions in approximately equal concentrations with a small addition of free electrons [41, 42, 44, 46]. At certain moments of the RF period, double layers of space charge may appear in the discharge [44, 54–58]. The enhanced electric field of the double layer leads to ionization bursts, which allows maintaining stable discharge operation. We will consider this problem in more detail below.

In addition, the RF capacitive discharge is widely used in pumping CO_2 gas lasers [59–62]. Recently, a separate line of research has actually formed, dedicated to the plasma conversion of carbon dioxide [63–76]. These studies aim to solve the problem of the greenhouse effect associated with emissions of carbon dioxide into the atmosphere formed during the combustion of fossil fuels. The researchers are seeking an efficient method of splitting CO_2 molecules into carbon monoxide and oxygen, which can be used both in terrestrial conditions and to provide future colonies on Mars with fuel and oxygen. In this case, high values of the conversion coefficient of CO_2 molecules can be achieved in the plasma of the RF capacitive discharge [65–70]. However, the conversion process in such a discharge is quite complicated and not well understood due to the high level of spatial inhomogeneity of the discharge plasma and the significant and fast change of plasma parameters distribution during the RF period.

In this paper, the dynamics of processes in a RF capacitive discharge in carbon dioxide is investigated using the SIGLO-rf fluid code. Particular attention is paid to the mechanisms of direct ionization of CO_2 molecules by electron impact, and the clarification of the reasons for their appearance in certain places of the discharge at certain moments of the RF electric field period. The appearance of intense ionization in a certain part of the discharge should be accompanied by increased dissociation of CO_2 molecules, which is of interest for solving the problem of plasma conversion of carbon dioxide.

SIGLO-RF CODE DESCRIPTION

1D fluid code SIGLO-rf is the software intended for simulation of RF capacitively coupled discharge. It is based on the equations and assumptions given in the papers of Prof. J.-P. Boeuf and Prof. L.C. Pitchford [56,58] and was developed at the University of Toulouse.

SIGLO-rf allows self-consistent calculation of temporal and average axial profiles of the density of charged particles (electrons, positive and negative ions), as well as potential and electric field strength over the RF period. In addition, it is possible to determine the density of the discharge current (electrons and ions both in the plasma and on the electrode, full current, displacement current), the power absorbed by ions and electrons, the electron temperature T_e, etc. At the same time, SIGLO-rf numerically integrates the system of balance equations for electrons, positive and negative ions, as well as Poisson's equation. Calculations are carried out from the initial value of the density of charged particles, which can be changed before starting the calculations, until a periodic steady state is reached. At the very beginning, the type and pressure of the gas p, the frequency of the RF electric field f, the distance between the electrodes d, and the gas temperature T_g are defined. Ion-induced electron emission is not taken into account, the corresponding coefficient $\gamma = 0$. That is, the SIGLO-rf code can be used only for calculations of the low-current α-mode of the RF capacitive discharge. At the same time, it is considered that 25% of electrons are reflected from the surface of the electrodes.

The input file with the gas parameters must contain the dependences of the average electron energy ε, their mobility μ_e, the ionization coefficient $\alpha = v_i/(\mu_e E)$, and the electron attachment coefficient $\eta = v_a/(\mu_e E)$, as a function of the reduced electric field E/p at a gas temperature of 300 K. Next, the SIGLO-rf code determines the dependences of the electron mobility μ_e, the ionization frequency v_i, the attachment frequency v_a, the energy loss frequency, and the diffusion coefficient D_e (which is determined using the Einstein's relation) on the average electron energy ε. Additionally, it is assumed that μ_e, D_e, v_i and v_a depend on the local average electron energy $\varepsilon(x,t)$ in the same way as under equilibrium conditions.

The input file should also contain the dependence of ion mobility on the local reduced electric field E/p. The diffusion coefficient of ions (both positive D_p and negative D_n) is determined from Einstein's relation at a weak field and is considered constant.

The densities of electrons n_e, positive n_p and negative ions n_n, the average electron energy ε and the potential V distribution are determined using the following equations. First, the balance equation for the density (continuity equation) is used for electrons:

$$\frac{\partial n_e}{\partial t} + \frac{\partial}{\partial x}\Phi_e = S_e, \tag{1}$$

where

$$S_e = (v_i - v_a)n_e + v_{detach}n_n - k_{recomb(e-i)}n_e n_p.. \tag{2}$$

It can be seen from equation (2) that the detachment of electrons from negative ions with the frequency v_{detach} is taken into account, and the coefficient $k_{recomb(e-i)}$ describes the loss of electrons during their recombination with positive ions.

Secondly, flow equations are also used to describe electrons

$$\Phi_e = -e\mu_e E n_e - D_e \frac{\partial n_e}{\partial x} \tag{3}$$

as well as the energy balance equation

$$\frac{\partial(n_e \varepsilon)}{\partial t} + \frac{5}{3}\frac{\partial}{\partial x}\Phi_\varepsilon = S_\varepsilon. \tag{4}$$

As already mentioned above, the dependence of the electron diffusion coefficient D_e on the average energy ε is found using the Einstein relation,

$$\frac{D_e}{\mu_e} = \frac{k_B T_e}{e} = \frac{2}{3}\frac{\varepsilon}{e}, \tag{5}$$

where k_B is Boltzmann constant, e is elementary charge.

The energy flux Φ_ε in equation (4) is defined as

$$\Phi_\varepsilon = -n_e \varepsilon \mu_e E - D_e \frac{\partial}{\partial x}(n_e \varepsilon). \tag{6}$$

The right-hand side of equation (4) contains

$$S_\varepsilon = -e\Phi_e E - n_e L(\varepsilon). \tag{7}$$

Here, the energy loss term $L(\varepsilon) = e\mu_e E^2$ is assumed to be the same as under equilibrium conditions (where $S_\varepsilon = 0$).

For positive ions, the balance (continuity) equation is solved:

$$\frac{\partial n_p}{\partial t} + \frac{\partial}{\partial x}\Phi_p = S_p, \tag{8}$$

where

$$S_p = \nu_i n_e - k_{recomb(e-i)} n_e n_p - k_{recomb(i-i)} n_n n_p. \tag{9}$$

The coefficient $k_{recomb(i-i)}$ takes into account the process of ion-ion recombination, that is, the loss of positive ions due to their recombination with negative ions. In equation (8), the flow of positive ions

$$\Phi_p = +e\mu_p E n_p - D_p \frac{\partial n_p}{\partial x} \tag{10}$$

where μ_p and D_p are mobility and diffusion coefficient of positive ions, respectively.

Similarly, the balance (continuity) equation is solved for negative ions:

$$\frac{\partial n_n}{\partial t} + \frac{\partial}{\partial x}\Phi_n = S_n, \tag{11}$$

where

$$S_n = \nu_a n_e - k_{recomb(i-i)} n_n n_p - \nu_d n_n. \tag{12}$$

Here it is taken into account that negative ions can be lost not only during ion-ion recombination but also when electrons are detached from them with frequency ν_d. Recall that negative ions are formed with a frequency of ν_a as a result of free electron attachment to the molecules of an electronegative gas.
The flux of negative ions is described by the formula

$$\Phi_n = -e\mu_n E n_n - D_n \frac{\partial n_n}{\partial x}, \tag{13}$$

where μ_n is mobility of negative ions, D_n is their diffusion coefficient.

Poisson's equation for the electric potential should be added to the above fluid equations

$$\frac{\partial^2}{\partial x^2}V = -\frac{e}{\varepsilon_0}\left(n_p - n_e - n_n\right). \tag{14}$$

At the same time, the potential is related to the electric field E by the equation

$$E = -\frac{\partial V}{\partial x}. \tag{15}$$

Now consider the boundary conditions. For the fluxes or densities of charged particles on the electrodes, they were as follows. The electron flux is equal to the thermal flow $n_e v_{the}/4$, where v_{the} is the thermal velocity of electrons. The ion density on the electrode is zero. Taking into account the small diffusion coefficient of ions, this means that their flow is equal to the drift flow when the ion velocity is directed towards the electrode. Otherwise, the ion flux is zero. We have already noted above that the reflection coefficient of electrons from the surface of the electrodes does not depend on their energy and is equal to 25%.

In addition, we consider the left electrode to be grounded ($V(0) = 0$), and the voltage from the RF generator with the waveform $V(d)=V_{rf}\cos(\omega t))$ is applied to the right electrode.

Calculations are made for carbon dioxide. Preliminary, the dependences of the electron mobility μ_e, the average electron energy ε, the ionization coefficient (the first Townsend coefficient α/p) and the attachment coefficient η/p on the reduced electric field E/p. At the same time, cross sections of electron collisions with carbon dioxide molecules were used, given in the LXCat database (www.lxcat.net) [78], where the cross sections from the Itikawa set [79] were chosen for CO_2. In addition, the values of electron mobility in CO_2 given in [80] were used.

For CO_2, the mobility of positive CO_2^+ ions in its own gas was taken from [81, 82], for the mobility of negative ions, the results of [81, 83] were used. The coefficient of recombination of positive and negative ions of $2\cdot10^{-7}$ cm^3/sec was taken from [84]. Coefficient of ion-electron dissociative recombination

$$CO_2^+ + e^- (300K) \rightarrow CO + O$$
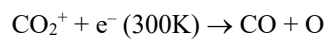
for cold electrons (300 K) is given in the paper [85]. Consider that this coefficient decreases with increasing electron temperature [86]. Then, for electron temperatures of several eV, this coefficient should be equal to $3.8\cdot10^{-8}$ cm^3/sec. To take into account the process of detachment of electrons from negative ions

$$O^- + CO_2 \rightarrow O + CO_2 + e^-$$
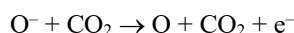
we used the dependence of the detachment coefficient on the reduced electric field given in [87].

SIMULATION RESULTS

Now let's consider the results of calculating the parameters of the RF capacitive discharge in CO_2, obtained using the SIGLO-rf code.

Carbon dioxide is one of the so-called "electronegative" gases. Collision of an electron with an energy higher than 3.3 eV [79] with a carbon dioxide molecule can lead to dissociative attachment

$$CO_2 + e^- \rightarrow CO + O^-,$$
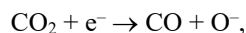
as a result of which a negative atomic ion of oxygen is formed. The attachment process worsens the conditions for maintaining the discharge. Free electrons can acquire high energy from the electric field and ionize gas molecules (that is, create new charged particles instead of those lost in the plasma volume, on the electrodes and walls of the discharge chamber), and must also carry the discharge current. An atom or gas molecule to which an electron has attached becomes a negative ion, the mass of which is thousands of times greater than the mass of the electron. Such an ion is not able to acquire high energy in the discharge to ionize gas molecules. Also, due to its inertness, it can carry only a small part of the discharge current. Therefore, the electrons lost due to attachment must be compensated in ionization processes.

Therefore, positive ions CO_2^+, electrons, and negative ions O^- should be present in the quasi-neutral plasma of the RF discharge in carbon dioxide (see Fig.1). At the same time, to fulfill the condition of quasi-neutrality, the positive ion density must be equal to the sum of the densities of electrons and negative ions, i.e. $n_p = n_e + n_n$. So, from Figure 1 we have, firstly, that in the center of the discharge $n_p = 4.52 \cdot 10^{10}$ cm^{-3}, $n_n = 4.3 \cdot 10^{10}$ cm^{-3}, $n_e = 2.2 \cdot 10^9$ cm^{-3}, so the quasi-neutrality is indeed fulfilled. Secondly, the negative ion density is about 20 times greater than the electron density. In fact, in the central part of the discharge, we have an ion-ion plasma with a small admixture of free electrons. However, in the near-electrode layers, the electron density is significantly higher than the negative ion density. It should be noted that electrons fill the near-electrode layers gradually, and are present there only during some part of the RF period [14,20,21]. At the same time, the closer to the electrodes, the shorter the time the electrons stay there. Therefore, the time-averaged electron density n_e in Figure 1 is much smaller than the positive ion density. But below we will see that when the near-electrode sheath adjacent to the temporary anode is filled, the electron density will be practically the same in the layer as the positive ion density.

Now consider negative ions. The high density of negative ions in the discharge is explained by the fact that the time-averaged potential of quasi-neutral plasma of the RF discharge in CO_2 is always positive (see Fig. 2). This leads to the retention of negative ions in the plasma volume, these ions cannot get to the electrodes. Negative ion density is regulated by the balance between their appearance as a result of attachment and losses due to detachment and ion-ion recombination. These listed loss processes are not fast, due to which the concentration of negative ions in the plasma can be quite large. Accordingly, the accumulation of negative ions in the plasma, firstly, reduces the ambipolar losses of positive ions [46,47], and secondly, it reduces the average plasma potential. The value of this potential (207 V) is lower than the average plasma potential in argon (230 V [88]).
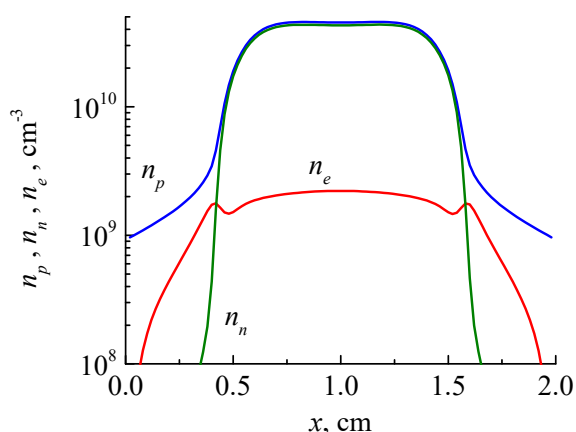

Figure 1. Time-averaged axial profiles of the density of electrons, negative and positive ions. RF discharge in CO_2 at gas pressure $p = 1$ Torr, frequency $f = 13.56$ MHz, distance between electrodes $d = 2$ cm, RF voltage amplitude $U_{rf} = 500$ V.
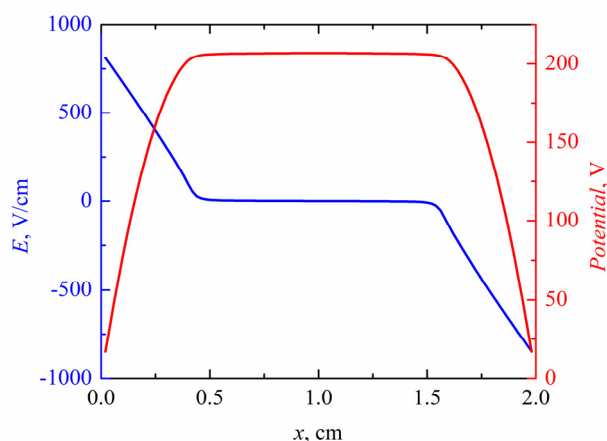
Figure 2. Time-averaged axial profiles of potential and electric field strength. RF capacitive discharge in CO_2. $p = 1$ Torr, $f = 13.56$ MHz, $d = 2$ cm, $U_{rf} = 500$ V

The RF discharge in CO_2 has a greater thickness of the near-electrode sheath (approximately 4.5 mm) than in argon under the same conditions (3 mm [88]). Therefore, the RF field strength near the electrode surface in CO_2 is significantly lower, it approaches 850 V/cm (compared to 1400 V/cm for argon).

The time-averaged electron energy (see Fig. 3) in the quasi-neutral plasma of RF discharge in CO_2 (approximately 3.5 eV) is significantly lower than for argon (reaches 6 eV [88]). The ionization rate, shown in Fig. 3, has two double maxima, which indicates the presence of an additional charged particle bearing process in the RF discharge in CO_2 compared to argon [88]. Below we will consider it in detail.

Regarding the average electron energy, we note that its value of 3.5 eV indicates that the main contribution to the CO_2 conversion process under the conditions considered in Figures 1–3 ($p = 1$ Torr, $U_{rf} = 500$ V) is not the direct dissociation of molecules by electron impact, but "climbing the ladder" of vibrational levels of molecules followed by their decomposition into CO and O [65,66, 89,90]. Electrons excite vibrational levels of CO_2 molecules, which then exchange the vibrational energy, and some part of CO_2 molecules can get enough vibrational energy to reach the dissociation threshold.

Now consider the dynamics of the plasma parameters, namely the change of their axial profiles over time. Fig. 4 shows the axial profiles of potential for several moments of the RF period.
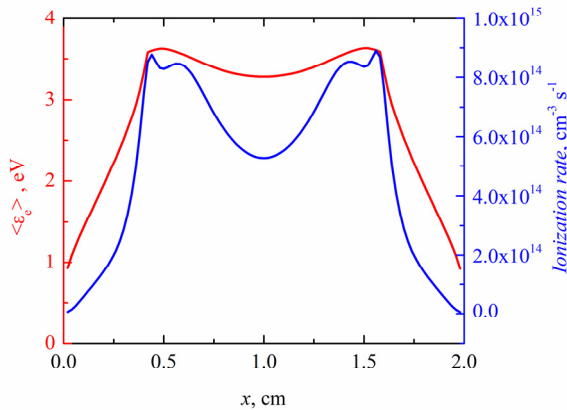

Figure 3. Time-averaged axial profiles of average electron energy and ionization rate. RF capacitive discharge in CO_2. $p = 1$ Torr, $f = 13.56$ MHz, $d = 2$ cm, $U_{rf} = 500$ V
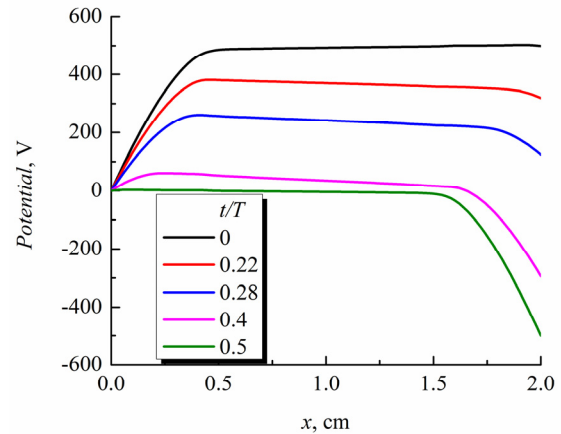
Figure 4. Axial profiles of potential for different parts of the RF period. RF capacitive discharge in CO_2. $p = 1$ Torr, $f = 13.56$ MHz, $d = 2$ cm, $U_{rf} = 500$ V

At first glance, these profiles are similar to the corresponding profiles for argon [88]. However, in the quasi-neutral plasma, the slope of the profiles in CO_2 is greater, which indicates a higher RF electric field strength. In addition, near the boundary of the collapsing near-electrode layer, the potential increases faster than in the plasma, and a so-called "double layer" is formed [41, 44, 54–58]. This is best seen on the axial profile of the electric field strength, one of which is shown in Fig. 5. In fact, the so-called "passive" (DL_1) and "active" (DL_2) double layers (by the definition in [41]) can be seen on this axial profile. Note that an additional third double layer (DL_3) began to appear in Figure 3, the presence of which is not mentioned in the papers of other authors. The role of these double layers, the conditions and causes of their occurrence will be considered below.
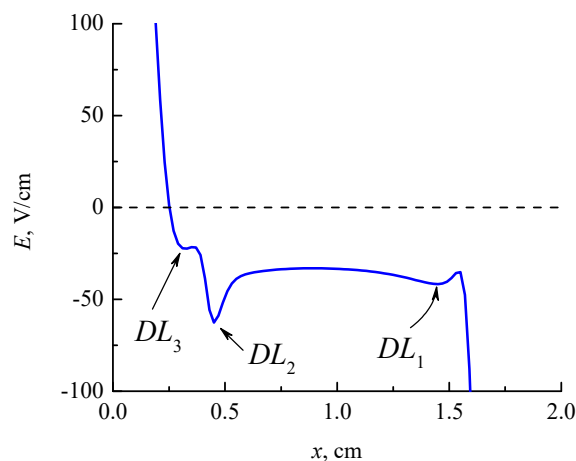

Figure 5. Axial profile of the electric field strength for the moment of the RF period $t/T = 0.4$. RF capacitive discharge in CO_2. "DL" stands for double layer. $p = 1$ Torr, $f = 13.56$ MHz, $d = 2$ cm, $U_{rf} = 500$ V

Figure 5 shows that in the central region of the plasma the field is approximately equal to 33 V/cm, and in the "active" double layer it reaches 63 V/cm. Due to the exponential dependence of the ionization frequency on the electric field strength, the ionization rate in the double layer (with approximately twice the electric field strength) should be two dozen times higher than in the plasma volume.

Let's find out why these double layers are needed in RF capacitive discharge in CO_2. To do this, first consider the dynamics of the electron density shown in Fig. 6. The densities of positive and negative ions practically do not change during the RF period, so here we give them only for the initial moment $t/T = 0$. At this moment, the electrons are completely pushed out of the left near-electrode sheath by a strong electric field, fill the right sheath, and partially hit the right electrode, which is a temporary anode. At the same time, on the corresponding profile in Fig.6 near the boundary of the right sheath (approximately at $x = 1.6$ cm), we can see a spike in the electron density, in which n_e is even higher than in the central region of the discharge.
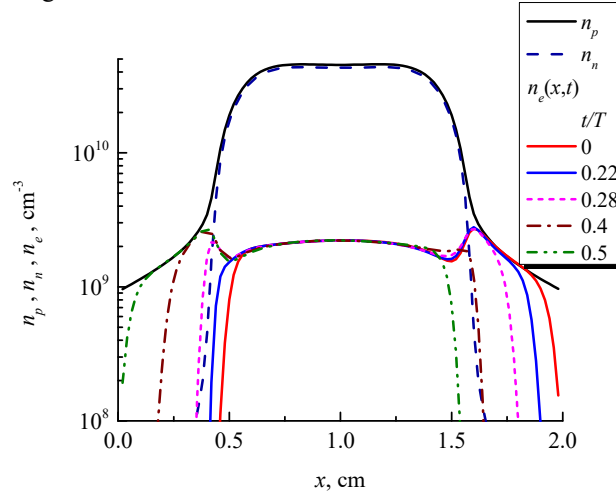

Figure 6. Axial density profiles of positive ions, negative ions and electrons for different parts of the RF period. RF capacitive discharge in CO_2. $p = 1$ Torr, $f = 13.56$ MHz, $d = 2$ cm, $U_{rf} = 500$ V

The electron density peak appeared due to the formation of an "active" double layer near the boundary of the right sheath during the previous half of the RF period. This double layer should, firstly, approximate the density of electrons and positive ions in the sheath to ensure quasi-neutrality, and secondly, bring to the right electrode the number of electrons necessary to maintain the balance of the positive and negative charges throughout the RF period. This balance must be fulfilled to ensure the stability of the discharge. But only positive ions and electrons in equal quantities can enter the electrode, while the flow of negative ions to the electrode is zero (see Fig. 7).
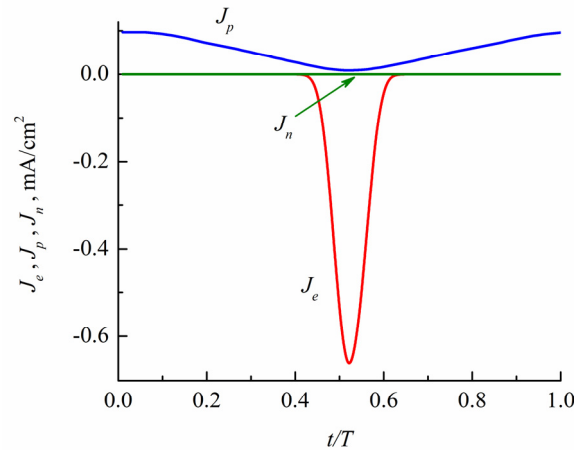

Figure 7. Time dependence of the current density of positive J_p and negative ions J_n, as well as electrons J_e on the left electrode. $p = 1$ Torr, $f = 13.56$ MHz, $d = 2$ cm, $U_{rf} = 500$ V

In the RF discharge in argon [88], where the concentrations of positive ions and electrons in a quasi-neutral plasma were equal, there were no problems with ensuring the balance of charge flows to the electrodes. However, in the CO_2 case, the electron density is approximately 20 times lower than that of positive ions. Therefore, for the required number of electrons to enter the electrode, it must be generated as a result of increased ionization. Electrons born in the plasma may not reach the electrode and stick to the gas molecules. Thus, the additional electron generation should appear just in the sheath, if possible, near the electrode. This is the reason for the formation of an "active" double layer with an increased RF electric field near the boundary of the near-electrode sheath.

Note that the presence of a maximum electron density in the region of the active double layer near the boundary of the near-electrode sheath plays an important role. When the corresponding sheath borders the temporary anode, i.e. is in the anodic phase, the electric field attracts electrons to this electrode. But from Figures 5 and 8, we see that closer to the

temporary anode, the electric field changes its sign and pushes electrons away from it. Therefore, the electrons density between the double layer and the point of the electric field sign-change increases due to their accumulation in this area. Some of the electrons pass through the potential barrier, and some are reflected back. The electron density increase leads to an increase in the diffusion current towards the temporary anode, as well as a decrease in the height of the potential barrier. Thanks to this, the necessary number of electrons can reach the temporary anode, which allows for maintaining the charge balance during the RF period.
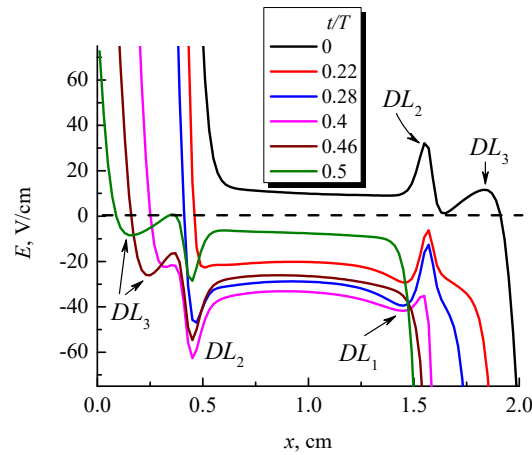

Figure 8. Axial profiles of the electric field strength for different moments of the RF period t/T. p = 1 Torr, f = 13.56 MHz, d = 2 cm, U_{rf} = 500 V

While the active double layer ensures the balance of the number of charges on the temporary anode, a "passive" double layer is also observed near the border of the opposite near-electrode sheath that is in the cathodic phase. It maintains the electron density in the plasma at a level sufficient for stable burning of the discharge, when ionization compensates for all electron losses. The electric field in the plasma volume is weaker than in the passive double layer and mainly transfers the discharge current through the plasma.

Now let's consider the reasons for the formation of the third double layer (in Figures 5 and 8 it is marked as DL_3). The thickness of the near-electrode sheath is a complex function of the frequency and amplitude of the RF voltage, the gas pressure, the electric field strength in the plasma volume, and the distance between the electrodes [2], and this is valid for electropositive gases. In electronegative gases, this dependence is even more complicated. We said above that the active double layer is formed near the boundary of the near-electrode sheath, which is in the anodic phase. Electrons born in it move towards the temporary anode. However, it is necessary to consider the process of their loss due to attachment to gas molecules. Suppose these losses are high enough so that fewer electrons pass through the near-electrode layer to the electrode than is necessary to balance the charge on its surface. In that case, another double layer is formed closer to the surface of the temporary anode, which is auxiliary and keeps the ionization rate higher than the attachment rate.

Let's return to the density profiles in Fig. 6. We considered only the profile for the initial moment $t/T = 0$. Recall that at this moment a positive amplitude value of the RF voltage (+500 V) is applied to the right electrode.

Next, the voltage on the right electrode decreases, and potential difference between the electrode and the plasma increases (which we have already seen in Fig. 4). As a result, the thickness of the right sheath increases, and its border begins to move away from the electrode. Accordingly, the electrons that previously filled the right layer began to be pushed out of it. Electron density profiles move away from the right electrode.

In the case of low gas pressure, when electrons rarely collide with gas molecules, the reflection of electrons from the boundary of the expanding near-electrode layer plays a significant role in maintaining the discharge, and it is called "stochastic heating" [1, 4, 27]. Fluid modeling cannot describe the process of stochastic heating due to its non-local nature, but we consider here only the case of higher pressure. Electrons that filled the near-electrode layer during the anodic phase are pushed into the plasma by the electric field of the layer during the transition to the cathodic phase. However, the frequent collisions of electrons with gas molecules make it possible to describe this process using a fluid code. The term "wave-riding" electron heating is sometimes used in the literature just for the process of electron heating in the cathode phase of the near-electrode sheath [57]. But usually, this heating is also called stochastic. We will continue to use this name as well, but with the above in mind.

Due to stochastic heating of electrons a spike in the ionization rate appears in Fig. 9 in the right sheath and near its boundary (in the figure it is marked as StH - "Stochastic Heating"). After a time of approximately $t/T = 0.2$, a passive double layer (marked in Figure 9 as DL_1 – "Double Layer") appears near the border of the expanding near-electrode sheath, and after $t/T = 0.25$, near the border of the left sheath, an active double layer (DL_2) is formed. Thanks to the increased ionization rate in it, electrons gradually fill the left near-electrode layer, maintain quasi-neutrality in the filled part, and then partially escape to the left electrode to ensure the balance of the charge of the opposite sign. At $t/T = 0.4$, the formation of the third double layer (DL_3) is observed. The corresponding behavior of the electric field strength is

visible in Fig. 8. Later, at $t/T > 0.5$, stochastic heating and a double layer are formed in the reverse order, which we can see in Fig. 9. Note that approximately in the place where there was an active double layer with the maximum electric field strength, then a region with a minimum field appears since a high level of ionization is maintained due to stochastic heating (deeper in the sheath) and in the passive double layer, which is further from the electrode, deeper in the plasma volume.
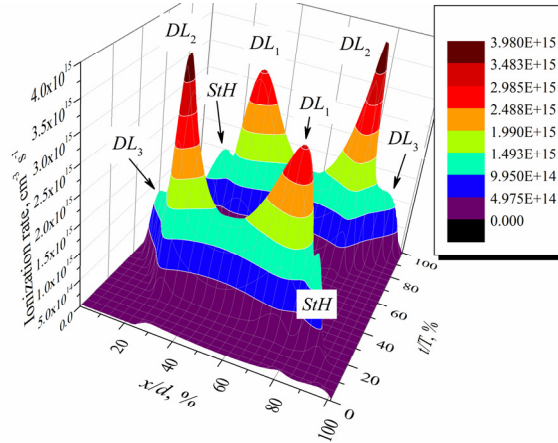

Figure 9. Space-time dependence of the ionization rate. Peaks corresponding to stochastic heating (StH) and the formation of double layers (DL) are marked. $p = 1$ Torr, $f = 13.56$ MHz, $d = 2$ cm, $U_{rf} = 500$ V

Now let's find out how the RF voltage amplitude under fixed other conditions affects the ionization processes in the discharge during the RF period. The corresponding space-time dependencies are shown in Fig. 10.
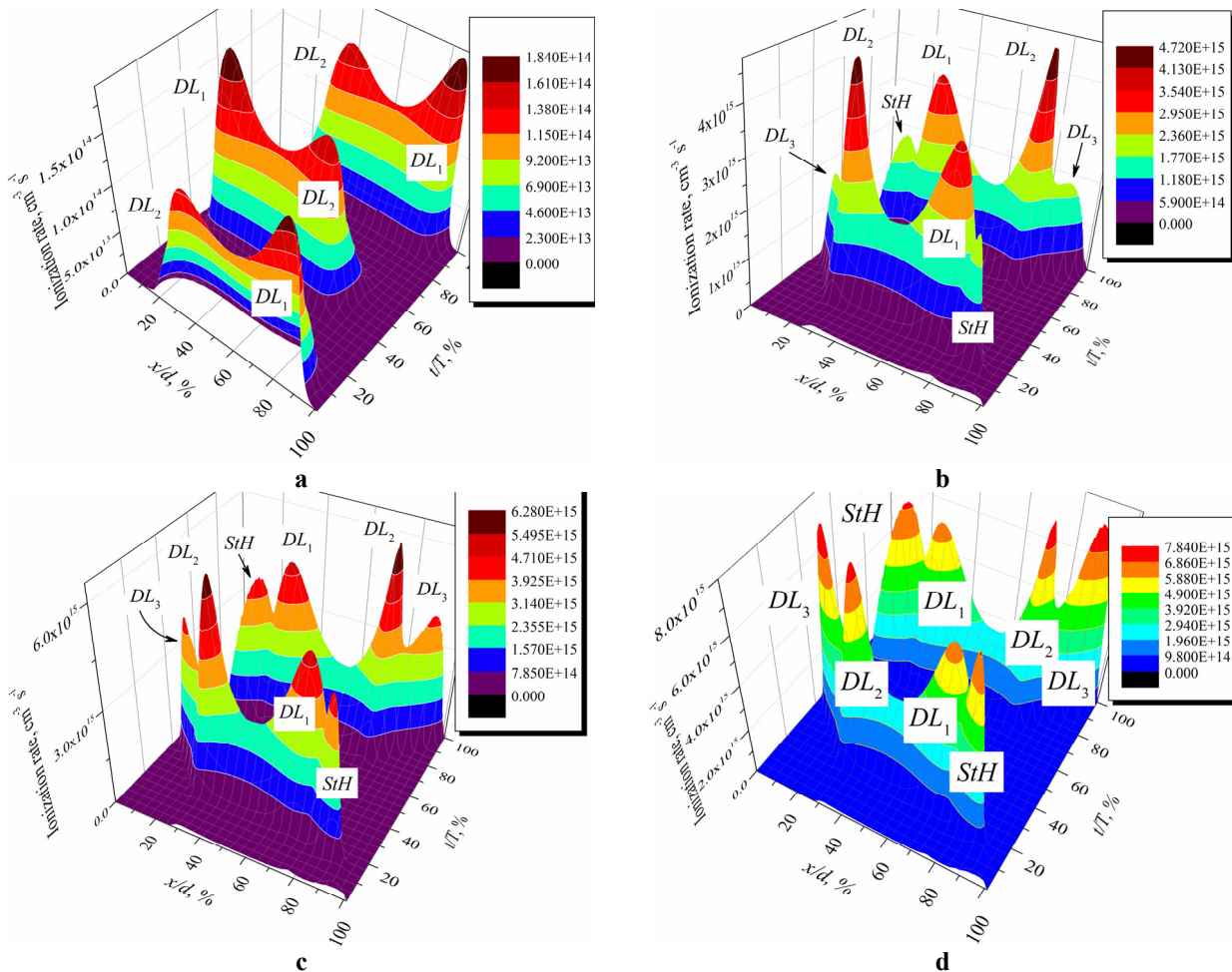

Figure 10. Space-time dependence of the ionization rate. $p = 1$ Torr, $f = 13.56$ MHz, $d = 2$ cm, $U_{rf} =$ a) 85 V, b) 600 V, c) 800 V, d) 1000 V

At the lowest RF voltage (85 V at a pressure of 1 Torr), we see only two peaks corresponding to the passive (DL_1) and active (DL_2) double layers. Stochastic heating of electrons does not yet play a significant role in the discharge under

these conditions. The ionization peak, corresponding to the third double layer, is also missing. At a voltage of 500 V (see Figure 9), peaks of the ionization rate appear due to stochastic heating and the formation of the third double layer (DL_3). Their intensity increases rapidly with the increase of the RF voltage amplitude, and at the maximum voltage of 1000 V considered by us, the intensities of all 4 peaks (StH, DL_1, DL_2, DL_3) become almost the same. That is, during the half of the RF period, the discharge is supported by 4 bursts of ionization in different parts of the gap between the electrodes, which, with some overlap in time, take place alternately $StH \rightarrow DL_1 \rightarrow DL_2 \rightarrow DL_3$.

Let's consider this procedure in more detail for the RF voltage amplitude of 1000 V. Figure 11 shows the axial profiles of the ionization and attachment rates for several moments of the RF period. At the initial moment, when the right electrode is a temporary anode and electron flow enters it, we see the presence of a peak near the electrode itself, which corresponds to the third double layer DL_3. It is in this region that the ionization process occurs faster than the attachment. In other parts of the discharge, where the electrons are present (plasma volume and part of the right near-electrode layer), electron losses prevail. Next, the sign of the potential on the right electrode changes, it becomes a temporary cathode. The ionization rate for some time becomes small compared to the attachment rate ($t/T = 0.16$). Next, RF potential on the right electrode increases, the thickness of the right sheath increases, and at $t/T = 0.29$, the StH peak of stochastic electron heating is visible, and the passive DL_1 and active DL_2 double layers begin to form. Over time, the intensities of these three peaks increase, and at $t/T = 0.35$, when the RF current amplitude reaches a maximum, the ionization rate in the entire interval significantly exceeds the electron loss rate due to attachment. At $t/T > 0.4$, the peak of stochastic heating practically disappears, but the peak of the ionization rate appears near the left electrode (temporary anode) due to the formation of the third double layer DL_3, which becomes dominant by the end of the half-period $t/T = 0.5$.
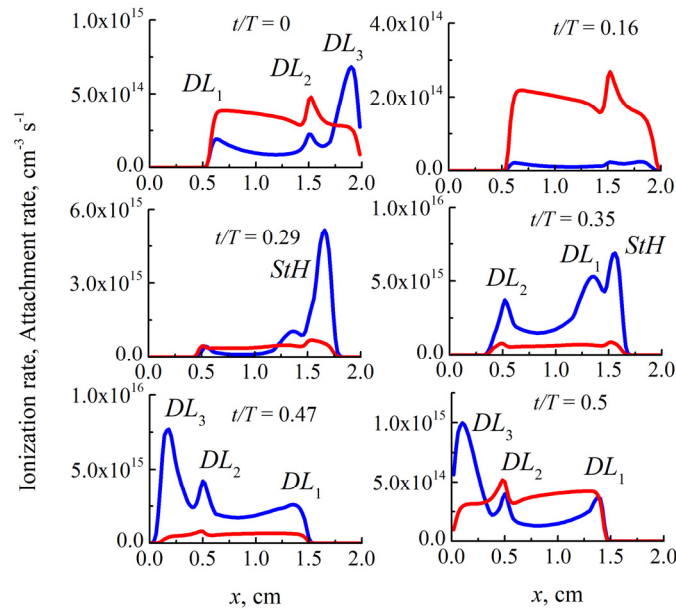

Figure 11. Axial profile of ionization (blue lines) and attachment (red lines) rates for different moments of the RF period t/T.
$p = 1$ Torr, $f = 13.56$ MHz, $d = 2$ cm, $U_{rf} = 1000$ V

Next, we will consider ionization processes in a wide range of carbon dioxide pressures. The corresponding space-time dependences of the ionization rate are shown in Fig. 12 for the RF voltage amplitude of 1000 V. At a low pressure of 0.1 Torr, one broad peak of the ionization rate is observed during half of the RF period. To find out its nature, we will additionally analyze the axial profiles of reduced electric field strength E/p, shown in Fig. 13. From this figure, we can see that the ionization peak appeared as a result of the simultaneous action of stochastic heating and additional heating of electrons by the RF electric field in the plasma volume. Double layers are not observed under these conditions. When the gas pressure increases to 0.2 Torr, the ionization rate during half of the RF period has two maxima: first, stochastic heating occurs, and after $t/T > 0.25$, a wide double layer is formed, occupying most of the left near-electrode sheath. It is the same third, auxiliary double layer, which we talked about above.

At a gas pressure of 0.5 Torr, the peak of the active double layer is added to the ionization peaks of stochastic heating, and the third double layer, which is located near the boundary of the near-electrode sheath, while the passive double layer is still missing. It begins to appear at a gas pressure of 0.75 Torr and above. The peaks of the ionization rate for a carbon dioxide pressure of 1 Torr are shown in Fig. 10, and we found that at this pressure, all three double layers and stochastic heating are observed during half of the RF period. With a further increase in pressure to 1.5 Torr, the peak of stochastic heating weakens significantly, and the peak of the third double layer also becomes significantly weaker. In the case of a high gas pressure of 9.9 Torr, the peak of the active double layer dominates, the peak of the passive double layer is approximately twice as large, and we also see a constant level of ionization in the RF electric field in the plasma bulk.
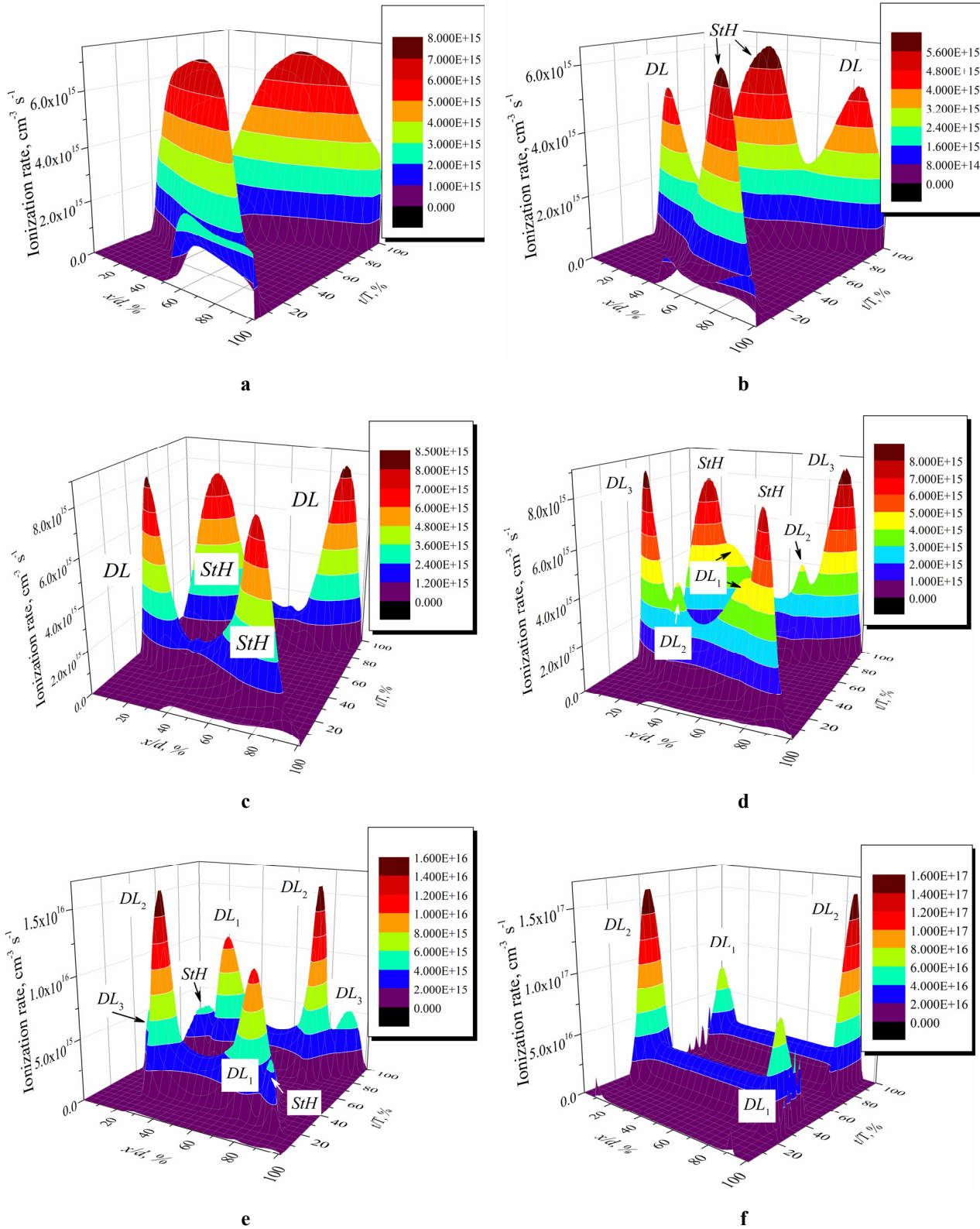
Figure 12. Space-time dependence of the ionization rate for different values of the gas pressure. $f = 13.56$ MHz, $d = 2$ cm, $U_{rf} = 1000$ V: a) 0.1 Torr; b) 0.2 Torr; c) 0.5 Torr; d) 0.75 Torr; e) 1.5 Torr; f) 9.9 Torr
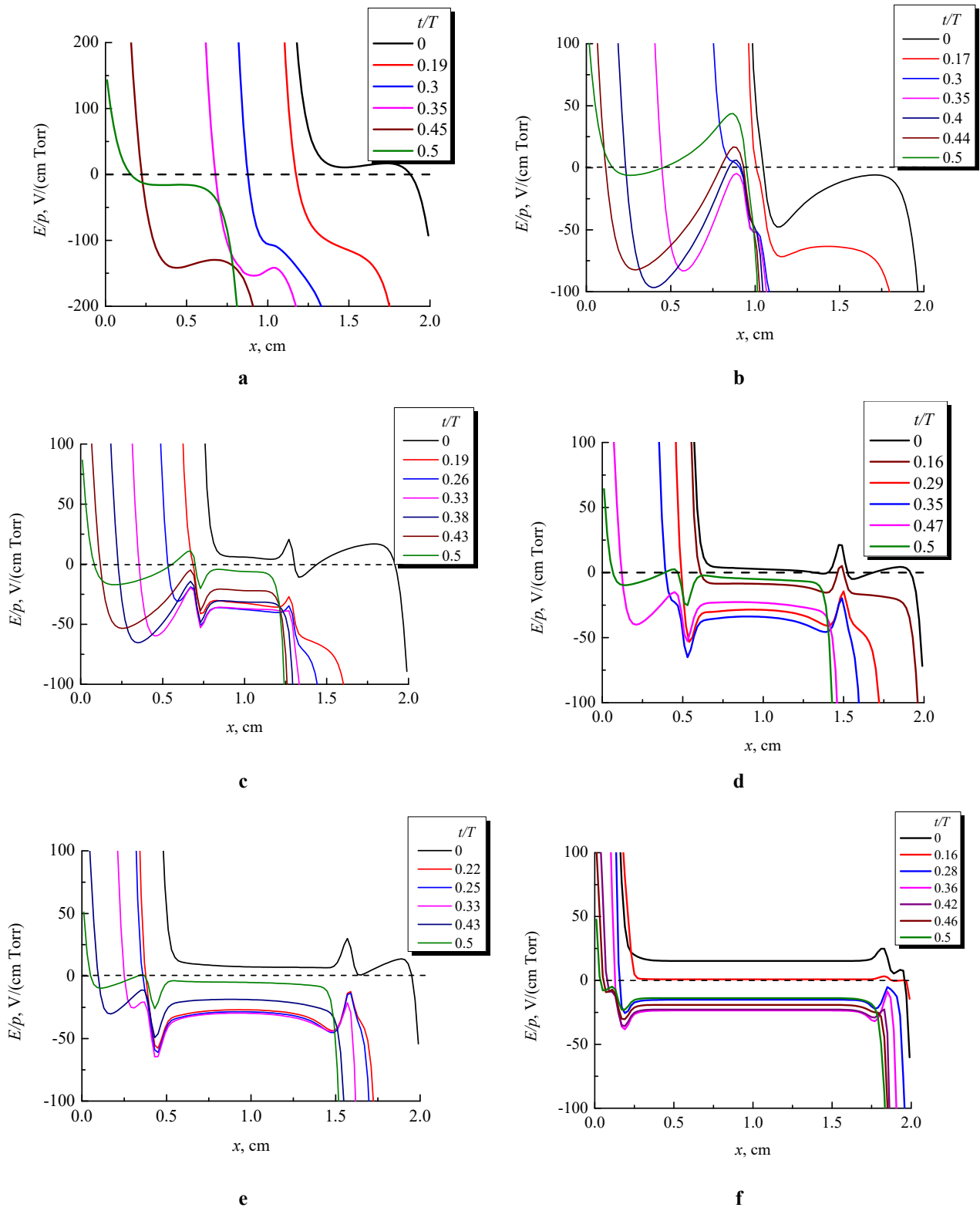
Figure 13. Axial profiles of the reduced electric field strength E/p at different moments of the RF period for different values of the gas pressure. f = 13.56 MHz, d = 2 cm, U_{rf} = 1000 V: a) 0.1 Torr; b) 0.2 Torr; c) 0.5 Torr; d) 1 Torr; e) 1.5 Torr; f) 9.9 Torr

As it follows from the above results, there is a narrow range of conditions under which 4 intensive ionization sources, stochastic heating, and 3 double layers (passive, active, and auxiliary) can participate in the discharge. This phenomenon is most clearly observed $p = 1 \pm 0.05$ Torr, $f = 13.56$ MHz and $d = 2$ cm at high RF voltages $U_{rf} = 500–1000$ V. For these conditions, $pd = 2$ Torr cm and $fd = 27.12$ MHz cm.

In [91], it was shown that RF gas breakdown and, in general, processes in RF capacitive discharge are controlled by the similarity law

$$U_{rf} = \psi\left(pd, fd, \frac{d}{R}\right),$$

where R is the radius of the discharge tube. Further analysis of the similarity law was carried out in papers [92–94].

Let's find out whether the presence of 4 intense ionization peaks will be observed at other distances between the electrodes, RF field frequencies, and gas pressure values. We will conduct the analysis for fixed values of the similarity parameters $pd = 2$ Torr cm and $fd = 27.12$ MHz cm. That is, after changing the frequency of the RF electric field, we must adjust the values of the distance between the electrodes and the gas pressure accordingly. For example, at a frequency of 3.89 MHz, the distance should be equal to 8 cm (to maintain $fd = 27.12$ MHz cm). Then the gas pressure should be 0.25 Torr (for $pd = 2$ Torr cm). We will do the same for other combinations of f, d and p. The calculation results presented in Fig. 14 show that at fixed values of the similarity parameters $pd = 2$ Torr cm and $fd = 27.12$ MHz cm, at least in the frequency range $f = 3.89 – 67.8$ MHz, 4 intense ionization peaks are observed. That is, our calculations using the SIGLO–rf code and the similarity law allow us to predict the behavior of ionization processes in a radio-frequency capacitive discharge.
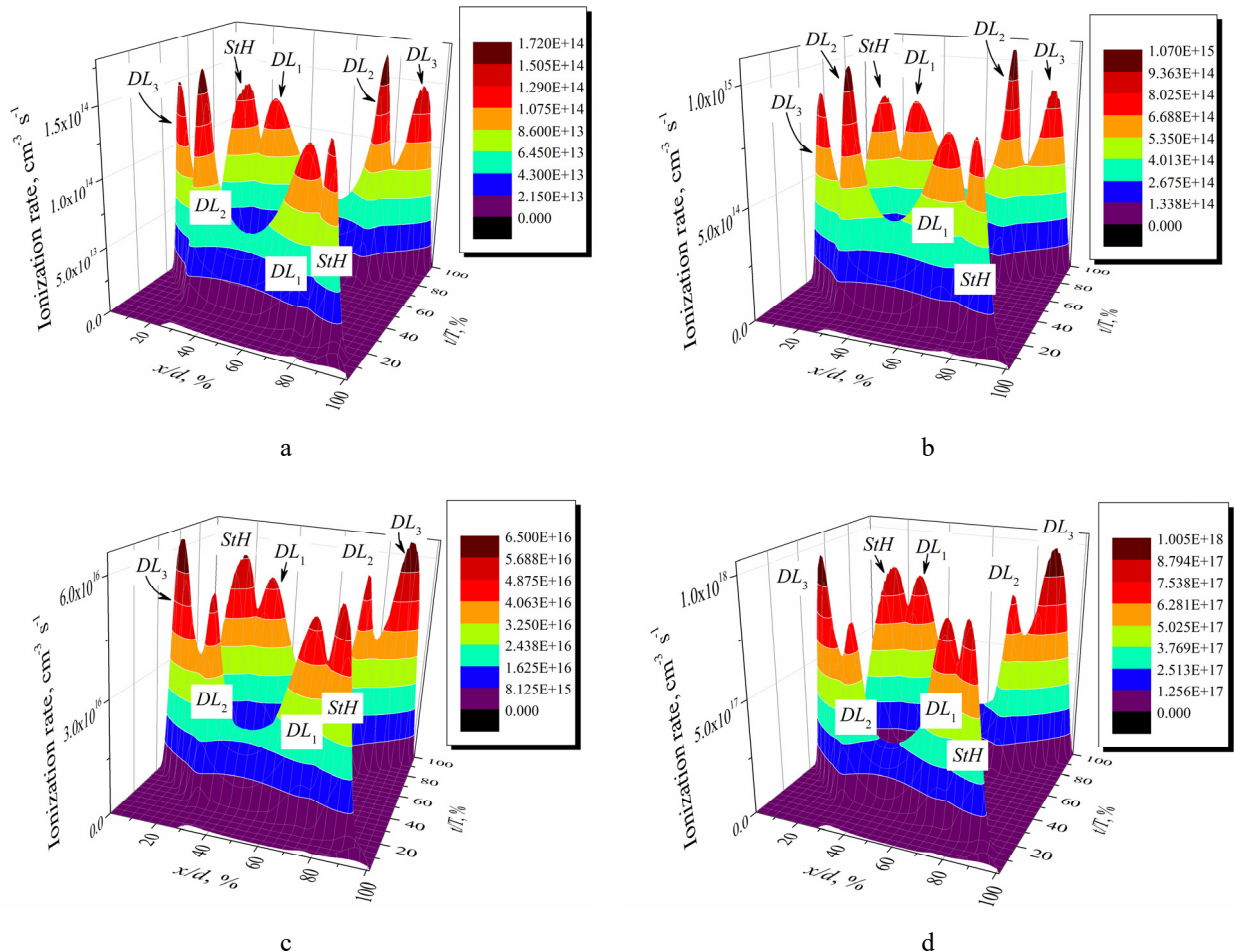

Figure 14. Space-time dependence of the ionization rate. $U_{rf} = 1000$ V:
a) $f = 3.89$ MHz, $d = 8$ cm, $p = 0.25$ Torr; b) $f = 6.78$ MHz, $d = 4$ cm, $p = 0.5$ Torr; c) $f = 27.12$ MHz, $d = 1$ cm, $p = 2$ Torr; d) $f = 67.8$ MHz, $d = 0.04$ cm, $p = 5$ Torr

CONCLUSIONS

In this paper, the time-averaged and spatio-temporal profiles of the parameters of the RF capacitive discharge in carbon dioxide were investigated using the one-dimensional fluid code SIGLO-rf, which numerically calculates the balance equation (continuity equation) of electrons and each of the ion species (positive and negative), the electron energy

balance equation, and Poisson's equation for the electric potential. The processes of ionization bearing of electrons and positive ions, attachment of electrons to gas molecules, their detachment from negative ions, as well as processes of recombination of positive ions with electrons and negative ions are taken into account. Processes of ion-induced electron emission from the electrode surface are ignored, which limits the applicability of the code only to the low-current mode of RF capacitive discharge.

With the help of this SIGLO-rf code, the averaged over the RF period axial profiles of the densities of electrons, positive and negative ions, as well as the potential and electric field strength, were calculated in carbon dioxide. Most of the results were obtained for the distance between the electrodes $d = 2$ cm and RF frequency $f = 13.56$ MHz, but additional calculations were also carried out at $d = 0.04$–8 cm and $f = 3.89$–67.8 MHz. In the RF discharge in CO_2, the quasi-neutral plasma consists of electrons and positive ions, and as a result of the process of dissociative attachment of electrons to gas molecules, negative ions of atomic oxygen appear. Their density in a quasi-neutral plasma is about ten times higher than the electron density. These negative ions are retained in the plasma volume and reduce the average potential of the plasma (compared to plasma in argon).

The spatio-temporal dynamics of electron density, potential and electric field strength, as well as ionization and attachment rates in RF capacitive discharge were also studied. It is shown that in the RF discharge in CO_2, to ensure the balance of positive and negative charges that escape to the electrodes during the RF period, as well as to maintain quasi-neutrality in the regions filled with plasma, near the boundary of the sheaths, passive and active double layers are formed. In these double layers, thanks to the increased electric field, gas molecules are intensively ionized by electrons. At the same time, during the first half of the RF period, three bursts of ionization are observed in the RF discharge in CO_2, which correspond to stochastic heating in one layer and the formation of double layers. This process is repeated in the reverse direction in the second half of the RF period.

It is shown that under certain conditions, $pd = 2$ Torr cm and $fd = 27.12$ MHz cm, even 4 ionization peaks can be observed during half of the RF period: resulting from stochastic heating, as well as the passive, active and auxiliary double layers. The auxiliary double layer occurs inside the near-electrode sheath near the surface of the temporary anode and contributes to bringing electrons to its surface. The simultaneous presence of 4 peaks was verified by calculations in a wide range of distances between electrodes, values of carbon dioxide pressure, and RF frequencies.

ORCID
Valeriy Lisovskiy, https://orcid.org/0000-0002-6339-4516; **Stanislav Dudin,** https://orcid.org/0000-0001-9161-4654
Vladimir Yegorenkov, https://orcid.org/0000-0002-7252-3711

REFERENCES
[1] A. Lieberman, and A.J. Lichtenberg, *Principles of Plasma Discharges and Materials Processing*, 2nd ed. (Wiley, Hoboken, USA, 2005). https://doi.org/10.1002/0471724254
[2] Yu.P. Raizer, M.N. Shneider, and N.A. Yatsenko, *Radio-frequency Capacitive Discharges* (CRC Press, Boca Raton, FL, 1995).
[3] J. Reece Roth, *Industrial Plasma Engineering. vol. 2: Applications to Nonthermal Plasma Processing* (Bristol, IOP Publishing, 2001).
[4] P. Chabert, and N. Braithwaite, *Physics of Radio-Frequency Plasmas* (Cambridge University Press, Cambridge, 2011).
[5] M. Keidar, and I. Beilis, *Plasma Engineering* (Academic Press, London, 2018).
[6] G. Colonna, and A. D'Angola, *Plasma Modeling: Methods and applications* (IOP Publishing, Bristol, 2022).
[7] J.F. Friedrich, and J. Meichsner, *Nonthermal Plasmas for Materials Processing: Polymer Surface Modification and Plasma Polymerization* (Wiley-Scrivener, Hoboken, 2022).
[8] L. Bardos, and H. Barankova, *Microwave Plasma Sources and Methods in Processing Technology* (Hoboken, Wiley-IEEE Press, 2022).
[9] T. Shao, and Ch. Zhang, editors, *Pulsed Discharge Plasmas: Characteristics and Applications* (Springer, Singapore, 2023).
[10] Ph. Belenguer, and J.P. Boeuf, Physical Review A, **41**, 4447 (1990), https://doi.org/10.1103/PhysRevA.41.4447
[11] V.A. Godyak, R.B. Piejak, and B.M. Alexandrovich, IEEE Transactions on Plasma Science, **19**, 660 (1991). https://doi.org/10.1109/27.90309
[12] V.A. Lisovskii, Technical Physics Letters, **24**, 308 (1998). https://doi.org/10.1134/1.1262093
[13] V. Lisovskiy, J.-P. Booth, S. Martins, K. Landry, D. Douai, and V. Cassagne, Europhysics Letters **71**, 407 (2005). https://doi.org/10.1209/epl/i2005-10108-1
[14] V. Lisovskiy, A. Minenkov, S. Dudin, S. Bogatyrenko, P. Platonov, and V. Yegorenkov, ACS Omega **7**, 47941 (2022). https://doi.org/10.1021/acsomega.2c05846
[15] S.Y. Moon, J.K. Rhee, D.B. Kim, and W. Choe, Physics of Plasmas, **13**, 033502 (2006), https://doi.org/10.1063/1.2177590
[16] V. Lisovskiy, J.-P. Booth, K. Landry, D. Douai, V. Cassagne, and V. Yegorenkov, J. Phys. D: Appl. Phys. **40**, 6631 (2007). https://doi.org/10.1088/0022-3727/40/21/023
[17] V. Lisovskiy, J.-P. Booth, J. Jolly, S. Martins, K. Landry, D. Douai, V. Cassagne, and V. Yegorenkov, J. Phys. D: Appl. Phys. **40**, 6989 (2007), https://doi.org/10.1088/0022-3727/40/22/020
[18] V. Lisovskiy, V. Yegorenkov, E. Artushenko, J.-P. Booth, S. Martins, K. Landry, D. Douai, and V. Cassagne, Plasma Sources Sci. Technol. **22**, 015018 (2013). https://doi.org/10.1088/0963-0252/22/1/015018
[19] V. Godyak, Phys. Plasmas, **27**, 013504 (2020). https://doi.org/10.1063/1.5122957

[20] M.A. Lieberman, IEEE Trans. Plasma Sci. **17**, 338 (1989). https://doi.org/10.1109/27.24645
[21] M.A. Lieberman, IEEE Trans. Plasma Sci. **16**, 638 (1988). https://doi.org/10.1109/27.16552
[22] A.J. Lichtenberg, V. Vahedi, M.A. Lieberman, and T. Rognlien, J. Appl. Phys. **75**, 2339 (1994). https://doi.org/10.1063/1.356252
[23] F. Hamaoka, T. Yagisawa, and T. Makabe, J. Phys: Conf. Series **86**, 012018 (2007). https://doi.org/10.1088/1742-6596/86/1/012018
[24] V.I. Kolobov, R.R. Arslanbekov, D. Levko, and V.A. Godyak, J. Phys. D: Appl. Phys. **53**, 25LT01 (2020). https://doi.org/10.1088/1361-6463/ab7ca0
[25] J.P. Verboncoeur, M. Alves, V. Vahedi, and C. Birdsall, Simultaneous potential and circuit solution for 1D bounded plasma particle simulation codes J. Comput. Phys. **104**, 321 (1993). https://doi.org/10.1006/jcph.1993.1034
[26] V. Vahedi, C.K. Birdsall, M.A. Lieberman, G. DiPeso, and T.D. Rognlien, Plasma Sources Sci. Technol. **2**, 273 (1993). https://doi.org/10.1088/0963-0252/2/4/007
[27] T. Lafleur, P. Chabert, and J.P. Booth, Plasma Sources Sci. Technol. **23**, 035010 (2014). https://doi.org/10.1088/0963-0252/23/3/035010
[28] E. Kawamura, M.A. Lieberman, A.J. Lichtenberg, and P. Chabert, J. Vac. Sci. Technol. A, **38**, 023003 (2020). https://doi.org/10.1116/1.5135575
[29] J.T. Gudmundsson, J. Krek, D.-Q. Wen, E. Kawamura, and M.A. Lieberman, Plasma Sources Sci. Technol. **30**, 125011 (2021). https://doi.org/10.1088/1361-6595/ac3ba1
[30] Z. Donkó, Plasma Sources Sci. Technol. **20**, 024001 (2011). https://doi.org/10.1088/0963-0252/20/2/024001
[31] J. Schulze, E. Schüngel, A. Derzsi, I. Korolov, Th. Mussenbrock, and Z. Donkó, IEEE Trans. Plasma Sci. **42**, 2780 (2014). https://doi.org/10.1109/TPS.2014.2306265
[32] M. Vass, S. Wilczek, T. Lafleur, R. P. Brinkmann, Z. Donko, and J. Schulze, Plasma Sources Sci. Technol. **29**, 085014 (2020). https://doi.org/10.1088/1361-6595/aba111
[33] D.A. Schulenberg, I. Korolov, Z. Donko, A. Derzsi, and J. Schulze, Plasma Sources Sci. Technol. **30**, 105003 (2021). https://doi.org/10.1088/1361-6595/ac2222
[34] D.-Q.Wen, J. Krek, J. T. Gudmundsson, E. Kawamura, M. A. Lieberman, P. Zhang, and J. P. Verboncoeur, Plasma Sources Sci. Technol. **32**, 064001 (2023). https://doi.org/10.1088/1361-6595/acd6b4
[35] A. Derzsi, B. Horváth, Z. Donkó, and J. Schulze, Plasma Sources Sci. Technol. **29**, 074001 (2020). https://doi.org/10.1088/1361-6595/ab9156
[36] S. Rauf, Plasma Sources Sci. Technol. **29**, 095019 (2020). https://doi.org/10.1088/1361-6595/abac4a
[37] L. Wang, P. Hartmann, Z. Donkó, Y.-H. Song, and J. Schulze, Plasma Sources Sci. Technol. **30**, 085011 (2021). https://doi.org/10.1088/1361-6595/abf206
[38] L. Wang, P. Hartmann, Z. Donkó, Y.-H. Song, and J. Schulze, J. Vac. Sci. Technol. A **39**, 063004 (2021). https://doi.org/10.1116/6.0001327
[39] S. Sharma, S. Patil, S. Sengupta, A. Sen, A. Khrabrov, and I. Kaganovich, Phys. Plasmas, **29**, 063501 (2022). https://doi.org/10.1063/5.0094409
[40] A. Picard, G. Turban, and B. Grolleau, J. Phys. D: Appl. Phys. **19**, 991 (1986). https://doi.org/10.1088/0022-3727/19/6/014
[41] N. Nakano, N. Shimura, Z. Lj. Petrovic, and T. Makabe, Phys. Rev. E, **49**, 4455 (1994). https://doi.org/10.1103/PhysRevE.49.4455
[42] Y.T. Lee, M.A. Lieberman, A.J. Lichtenberg, F. Bose, H. Baltes, and R. Patrick, J. Vac. Sci. Technol. A: Vacuum, Surfaces and Films, **15**, 113 (1997). https://doi.org/https://doi.org/.1116/1.580452
[43] M. Shibata, T. Makabe, and N. Nakano, Jpn. J. Appl. Phys. **37**, 4182 (1998). https://doi.org/10.1143/JJAP.37.4182
[44] V.A. Lisovskiy and V.D. Yegorenkov, Vacuum, **80**, 458 (2006). https://doi.org/10.1016/j.vacuum.2005.07.038
[45] J. Schulze, A. Derzsi, K. Dittmann, T. Hemke, J. Meichsner, and Z. Donkó, Phys. Rev. Lett. **107**, 275001 (2011). https://doi.org/10.1103/PHYSREVLETT.107.275001
[46] E. Kawamura, A.J. Lichtenberg, and M.A. Lieberman, J. Phys. D: Appl. Phys. **45**, 495201 (2012). https://doi.org/10.1088/0022-3727/45/49/495201
[47] V. Lisovskiy, and V. Yegorenkov, EPL, **99**, 35002 (2012). https://doi.org/10.1209/0295-5075/99/35002
[48] A. Proto, and J.T. Gudmundsson, J. Appl. Phys. **128**, 113302 (2020). https://doi.org/10.1063/5.0019340
[49] A. Proto, and J.T. Gudmundsson, Plasma Sources Sci. Technol. **30**, 065009 (2021). https://doi.org/10.1088/1361-6595/abef1d
[50] A. Derzsi, P. Hartmann, M. Vass, B. Horváth, M. Gyulai, I. Korolov, J. Schulze, and Z. Donko, Plasma Sources Sci. Technol. **31**, 085009 (2022). https://doi.org/10.1088/1361-6595/ac7b45
[51] C. Harvey, N. Sirse, C. Gaman, and A. R. Ellingboe, Phys. Plasmas, **27**, 110701 (2020). https://doi.org/10.1063/5.0022844
[52] A. Derzsi, M. Vass, R. Masheyeva, B. Horváth, Z. Donkó, and P. Hartmann, Plasma Sources Sci. Technol. **33**, 025005 (2024). https://doi.org/10.1088/1361-6595/ad1fd5
[53] R. Masheyeva, M. Vass, X.-K. Wang, Y.-X. Liu, A. Derzsi, P. Hartmann, J. Schulze, and Z. Donkó, Plasma Sources Sci. Technol. **33**, 045019 (2024). https://doi.org/10.1088/1361-6595/ad3c69
[54] R.A. Gottscho, Phys. Rev. A **36**, 2233 (1987). https://doi.org/10.1103/PhysRevA.36.2233
[55] R.A. Gottscho, and C.E. Gaebe, IEEE Trans. Plasma Sci. **PS-14**, 92 (1986). https://doi.org/10.1109/TPS.1986.4316511
[56] J.-P. Boeuf, Phys. Rev. A, **36**, 2782 (1987). https://doi.org/10.1103/PhysRevA.36.2782
[57] J. P. Boeuf, and P. Belenguer, in *Nonequilibrium Processes in Partially Ionized Gases*, edited by M. Capitelli and J. N. Bardsley (Springer, New York, 1990). pp. 155–186. https://doi.org/10.1007/978-1-4615-3780-9_9
[58] J.P. Boeuf, and L.C. Pitchford, Phys. Rev. E, **51**, 1376 (1995). https://doi.org/10.1103/PhysRevE.51.1376
[59] P. Vitruk, H. Baker, and D. Hall, IEEE J. Quantum Electronics, **30**, 1623 (1994). https://doi.org/10.1109/3.299494
[60] G.A.J. Markille, J.J. Baker, J.G. Betterton, and D.R. Hall, IEEE J. Quantum Electronics, **35**, 1134 (1999). https://doi.org/10.1109/3.777212

[61] R. Engelbrecht, R. Schulz, G. Seibert, J. Hagen, and L.-P. Schmidt, Frequenz, **59**, 154 (2005). https://doi.org/10.1515/freq.2005.59.5-6.154

[62] O. Svelto, *Principles of lasers*, (Springer, New York, 2009). 604 p.

[63] A. Bogaerts, T. Kozak, K. van Laer, and R. Snoeckx, Faraday Discuss. **183**, 217 (2015). https://doi.org/10.1039/C5FD00053J

[64] T. Kozak, and A. Bogaerts, Plasma Sources Sci. Technol. **24**, 015024 (2014). https://doi.org/10.1088/0963-0252/24/1/015024

[65] R. Snoeckx, and A. Bogaerts, Chem. Soc. Rev. **46**, 5805 (2017). https://doi.org/10.1039/C6CS00066E

[66] A. Bogaerts, and G. Centi, Frontiers in Energy Research, **8**, 111 (2020). https://doi.org/10.3389/fenrg.2020.00111

[67] G. Chen, R. Snyders, and N. Britun, J. CO_2 Utilization, **49**, 101557 (2021). https://doi.org/10.1016/j.jcou.2021.101557

[68] S. Dudin, V. Lisovskiy, P. Platonov, and S. Rezunenko, Problems of Atomic Science and Technology, 6(142), 84 (2022). https://vant.kipt.kharkov.ua/ARTICLE/VANT_2022_6/article_2022_6_84.pdf

[69] V.A. Lisovskiy, S.V. Dudin, P.P. Platonov, and V.D. Yegorenkov, East European J. Phys. (4), 152 (2021). https://doi.org/10.26565/2312-4334-2021-4-20

[70] V.A. Lisovskiy, S.V. Dudin, P.P. Platonov, and V.D. Yegorenkov, Problems of atomic science and technology, 6(130), 179 (2020). https://vant.kipt.kharkov.ua/ARTICLE/VANT_2020_6/article_2020_6_179.pdf

[71] A.S. Morillo-Candas, V. Guerra, and O. Guaitella, J. Phys. Chem. C, **124**, 17459 (2020). https://doi.org/10.1021/acs.jpcc.0c03354

[72] R. Vertongen, G. Trenchev, R. Van Loenhout, and A. Bogaerts, J. CO_2 Utilization, **66**, 102252 (2022). https://doi.org/10.1016/j.jcou.2022.102252

[73] Q. Fu, Y. Wang, and Zh. Chang, J. CO_2 Utilization, **70**, 102430 (2023). https://doi.org/10.1016/j.jcou.2023.102430

[74] E.R. Mercer, S. Van Alphen, C.F.A.M. van Deursen, T.W.H. Righart, W.A. Bongers, R. Snyders, A. Bogaerts, *et al.*, Fuel, **334**, 126734 (2023). https://doi.org/10.1016/j.fuel.2022.126734

[75] S. Kelly, E. Mercer, Y. Gorbanev, I. Fedirchyk, C. Verheyen, K. Werner, P. Pullumbi, A. Cowley, and A. Bogaerts. J. CO_2 Utilization, **80**, 102668 (2024). https://doi.org/10.1016/j.jcou.2024.102668

[76] Y. Long, X. Wang, H. Zhang, K. Wang, W.-L. Ong, A. Bogaerts, K. Li, *et al.*, JACS Au, **4**, 7 2462 (2024). https://doi.org/10.1021/jacsau.4c00153

[77] G.J.M. Hagelaar and L.C. Pitchford, Plasma Sources Sci. Technol. **14**, 722 (2005). https://doi.org/10.1088/0963-0252/14/4/011

[78] L.C. Pitchford, L.L. Alves, K. Bartschat, S.F. Biagi, M.C. Bordage *et al.*, Plasma Process. Polym. **14**, 1600098 (2017). https://doi.org/10.1002/ppap.201600098

[79] Y. Itikawa, J. Phys. Chem. Reference Data, **31**, 749 (2002). https://doi.org/10.1063/1.1481879

[80] V.A. Lisovskiy, S.V. Dudin, P.P. Platonov, and V.D. Yegorenkov, Physica Scripta, **98**, 025601 (2023). https://doi.org/10.1088/1402-4896/acae48

[81] H.W. Ellis, R.Y. Pai, E.W. McDaniel, E.A. Mason, and L.A. Viehland, Atomic Data and Nuclear Data Tables, **17**, 177 (1976). https://doi.org/10.1016/0092-640X(76)90001-2

[82] P. Coxon, and J. Moruzzi, J. Phys. Colloques, **40**, 117 (1979). https://doi.org/10.1051/jphyscol:1979758

[83] E.W. McDaniel, and H. Crane, Rev. Sci. Instruments, **28**, 684 (1957). https://doi.org/10.1063/1.1715976

[84] W.L. Nighan, and W.J. Wiegand, Phys. Rev. A, **10**, 922 (1974). https://doi.org/10.1103/PhysRevA.10.922

[85] C.S. Weller, and M.A. Biondi, Phys. Rev. Lett. **19**, 59 (1967). https://doi.org/10.1103/PhysRevLett.19.59

[86] Yu.P. Raizer, *Gas discharge physics*, (Springer, Berlin, 1991).

[87] T.D. Fansler, L.M. ColonnaRomano, and R.N. Varney, J. Chem. Phys. **66**, 3246 (1977). https://doi.org/10.1063/1.434300

[88] V. Lisovskiy, S. Dudin, A. Shakhnazarian, P. Platonov, and V. Yegorenkov, Problems of Atomic Science and Technology, 4(129), (2023). https://vant.kipt.kharkov.ua/ARTICLE/VANT_2023_4/article_2023_4_129.pdf

[89] V.A. Lisovskiy, S.V. Dudin, M.M. Vusyk, R.O. Osmayev, V.D. Yegorenkov, and P.P. Platonov, Problems of Atomic Science and Technology, 186, (2023). https://vant.kipt.kharkov.ua/ARTICLE/VANT_2023_1/article_2023_1_86.pdf

[90] P. Capezzuto, F. Cramarossa, R. D'Agostino, and E. Molinari, J. Phys. Chem. **80**, 882 (1976). https://doi.org/10.1021/j100549a024

[91] V. Lisovskiy, J.P. Booth, K. Landry, D. Douai, V. Cassagne, and V. Yegorenkov, Europhys. Lett. **82**, 15001 (2008). https://doi.org/10.1209/0295-5075/82/15001

[92] Y. Fu, H. Wang, and X. Wang, Rev. Modern Plasma Phys. **7**, 10 (2023). https://doi.org/10.1007/s41614-022-00112-1

[93] Y. Fu, B. Zheng, P. Zhang, Q.H. Fan, J.P. Verboncoeur, and X. Wang, Phys. Plasmas, **27**, 113501 (2020). https://doi.org/10.1063/5.0022788

[94] [Y. Fu, B. Zheng, D.-Q. Wen, P. Zhang, Q.H. Fan, and J.P. Verboncoeur, Appl. Phys. Lett. **117**, 204101 (2020). https://doi.org/10.1063/5.0029518

ЧИСЕЛЬНЕ МОДЕЛЮВАННЯ ДИНАМІКИ ВЧ ЄМНІСНОГО РОЗРЯДУ У ВУГЛЕКИСЛОМУ ГАЗІ

Валерій Лісовський, Станіслав Дудін, Амалія Шахназарян, Павло Платонов, Володимир Єгоренков

Харківський національний університет імені В.Н. Каразіна, майдан Свободи, 4, Харків, 61022, Україна

У цій роботі одновимірний гідродинамічний код SIGLO-rf було використано для дослідження внутрішніх параметрів ВЧ ємнісного розряду у вуглекислому газі. Проведено моделювання середніх за часом та просторово-часових профілів параметрів розряду. Для цього чисельно розв'язано рівняння балансу концентрації для кожного з видів заряджених частинок та рівняння балансу енергії електронів, які були доповнені також рівнянням Пуассона для електричного потенціалу. За допомогою цього коду SIGLO-rf в діапазоні відстаней між електродами $d = 0,04 - 8$ см, частот ВЧ електричного поля $f = 3,89 - 67,8$ МГц та значень тиску вуглекислого газу $p = 0,1 - 9,9$ Торр розраховано середні за ВЧ період осьові профілі густини електронів, позитивних та негативних іонів, а також потенціалу та напруженості електричного поля. Показано, що розрядна плазма в CO_2 містить електрони, позитивні іони, а також негативні іони. Вони утворилися при дисоціативному прилипанні електронів до молекул CO_2 й є негативними іонами атомарного кисню. Зазвичай плазма ВЧ ємнісного розряду є фактично іон-іонною, тому що концентрація вільних електронів у декілька десятків разів менша за концентрацію негативних іонів. Негативні іони накопичуються у плазмі завдяки утриманню в середній за часом потенціальній ямі, що призводить до

зменшення потенціалу плазми. Дослідження просторово-часової динаміки параметрів плазми (густини електронів, потенціалу та напруженості електричного поля, а також швидкостей іонізації та прилипання) у ВЧ ємнісному розряді в CO_2 показали, що протягом однієї половини ВЧ періоду зазвичай спостерігаються від 1 до 3 сплесків іонізації. Вони відповідають стохастичному нагріву у приелектродному шарі, що є у катодній фазі й межує з тимчасовим негативним електродом, та формуванню пасивного та активного подвійних шарів біля меж приелектродних шарів. Пасивний подвійний шар знаходиться біля межі приелектродного шару у катодній фазі й підтримує розрядну плазму. Активний шар формується біля межі приелектродного шару в анодній фазі й забезпечує баланс позитивного та негативного зарядів, що надходять в електрод протягом усього ВЧ періоду. З'ясовано, що при одночасному виконанні умов $pd = 2$ Торр см та $fd = 27{,}12$ МГц см протягом половини ВЧ періоду спостерігаються 4 інтенсивних іонізаційних піки: внаслідок стохастичного нагріву, а також формування пасивного, активного та додаткового (допоміжного) подвійних шарів. Додатковий подвійний шар сприяє підведенню електронів до поверхні тимчасового анода й виникає поблизу його поверхні всередині приелектродного шару. За допомогою закону подібності перевірено умови існування цих 4 піків іонізації в широкому діапазоні ВЧ частот f, значень тиску вуглекислого газу p та відстаней між електродами d.

Ключові слова: *високочастотний ємнісний розряд; гідродинамічне моделювання; вуглекислий газ; швидкість іонізації; подвійні шари, негативні іони*

NUMERICAL STUDY OF CONVECTIVE FLOW OF CASSON FLUID THROUGH AN INFINITE VERTICAL PLATE WITH INDUCED MAGNETIC FIELD

Hiren Deka[a], Parismita Phukan[a,b]*

aDepartment of Mathematics, Cotton University, Assam, India
bDepartment of Mathematics, Royal Global University, Assam, India
Corresponding Author e-mail: parismita12007@gmail.com
Received April 17, 2024; revised June 3, 2024; accepted June 21, 2024

The present objective is to numerically analyze the induced magnetic field (IMF) effect of an unsteady MHD flow of Casson fluid through two infinite vertical plates. The effect of radiative heat has been scrutinized. Governing non-dimensional PDEs of the flow are discretized by the finite difference method to some algebraic system of equations, which is then numerically solved concerning the boundary conditions. The effects of the radiations, magnetic Prandtl number, Prandtl number, Hartmann number, and Casson parameter on temperature profile, velocity profile, and induced magnetic field have been depicted through graphs. The radiative effect and Prandtl number have considerable influence on the surface drag force and also on the rate of heat transfer.

Keywords: *MHD; Casson; induced magnetic field; FDM*
PACS: 44.05.+e, 44.40.+a,47.11.-j
MSC 2010: *76W05*

1   INTRODUCTION

Convective heat transfer takes place between a moving fluid and its surrounding surface when there is difference in temperature. Such convective flows have wide applications in different fields of engineering and industries. It also has its vast applications in many agricultural and industrial water distribution, geothermal mining and groundwater flows. Magnetohydrodynamic convective flows have drawn more attention in the past few decades owing to its applications in the study of chemical engineering, planetary magnetospheres and electronics.

For a free convective, the flow is induced by buoyancy forces. Free convection plays an important role to design performance of several system as it provides large resistance to heat

transfer. The convection of non-Newtonian fluid has recently been able to draw the attentions of many researchers as it has more explicable properties then the Newtonian fluid. A non- Newtonian fluid has the property that the deformation rate varies with viscosity. It has its wide applications in crude oil extraction. Casson fluid is a most popular non-Newtonian fluid that has its rheological effects on viscoelastic fluids. Casson fluid is a fluid with the properties of high viscosity shear thinning and yield stress below which flow is restricted. It has its significant applications in the field of chemistry and mechanics. Several mathematicians, engineers and scientists have analyzed the applications of Casson fluids. Many researchers have also contributed their work on convection of a Casson fluid. Rodi and Mopuri [1] have recently analyzed the convective flow a Casson fluid. They analytically deliberated the influence of magnetic field, chemical reaction along with Soret effect of flow through an inclined semi-infinite plate. Vijayaragavan and Karthikeyan [2] have examine the Hall current effect along with diffusion-thermo-effect, chemical reaction and radiative effect. In 2021, Vijayaragavan et al [3] have investigated transient convective flow pass an inclined vertical plate. Their work was concerned on transfer of mass and heat of a conducting Casson fluid. For a rotating system Pushpalatha [4] explored free convection of Casson fluid. Perturbation technique was applied in solving the equations. Throughout their study, they conclude that Casson parameter controls the fluid velocity profile and thermodiffusion effect enhance both concentrations and velocity profiles.

The study of fluid flow via various physical configurations and media has been able to capture the interest of many experts. Due to various significance of mass and heat transfer, magnetohydramic flow of fluid with the influence of reaction by chemical has drag a lot of interest in the intervening years. Additionally, the radiative transport of heat has several uses in the construction of nuclear power plants and different missile, satellite, and other technologies. Considering all of these important applications, Sarma et al., [5] examine the mass transfer for a flow through an infinite plate. Laplace transform method is applied in solving the governing equations. Their results show considerable changes due to influence of different parameters and along with it the porosity of the medium slows down the fluid velocity which is in agrees with physical reality. Through a flat plate and vertical cone Kumar et al., [6] have analyzed the non-Darcy convective flow. Muhammad Waqas et al [7] addresses the mixed convective flow of a viscous micropolar liquid with joule heating. The occurrence of fluid is towards non-linear stretched surface. The equations governing the problem are solved by homotopic procedure. A.K. Agrawal et al [8] have extended their work on transfer of mass of convective flow past a vibrating circular cylinder.

The research mentioned above have often been limited to relatively low magnetic Reynolds numbers, allowing for the disregard of magnetic induction effects. If magnetic Reynolds number is relatively high, such effects is considered. Due to its employment in numerous technological and scientific phenomena, such as MHD power generation, geophysics, crude oil purification, glass making, etc., the IMF has many essential applications in the theoretical and experimental studies. The study of mixed convective constant flow of a Newtonian fluid through a vertical infinite plate in porous material was examined by Ahmed and Chamkh [9]. In presence of IMF the main objective was to study the rate of transfer of heat and mass with the effects of chemical reaction, thermal radiation. Sarveshanand and Singh [10] analyzed the free convective steady flow between two vertical infinite porous plate in addition of suction velocity. Fadzilah Md. Ali et al., [11] numerically illustrated the transfer of heat of a steady convective flow through a stretching sheet. Hazarika et al [12] numerical analyzed the convective flow with fuzzified boundary conditions and with the effect of IMF. The impact of an IMF on a free convective unsteady flow of conducting fluid across a vertical semi-infinite plate has been analyzed by Kumar and Singh [13]. The implicit finite difference approach of Crank-Nicolson type was applied in solving the PDEs. Ahmed [14] precisely solved a continuous Poiseuille flow with mass and heat transfer under the influence of a transverse magnetic field with effect of thermal diffusion and IMF.

The present study of MHD convective flow of Casson fluid through infinite vertical plates with induced magnetic field is presumed to be used in various technological phenomena and will have significant role in many scientific experimental processes. The effect of radiation can be seen in various space technology and in design of nuclear power plants. The suction velocity plays an important role in artificially controlling the behavior of the boundary layer and hence it has wide application in industries and aeronautical engineering. Hence, from the above properties of different parameters and its wide applications in various fields has motivated to do the present analysis. The novelty of the present study is to analyze MHD convective flow of fluid in addition with significant impact of magnetic Reynold's number so that the effect of induced magnetic field is considered along with the radiative effect.

2. PROBLEM FORMULATION

A free convective flow of a Casson fluid passing through two infinite vertical plates is assumed. Let d be the distance between the two plates. The x' −axis is chosen vertically along the plate and the y' −axis is chosen perpendicular to the plate. B_0 is a uniform magnetic field applied along the y' −direction as shown in Figure 1. Initially, the fluid and the plate are at a same temperature T_0. With time $t > 0$ the temperature of the first plate increases to T_1 while temperature of the second plate is kept at temperature T_0. The magnetic Reynold's number is not assumed to be small and so the induced magnetic field is not insignificant.
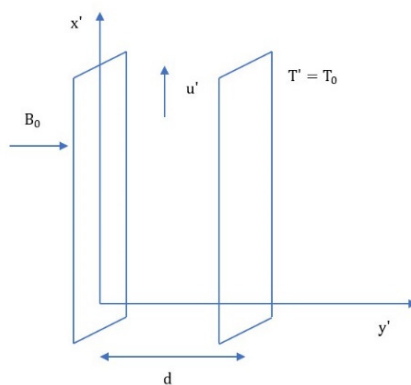

Figure 1. Configuration of the flow problem

Equations governing the flow problem are:

$$\frac{\partial u'}{\partial t'} + v'\frac{\partial u'}{\partial y'} = v_\infty\left(1 + \frac{1}{\alpha}\right)\frac{\partial^2 u'}{\partial y'^2} + g\beta(T' - T_0') + \frac{\mu_e B_0}{\rho}\frac{\partial H'}{\partial y'} \tag{1}$$

$$\frac{\partial T'}{\partial t'} + v'\frac{\partial T'}{\partial y'} = \frac{k}{\rho C_p}\frac{\partial^2 T'}{\partial y'^2} - \frac{1}{\rho C_p}\frac{\partial q_r'}{\partial y'} \tag{2}$$

$$\frac{\partial H'}{\partial t'} + v'\frac{\partial H'}{\partial y'} = \frac{1}{\sigma\mu_e}\frac{\partial^2 H'}{\partial y'^2} + B_0\frac{\partial u'}{\partial y'} \tag{3}$$

Boundary conditions are:

$$u' = 0, T' = T_1, H' = 0 \text{ at } y' = 0 \tag{4}$$

$$u' = 0, T' = T_0, H' = 0 \text{ at } y' = d. \tag{5}$$

Where velocity along x' −axis is u', the suction velocity is v', t', T', H' are the dimensional time, temperature and induced magnetic field respectively. The kinematic viscosity is v_∞, g is the acceleration due to gravity, α is the casson parameter,

β is the thermal expansion coefficient, μ_e is the magnetic permeability, σ is the electrical conductivity and ρ is the fluid density.

The radiative term $\frac{\partial q_r}{\partial y}$ present in the energy Eq. (2.2) can be simplified by using Rosseland approximation as given below:

$$q_r' = -\frac{4\sigma_1}{3k_1}\frac{\partial T'^4}{\partial y'}, \tag{6}$$

where Stefan-Boltzmann constant is σ_1 and the mean absorption coefficient is k_1.
With the application of Taylor's series, we expand linear function T'_4 about the free stream
temperature. Hence neglecting the high order terms the result of the approximation transforms into the form:

$$T'^4 \cong 4T_0^3 T' - 3T_0^4. \tag{7}$$

Using Eq. (2.6) and Eq. (2.7), we have

$$\frac{dq_r'}{dy} = -\frac{16\sigma_1 T_0^3}{3k_1}\frac{\partial^2 T'}{\partial y'^2}. \tag{8}$$

Then Eq. (2.2) takes the form:

$$\frac{\partial T'}{\partial t'} + v'\frac{\partial T'}{\partial y'} = \frac{k}{\rho C_p}\frac{\partial^2 T'}{\partial y'^2} + \frac{16\sigma_1 T_0^3}{3k_1\rho C_p}\frac{\partial^2 T'}{\partial y'^2}. \tag{9}$$

Using the following non-dimensional quantities:

$$y = \frac{y'}{d}, t = \frac{t'v_\infty}{d^2}, v = \frac{v'd}{v_\infty}, H = \frac{H'v_\infty\sqrt{\frac{\mu_e}{\rho}}}{d^2 g\beta(T_1 - T_0)}, u = \frac{u'v_\infty}{d^2 g\beta(T_1 - T_0)}, \theta = \frac{T' - T_0}{T_1 - T_0},$$

$$M = \frac{dB_0}{v_\infty}\sqrt{\frac{\mu_e}{\rho}}, Pr = \frac{\mu_e C_p}{k}, N = \frac{kk_1}{4\sigma_1 T_\infty^3}, \lambda = \frac{3N + 4}{3N}, P_m = \sigma\mu_e v_\infty.$$

he corresponding non-dimensional governing equations takes the form:

$$\frac{\partial u}{\partial t} + v\frac{\partial u}{\partial y} = \left(1 + \frac{1}{\alpha}\right)\frac{\partial^2 u}{\partial y^2} + \theta + M\frac{\partial H}{\partial y}. \tag{10}$$

$$\frac{\partial \theta}{\partial t} + v\frac{\partial \theta}{\partial y} = \frac{\lambda}{Pr}\frac{\partial^2 \theta}{\partial y^2}. \tag{11}$$

$$\frac{\partial H}{\partial t} + v\frac{\partial H}{\partial y} = \frac{1}{Pm}\frac{\partial^2 H}{\partial y^2} + M\frac{\partial u}{\partial y}. \tag{12}$$

and the boundary conditions are:

$$u = 0, \theta = 1, H = 0 \text{ at } y = 0, \tag{13}$$

$$u = 0, \theta = 0, H = 0 \text{ at } y = 1. \tag{14}$$

The non-dimensional skin friction (τ) and Nusselt number (Nu) is given by:

$$\tau = -\left(\frac{\partial u}{\partial y}\right)_{y=0}, Nu = -\left(\frac{\partial \theta}{\partial y}\right)_{y=0}$$

3. METHOD OF SOLUTION

The above transformed equation Eq. (2.10) - Eq. (2.12) are coupled non-linear partial differential equations. As the analytical or exact solutions seems to be not feasible so we use Finite Difference Method (FDM) in order to solve the differential equations. This method is comparatively precise, effective and has better stability characteristics. Here we discretized the governing PDE about the point (i, j) and reduce it to a system of algebraic equations. The following equations are the reduced form of finite difference approximation by truncating the higher order terms:

$$\frac{\partial u}{\partial t}\Big|_{i,j} = \frac{u_{i+1,j} - u_{i,j}}{\Delta t}$$

$$\frac{\partial u}{\partial y}\Big|_{i,j} = \frac{u_{i,j+1} - u_{i,j}}{\Delta y}$$

$$\frac{\partial^2 u}{\partial y^2}\Big|_{i,j} = \frac{u_{i,j+1} - 2u_{i,j} + u_{i,j-1}}{(\Delta y)^2}$$

The above equations discretize the dimensionless PDEs to a system of algebraic equations. The equivalent finite difference scheme for equation Eq. (2.10)-Eq. (2.12) is as follows:

$$\frac{u_{i+1,j} - u_{i,j}}{\Delta t} - v_0 \frac{u_{i,j+1} - u_{i,j}}{\Delta y} = \frac{\left(1 + \frac{1}{\alpha}\right)u_{i,j+1} - 2u_{i,j} + u_{i,j-1}}{(\Delta y)^2} + \theta_{i,j} + M \frac{H_{i,j+1} - H_{i,j}}{\Delta y}, \tag{15}$$

$$\frac{\theta_{i+1,j} - \theta_{i,j}}{\Delta t} - v_0 \frac{\theta_{i,j+1} - \theta_{i,j}}{\Delta y} = \left(\frac{\lambda}{Pr}\right)\frac{\theta_{i,j+1} - 2\theta_{i,j} + \theta_{i,j-1}}{(\Delta y)^2}, \tag{16}$$

$$\frac{H_{i+1,j} - H_{i,j}}{\Delta t} - v_0 \frac{H_{i,j+1} - H_{i,j}}{\Delta y} = \frac{1}{Pm} \frac{H_{i,j+1} - 2H_{i,j} + H_{i,j-1}}{(\Delta y)^2} + M \frac{u_{i,j+1} - u_{i,j}}{\Delta y}, \tag{17}$$

Where Δt and Δy are the dimensionless time-step and finite difference grid size in the y−direction respectively. Here i is the grid point in the time variable t and j designates the grid points along the y−directions. The mesh size is considered as $\Delta y = 0.1$ with time step $\Delta t = 0.14$. The order of accuracy of this method is $o[(\Delta y), (\Delta y)^2]$. The scheme is unconditionally stable and so this method is compatible.

4. RESULT AND DISCUSSION

An unsteady MHD convective flow of a Casson fluid through vertical infinite plate with IMF has been examined. The governing non-dimensional equations has been discretized to algebraic system of equations. Along with the boundary conditions the system of equations are numerically solved by Gauss-Seidel iterative method. The numerical results along with the influence of the parameters have been depicted through tables and figures. Throughout our discussion we have chosen arbitrarily some of the values for the parameters such as radiation parameter (N = 5), suction parameter (v = 1), Casson parameter (α = 0.5), magnetic parameter (M = 5) and magnetic Prandtl number (Pm = 1). We have considered the Prandtl number Pr to be 0.7 that corresponds to air in a range where the dynamic and the thermal boundary layer are approximately equal. Figure 2 - Figure 5 displays the influence of Prandtl number, Hartmann number, radiation effect and Casson parameter on velocity profile respectively.
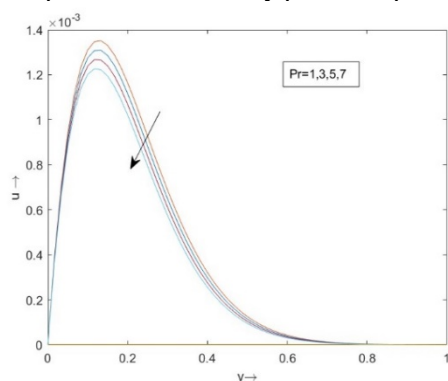

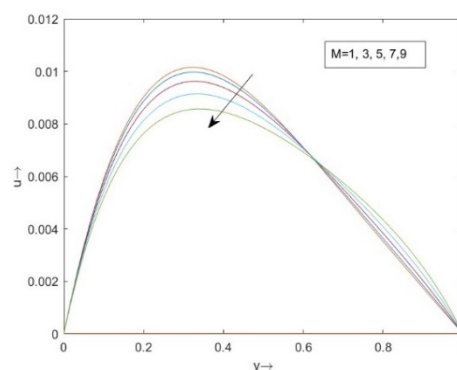**Figure 2.** Variation of Prandtl number(Pr) on velocity

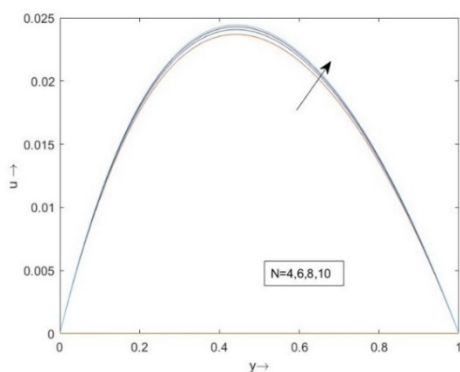**Figure 3.** Variation of Hartmann number(M) on velocity

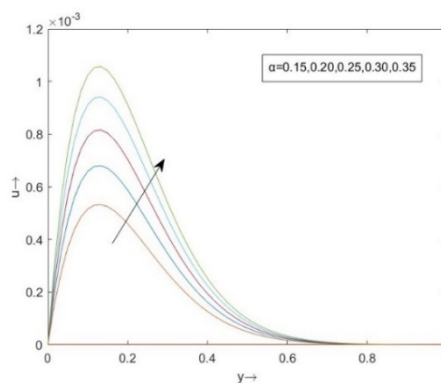**Figure 4.** Variation of radiation parameter(N) on velocity

Figure 5. Variation of Casson parameter(α) on velocity

The Prandtl number is a quantity that shows how the molecular diffusivity of heat and momentum are related. It calculates the relative amount of heat and momentum in the velocity and thermal boundary layer. Figure 2 clearly depicts the rise in Prandtl number, lowers the velocity boundary layer thickness. Figure 3 examines that with the rise in Hartmann number the flow velocity lowers and reverse is the case as y increases. The velocity profile in Figure 4 shows a parabolic

shape with the addition of radiation parameter with maximum value somewhere in the middle region. It also examines that due to high effect of radiation, the velocity increases. Casson fluid exhibits high viscosity shear thinning characteristics as well as yield stress. The impact of the Casson parameter on the fluid velocity is anticipated. Figure 5 demonstrates that as α rise, the rate of motion considerably increases. Figure 6 and Figure 7 depict how temperature changes with the addition of N and Pr. In both the figures temperature tends to zero at maximum value of y. The thermal boundary layer thickness rise with the rise in radiation effect whereas it lowers with the rise in Pr. Figure 8 and Figure 9 demonstrate how the induced magnetic field is influenced by the M and Pm.
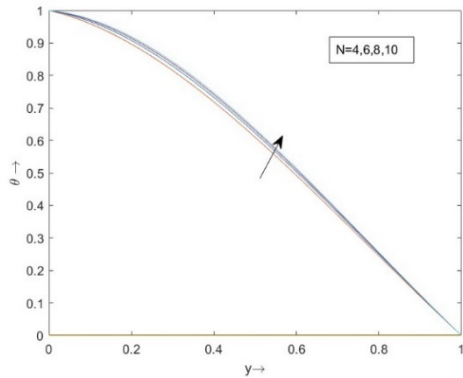

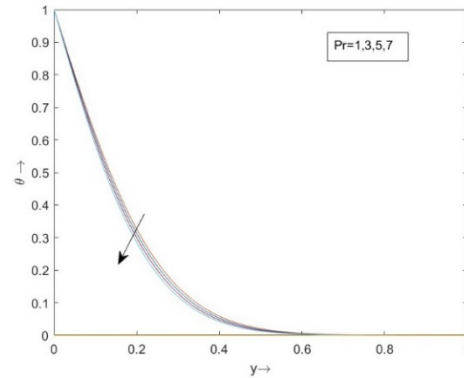**Figure 6.** Variation of radiation parameter (N) on temperature

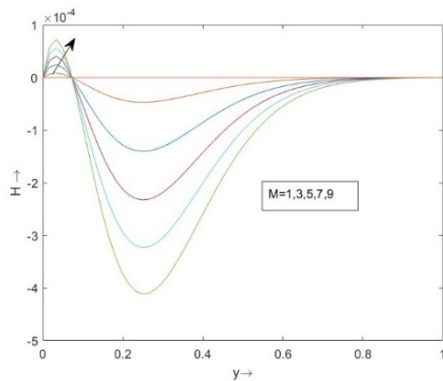**Figure 7.** Variation of Prandtl number (Pr) on temperature

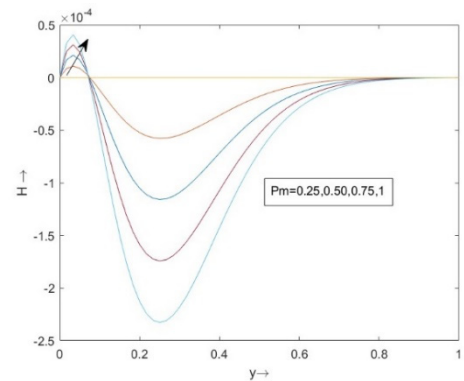**Figure 8.** Variation of Hartmann number (M) on induced magnetic field

Figure 9. Variation of magnetic Prandtl number (Pm) on induced magnetic field

It is clear that the variation of Hartmann number initially increases the induced magnetic field, which falls down after a certain value of y. The same observation is seen in case of variation of magnetic Prandtl number on IMF. Nusselt number is a non-dimensional heat transfer coefficient. It is a coefficient that is used to determine the conduction or convection of heat transfer. Table 1 and Table 2 shows how the N and Pr affect the heat transfer rate. It follows that when the radiation rise, the heat transfer rate lowers. Similarly, the rate of heat transmission is slowed down as the Pr increases. Table 3 -Table 7 exhibit the variation of Skin friction with influence of Casson parameter, Hartmann number, radiation parameter, Prandtl number and magnetic Prandtl number. The viscous drag force is enhanced with rise in Casson parameter. Table 4 illustrates that rise in M results in a steady decrease in the magnitude of skin friction. That is the frictional force lowers due to addition of magnetic field. Table 5, Table 6 and Table 7 shows that the direction of drag force is reversed as radiation parameter, Prandtl number and magnetic Prandtl number increases.

Table 1. Nusselt Number with change in radiation parameter.

N	Pr	Nusselt number
1.0	0.7	-4.04438
3.0	0.7	-4.06635
5.0	0.7	-4.07465
7.0	0.7	-4.07901

Table 2. Nusselt Number with change in Prandtl number.

N	Pr	Nusselt number
1.0	**1.0**	-4.0596
1.0	**3.0**	-4.1710
1.0	**5.0**	-4.3003
1.0	**7.0**	-4.4480

Table 3. Skin friction with change in Casson parameter

α	M	N	Pr	Pm	Skin friction
0.15	5.0	1.0	0.7	1.0	0.00920
0.20	5.0	1.0	0.7	1.0	0.01177
0.25	5.0	1.0	0.7	1.0	0.01413
0.30	5.0	1.0	0.7	1.0	0.01632
0.35	5.0	1.0	0.7	1.0	0.01834

Table 4. Skin friction with change in Hartmann number

α	M	N	Pr	Pm	Skin friction
0.5	**1**	1.0	0.7	1.0	0.02374
0.5	**3**	1.0	0.7	1.0	0.02370
0.5	**5**	1.0	0.7	1.0	0.02362
0.5	**7**	1.0	0.7	1.0	0.02350
0.5	**9**	1.0	0.7	1.0	0.02334

Table 5. Skin friction with change in radiation parameter

α	M	N	Pr	Pm	Skin friction
0.5	5.0	**1.0**	0.7	1.0	0.02362
0.5	5.0	**3.0**	0.7	1.0	0.02354
0.5	5.0	**5.0**	0.7	1.0	0.02352
0.5	5.0	**7.0**	0.7	1.0	0.02350
0.5	5.0	**9.0**	0.7	1.0	0.02349

Table 6. Skin friction with change in Prandtl number

α	M	N	Pr	Pm	Skin friction
0.5	5.0	1.0	**0.25**	1.0	0.02369
0.5	5.0	1.0	**0.50**	1.0	0.02365
0.5	5.0	1.0	**0.75**	1.0	0.02361
0.5	5.0	1.0	**1.00**	1.0	0.02357
0.5	5.0	1.0	**1.25**	1.0	0.02348

Table 7. Skin friction with change in Magnetic Prandtl number

α	M	N	Pr	Pm	Skin friction
0.5	5.0	1.0	0.7	**0.25**	0.02371
0.5	5.0	1.0	0.7	**0.50**	0.02368
0.5	5.0	1.0	0.7	**0.75**	0.02365
0.5	5.0	1.0	0.7	**1.00**	0.02362
0.5	5.0	1.0	0.7	**1.25**	0.02358

5. CONCLUSION

We examined the free convection of an unsteady flow of a Casson fluid through vertical plates of infinite length with the effect of IMF. Here, an electrically conducting and viscous fluid is considered. The equations which govern are non-dimensionalized to a system of PDE's and then solve numerically. The graphical representations of the fluid properties under the influence of embedded parameters shows considerable changes. The tabular illustration of rate of heat transfer and the surface drag force shows significant influence of the parameters. The present study of fluid through infinite vertical plates is frequently used in many technological phenomena.

The results of the present study can be concluded as below:

- The rise in Prandtl number leads to the fall in velocity profile and the rise in Hartmann number initially lowers the velocity profile which is then reverse later on.
- The velocity profile falls with the rise in Casson parameter and radiation parameter.
- The fluid temperature falls with the application of Prandtl number and rise with the rise in radiation parameter.
- Induced magnetic field initially rise with the rise in magnetic Prandtl number and Hartmann number which decreases later on.
- The heat transfer rate for the fluid problem is decreased with the radiation parameter and Prandtl number.
- With the application of Casson parameter the viscous drag force increases. The viscous drag force falls as the radiation effect, magnetic Prandtl number and Prandtl number rises.

ORCID

⊙**Hiren Deka,** https://orcid.org/0009-0002-1512-5984

REFERENCES

[1] R. Kodi, and O. Mopuri, "Unsteady MHD oscillatory Casson fluid flow past an inclined vertical porous plate in the presence of chemical reaction with heat absorption and Soret effects," Heat Transfer, **623**, 1-20 (2021). https://doi.org/10.1002/htj.22327

[2] R. Vijayaragavan, and S. Karthikeyan, "Hall Current Effect on Chemically Reacting MHD Casson Fluid Flow with Dufour Effect and Thermal Radiation," Asian Journal of Applied Science and Technology, 228–245 (2018). https://ajast.net/data/uploads/4032.pdf

[3] R. Vijayaragavan, M. Ramesh, and S. Karthikeyan, "Heat and Mass Transfer Investigation on MHD Casson Fluid Flow past an Inclined Porous Plate in the Effects of Dufour and Chemical Reaction," Journal of Xi'an University of Architecture and Technology, **13**, 860–873 (2021).

[4] K. Pushpalatha, V. Sugunamma, J. V. Ramana Reddy, and N. Sandeep, "Heat and Mass Transfer in Unsteady MHD Casson Fluid Flow with Convective Boundary Conditions," International Journal of Advanced Science and Technology, **91**, 19–38 (2016). http://dx.doi.org/10.14257/ijast.2016.91.03

[5] D. Sarma, N. Ahmed, and H. Deka, "MHD free convection and mass transfer flow past an accelerated vertical plate with chemical reaction in presence of radiation," Latin American Applied Research, **44**, 1–8 (2014). https://doi.org/10.52292/j.laar.2014.412

[6] B.R. Kumar, and R. Sivaraj, "MHD viscoelastic fluid non-Darcy flow over a vertical cone and a flat plate," International Communications in Heat and Mass Transfer, **40**, 1–6 (2013). https://doi.org/10.1016/j.icheatmasstransfer.2012.10.025

[7] M. Waqas, M. Farooq, M.I. Khan, A. Alsaedi, T. Hayat, and T. Yasmeen, "Magnetohydrodynamic (MHD) mixed convection flow of micropolar liquid due to Nonlinear stretched sheet with convective condition," International Journal of Heat and Mass Transfer, **102**, 766–772 (2016). https://doi.org/10.1016/j.ijheatmasstransfer.2016.05.142

[8] A.K. Agrawal, B. Kishor, and A. Raptis, "Effects of MHD free convection and mass transfer on the flow past a vibrating infinite vertical circular cylinder," Waerme- und Stoffuebertragung, **24**, 243–250 (1989). https://doi.org/10.1007/BF01625500

[9] S. Ahmed, and A.J. Chamkha, "Effects of Chemical Reaction, Heat and Mass Transfer and Radiation on MHD Flow along a Vertical Porous Wall in the Present of Induced Magnetic Field," Int. J. Industrial Mathematics, **2**, 245–261 (2010). https://sid.ir/paper/584929/en

[10] Sarveshanand, and A.K. Singh, "Magnetohydrodynamic free convection between vertical parallel porous plates in the presence of induced magnetic field," SpringerPlus, **4**, 333 (2015). https://doi.org/10.1186/s40064-015-1097-1

[11] F.M. Ali, R. Nazar, N.M. Arifin, and I. Pop, "MHD boundary layer flow and heat transfer over a stretching sheet with induced magnetic field," Heat and Mass Transfer, **47**, 155-162 (2011). https://doi.org/10.1007/s00231-010-0693-4

[12] G.C. Hazarika, P. Dutta, and J. Borah, "Numerical analysis of an MHD flow in fuzzy environment in presence of induced magnetic field," Heat Transfer, 1–11 (2021). https://doi.org/10.1002/htj.22163

[13] A. Kumar, and A.K. Singh, "Unsteady MHD free convective flow past a semi-infinite vertical wall with induced magnetic field," Applied mathematics and computation, **222**, 462–471 (2013). https://doi.org/10.1016/j.amc.2013.07.044

[14] N. Ahmed, "Heat and Mass Transfer in MHD Poiseuille Flow with Porous Walls," J. Eng. Phys. Thermophy. **92**, 122-131 (2019). https://doi.org/10.1007/s10891-019-01914-w

ЧИСЕЛЬНЕ ДОСЛІДЖЕННЯ КОНВЕКТИВНОГО ПОТОКУ КАССОНОВОЇ РІДИНИ ПОВЗ НЕСКІНЧЕННУ ВЕРТИКАЛЬНУ ПЛАСТИНУ З ІНДУКОВАНИМ МАГНІТНИМ ПОЛЕМ

Хірен Дека[a], Парісміта Пхукан[a,b]
[a]Факультет математики, Університет Коттон, Ассам, Індія
[b]Департамент математики, Королівський глобальний університет, Ассам, Індія

Поточна мета полягає в чисельному аналізі ефекту індукованого магнітного поля (ІМП) нестаціонарного МГД потоку рідини Кассона через дві нескінченні вертикальні пластини. Вплив радіаційного тепла було ретельно вивчено. Керівні безрозмірні часткові часткові деталі потоку дискретизуються методом скінченних різниць до деякої алгебраїчної системи рівнянь, яка потім чисельно розв'язується щодо граничних умов. Вплив випромінювань, магнітного числа Прандтля, числа Прандтля, числа Гартмана та параметра Кассона на профіль температури, профіль швидкості та індуковане магнітне поле було зображено на графіках. Радіаційний ефект і число Прандтля мають значний вплив на силу поверхневого опору, а також на швидкість теплопередачі.

Ключові слова: *МГД; рідина Кассона; індуковане магнітне поле; FDM*

EFFECT OF RAREFACTIONS AND CONVECTIVE HEAT CHANGE ON FREE CONVECTIVE UNSTEADY MHD FLOW IN A SLIP-FLOW REGIME PAST A VERTICAL WALL WITH CONVECTIVE SURFACE BOUNDARY CONDITION

Hemant Agarwal[a]*, Shyamanta Chakraborty[b]#

aDepartment of Mathematics, Gauhati University, Guwahati-781014, Assam, India
bUGC-HRDC, Gauhati University, Guwahati-781014, Assam, India
#E-mail: schakrabortyhrdc@gauhati.ac.in
*Corresponding Author email: hemantagarwal55@gmail.com

The study investigates the unsteady free convective two-dimensional MHD flow past a vertical porous plate with convective surface boundary condition in porous medium in slip flow regime under the action of variable suction velocity. Analytical solutions are obtained for the system using perturbation technique that converts non-linear coupled governing partial differential equations into non-dimensional form of ordinary differential equations. Effects of variable suction velocity, rarefactions parameter and heat change parameter are analysed and discussed graphically for various values of effective physical parameter such as Grasshof number, Magnetic field parameter, Prandtl number, Permeability parameter on fluid velocity and temperature, skin friction, and heat transfer.

Keywords: *Magneto hydrodynamic flow; Permeability; Rarefaction; Convective heat change; Variable suction-velocity*
**PACS:** 47.35.Tv, 47.65.-d ; 47.56.+v

INTRODUCTION

Magneto hydrodynamic (MHD) flow under various physical situations has been of great interest in the recent years because of numerous applications in the field of science and technology, and industry; e.g. in production of Rayon and Nylon, Purification of crude oil, MHD generator and pumps, functioning of a nuclear reactor, etc. Such flows that are buoyancy induced, density varied driven by temperature gradient in presence magnetic field occurs in many situations in our everyday life as well; in the atmospheric flow (movement of air around solar system), extracting geothermal energy, exploring oil from ground etc. Over the years, many researchers have studied unsteady free MHD convective flow past a flat solid plate with oscillating temperature or with a constant temperature. Martynenko et al. [1], Das et al. [2], Hossain et al. [3]. Sahoo et al. [4] have studied on such unsteady MHD free convective flow with suction parameter and with heat source. MHD flow over a moving permeable vertical surface using perturbation technique was studied by Abdelkhalek [5]. Flow over a solid wall with no-slip boundary condition where fluid particles acquire no velocity but have finite tangential velocity commonly called a slip-flow regime. Such flow over a solid surface or wall plays importance role in many practical applications in science-technology, industry, atmospheric phenomenon etc. Sharma and Chaudhary [6], Khaled and Vafai [7], Mehmood and Ali [8], Chaudhary and Jha [9], Hayat et al. [10] have studied heat transfer problems which have effect of slip flow regime on Unsteady MHD flow. Makinde[11], Gangadhar et al. [12], Olanjrewaju et al. [13] and Garg et al. [14] have studied such type of fluid flow under the condition convective heating of surfaces. Garg et al. [15] have studied free convective unsteady MHD flow past a vertical plate with convective surface boundary condition in slip flow regime. N. Kalita et al. [16] studies on a unsteady flow which passed over an vertically plate in presence of some chemical reaction. S. Sarma et al. [17] investigate on different frequency of waves on unsteady MHD flow over different temperature in porous medium. A. Selvaraj et al. [19] studies on MHD parabolic flow which passed over isothermal plate with rotation effect in mass, heat diffusion. Mv Krishna [20] investigate on Unsteady MHD rotating flow in various temperature in Jeffrays fluid. P.K. Pattnaik et al. [20] studies on the effect of chemical reaction in MHD flow over a stretching sheet. R.S. Nath et al. studies on various stratification effect in Magnetohydrodynamics Nanofluid which passed over an vertical plate in porous medium in the presence of radiation, heat source.

In this paper, two dimensional unsteady free convective viscous MHD flow past a vertical plate in porous medium in slip-flow regime under the action of variable suction velocity has been studied. A uniform magnetic field acts perpendicular to the surface and a suction velocity varies with time. Analytical equations are obtained for the flow system using perturbation technique. The objective this study is to analysis the rarefaction effect and convective heat change within the medium of the of the free convective flow system in presence of magnetic field past a vertical wall with surface boundary condition in slip flow regime. The flow patterns are analysed and discussed with the help of a graphs for different values of Magnetic field, Suction velocity, medium permeability, Grasshof number, Prandtl number, etc.

FORMULATION OF PROBLEMS

Consider an unsteady free two-dimensional flow which passes through porous medium with convective surface boundary condition in slip flow regime. The variable suction velocity $V = V_0(1 + \epsilon A e^{i\omega t})$ and magnetic field are applied perpendicular to the wall. We take x-axis along the wall and y-axis normal to the wall. As shown in Figure below.
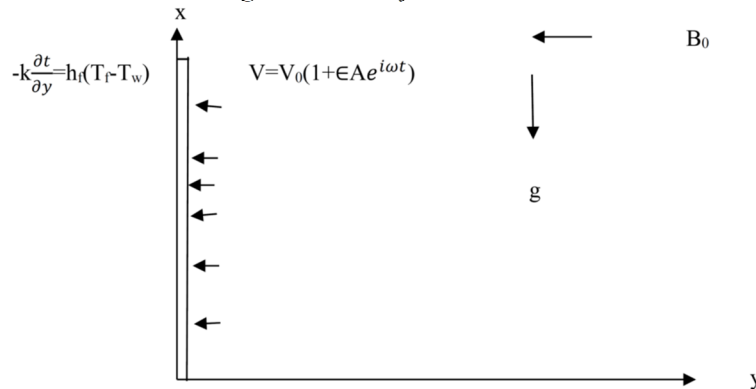
Since the pate is considered to be infinite in x-direction, therefore its flow of variable are function of y and t only. After neglecting viscous and magnetic dissipation along with Boussinesq approximations, the governing equations can be written as

$$\frac{\partial u'}{\partial t'} - V_0(1 + \varepsilon A e^{i\omega' t'})\frac{\partial u'}{\partial y'} = \upsilon\frac{\partial^2 u'}{\partial y'^2} + g\beta(T - T_\infty) - \frac{\sigma}{\rho}B_0^2 u' - \frac{\Upsilon}{K}u', \tag{1}$$

$$\frac{\partial T}{\partial T'} - nV_0(1 + \varepsilon A e^{i\omega' t'})\frac{\partial T'}{\partial y'} = \alpha\frac{\partial^2 T}{\partial y'^2}, \tag{2}$$

where u and v are the x and y components of the velocities respectively, A is the variable suction velocity, T is the temperature, ω is the frequency, ϑ is the kinematic viscosity of the fluid, ρ is the fluid density, $\alpha(=\frac{k}{\rho c_p})$ is the thermal diffusity of the fluid, β is the thermal expansion coefficient, k is the thermal conductivity, g is the acceleration due to gravity, σ is the electrical conductivity, B_0 is the magnetic field in y direction.

The boundary condition are:

$$u' = L\left(\frac{\partial u'}{\partial y'}\right), \ -k\left(\frac{\partial T}{\partial y'}\right) = h_f(T_f - T_w) \text{ at } y' = 0, \tag{3}$$

$$u' \to 0, \ T \to T_\infty \text{ as } y' \to \infty, \tag{4}$$

where $T_w = T(0, t)$ and L is some body dimension defined by characteristics dimension flow field.

We now introduce the non-dimensional variables into equations 1-4 as follows

$$y = \frac{y'V_0}{v}, \ t = \frac{t'V_0^2}{4v}, \ \omega = \frac{4v\omega'}{V_0^2}, \ u = \frac{u'}{V_0}, \ \theta = \frac{T - T_\infty}{T_f - T_\infty}, \ k = \frac{\vartheta^2}{Kv_0^2}, \tag{5}$$

Now, equation 1 and 2 reduces to

$$\frac{1}{4}\frac{\partial u}{\partial t} - (1 + \epsilon A e^{i\omega t})\frac{\partial u}{\partial y} = \frac{\partial^2 u}{\partial y^2} + G_r\theta - Mu - \frac{1}{K}u, \tag{6}$$

$$\frac{1}{4}\frac{\partial \theta}{\partial t} - (1 + \epsilon A e^{i\omega t})\frac{\partial \theta}{\partial y} = \frac{1}{Pr}\frac{\partial^2 \theta}{\partial y^2}, \tag{7}$$

The boundary condition (3) and (4) in the dimensional form below

$$u = H\frac{\partial u}{\partial y}, \ \frac{\partial \theta}{\partial y} = -H_f(1 - \theta) \text{ at } y = 0$$

$$u = 0, \ \theta = 0 \text{ as } y \to \infty, \tag{8}$$

where $Gr = \frac{g\beta v}{V_0^3}(T_f - T_\infty)$ is the Grashof number , $M = \frac{\sigma\vartheta B_0^2}{\rho V_0^2}$ is the magnetic field parameter, $H = \frac{LV_0}{\vartheta}$ is the Rarefaction parameter , $Hf = \frac{\vartheta h_f}{kV_0}$ is the convective Heat change parameter and $Pr = \frac{\mu c_p}{k}$ is the prandtl number

SOLUTION OF THE PROBLEM

In order to solve the boundary value problem, it is first reduced to ordinary differential equation from partial differential equation using perturbation technique. Assuming small amplitude $\epsilon \ll 1$, the velocity u and temperature θ near the plate can be represented as

$$u(y,t) = u_0(y) + \epsilon e^{i\omega t}u_1(y) + \epsilon^2 e^{2i\omega t}u_2(y), \tag{9}$$

$$\theta(y,t) = \theta_0(y) + \epsilon e^{i\omega t}\theta_1(y) + \epsilon^2 e^{2i\omega t}\theta_2(y). \tag{10}$$

Substituting the value of equation (9) and (10) into equation (6) and (7) and comparing the coefficient of identical powers of ε we obtain

$$u_0''(y) + G_r\theta_0(y) + u_0'(y) - \xi u_0(y) = 0, \tag{11}$$

$$u_1''(y) + u_1'(y) + Au_0'(y) - \frac{1}{4}i\omega u_1(y) + G_r\theta_1(y) - \xi u_1(y) = 0, \tag{12}$$

$$u_2''(y) + u_2'(y) + Au_1'(y) - \frac{1}{2}i\omega u_1(y) + G_r\theta_1(y) - \xi u_1(y) = 0, \tag{13}$$

$$\theta_0''(y) + P_r\theta_0'(y) = 0, \tag{14}$$

$$\theta_1''(y) - P_r\frac{i\omega}{4}\theta_1(y) + P_r\theta_1'(y) + AP_r\theta_0'(y) = 0, \tag{15}$$

$$\theta_2''(y) - \frac{i\omega}{2}P_r\theta_2(y) + P_r\theta_2'(y) + AP_r\theta_1'(y) = 0. \tag{16}$$

The corresponding boundary condition (8) reduces to

$$u_0 = H\frac{\partial u_0}{\partial y}, u_1 = H\frac{\partial u_1}{\partial y}, u_2 = H\frac{\partial u_2}{\partial y} \frac{\partial \theta_0}{\partial y} = -H_f(1-\theta_0), \frac{\partial \theta_1}{\partial y} = H_f\theta_1 \text{ at y=0}$$

$$\frac{\partial \theta_2}{\partial y} = H_f\theta_2 \text{ at y=0}, \tag{17}$$

$$u_0 = 0, u_1 = 0, u_2 = 0, \theta_0 = 0, \theta_1 = 0, \theta_2 = 0 \text{ } asy \to \infty, \tag{18}$$

Solving the set of equation (11) – (16) under boundary condition (18), we get

$$u_0(y) = A_7e^{-m_1y} - A_8e^{-Pry}, \tag{19}$$

$$u_1(y) = A_{10}e^{-m_2y} - A_{11}e^{-Pry} - A_{12}e^{-m_1y} + A_9e^{-m_3y}, \tag{20}$$

$$u_2(y) = A_{13}e^{-m_4y} + A_{14}e^{-m_3y} - A_{15}e^{-Pry} + A_{16}e^{-m_2y} - A_{17}e^{-m_1y}, \tag{21}$$

$$\theta_0(y) = A_2e^{-Pry}, \tag{22}$$

$$\theta_1(y) = -A_3e^{-m_2y} + A_4e^{-Pry}, \tag{23}$$

$$\theta_2(y) = A_5e^{-m_3y} + A_6e^{-Pry} + A_{18}e^{-m_2y}, \tag{24}$$

The final equation for temperature and velocity are as follows:

$$\theta(y) = A_2e^{-Pry} - A_3e^{-m_2y} + A_4e^{-Pry} + A_5e^{-m_3y} + A_6e^{-Pry} + A_{18}e^{-m_2y}, \tag{25}$$

$$u(y) = A_7e^{-m_1y} - A_8e^{-Pry} + A_{10}e^{-m_2y} - A_{11}e^{-Pry} - A_{12}e^{-m_1y} + A_9e^{-m_3y} + A_{13}e^{-m_4y} +$$

$$+A_{14}e^{-m_3y} - A_{15}e^{-Pry} + A_{16}e^{-m_2y} - A_{17}e^{-m_1y} \tag{26}$$

Skin-Friction

The equation of Skin Friction is

$$\tau_x = (\frac{\partial u}{\partial y})_{y=0} = -m_1A_7 + PrA_8 + \varepsilon(-A_{10}m_2 + A_{11}Pr + A_{12}m_1 - A_9m_3)e^{-\omega t} -$$

$$-\varepsilon^2(A_{13}m_4 + A_{14}m_3 - A_{15}Pr + A_{16}m_2 - A_{17}m_1). \tag{27}$$

Coefficient of Heat Transfer

The coefficient of Heat transfer is Nusselt number which is dimensionless

$$Nu = (\frac{\partial \theta}{\partial y})_{y=0} = -A_2Pr + A_3m_2 - A_4Pr - A_5m_3 - A_6Pr. \tag{28}$$

RESULTS AND DISCUSSION

The purpose the study is to investigate effects of variable suction velocity A, rarefactions parameter H and convective heat change parameter H_f on fluid velocity and temperature, skin friction, and heat transfer represented by Nusselt number at the plate. Momentum and energy equations of the flow system are solved by perturbation technique. Expressions for fluid temperature and velocity, skin-friction and Nusselt Number on the wall are shown in equation 1.25 - 1.28 respectively. While calculating the numerical values of physical quantities of our interest, the values of non-

dimensional quantities are considered as Gr=5.0, ω =5.0, Pr=0.71, K=1.0, H= 0.4, H_f=1.0, M=1.5. The effects of A, H & H_f on transient velocity and temperature profiles, Skin friction and Nusselt number over the wall are shown in Figures (i) - (xv) as given below.

Fig(i) shows velocity profile (y ≥ 0.0) for various values of suction parameter A ($\cong$ 0.0 to 5.0) at M =1.5 & 2.5. The plots show that fluid velocity decreases gradually away from the wall and then rises slowly. Near the wall (y≅0.0 to 1.0) fluid velocity higher for higher values of A while away (y ≅ 0.1 to 7.0) velocity is lower for higher values of A. Further away from the wall (y ≥ 7.0), fluid velocity is less variable with rise of A. Nature of this variations are same for variation of magnetic parameter M $\cong$ 1.5 & 2.5, however, the critical point from where the nature of variation of fluid velocity rises slowly is decreased with the increase of M (e.g. for M=1.5 at y≅1.0 whereas, for M $\cong$ 2.5 at y $\cong$ 0.6). Rise of value of M causes decrease of u at a point y≥ 0.0.
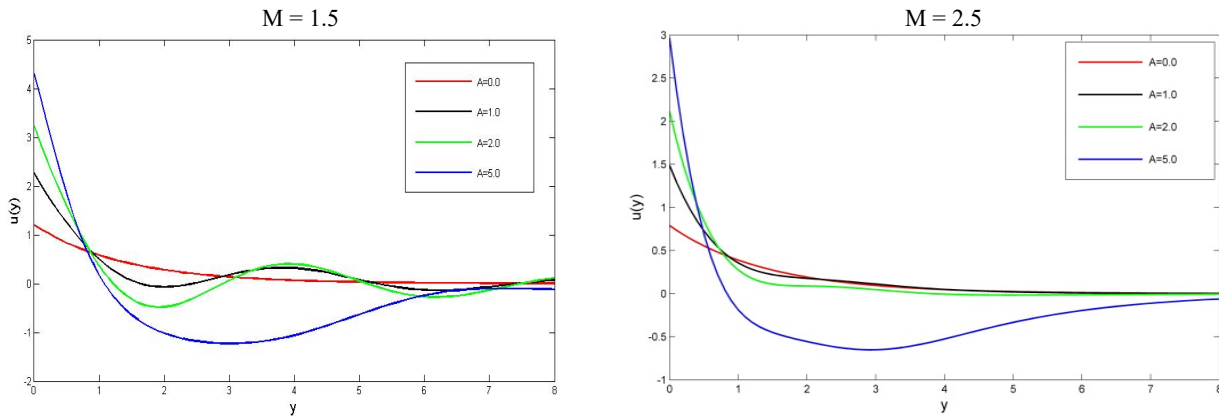
Figure (i). Effect of suction parameter A on velocity profiles

Fig(ii) shows velocity profile (y ≥ 0.0) for various values of heat change parameter H_f ($\cong$0.1 to 2.0) at M =1.5 & 2.5. The plots show that fluid velocity decreases gradually from the wall to a certain extent and then rises slowly. Near the wall (y≅ 0.0 to 1.5) fluid velocity higher for higher values of H_f while away (y $\cong$ 0.1 to 8.0) velocity is less for higher values of H_f. Further away from the wall (y≥ 8.0), variation of fluid velocity is less variable with rise of H_f. The nature of this variation is same for M ($\cong$ 1.5 & 2.5). Rise of value of M decreases the values of u at a point y ≥ 0.0.
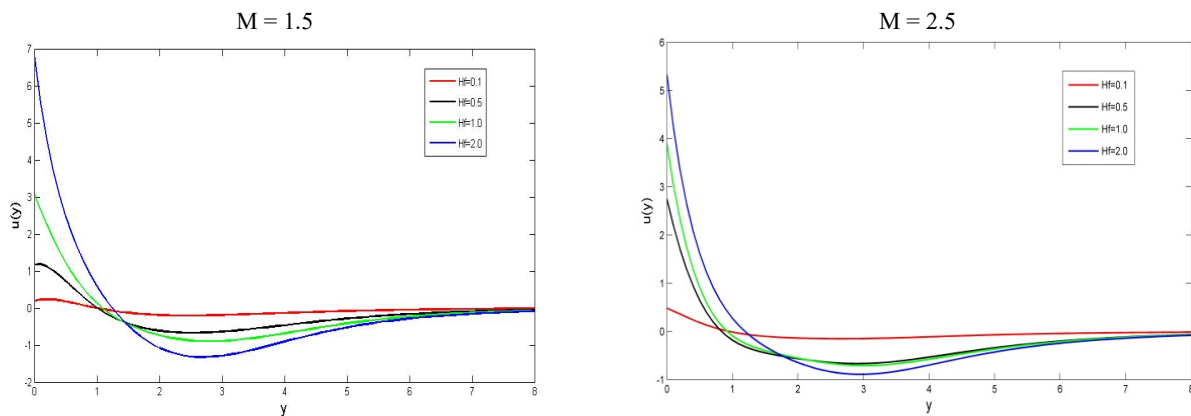

Figure (ii). Effect of H_f on velocity profiles

Fig(iii) shows effect of Rarefaction parameter (H) on velocity field at y ≥ 7.0 at M =1.5 & 2.5. For all values of H, fluid velocity near the wall decreases, then gradually increases away from it. Near the wall, at a point y ≤ 6.0 fluid velocity decreases with the rise of H($\cong$0.0 to 5.0); away from it gradually becomes less significant ; nature of these variation are same for magnetic parameter M($\cong$ 1.5 & 2.5). Fig(iv) shows velocity profile (y ≥ 0.0) for various values of K ($\cong$1.0 to 10.0) at M = 1.5 & 2.5. For all values of K, near the wall y ≤ 6 velocity decreases with the rise of K and slowly increases away from it. For higher values of K, magnitude of velocity also more. Nature of variations are same for M ($\cong$1.5& 2.5). Fig(v) shows velocity profile (y ≥ 0.0) for various values of Prandtl number (Pr) for M =1.5 &2.5. As Pr varies from 0.71 to 10.0, fluid velocity (u)has significant change near the wall but not that away from it. Near the wall y ≤ 1.0 fluid velocity increases with the rise of Pr. Higher the value of Pr higher is the fluid velocity (u) near the wall. But away from it velocity is almost independent to the variation to the variation of Pr. This nature of variation is same for M = 1.5 & 2.5. Fig(vi) show velocity profile (y ≥ 0.0) for various values of M($\cong$0.01 to 2.0). With the rise of magnetic field M velocity gradually decreases; the rate of decrease is much higher near the wall y ≤ 2.0. Away from it, the effect of magnetic field gradually

becomes less significant. Fig(vii) show velocity profile (y ≥ 0.0) for various values of Gr(=1.0 to 15.0). Near the wally ≤ 3.5, fluid velocity largely depends upon changing values of Gr. Higher the value of Gr, fluid velocity is higher. Away from the wall y ≥ 3.5 (approx.) velocity gradually becomes less dependent to Gr.

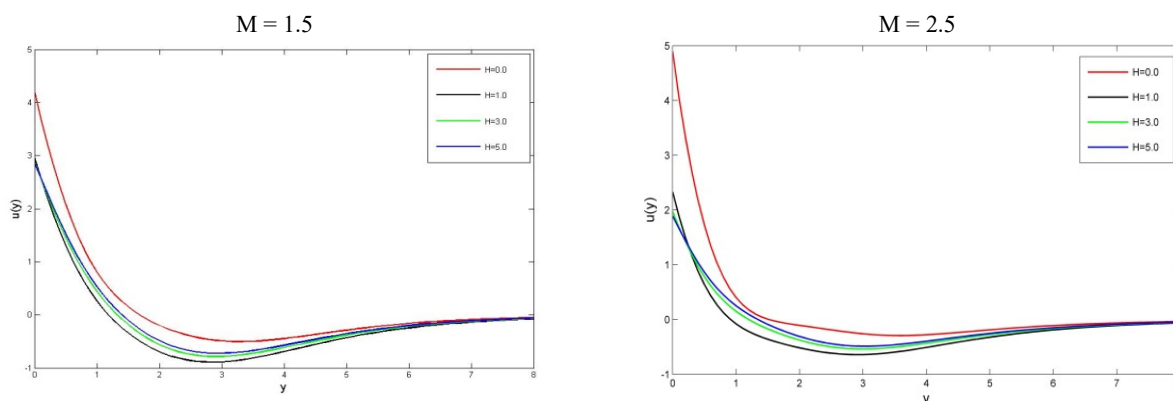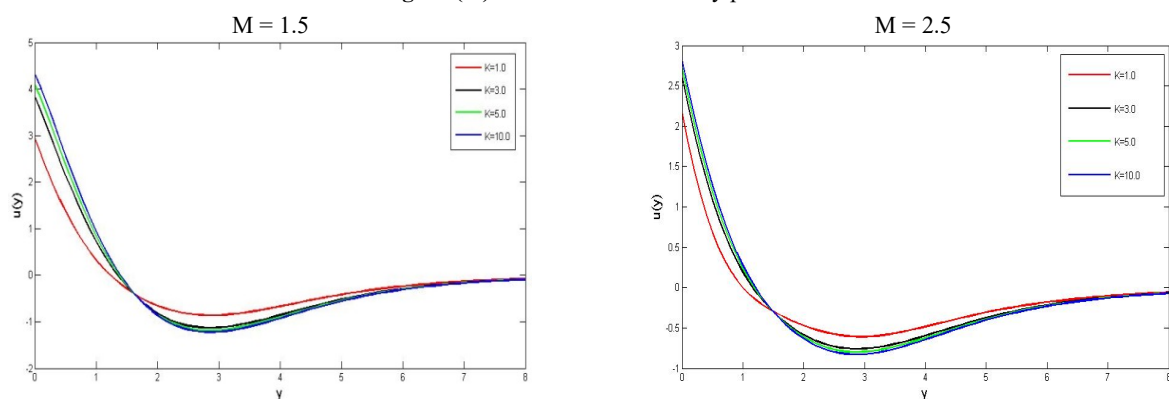**Figure (iii).** Effect of H on velocity profiles
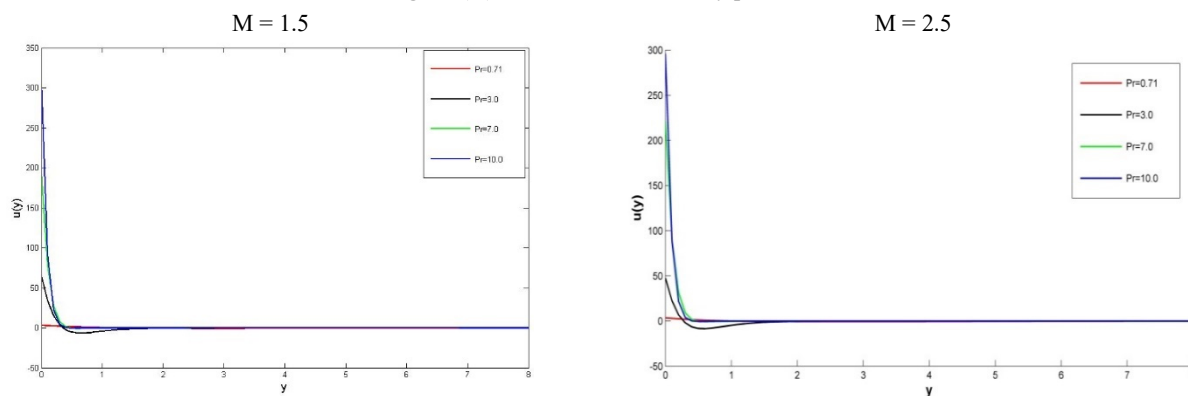

Figure (iv). Effect of K on velocity profile
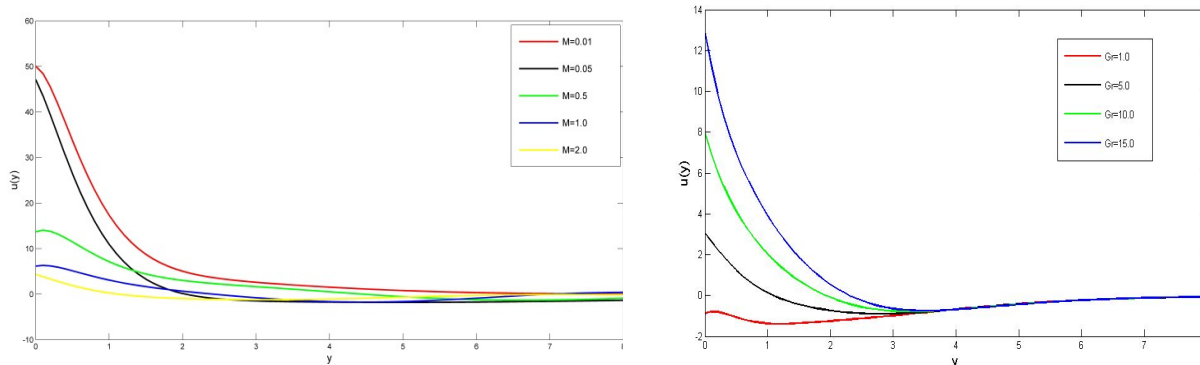

Figure (v). Effect of Pr on velocity profile

Figure (vi). Effect of M on velocity profile   **Figure (vii).** Effect of Gr on velocity profile

Fig(viii) show temperature (θ)profile (y ≥ 0.0) for various values frequency ω(frequency by which suction velocity changes). It is seen that away from the wall, with the rise of ω(≅1.0 to 2.0), θ decreases gradually. Effect of ω is significantly effective near the wall y≤4.0 while away from it much less. Fig(ix) show temperature (θ) profile (y ≥ 0.0) for various values of Heat change parameter H_f; the plots show much significant effect of H_f on fluid temperature near the wall in compare to away from it. In the neighbourhood of the wall, with the rise of H_f(≅0.1to 5.0), temperature(θ) first increases and then decreases sharply toward y≅ 5.0; thereafter almost no impact of H_f on temperature (θ). Within the very near to the wall y≤0.5 temperature rises then deceases sharply towards y≅ 5.0 (approx.). Fig(x) show temperature (θ) profile (y≥ 0.0) for various values of Prandtl number (Pr). It is seen that with the increase of Pr (≅ 0.1to 0.5), θ decreases gradually away from the wall. The rate of decrease is significant within near the wall y ≤ 3.0, beyond which it is very less. Fig(xi) show temperature (θ) profile (y ≥ 0.0) for various values of Suction parameter A. It is seen that rise of A(≅1.0 to 5.0) fluid temperature θ first increases then decreases slowly away from the wall. At near to the wall y≤0.5 temperature rises up but then deceases sharply to the away from it. At away from the wall, temperature has less effective with rise of A.
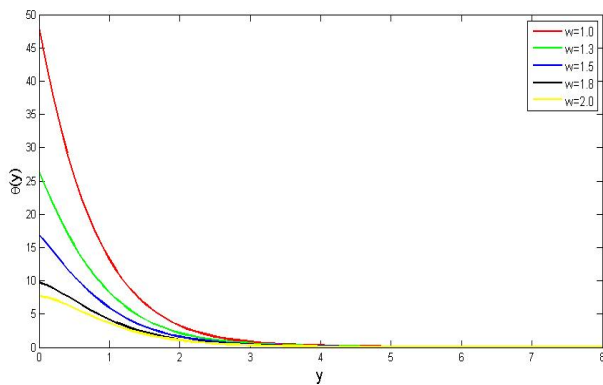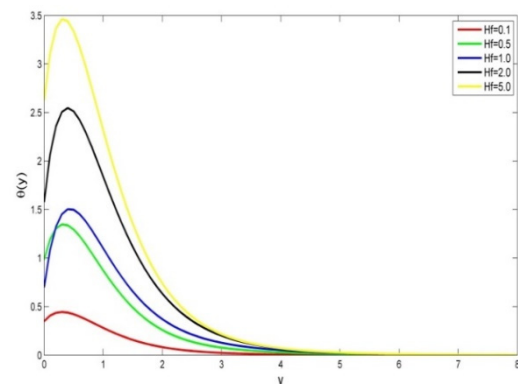

Figure (viii). Effect of ω on temperature profile

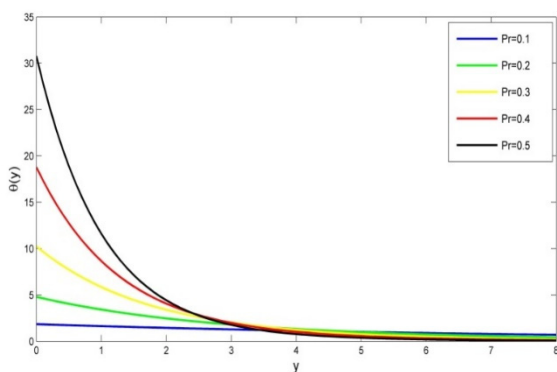**Figure (ix).** Effect of H_f on temperature profile

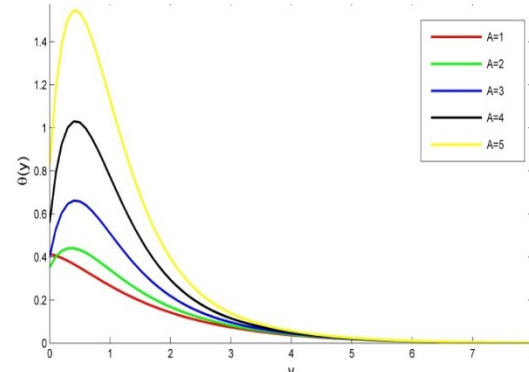**Fig (x):** Effect of Pr on temperature profile

Fig (xi): Effect of A on temperature profile

Fig(xii) shows effect of rarefaction parameter H & Suction parameter A on skin frictionτ. It is seen that skin friction on the wall gradually decreases with the rise of A for all values of H(≅ 0.0 to 1.0). Skin friction on the wall increases with the rise of H. this nature of variation is almost same for M ≅ 1.5 & 2.5.

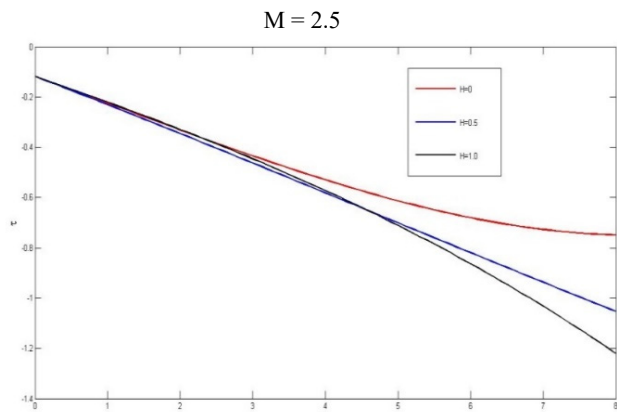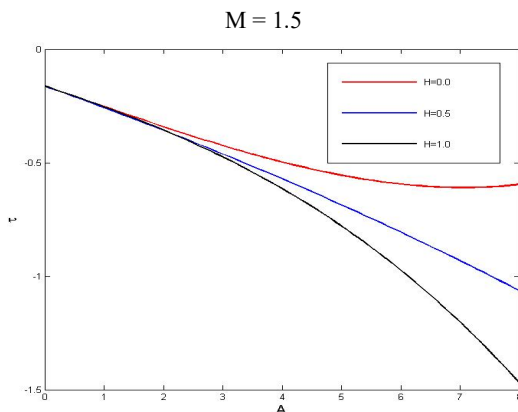**Figure (xii).** Effect of H on skin friction

Fig(xiii) shows effect of heat change parameter H_f & Suction parameter A on skin frictionτ on the wall. It is seen thatτgradually decreases with the rise of A for all values of $H_f (\cong 0.2$ to 1.0). skin friction τ decreases from higher values of H_f, nature of this variation is same for M = 1.5 & 2.5. Fig. (xiv) show effect the variation of Nusselt number Nu (i.e. the rate of heat transfer) with different values of Heat change parameter H_f & Suction parameter A. Nu gradually increases with the increase of A. Further, Nu is higher for higher values of H_f. Fig. (xv) show effect the variation of Nusselt number Nu with different values of Prandtl number Pr and & Suction parameter A. Nu gradually increases with the increase of A; Nu is higher for higher values of Pr(0.2 to 5.0).
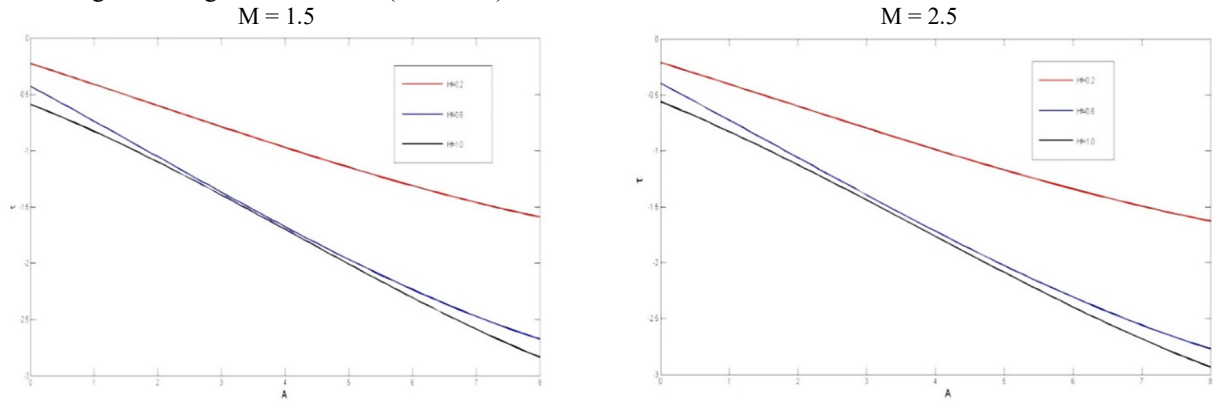
M = 1.5   M = 2.5

Figure (xiii). Effect of H_f on skin friction
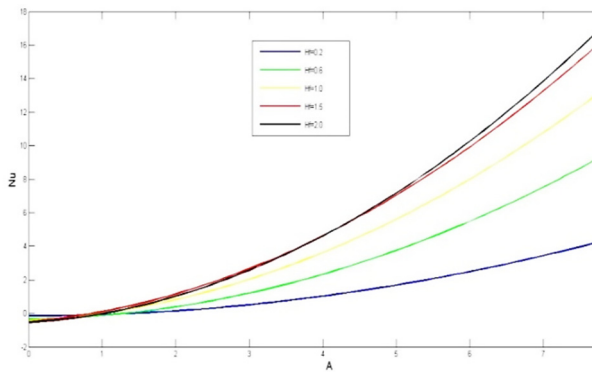

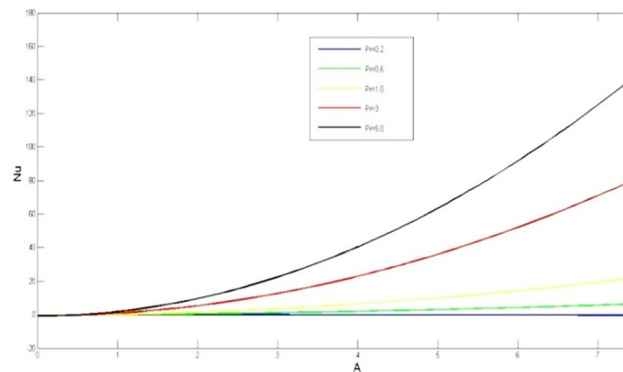**Figure (xiv).** Effect of H_f on Nusselt number   **Figure (xv).** Effect of Pr on Nusselt number

CONCLUSIONS

(i)   The effect of slip-flow regime is such that fluid velocity is maximum at the wall and away from it gradually decreases. Effects of suction parameter, heat change parameter, Rarefaction parameter and medium permeability are distinctively visible at the wall while away from it less dependent. At the wall, and near it fluid velocity increases directly with the increase of suction parameter, heat change parameter and permeability parameter; whereas decreases with the increase of effects of rarefaction parameter. Change of Prandtl number has direct impact on velocity within very near the wall only. Nature of these variations is same for rise of magnetic field.

(ii) Within the slip flow regime Grashoff number has direct effect while magnetic field has opposite effect.

(iii) Unlike the fluid velocity, fluid temperature, within the slip-flow regime initially increases and then decreases exponentially away from the wall. With the rise of heat change parameter and suction parameter, temperature rises whereas it decreases with the rise of frequency.

(iv) Skin friction on the wall decreases with the rise of suction parameter whereas it decreases for higher values of heat change parameter and rarefaction parameter. This nature variation is same for increase of magnetic field.

(v)   Nusselt number that represents the rate of heat transfer within the fluid, increases with rise of suction parameter; it increases with the rise of heat change parameter, rarefaction parameter and Prandtl number.

APPENDICES

$$A_2 = \frac{H_f}{P_r + H_f}, A_3 = \frac{(H_f + P_r)A_4}{m_2 - H_f}, A_4 = \frac{i4AA_2P_r}{\omega}, A_5 = \frac{A_6(1+P_r)}{1-m_3}, A_6 = \frac{-2iAP_rA_4e^{-Pry}}{\omega},$$

$$A_7 = \frac{A_6(1+HP_r)}{1+Hm_1}, A_8 = \frac{G_rA_2}{P_r^2 - P_r - \xi}, A_9 = \frac{-(1+Hm_2)A_{10}+(1+HPr)A_{11}+(1+Hm_1)A_{12}}{1+Hm_3},$$

$$A_{10} = \frac{G_rA_3}{m_2^2 - m_2 - (\xi + \frac{i\omega}{4})}, A_{11} = \frac{G_rA_4 - AA_8}{P_r^2 - P_r - (\xi + \frac{i\omega}{4})}, A_{12} = \frac{AA_7}{m_1^2 - m_1 - (\xi + \frac{i\omega}{4})},$$

$$A_{13} = \frac{-(1+m_3)A_{14}+(1+\mathrm{Pr})A_{15}-(1+m_2)A_{16}+(1+m_1)A_{17}}{1+Hm_4}, A_{14} = \frac{-G_rA_5+AA_9m_3}{m_3^2-m_3-(\xi+\frac{i\omega}{2})},$$

$$A_{15} = \frac{-G_rA_6+AA_{11}Pr}{P_r^2-P_r-(\xi+\frac{i\omega}{2})}, A_{16} = \frac{AA_{10}m_2e^{-m_2y}}{m_2^2-m_2-(\xi+\frac{i\omega}{2})}, A_{17} = \frac{AA_{12}m_1e^{-m_1y}}{m_1^2-m_1-(\xi+\frac{i\omega}{2})}, m_1 = \frac{-1+\sqrt{(1-4(m+\frac{1}{K})}}{2}$$

$$m_2 = -\frac{Pr}{2}(1+\sqrt{(1+\frac{i\omega}{Pr})}), m_3 = \frac{-Pr}{2}(1+\sqrt{(1+\frac{2i\omega}{Pr})}, m_4 = \frac{-1+\sqrt{(1+4(m+\frac{1}{K})+2i\omega)}}{2}$$

ORCID

◎**Hemant Agarwal,** https://orcid.org/0009-0004-2115-6482; ◎**Shyamanta Chakraborty,** https://orcid.org/0000-0001-5839-4856

REFERENCES

[1] O.G. Martynenko, A.A. Berezovsky, and Y.A. Sokovishin, "Laminar free convection from of a vertical plate," Int. J. Heat Mass Transfer. **27**, 869-881 (1984), https://doi.org/10.1016/0017-9310(84)90008-5

[2] U.N. Das, R.K. Deka, and V.M. Soundalgekar, "Transient free convection flow past an infinite vertical plate with periodic temperature variation," J. Heat Transfer, (ASME), **121**, 1091-1094 (1999). https://doi.org/10.1115/1.2826063

[3] M.A. Hossain, S. Hussain, and D.A. Rees, "Influence of fluctuating surface temperature and concentration on natural convection flow from a vertical flate plate," Z. angew. Math. Mech. **81**, 699-709, (2001). https://doi.org/10.1002/1521-4001(200110)81

[4] P.K. Sahoo, N. Datta, and S. Biswal, "Magneto hydrodynamics unsteady free convection flow past an infinite vertical plate with constant suction and heat sink," Ind. J. Pure Appl. Math. **34**, 145-155 (2003).

[5] M.M. Abdelkhalek, "Heat and mass transfer in MHD free convection from a moving permeable vertical surface by a perturbation technique," Commun. Nonlinear Sci. Numer. Simulat. **14**, 2091-2012 (2009). https://doi.org/10.1016/j.cnsns.2008.06.001

[6] P.K. Sharma, and R.C. Chaudhary, "Effect of variable suction on transient free convection viscous incompressible flow past a vertical plate with periodic temperature variations in slip-flow regime," Emirates Journal for Engineering Research, **8**, 33-38 (2003).

[7] A.R.A. Khaled, and K. Vafai, "The effect of the slip condition on stokes and couette flows due to an oscillatory wall: exact solution," Int. J. Nonlinear Mech. **39**, 795-809 (2004). https://doi.org/10.1016/s0020-7462(03)00043-X

[8] A. Mehmood, and A. Ali, "The effect of slip condition on unsteady MHD oscillatory flow of a viscous fluid in a planer channel," Rom. Journ. Phys. **52**, 85-91 (2007).

[9] R.C. Chaudhary, and A.K. Jha, "Effects of chemical reactions on MHD micropolar fluid flow past a vertical plate in slip flow regime," Appl. Math. Mech. Engl. Ed, **29**, 1179-1194 (2008). https://doi.org/10.1007/s10483-008-0907-x

[10] T. Hayat, T. Javed, and Z Abbas, "Slip flow and heat transfer of a second grade fluid past a stretching sheet through a porous sheet," International Journal of Heat and Mass Transfer, **51**, 4528-4534 (2008). https://doi.org/10.1016/j.ijheatmasstransfer.2007.12.022

[11] O.D. Makinde, "Effect of variable viscosity on thermal boundary layer over a permeable flat plate with radiation and a convective surface boundary condition," Journal of Mechanical Science and Technology, **26**, 1615-1622 (2012). https://doi.org/10.1007/s12206-012-0302-1

[12] K. Gangadhar, N.B. Reddy, and P.K. Kameshwaran, "Similarity solution of hydro magnetic heat and mass transfer over a vertical plate with a convective surface boundary condition and chemical reaction," International Journal of Nonlinear Science, **13**(3), 298-307 (2012).

[13] P. Olanrewaju, T. Anake, O.T. Arulogun, and D. Ajadi, "Further results on the effects of variable viscosity and magnetic field on flow and heat transfer to a continuous flat plate in the presence of heat generation and radiation with a convective boundary condition," American Journal of Computational and Applied Mathematics, **2**, 42-48 (2012). https://doi.org/10.5923/j.ajcam.20120202.08

[14] P. Garg, G.N. Purohit, and R.C. Chaudhary, "Similarity solutions for combined free-forced convection past a vertical porous plate in a porous medium with a convective surface boundary condition," Int. J. of Applied Mechanics and Engineering, **21**(4), 827-836 (2016). https://doi.org/101515/ijame-2016-0048

[15] P. Garg, G.N. Purohit, and R.C. Chaudhary, "Free convective unsteady MHD flow in slip flow Regime past a vertical plate with a convective surface boundary condition," Journal of Informatics and Mathematical sciences, **10**, 261-270 (2018). https://dx.doi.org/10.26713/jims.v10i1-2.1050

[16] N. Kalita, R.K. Deka, and R.S. Nath, "Unsteady flow Past an accelerated vertical plate in presence of chemical reaction," East Eur. J. Phys. (3), 223-232 (2023). https://doi.org/10.26565/2312-4334-2023-3-49

[17] S. Sarma, N. Ahmed, "Dufour effect on unsteady MHD flow past a vertical plate embedded in porous medium with ramped temperature," Sci. Rep. **12**(1), 13343 (2022). https://doi.org/10.1038/s41598-022-15603-x

[18] A. Selvaraj, S.D. Jose, R. Muthucumaraswamy, and S. Karthikeyan, "MHD-Parabolic flow past an accelerated isothermal vertical plate with heat and mass diffusion in the presence of rotation," Material Today Proc. **46**, 3546-3549 (2021). https://doi.org/10.1016/j.matpr.2020.12.499

[19] M.V. Krishna, "Hall and ion slip impacts on unsteady MHD free convective rotating flow of Jeffreys fluid with ramped wall temperature," Int. Commun. Heat. Mass. Transfer, **119**, 104927 https://doi.org/10.1016/j.icheatmasstransfer,2020.104927

[20] P.K. Pattnaik, S. Mishra, A. Barik, and A. Mishra, "Influence of chemical reaction on magnetohydrodynamic flow over an exponential stretching sheet: a numerical study," Int. J. Fluid Mech. Res. **47**(3), (2020). https://doi.org/10.1615/InterJFluidMechRes.2020028543

[21] R.S. Nath, and R.K. Deka, "Theoretical study of Thermal and Mass Stratification Effects on MHD Nanofluid past an Exponentially Accelerated Vertical Plate in a Porous Medium in Presence of Heat Source, Thermal Radiation and Chemical Reaction," Int. J. Appl. Comput. Math. (2024). https://doi.org/10.1007/s40819-024-01721-9

ВПЛИВ РОЗРІДЖЕНЬ ТА КОНВЕКТИВНОЇ ТЕПЛОЗМІНИ НА ВІЛЬНИЙ КОНВЕКТИВНИЙ НЕСТАЦІЙНИЙ МГД-ПОТІК У РЕЖИМІ КОВЗАННЯ ПОВЗ ВЕРТИКАЛЬНУ СТІНКУ З ГРАНИЧНОЮ УМОВОЮ КОНВЕКТИВНОЇ ПОВЕРХНІ

Хемант Агарвал[a], Шьяманта Чакраборті[b]
[a]Кафедра математики, університет Гаухаті, Гувахаті-781014, Ассам, Індія
[b]UGC-HRDC, університет Гаухаті, Гувахаті-781014, Ассам, Індія

Досліджено нестаціонарний вільний конвективний двовимірний МГД-течія повз вертикальну пористу пластину з граничною умовою конвективної поверхні в пористому середовищі в режимі ковзання під дією змінної швидкості всмоктування. Аналітичні розв'язки отримані для системи з використанням методу збурень, який перетворює нелінійні зв'язані керівні диференціальні рівняння в часткових похідних у безрозмірну форму звичайних диференціальних рівнянь. Вплив змінної швидкості всмоктування, параметра розрідження та параметра зміни тепла аналізується та обговорюється графічно для різних значень ефективного фізичного параметра, такого як число Грассгофа, параметр магнітного поля, число Прандтля, параметр проникності, на швидкість рідини та температуру, тертя шкіри та теплопередачу.

Ключові слова: *магнітогідродинамічний потік; проникність; розрідження; конвективна зміна тепла; змінна швидкість всмоктування*

ENTROPY GENERATION ANALYSIS ON HYBRID DUSTY NANOFLUID FLOW OVER A HEATED STRETCHING SHEET: AEROSPACE TECHNOLOGY

Gunisetty Ramasekhar[a]*, P.D. Selvi[b], Madduru Sudhakara Reddy[c], S.R.R. Reddy[d], Shaik Jakeer[e], Sangapatnam Suneetha[f#]

[a]*Department of Mathematics, Rajeev Gandhi Memorial College of Engineering and Technology (Autonomous), Nandyal 518501, Andhra Pradesh, India*
[b]*Department of Applied Mathematics, Sri Padmavathi Mahila Visva Vidyalayam, Tirupati, India*
[c]*Department of Mathematics, SVR Engineering College, Nandyal 518502, India*
[d]*Department of Mathematics, Koneru Lakshmaiah Education Foundation, Bowrampet, Hyderabad, Telangana, 500043, India*
[e]*School of Technology, The Apollo University, Chittoor, Andhra Pradesh, 517127, India*
[f]*Department of Applied Mathematics Yogi Vemana University Kadapa, 516003, Andhra Pradesh, India*
*#Corresponding Author's e-mail: gunisettyrama@gmail.com, #e-mail suneethayvu@gmail.com

The past few years have seen enormous investments in research and development of next generation technologies with potential use in aerospace. Engine oil provides grease, air conditioning, maintenance, rust prevention, reduced sound and turbine functioning among its many functions within an airplane engine. Among these, lubrication is paramount. Without lubrication, it goes without saying that any moving components would wear out very fast. The present study investigates the significance of heat transport properties entropy generation on MHD dusty hybrid nanofluid flow over a heated stretching sheet in the presence of heat generation. By using the suitable self-similarity variables, the partial differential equation is transformed into ordinary differential equations. After then, the dimensionless equations are solved by using the MATLAB solver in bvp4c scheme. Graphs and tables are explained how the operational factors affect fluid flow efficiency. The velocity profile enhanced for increasing magnetic field values, however the energy outline exhibited the reverse behavior, which we observed. During the course of our research, we came to the conclusion that mixed nanofluids are superior to dusty small fluids in terms of their ability to transport energy transporters.

Keywords: *Entropy generation; Dusty fluid; MHD; Thermal radiation; Hybrid nanofluid*
PACS: 44.05.+e, 44.30.+v, 44.40.+a, 47.10.ad.

1. INTRODUCTION

Researchers across a wide variety of scientific and technological sectors have been increasingly interested in tiny fluids over the course of a lengthy period of time. To produce a fluid that is devoid of impurities, such as dust tiny particles, into the surroundings represents an incredibly difficult activity. This means that regular fluids' heat transmission capacities may be enhanced by adding these millimeter- or microscopic-shaped atoms, called dust tiny particles. The identification of this group may be traced back to the presence of dusty liquids. The study and investigation that is related to such substances has shown to be beneficial in a wide range of practical scenarios, such as oil transportation, combustion, reactor tubes, and a great number of other technical sectors; a number of scientific studies are available in this field [1][2][3]. Through the use of a variety of presumptions regarding dust particles, That was the calendar year 1962, Saffman [4] discovered the mathematical formulas that govern the velocity at which dust grains move. Because it was thought that dusty molecules accumulated in the belief area formed a pseudo-fluid, he neglected to take into consideration for the relationships among individual dust grains when he used his method, Marble [5] investigated the problem of a gas containing trace amounts of solid.

Over the last several years, a significant number of researchers have been concentrating their efforts on finding methods to improve heat transfer. This has happened due to the fact that this subject is significant in a variety of corporate and technical settings. It is common practice to use biological fluids in thermal transfer, including glycol, water, and crude oil. The restricted circulation of heat which is associated using these types of liquids leads in a restriction to the thermal transfer, which is an additional aspect to consider that should be taken into consideration. The concept of small liquids was conceived with the intention of including several small particles that were dispersed across the initial substance at the same time. Because of this, the word "hybrid nanofluid" came into being as a consequence [6][7][8]. In the process of creating methods for burning and cooling, mixed nanofluids represent a major step forward. Within the moment, these small particles have been used to enhance the thermal look of liquids. Incorporating a number of different kinds of tiny particles results in the formation of a fluid with improved heat transmission. The substances in question have a broad range of applications, including but not limited to the usage of steaming water and braking fluid for automobiles. Additionally, it is used in thermal transfer systems and transformations, in addition to being utilized in frequently used domestic appliances like refrigerators. Extensive research has previously been carried out by a multitude of researchers using hybrid tiny particles in their examinations, as shown in Refs. [9][10][11][12].

Dusty liquid atoms, measuring micro meters of in size, are dispersed throughout the foundation solution. Numerous researchers and experts are currently motivated to support the movement of dusty liquid as a consequence of its present improvements and increasing importance in the demands of connected to mechanical, commercial, technical, and pharmaceutical domains. This is due to the fact that dusty liquid is becoming increasingly prevalent. Natural gas shipment, refinery cleaning, power plant transmission lines, combustion, adaptable steel coverings, substance drying out, soil preservation by natural storms, natural reliability, health, and medical care (especially in bacterial agriculture, developing stem cells differentiation, particular molding of plastic, tumors diagnosis and treatment, and cold therapies) all make utilize dusty water [13].

The present study aims to scrutinize the carrying of hybrid nanofluid across a stretching sheet in existence of MHD and porosity with engine oil as base fluid. Also, thermal radiation is taken into account. Notwithstanding the utility of the investigation, the flow framework in problem has never been shared before and its movement characteristics have never been tested. The availability of several research addressing the industrial uses and improvements of mixed nanofluids generated the investigation. A computer technique called the bvp4c method is used to resolve the mathematical framework. In this study, we provide a qualitative evaluation of the system's characteristics. The present model may be applicable in the aerospace industry. Considering that oil is used over cooling functions in aviation machines much more frequently than water is used in automobile engines.

2. MATHEMATICAL MODEL

In the current of dusty hybrid particles, steady 2D leading hybrid nanofluid flow has been considered into the model. In this model we considered the sheet is taken as along the $x-$axis and the flow confined to $y > 0$. Here we taken the $y-$axis is normal to the sheet. The movement of the heated stretching sheet taking the $x-$axis is $U=rx$. And also, an additional M field strength B_0 is forced through $x-$axis see in (Fig. 1). Table 1 show that clear-cut outputs of the base fluid and nanoparticles. The arranged governing flow equations are [14][15][16].
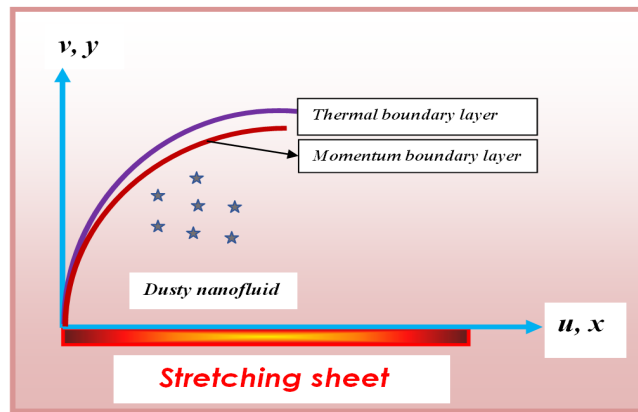

Figure 1. Geometry of the problem

Fluid phase

$$\frac{\partial u}{\partial x} + \frac{\partial v}{\partial y} = 0, \tag{1}$$

$$u\frac{\partial u}{\partial x} + v\frac{\partial u}{\partial y} = \frac{\mu_{hnf}}{\rho_{hnf}}\left(\frac{\partial^2 u}{\partial y^2}\right) + \frac{KN}{\rho_{hnf}}\left(u_p - u\right) - \frac{\sigma_{hnf}B^2}{\rho_{hnf}}(u), \tag{2}$$

$$u\frac{\partial T}{\partial x} + v\frac{\partial T}{\partial y} = \frac{k_{hnf}}{(\rho c_p)_{hnf}}\left(\frac{\partial^2 T}{\partial y^2}\right) + \frac{N_1(c_p)_f}{\tau_T}\left(T_p - T\right) + \frac{N_1}{\tau_v}\left(u_p - u\right)^2$$
$$- \frac{1}{(\rho c_p)_{hnf}}\left(\frac{\partial q_r}{\partial y}\right) + \frac{\sigma_{hnf}B^2}{(\rho c_p)_{hnf}}u^2. \tag{3}$$

Dusty phase

$$\frac{\partial \overline{u_p}}{\partial x} + \frac{\partial \overline{v_p}}{\partial y} = 0, \tag{4}$$

$$\overline{u_p}\frac{\partial \overline{u_p}}{\partial x} + \overline{v_p}\frac{\partial \overline{u_p}}{\partial y} = \frac{K}{m}\left(u - \overline{u_p}\right), \tag{5}$$

$$N_1 r_m \left(\overline{u_p} \frac{\partial \overline{T_p}}{\partial x} + \overline{v_p} \frac{\partial \overline{T_p}}{\partial y} \right) = \frac{N_1 (c_p)_f}{\tau_T} (\overline{T_p} - T).$$

(6)

The appropriate flow boundary requirements that have been enforced for hybrid nano- fluid and dust phases can be stated as follows:

$$\left.\begin{array}{ll} u = U = u_w(x), \quad v = 0, \ T = T_w & at \quad y = 0 \\ u \to 0, \overline{u_p} \to 0, \overline{v_p} \to v, T \to T_\infty, \overline{T_p} \to T_\infty & as \ y \to \infty \end{array}\right\}.$$

(7)

Thermo-physical properties of *hnf* are:

$$\mathbb{Z}_1 = \frac{\mu_{hnf}}{\mu_f}, \mathbb{Z}_2 = \frac{\rho_{hnf}}{\rho_f}, \mathbb{Z}_3 = \frac{\sigma_{hnf}}{\sigma_f}, \mathbb{Z}_4 = \frac{(\rho c_p)_{hnf}}{(\rho c_p)_f}, \mathbb{Z}_5 = \frac{k_{hnf}}{k_f},$$

(8)

$$\upsilon_{hnf} = \frac{\mu_{hnf}}{\rho_{hnf}}, \quad \alpha_{hnf} = \frac{k_{hnf}}{(\rho c_p)_{hnf}}.$$

$$\left.\begin{array}{l} \mathbb{Z}_1 = \dfrac{1}{(1-\phi_1)^{2.5}(1-\phi_2)^{2.5}}, \\[3mm] \mathbb{Z}_2 = \left\{ (1-\phi_2)\left[(1-\phi_1) + \phi_1\left(\dfrac{\rho_{s_1}}{\rho_f}\right)\right] + \phi_2 \dfrac{\rho_{s_2}}{\rho_f} \right\}, \\[3mm] \mathbb{Z}_3 = \dfrac{\sigma_{s_2} + 2\sigma_{nf} - 2\phi_2(\sigma_{nf} - \sigma_{s_2})}{\sigma_{s_2} + 2\sigma_{nf} + \phi_2(\sigma_{nf} - \sigma_{s_2})} \times \dfrac{\sigma_{s_1} + 2\sigma_f - 2\phi_1(\sigma_f - \sigma_{s_1})}{\sigma_{s_1} + 2\sigma_f + \phi_1(\sigma_f - \sigma_{s_1})}, \\[3mm] \mathbb{Z}_4 = (1-\phi_2)\left[(1-\phi_1) + \phi_1\left(\dfrac{(\rho c_p)_{s_1}}{(\rho c_p)_f}\right)\right] + \phi_2 \dfrac{(\rho c_p)_{s_2}}{(\rho c_p)_f}, \\[3mm] \mathbb{Z}_5 = \dfrac{k_{s_1} + 2k_{bf} - 2\phi_2(k_{bf} - k_{s_2})}{k_{s_2} + 2k_{bf} + \phi_2(k_{bf} - k_{s_2})} \times \dfrac{k_{s_1} + 2k_f - 2\phi_1(k_f - k_{s_1})}{k_{s_1} + 2k_f + \phi_1(k_f - k_{s_1})} \end{array}\right\}.$$

(9)

Defining the similarity variables and transformations are

$$\left.\begin{array}{l} u = rxf'(\eta), \ v = -\sqrt{\upsilon_f r} f(\eta), \ \eta = \sqrt{\dfrac{r}{\upsilon_f}} y, \ \theta(\eta) = \dfrac{T - T_\infty}{T_w - T_\infty} \\[3mm] \overline{u_p} = rxF_p'(\eta), \ \overline{v_p} = -\sqrt{\upsilon_f r} F_p(\eta), \ \theta_p(\eta) = \dfrac{\overline{T_p} - T_\infty}{T_w - T_\infty} \end{array}\right\}.$$

(10)

The following is a transformation of equations (2)–(6) and their corresponding boundary conditions using mathematical equations (8)–(10) and the corresponding authorities.
Fluid phase

$$\frac{\mathbb{Z}_1}{\mathbb{Z}_2} f''' - (f')^2 + ff'' + \frac{1}{\mathbb{Z}_2} I^* \beta^* (F' - f') - \frac{\mathbb{Z}_3}{\mathbb{Z}_2} Mf' = 0,$$

(11)

$$\frac{1}{\mathbb{Z}_4}\left(\frac{k_{hnf}}{k_f} + \frac{4}{3} Rd\right) Pr\theta'' + Prf\theta' + PrI^*\beta_t(\theta_p - \theta) + \beta_v EcPr(F' - f')^2 + \frac{\mathbb{Z}_3}{\mathbb{Z}_4} MEc(f')^2 = 0.$$

(12)

Dusty phase

$$(F')^2 - FF'' - \beta^*(f' - F') = 0,$$

(13)

$$F\theta_p' + \gamma\beta_t(\theta_p - \theta) = 0,$$

(14)

$$\left.\begin{array}{ll} f'(\eta) = 1, f(\eta) = 0, \theta(\eta) = 1, & at \ \eta = 0 \\ f'(\eta) = 0, F'(\eta) = 1, F(\eta) = f(\eta), \theta(\eta) = 0, \theta_p(\eta) = 0 \ as \ \eta \to \infty \end{array}\right\}$$

(15)

The nondimensional parameters are:

$I^* = \dfrac{Nm}{\rho_f}$ Dust particles with mass concentration	$Br = \dfrac{\mu_f U^2}{k\Delta T}$ Brinkman number
$\alpha = \dfrac{\Delta T}{T_w}$ is the Temperature ratio parameter	$\beta_v = \dfrac{1}{r\tau_v}$ Fluid - particle interaction parameter
$\gamma = \dfrac{(c_p)_f}{r_m}$ Ratio of specific heat	$M = \dfrac{\sigma_f B^2}{r\rho_f}$ magnetic field parameter
$Rd = \dfrac{4\sigma^* T_1^3}{3k^* k_f}$ Radiation parameter	$Ec = \dfrac{U^2}{(c_p)_f (T_w - T_\infty)}$ Eckert number
$\beta_t = \dfrac{1}{r\tau_T}$ Fluid - particle interaction parameter for temperature	$Pr = \dfrac{\mu_f (c_p)_f}{k_f}$ Prandtl number
$\beta^* = \dfrac{K}{rm}$ Particle interaction parameter	

The dimensional form of C_f and Nu_r are given by

$$C_f = \frac{\tau_w}{\rho_f u_w^2} \tag{16}$$

Where shear stress τ_w is

$$\tau_w = \mu_{hnf} \left. \frac{\partial u}{\partial y} \right|_{y=0}$$

$$Nu_r = -\left(k_{hnf} + \frac{16\,\sigma^* T_1^3}{3k^* k_f} \right) \frac{r\left(\dfrac{\partial T}{\partial z} \right)_{z=0}}{(T_w - T_\infty)} \tag{17}$$

The non-dimensional form of Eqs. (16 –17) are converted as

$$Re_r^{1/2} C_f = \mathbb{Z}_1 f''(0), \tag{18}$$

$$(Re_r)^{-1/2} Nu_r = -\left(\frac{k_{hnf}}{k_f} + \frac{4}{3} Rd \right) \theta'(0) \tag{19}$$

Where Re_r is the local Reynolds number.

Entropy generation analysis

$$S_{gen}''' = \frac{k_f}{T_\infty^2} \left[k_{hnf} + \frac{16\sigma^* T_1^3}{3k^* k_f} \right] \left(\frac{\partial T}{\partial z} \right)^2 + \frac{\mu_{hnf}}{T_w} \left(\frac{\partial u}{\partial y} \right)^2 + \left(\frac{\sigma B^2}{T_w} \right) u^2 \tag{20}$$

The Entropy generation number N_G becomes

$$N_G = \frac{S_{gen}'''}{\left(k_f r \Delta T / T_w \upsilon_f \right)}$$
$$= \alpha\left(\mathbb{Z}_5 + \frac{4}{3} Rd \right)(\theta')^2 + \frac{Br}{(1-\phi_1)^{2.5}(1-\phi_2)^{2.5}} (f'')^2 + MBr (f')^2 \tag{21}$$

The Bejan number is

$$Be = \frac{\alpha\left(\mathbb{Z}_5 + \dfrac{4}{3} Rd \right)(\theta')^2}{\alpha\left(\mathbb{Z}_5 + \dfrac{4}{3} Rd \right)(\theta')^2 + \dfrac{Br}{(1-\phi_1)^{2.5}(1-\phi_2)^{2.5}} (f'')^2 + MBr (f')^2} \tag{22}$$

Table 1. Hybrid nanoparticles of thermo physical properties [17][18][19].

Property	Engine oil	Cu	Al₂O₃
Density ρ (kgm^{-3})	884	8933	3970
Specific heat C_p $(Jkg^{-1}K^{-1})$	1910	385	375
Heat conductivity k_f $(Wm^{-1}K^{-1})$	0.144	401	40
Electrical conductivity σ $(\Omega m)^{-1}$	0.125×10^{-11}	5.96×10^{7}	131.7×10^{-2}

3. NUMERICAL METHOD

The Bvp4c method was used to numerically solve the non-dimensional system of Eqs. (11) – (14) and (15). With this technique, we started by transforming the fundamental Differential equations into a set of first-order ODEs, so that we introduced the new set of variables are

$$f = j_1, f' = j_2, f'' = j_3, f''' = j_3', \theta = j_4, \theta' = j_5, \theta'' = j_5', F = j_6,$$

$$F' = j_7, F'' = j_7', \theta_p = j_8, \theta_p' = j_8'$$

$$
\begin{cases}
j_1' = j_2 \\[4pt]
j_2' = j_3 \\[4pt]
j_3' = -\left[\dfrac{-(j_2)^2 + j_1 j_3 + \dfrac{1}{\mathbb{Z}_2} I^* \beta^* (j_7 - j_2) - \dfrac{\mathbb{Z}_3}{\mathbb{Z}_2} M j_2}{\dfrac{\mathbb{Z}_1}{\mathbb{Z}_2}} \right] \\[18pt]
j_4' = j_5 \\[4pt]
j_5' = -\left[\dfrac{Pr\, j_1 j_5 + Pr I^* \beta_t (j_8 - j_4) + \beta_v Ec Pr (j_7 - j_2)^2 + \dfrac{\mathbb{Z}_3}{\mathbb{Z}_4} MEc (j_2)^2}{\dfrac{1}{\mathbb{Z}_4}\left(\dfrac{k_{hnf}}{k_f} + \dfrac{4}{3} Rd\right) Pr} \right] \\[18pt]
j_6' = j_7 \\[4pt]
j_7' = -\left[\dfrac{(j_7)^2 - \beta^* (j_2 - j_7)}{j_6} \right] \\[10pt]
j_8' = j_9 \\[4pt]
j_9' = -\left[\dfrac{\gamma \beta_t (j_8 - j_4)}{j_4} \right]
\end{cases}
$$

As well as the boundary conditions are

$$
\begin{cases}
j_2(0) = 1, \\
j_1(0) = 0, \\
j_4(0) = 1, \\
j_2(\infty) = 0, \\
j_6(\infty) = 0, \\
j_7(\infty) = 0, \\
j_4(\infty) = 0, \\
j_8(\infty) = 0.
\end{cases}
$$

4. CODE VALIDATION

The results of the present code were compared to those obtained by Mishra et al. for the case of various values of Prandtl number, as shown in Table 2. We discovered a significant level of convergence between the current findings. In

this case, the step size in the technique is $(h = 0.001)$, and the operation is frequent until the desired level (1×10^{-8}) of accuracy is reached. As a result, the current code is justified.

Table 2. Comparison of $-\theta'(0)$ for $\beta = \beta_T = Ec = \phi_1 = \phi_2 = \phi_p = 0$

Pr	Mishra et al.[14]	Present results (Bvp4c)
0.72	1.088623	1.088621
1	1.333333	1.333333
10	4.796819	4.796818

5. RESULTS AND DISCUSSION

The comparison results are obtained from Table 2, which shows the in local heat transfer rate for different values of the Pr. The findings of both investigations were determined to be quite accurate. The M, Rd, β_v, I^* all are given a physical explanation in this section. The trend of M against the $f'(\eta)$ and $\theta(\eta)$ outlines are presented in Figs 2 and 4. For the larger values of M the $f'(\eta)$ outline decreased. Physically, the magnetic field M increases, it generates a Lorentz force, which converts slows down the fluid movement. Notwithstanding the fact that the Lorentz force operates in opposite to the movement of a liquid, causing it to accelerate down and consequently diminishing the velocity field, we noticed that the opposite trend was seen with regards to the profile of temperatures. The impact of I* on the velocity outline is presented in Fig 3. For the higher values of I* parameter the velocity profile declined. The impact of Rd on energy profile is seen in Fig. 5. Increasing the values of the radiation parameter will result in an improvement to the thermal profile. When viewed from a physical viewpoint, the energy barrier layer is connected to the greater temperature.
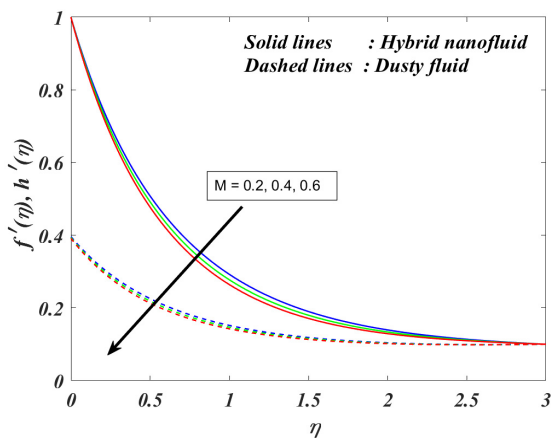

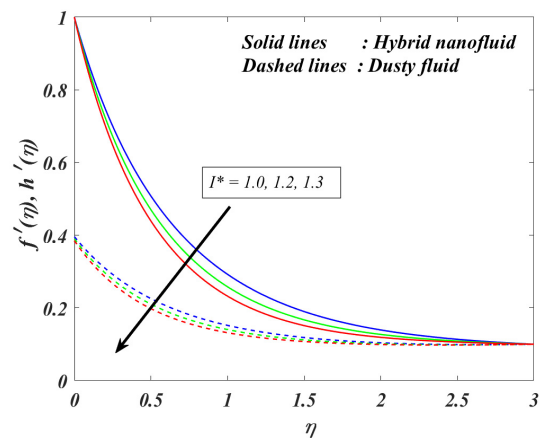**Figure 2.** Sway of M on $f'(\eta), F'_p(\eta)$

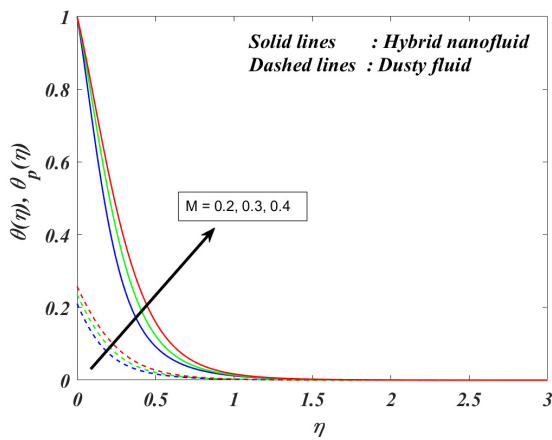**Figure 3.** Sway of I^* on $f'(\eta), F'_p(\eta)$

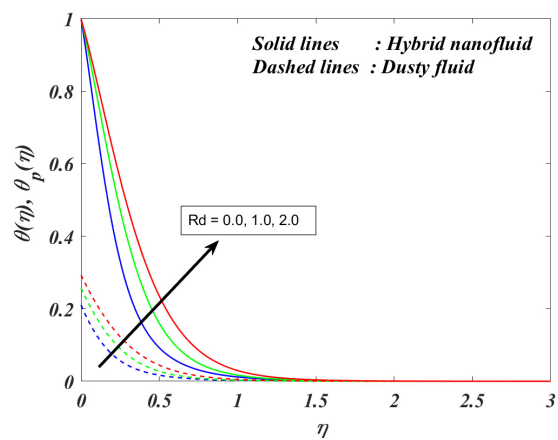**Figure 4.** Sway of M on $\theta(\eta), \theta_p(\eta)$

Figure 5. Sway of Rd on $\theta(\eta), \theta_p(\eta)$

Fig 6 impacts on the energy profile by changing the β_v parameter. When greater values are assigned, the β_v parameter for both the hybrid and dusty scenarios decreased, influencing the temperature profile. Fig 7 demonstrates the impact of the I^* and M on $C_f (Re)_r^{0.5}$.
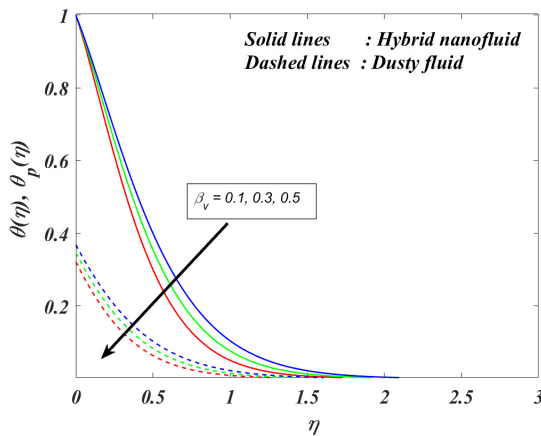
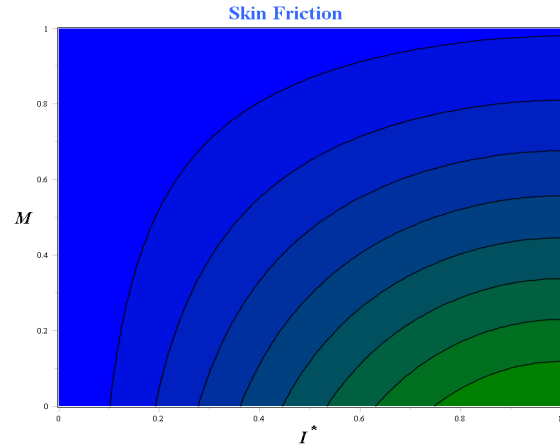**Figure 6.** Sway of β_v on $\theta(\eta), \theta_p(\eta)$

Figure 7. Sway of I^* and M on $C_f \left(Re \right)_r^{0.5}$

It shows that the $C_f \left(Re \right)_r^{0.5}$ is decreasing in increasing values of M, while the enhanced nature we noticed on enlarging the *M* parameter values, which is presented in Fig 8.

Fig 9. Impact of *Br* parameter on entropy generation outline. When increasing *Br* values the entropy generation profile enhanced. From a strictly physical point of view, when the *Br* rises, viscous dissipation becomes more important than heat transfer. The presence of an increased Brinkman number suggests that the entire system is experiencing an increased amount of viscous dissipation. In the process of viscous dissipation, the transformation of mechanical force towards temperature takes place inside the movement of the liquid. This is a consequence of the motion of friction that happens inside the fluid itself.
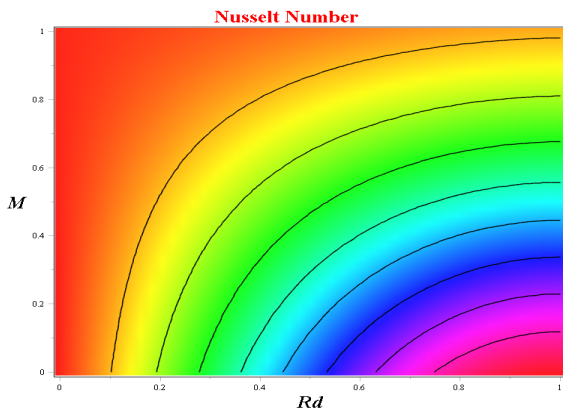

Figure 8. Sway of Rd and M on $Nu_r \left(Re \right)_r^{-0.5}$
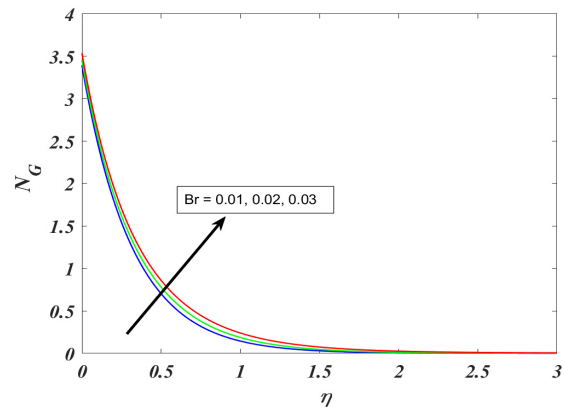

Figure 9. Sway of Br on N_G

Inside the liquid, the creation of entropy is facilitated by the transformation of energy from movement towards thermal power via this process, while the opposite trend we noticed on Fig 10.
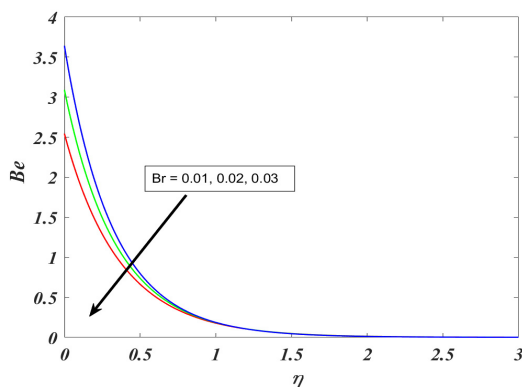

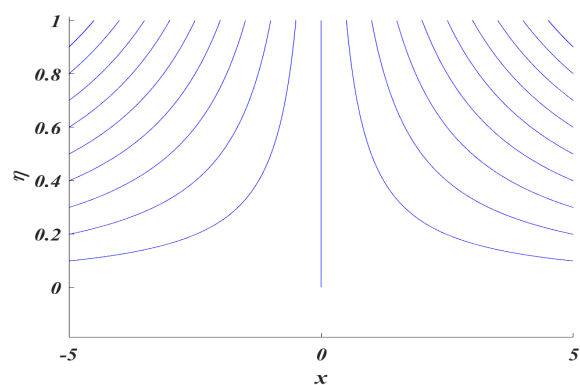**Figure 10.** Sway of Br on Be

Figure 11. Sway of $M = 1.0$ for Stream lines

Through the utilization of streamlines, it is possible to demonstrate the flow of a fluid throughout a particular area in an approach that is not only clear but also simple for anyone to understand. It is possible that the utilization of streamlines will allow for an improved understanding of significant flow characteristics, such as the places for splitting,

recycling zones, and areas of differential motion. The flow of fluids in a variety of structures, such as pipes, pathways, through things, and other infrastructure, may be shown and described with the use of streamlines, which are designed to guide investigators and programmers.

Figs 11, 12 and 13 shows that the $\left(M = 1.0, 2.0, 3.0 \right)$ impacts on streamlines. Changing the magnetic field intensity may influence streamlines in a moving fluid structure, especially in MHD fluxes where the liquid is conductive to electricity and combines with a field of magnets. The major explanation for the influence that raising the intensity of the field of magnetic attraction has on streamlines is the Lorentz force, and this is a consequence of the relationship among the magnet domain and the positively charged particles that are present in the liquid.
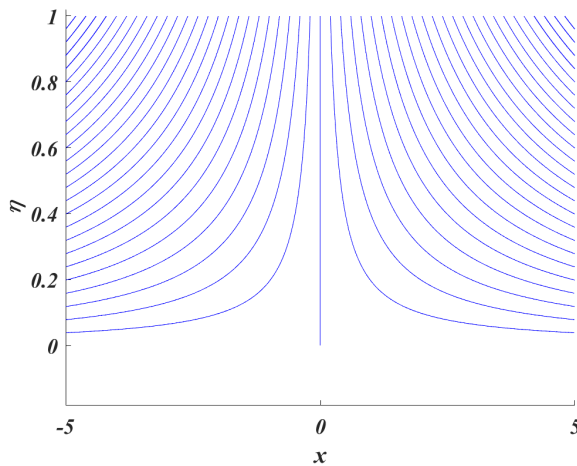

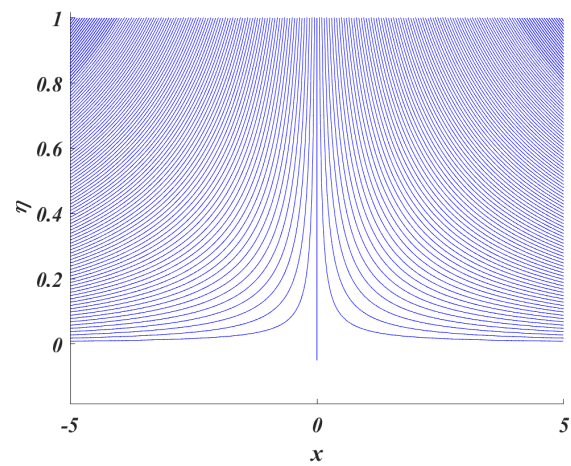
Figure 12. Sway of $M = 2.0$ for Stream lines

Figure 13. Sway of $M = 3.0$ for Stream lines

6. CONCLUSIONS

An investigation of a numerical model used in the entropy generation on MHD of hybrid nanofluid composed of Cu-Al$_2$O$_3$ and engine oil was carried out in the present investigation. For the purpose of resolving the problem of velocity and temperature, the numerical approach, also known as the bvp4c method. The research produced several of interesting findings, which are listed below:

- Velocity profile declined for the higher values of the magnetic field parameter values.
- The energy profile enhanced with an increasing radiation parameter value.
- The skin friction factor decreased for the larger values of the M parameter.
- The Nu outline increased, for the increasing values of the M.
- Streamlines have an oscillating character, which is necessary for magnifying the magnetic field parameter.

Disclosure statement
No potential conflict of interest was reported by the author(s).

ORCID
Gunisetty Ramasekhar, https://orcid.org/0000-0002-3256-3145.

REFERENCES
[1] H.A. Nabwey, and A. Mahdy, "Transient flow of micropolar dusty hybrid nanofluid loaded with Fe$_3$O$_4$-Ag nanoparticles through a porous stretching sheet," Results Phys. **21**, (2021). https://doi.org/10.1016/j.rinp.2020.103777
[2] S. Jakeer, and P.B.A. Reddy, "Entropy generation on the variable magnetic field and magnetohydrodynamic stagnation point flow of Eyring–Powell hybrid dusty nanofluid: Solar thermal application," Proc. Inst. Mech. Eng. Part C, J. Mech. Eng. Sci. **236**(13), 7442–7455 (2022). https://doi.org/10.1177/09544062211072457
[3] A. Divya, and P. Bala Anki Reddy, "Aerospace aspects of electromagnetohydrodynamic dusty flow of hybrid nanofluid with entropy generation over a rotating disk," Proc. Inst. Mech. Eng. Part E, J. Process Mech. Eng. **237**(2), 196-206 (2022). https://doi.org/10.1177/09544089221102417
[4] P. Saffman, "On the stability of laminar flow of a dusty gas," J. fluid mech, **13**(1), 120-128 (1962). https://doi.org/10.1017/S0022112062000555
[5] F.E. Marble, "Dynamics of Dusty Gases," Annu. Rev. Fluid Mech. **2**(1), 397–446 (1970). https://doi.org/10.1146/ANNUREV.FL.02.010170.002145
[6] G. Ramasekhar, *et al.*, "Heat transfer exploration for bioconvected tangent hyperbolic nanofluid flow with activation energy and joule heating induced by Riga plate," Case Stud. Therm. Eng. **55**, 104100 (2024). https://doi.org/10.1016/j.csite.2024.104100
[7] G. Ramasekhar, and M. Jawad, "Numerical Heat Transfer , Part A : Applications Characteristics of MWCNT , SWCNT , Cu and water based on magnetized flow of nanofluid with Soret and Dufour effects induced by moving wedge : Consequence of Falkner – Skan power law," Numer. Heat Transf. Part A, Appl. 1–15, 2024, https://doi.org/10.1080/10407782.2024.2341270
[8] G. Ramasekhar, "Scrutinization of BVP Midrich Method for Heat Transfer Analysis on Various Geometries in the Presence of Porous Medium and Thermal Radiation ," **13**(1), 100–107 (2024). https://doi.org/10.1166/jon.2024.2130

[9]   A. Divya, and P.B.A. Reddy, "Electromagnetohydrodynamic unsteady flow with entropy generation and hall current of hybrid nanofluid over a rotating disk: An application in hyperthermia therapeutic aspects," Proc. Inst. Mech. Eng. Part C, J. Mech. Eng. Sci. **236**(13), 7511–7528 (2022). https://doi.org/10.1177/09544062221076294

[10]   A.J. Chamkha, A.S. Dogonchi, and D.D. Ganji, "Magneto-hydrodynamic flow and heat transfer of a hybrid nanofluid in a rotating system among two surfaces in the presence of thermal radiation and Joule heating," AIP Adv. **9**(2), 1–14 (2019). https://doi.org/10.1063/1.5086247

[11]   S. Shaw, S.S. Samantaray, A. Misra, M.K. Nayak, and O.D. Makinde, "Hydromagnetic flow and thermal interpretations of Cross hybrid nanofluid influenced by linear, nonlinear and quadratic thermal radiations for any Prandtl number," Int. Commun. Heat Mass Transf. **130**, 105816 (2022). https://doi.org/10.1016/j.icheatmasstransfer.2021.105816

[12]   S. Jakeer, and S.R.R. Reddy, "Electrokinetic membrane pumping flow of hybrid nanofluid in a vertical microtube with heat source/sink effect," Eur. Phys. J. Plus, **138**(6), 489 (2023). https://doi.org/10.1140/EPJP/S13360-023-04118-7

[13]   S. Jakeer and P.B.A. Reddy, "Entropy generation on the variable magnetic fi eld and magnetohydrodynamic stagnation point fl ow of Eyring-Powell hybrid dusty nano fluid : Solar thermal application," **236**(13), 1–14 (2022). https://doi.org/10.1177/09544062211072457

[14]   S. Mishra, M. Khan, and B.C. Rout, International Communications in Heat and Mass Transfer, "Dynamics of dust particles in a conducting dusty nanomaterials: A computational approach," **119**, 104967 (2020). https://doi.org/10.1016/j.icheatmasstransfer.2020.104967

[15]   M. Reddy, M. Rani, *et al.*, "Hybrid dusty fluid flow through a Cattaneo–Christov heat flux model," Physica A: Statistical Mechanics and its Applications, **551**, 123975 (2020). https://doi.org/10.1016/j.physa.2019.123975

[16]   S.K. Parida, *et al.*, "Dynamics of dust particles in a conducting water-based kerosene nanomaterials: A computational approach," Int. J. Chem. React. Eng. **19**(8), 787–797 (2021). https://doi.org/10.1515/ijcre-2020-0204

[17]   M.A. Qureshi, "A case study of MHD driven Prandtl-Eyring hybrid nanofluid flow over a stretching sheet with thermal jump conditions," Case Stud. Therm. Eng. **28**, 101581 (2021). https://doi.org/10.1016/J.CSITE.2021.101581

[18]   G. Ramasekhar, and P. Bala Anki Reddy, "Entropy generation on Darcy–Forchheimer flow of Copper-Aluminium oxide/Water hybrid nanofluid over a rotating disk: Semi-analytical and numerical approaches," Sci. Iran. **30**(6), 2245–2259 (2023). https://doi.org/10.24200/sci.2023.60134.6617

[19]   A. Almaneea, "Numerical study on heat and mass transport enhancement in MHD Williamson fluid via hybrid nanoparticles," Alexandria Eng. J. (2022). https://doi.org/10.1016/j.aej.2022.01.041

АНАЛІЗ ГЕНЕРАЦІЇ ЕНТРОПІЇ НА ГІБРИДНОМУ ПИЛОВОМУ ПОТОКУ НАНОРІДИНИ НАД НАГРІТИМ РОЗТЯГУЮЧИМ ЛИСТОМ: АЕРОКОСМІЧНА ТЕХНОЛОГІЯ

Гунісетті Рамасекар[a], П.Д. Селві[b], Мадуру Судхакара Редді[c], С.Р.Р. Редді[d], Шаік Закір[e], Сангапатнам Суніта[f]

[a]*Кафедра математики, Меморіальний коледж інженерії та технологій імені Раджива Ганді (автономний), Нандял 518501, Андхра-Прадеш, Індія*

[b]*Департамент прикладної математики, Шрі Падмаватхі Магіла Вішва Відьялаям, Тірупаті, Індія*

[c]*Факультет математики, Інженерний коледж SVR, Нандял 518502, Індія*

[d]*Департамент математики, Освітній фонд Конеру Лакшмайя, Боурампет, Хайдарабад, Телангана, 500043, Індія*

[e]*Технологічна школа, Університет Аполло, Читтор, Андхра-Прадеш, 517127, Індія*

[f]*Департамент прикладної математики університет Йогі Вемана, Кадапа, 516003, Андхра-Прадеш, Індія*

За останні кілька років було зроблено величезні інвестиції в дослідження та розробку технологій наступного покоління з потенційним використанням в аерокосмічній галузі. Моторна олива забезпечує мастило, кондиціонування повітря, технічне обслуговування, запобігання іржі, зниження шуму та роботу турбіни серед багатьох функцій двигуна літака. Серед них першочергове значення має змащення. Зрозуміло, що без змащення будь-які рухомі компоненти дуже швидко зношуються. У цьому дослідженні досліджується значення генерації ентропії теплотранспортних властивостей у потоці пилової гібридної нанорідини МГД над нагрітим листом, що розтягується, за наявності тепла. Використовуючи відповідні змінні самоподібності, диференціальне рівняння в частинних похідних перетворюється на звичайне диференціальне рівняння. Після цього безрозмірні рівняння розв'язуються за допомогою розв'язувача MATLAB у схемі bvp4c. Графіки та таблиці пояснюють, як експлуатаційні фактори впливають на ефективність потоку рідини. Профіль швидкості посилювався для збільшення значень магнітного поля, однак енергетичний контур демонстрував зворотну поведінку, яку ми спостерігали. У ході нашого дослідження ми дійшли висновку, що змішані нанофлюїди перевершують пилоподібні невеликі рідини з точки зору їх здатності транспортувати переносники енергії.

Ключові слова: *генерація ентропії; пилова рідина; МГД; теплове випромінювання; гібридна нанофлюїд*

EXACT ANALYSIS OF MHD CASSON FLUID FLOW PAST AN EXPONENTIALLY ACCELERATED VERTICAL PLATE IN A POROUS MEDIUM WITH RADIATION ABSORPTION, HEAT GENERATION, AND DIFFUSION-THERMO EFFECTS WITH THERMAL AND SOLUTAL RAMPED CONDITIONS

 Dibya Jyoti Saikia[a,b]*, **Nazibuddin Ahmed[c], Ardhendu Kr. Nandi[b], Dip Jyoti Bora[c]**
aDepartment of Mathematics, Gauhati University, Guwahati 781014, India
bDepartment of Mathematics, Basugaon College, Basugaon-783372 Assam, India
cDepartment of Mathematics, Cotton University, Guwahati 781001, India
*Corresponding Author e-mail: dssaikia18@gmail.com

The current investigation aims at to examine the effect of radiation absorption, heat generation and Dufour number on MHD Casson fluid flow past an exponentially accelerated vertical plate in a porous medium with chemical reaction. The governing equations for momentum, energy and concentration are solved by implementing the Laplace transformation method. Skin friction, rate of heat transfer and rate of mass transfer expressions are also extracted and depicted in tabular form. Investigation simulates that Casson parameter diminished the fluid velocity, whereas energy flux due to a mass concentration gradient improves the temperature field of the flow problem. In addition to this, temperature field is observed to be developed under the influence of radiation absorption and heat generation. Furthermore, the effects of different non-dimensional parameters on velocity field, temperature fluid and species concentration are exhibited graphically.
Keywords: *MHD; Radiation absorption; Casson fluid; Heat generation; Dufour effect*
PACS: 44.25. f, 44.30. v, 44.40. a, 47.65. d

1. INTRODUCTION

Magnetohydrodynamics (MHD) has an extensive range of application in abundant areas of applied research such as engineering, astrophysics, biological science etc. Hannes Alfven [1], the great plasma physicist, initiated the field of MHD. The influence of unsteady MHD natural convective flow in the vicinity of an impulsively moving upright plate was cogitated by Seth *et al.* [2]. BS Goud [3] studied the effects of heat radiation on the MHD stagnation point stream across a stretched sheet with slip boundary conditions. Rath et al. [4] probed at the effects of Dufour and viscous dissipation on MHD natural convective flow through an accelerated vertical plate. Singh et al. [5] investigated the effects of time-varying wall temperature and concentration on MHD free convective flow of a rotating fluid owing to moving free-stream with hall and ion-slip currents.

In recent times, due to the significant growth of technological industries, the importance of the out-turn of thermal radiation on MHD heat transfer problems is seen to be increasing. There are numerous engineering activities that takes place at a very high temperature and therefore to avoid radiation from such activities, knowledge of thermal radiation becomes more important to build suitable equipment. Through a vertically travelling absorbent plate, the effect of radiation absorption on MHD convective flow was studied by Krishna *et al.* [6]. Using radiation absorption effect Rao *et al.* [7] analyzed the unsteady MHD flow past an exponentially accelerated plate surrounded by porous medium. In addition, Endalew and Nayak [8] also studied the effects of thermal radiation and inclined magnetic field on MHD flow past a linearly accelerated plate in the existence of porous medium.

Fluids that defiant Newton's law of viscosity termed as non-Newtonian fluids. This means that in case of a non-Newtonian fluid constant viscosity becomes independent of time. The most common example of non-Newtonian fluids is honey, butter, blood, saliva, Casson fluid etc. Kateria and Patel [9] investigated the influence of heat generation and chemical reaction on MHD Casson fluid flow over an upright plate surrounded by porous medium. Zhou *et al.* [10] investigated the two-dimensional time dependent radiative Casson fluid flow under the impact of heat source. Some other researcher such as, Sulochana *et al.* [11], Reyaz *et al.* [12], also performed their research work related to MHD heat and mass transfer by using Casson fluid.

In many engineering applications, the influence of heat generation has been found to be of considerable importance. There are many researchers, in whose research work the application of the effect of heat generation is observed. Among them, Jamuna and Balla [13], Ali *et al.* [14], Khan *et al.* [15] are the researcher who have studied the impact heat generation in their research work. The impact of non-uniform heat source/sink and temperature dependent viscosity modeled by Reynolds on Cattaneo-Christov heat flow was studied by Nayak et al. [16].

The energy flux due to a mass concentration gradient is called Dufour effect. Nayak *et al.* [17] investigated the impacts of Dufour and Soret on unsteady MHD flow past a stretching upright plate in porous medium. In addition, the impact of Dufour effect can also be seen in many other studies by various researchers such as Ahammad and Krishna [18], Jawad *et al.* [19] etc.

In recent times, it is observed that the chemical reaction becomes an integrated part of the research work of various researcher due to the extensive application of chemical reaction in various mechanisms of chemical engineering and heat and mass transfer problems.

Most recently, in the research work of Ahmed and Saikia [20] was found to be use of chemical reaction to investigate the changes of various flow characteristics such as fluid concentration and fluid velocity etc. In presence of chemical reaction, the unsteady MHD natural convective flow past an exponentially accelerated plate embedded in a porous medium was investigated by Rath and Nayak [21]. Moreover, we may also cited the research work of the researchers – Gopal *et al.* [22], Raddy *et al.* [23], Haq *et al.* [24] for their excellent work using chemical reaction.

The preeminent objective of this research work is to figure out an analytical solution for the effects of radiation absorption, Dufour, heat generation and chemical reaction on MHD Casson fluid flow past an exponentially accelerated vertical plate in a porous medium with thermal and solutal ramped conditions. Kateria and Patel [25], Mopuri *et al.* [26], Reddy and Chamkha *et al.* [27] are some of the prominent researchers in whose work the effects of radiation absorption, chemical reactions, the Dufour effect, and heat generation and absorption can be seen. Although the use of all effects such as Dufour, radiation absorption, chemical reactions, and heat generation in the presence of Casson fluid distinguishes our study from others.

2. MATHEMATICAL FORMULATION

As depicted in Figure 1, a rectangular cartesian coordinate system is set up so that x'-axis is taken in upward vertical direction along which the length of the plate is measured.
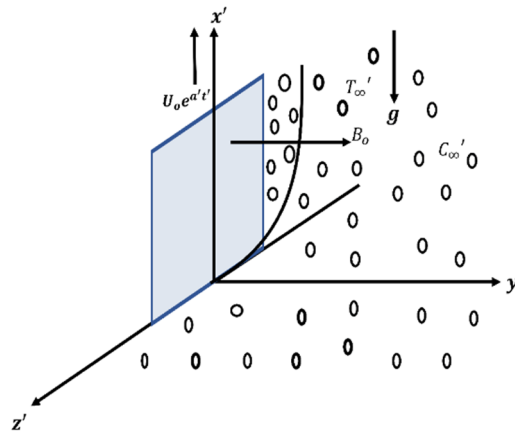

Figure 1. Physical outline of the flow problem

The y'-axis is taken parallel to the direction of the magnetic field and z'-axis is taken along the width of the plate. Now to idealize the flow problem the following assumptions are taken into account.

- Initially at $t' \leq 0$, the plate and the neighboring fluid are at static condition.
- The plate embedded in the porous medium maintain a uniform temperature T'_∞.
- The fluid adjacent to the plate maintain a uniform concentration C'_∞ at each point of the fluid.
- The plate accelerated exponentially with velocity $U_o e^{a't'}$ at time $t' > 0$ and at this period of time the concentration and temperature of the fluid is either gets improved or dropped to $C' = C'_\infty + \dfrac{(C'_w - C'_\infty)t'}{t_o}$ and $T' = T'_\infty + \dfrac{(T'_w - T'_\infty)t'}{t_o}$ respectively.
- There is no external electric field present.
- The fluid considered to be non-Newtonian in nature.

Under the above assumptions the governing equations for the flow problem are sated below:

Equation of continuity:

$$\frac{\partial u'}{\partial x'} = 0 \tag{1}$$

Momentum equation:

$$\frac{\partial u'}{\partial t'} = \nu\left(1 + \frac{1}{\beta}\right)\frac{\partial^2 u'}{\partial y'^2} - \frac{\sigma B_o^2 u'}{\rho} + g\overline{\beta'}\left(C' - C'_\infty\right) + g\beta'\left(T' - T'_\infty\right) \tag{2}$$

Energy equation:

$$\frac{\partial T'}{\partial t'} = \frac{\kappa}{\rho C_p}\frac{\partial^2 T'}{\partial y'^2} + \frac{Q_o}{\rho C_p}\left(T' - T'_\infty\right) + Q_l\left(C' - C'_\infty\right) + \frac{D_M K_T}{C_s}\frac{\partial^2 C'}{\partial y'^2}. \tag{3}$$

Species continuity equation:

$$\frac{\partial C'}{\partial t'} = D_M\frac{\partial^2 C'}{\partial y'^2} - \overline{k'}\left(C' - C'_\infty\right). \tag{4}$$

Equation of state:

$$\rho_\infty = \rho\left[1 + \beta'\left(T' - T'_\infty\right) + \overline{\beta'}\left(C' - C'_\infty\right)\right] \tag{5}$$

The initially opted boundary conditions are:

$$At\ y' \ge 0:\ u' = 0,\ T' = T'_\infty,\ C' = C'_\infty;\ t' \le 0,$$

$$\left.\begin{array}{l} u' = U_o\, e^{a't'},\ T' = T'_M,\ C' = C'_M\ ;\quad 0 < t' \le t_o \\ u' = U_o e^{a'i},\ T' = T'_w,\ C' = C'_w\ ;\qquad t' > t_o \end{array}\right\}\ at\ y' = 0; \tag{6}$$

$$As\ y' \to \infty:\ u' \to 0,\ T' \to T'_\infty,\ C' \to C'_\infty,\quad \forall t' > 0$$

where,

$$T'_M = T'_\infty + \left(T'_w - T'_\infty\right)\frac{t'}{t_o},\quad C'_M = C'_\infty + \left(C'_w - C'_\infty\right)\frac{t'}{t_o}.$$

Introducing the non-dimensional parameters:

$$\left.\begin{array}{l} y = \dfrac{U_o y'}{v},\ t = \dfrac{t'}{t_o},\ u = \dfrac{u'}{U_o},\ T = \dfrac{T' - T'_\infty}{T'_w - T'_\infty},\ C = \dfrac{C' - C'_\infty}{C'_w - C'_\infty},\ Gr = \dfrac{vg\beta'\left(T'_w - T'_\infty\right)}{U_o^3}, \\[3mm] Gm = \dfrac{vg\overline{\beta'}\left(C'_w - C'_\infty\right)}{U_o^3},\ M = \dfrac{\sigma B_o^2 v}{\rho U_o^2},\ H = \dfrac{Q_o v}{\rho C_p U_o^2},\ K = \dfrac{K'U_o^2}{v^2},\ a = a't_o, \\[3mm] Q_l^* = \dfrac{Q_l\left(C'_w - C'_\infty\right)t_o}{T'_w - T'_\infty},\ \Pr = \dfrac{v\rho C_p}{\kappa},\ Du = \dfrac{D_M K_T\left(C'_w - C'_\infty\right)}{C_s v\left(T'_w - T'_\infty\right)},\ Ra = \dfrac{U_o^2 t_o}{v}, \\[3mm] k = \overline{k'}t_o,\ Sc = \dfrac{v}{D_M}. \end{array}\right\}$$

Implementing the non-dimensional parameters, the governing equations (2), (4), (5) and the initial boundary condition (6) transform to the following structures:

$$\frac{\partial C}{\partial t} = \frac{Ra}{Sc}\frac{\partial^2 C}{\partial y^2} - kC. \tag{7}$$

$$\frac{\partial T}{\partial t} = \frac{Ra}{\Pr}\frac{\partial^2 T}{\partial y^2} + H\,Ra\,T + Q_l^*C + Du\,Ra\frac{\partial^2 C}{\partial y^2}. \tag{8}$$

$$\frac{\partial u}{\partial t} = Ra\left(1 + \frac{1}{\beta}\right)\frac{\partial^2 u}{\partial y^2} - Ra\left(M + \frac{1}{K}\right)u + Ra\,Gr\,T + Ra\,Gc\,Gm. \tag{9}$$

$$At\quad y \ge 0: u = 0,\ C = 0,\ T = 0;\ t \le 0,$$

$$At\quad y = 0:\ \left.\begin{array}{l} u = e^{at},\ T = t,\ C = t;\quad 0 < t \le 1 \\ u = e^{at},\ T = 1,\ C = 1;\qquad T > 1 \end{array}\right\} \tag{10}$$

$$As\quad y \to \infty:\ u \to 0,\ C \to 0,\ T \to 0,\ \forall t > 0.$$

4. METHOD OF SOLUTION

We have implemented the Laplace transformation method to find an analytical solution for concentration, temperature, and velocity field for the flow problem. The procedure for accomplishing these solutions is stated below:
Taking Laplace transformation of the equations (7)-(9) gives:

$$Ra\frac{d^2\overline{C}}{dy^2} - Sc\left(s + k\right)\overline{C} = 0, \tag{11}$$

$$\frac{Ra}{\Pr}\frac{d^2\overline{T}}{d\,y^2} + \left(H\,Ra - s\right)\overline{T} = -Q_l^*\overline{C} - Du\,Ra\frac{d^2\overline{C}}{d\,y^2}, \tag{12}$$

$$Ra\left(1+\frac{1}{\beta}\right)\frac{d^2\bar{u}}{dy^2}-(s+I)\bar{u}=-Ra\,Gr\,\bar{T}-Ra\,Gm\,\bar{C}, \tag{13}$$

Again, taking Laplace transformation of the non-dimensional initial boundary condition stated in (10) gives:

$$At\ \ y=0:\ \bar{T}=\frac{1}{s^2}\left(1-e^{-s}\right),\ \bar{C}=\frac{1}{s^2}\left(1-e^{-s}\right),\ \bar{u}=\frac{1}{s-a}\left.\begin{array}{c}\\\\\end{array}\right\} \tag{14}$$
$$As\ \ y\to\infty:\bar{T}\to0,\ \overline{C}\to0,\ \bar{u}\to0$$

The equations (11) - (13) are solved subject to the condition (14) and the solutions are obtained as follows:

$$\overline{C}=\frac{1-e^{-s}}{s^2}e^{-\sqrt{\lambda_1}\sqrt{s+k}\,y}. \tag{15}$$

$$\bar{T}=\frac{1-e^{-s}}{s^2}e^{-\sqrt{s+E}\sqrt{\lambda_2}\,y}+\lambda_4\frac{1-e^{-s}}{s^2}\frac{e^{-\sqrt{s+E}\sqrt{\lambda_2}\,y}}{s+\lambda_5}+\lambda_6\frac{1-e^{-s}}{s^2}\frac{s+k}{s+\lambda_5}e^{-\sqrt{s+E}\sqrt{\lambda_2}\,y}$$
$$-\lambda_4\frac{1-e^{-s}}{s^2}\frac{e^{-\sqrt{s+k}\sqrt{\lambda_1}\,y}}{s+\lambda_5}-\lambda_6\frac{1-e^{-s}}{s^2}\frac{s+k}{s+\lambda_5}e^{-\sqrt{s+k}\sqrt{\lambda_1}\,y}, \tag{16}$$

$$\bar{u}=\frac{1}{s-a}e^{-\sqrt{s+I}\sqrt{\delta}\,y}-\frac{\lambda_6\left(1-e^{-s}\right)}{s^2\left(s+\lambda_7\right)}e^{-\sqrt{s+I}\sqrt{\delta}\,y}-\frac{\lambda_6\,\lambda_3\left(1-e^{-s}\right)}{s^2\left(s+\lambda_7\right)\left(s+\lambda_4\right)}e^{-\sqrt{s+I}\sqrt{\delta}\,y}$$
$$-\frac{\lambda_6\,\lambda_5\left(1-e^{-s}\right)(s+k)}{s^2\left(s+\lambda_7\right)\left(s+\lambda_4\right)}e^{-\sqrt{s+I}\sqrt{\delta}\,y}-\frac{\lambda_8\,\lambda_3\left(1-e^{-s}\right)}{s^2\left(s+\lambda_9\right)\left(s+\lambda_4\right)}e^{-\sqrt{s+I}\sqrt{\delta}\,y}-\frac{\lambda_8\,\lambda_5\left(1-e^{-s}\right)(s+k)}{s^2\left(s+\lambda_4\right)\left(s+\lambda_9\right)}e^{-\sqrt{s+I}\sqrt{\delta}\,y}$$
$$-\frac{\lambda_{10}\left(1-e^{-s}\right)}{s^2\left(s+\lambda_9\right)}e^{-\sqrt{s+I}\sqrt{\delta}\,y}+\frac{\lambda_6\left(1-e^{-s}\right)}{s^2\left(s+\lambda_7\right)}e^{-\sqrt{s+E}\sqrt{\lambda_2}\,y}+\frac{\lambda_6\,\lambda_3\left(1-e^{-s}\right)}{s^2\left(s+\lambda_7\right)\left(s+\lambda_4\right)}e^{-\sqrt{s+E}\sqrt{\lambda_2}\,y} \tag{17}$$
$$+\frac{\lambda_6\,\lambda_5\left(1-e^{-s}\right)(s+k)}{s^2\left(s+\lambda_7\right)\left(s+\lambda_4\right)}e^{-\sqrt{s+E}\sqrt{\lambda_2}\,y}+\frac{\lambda_8\,\lambda_3\left(1-e^{-s}\right)}{s^2\left(s+\lambda_9\right)\left(s+\lambda_4\right)}e^{-\sqrt{s+k}\sqrt{\lambda_1}\,y}+\frac{\lambda_8\,\lambda_5\left(1-e^{-s}\right)(s+k)}{s^2\left(s+\lambda_4\right)\left(s+\lambda_9\right)}e^{-\sqrt{s+k}\sqrt{\lambda_1}\,y}$$
$$+\frac{\lambda_{10}\left(1-e^{-s}\right)}{s^2\left(s+\lambda_9\right)}e^{-\sqrt{s+k}\sqrt{\lambda_1}\,y},$$

where,

$$\delta=\frac{1}{\left(1+\frac{1}{\beta}\right)Ra},\quad \lambda_1=\frac{Sc}{Ra},\ I=\left(M+\frac{1}{K}\right)Ra,$$

$$\lambda_2=\frac{Pr}{Ra},\ \lambda_3=\frac{\lambda_1}{\lambda_2},\ \lambda_4=\frac{Q_l^*}{\lambda_3-1},$$

$$\lambda_5=\frac{\lambda_3 k-E}{\lambda_3-1},\ E=-H\,Ra,\ \lambda_6=\frac{\lambda_1\,Du\,Ra}{\lambda_3-1},$$

$$\lambda_7=\frac{-Ra\,Gr}{\delta\lambda_2-1},\ \lambda_8=\frac{\delta E\lambda_2-I}{\delta\lambda_2-1},\ \lambda_9=\frac{Ra\,Gr}{\delta\lambda_1-1},$$

$$\lambda_{10}=\frac{\delta k\lambda_1-I}{\delta\lambda_1-1},\ \lambda_{11}=-\frac{Ra\,Gm}{\delta\lambda_1-1},\ Z_1=-\frac{1}{\lambda_8^2},$$

$$Z_2=\frac{1}{\lambda_8},\ Z_3=\frac{1}{\lambda_8^2},\ J_1=\frac{\lambda_5+\lambda_8}{\lambda_5^2\lambda_8^2},$$

$$J_2=\frac{1}{\lambda_5\lambda_8},\ J_3=-\frac{1}{\lambda_5^2\left(\lambda_5-\lambda_8\right)},\ J_4=\frac{1}{\lambda_8^2\left(\lambda_5-\lambda_8\right)},$$

$$L_1=\frac{\lambda_5\lambda_8-k(\lambda_5+\lambda_8)}{\lambda_5^2\lambda_8^2},\ L_2=\frac{k}{\lambda_5\lambda_8},\ L_3=\frac{\lambda_5-k}{\lambda_5^2\left(\lambda_5-\lambda_8\right)},\ L_4=\frac{k-\lambda_8}{\lambda_8^2\left(\lambda_5-\lambda_8\right)},\ F_1=-\frac{(\lambda_5+\lambda_{10})}{\lambda_5^2\lambda_{10}^2}.$$

Finally, the following solutions for temperature profile, concentration profile and velocity profile are attained on picking inverse Laplace transformation of Equations (15)-(17):

$$C = f_1 - \overline{f_1} \tag{18}$$

where,

$$f_1 = f(\lambda_1, k, y, t), \quad \overline{f_1} = f(\lambda_1, k, y, t-1)H .$$

$$
\begin{aligned}
T &= (\lambda_4 A_2 + \lambda_6 B_2)(f_1 - \overline{f_1}) + (1 + \lambda_4 A_2 + \lambda_6 B_2)(h_2 - \overline{h_2}) \\
&+ (\lambda_4 A_1 + \lambda_6 B_1)(\psi_1 - \overline{\psi_1}) + (\lambda_4 A_3 + \lambda_6 B_3)(\psi_2 - \overline{\psi_2}) \\
&+ (\lambda_4 A_1 + \lambda_6 B_1)(\psi_3 - \overline{\psi_3}) + (\lambda_4 A_3 + \lambda_6 B_3)(\psi_4 - \overline{\psi_4}).
\end{aligned} \tag{19}
$$

where,

$$f_1 = f(\lambda_1, k, y, t) \qquad \overline{f_1} = f(\lambda_1, k, y, t-1)H$$

$$f_2 = f(\lambda_2, \beta, y, t) \qquad \overline{f_2} = f(\lambda_2, \beta, y, t-1)H$$

$$\psi_1 = \psi(\lambda_2, \beta, y, t) \qquad \overline{\psi_1} = \psi(\lambda_2, \beta, y, t-1)H$$

$$\psi_2 = e^{-\lambda_5 t}\psi(\lambda_2, \beta - \lambda_5, y, t)$$

$$\overline{\psi_2} = e^{-\lambda_5(t-1)}\psi(\lambda_2, \beta - \lambda_5, y, t-1)H$$

$$\psi_3 = \psi(\lambda_1, k, y, t) \qquad \overline{\psi_3} = \psi(\lambda_1, k, y, t-1)H$$

$$\psi_4 = e^{-\lambda_5 t}\psi(\lambda_1, k - \lambda_5, y, t)$$

$$\overline{\psi_4} = e^{-\lambda_5(t-1)}\psi(\lambda_1, k - \lambda_5, y, t-1)H.$$

$$
\begin{aligned}
u &= G + R_1\left\{(\psi_1 - \overline{\psi_1}) - (\psi_5 - \overline{\psi_5})\right\} + R_2\left\{(\psi_2 - \overline{\psi_2}) - (\psi_7 - \overline{\psi_7})\right\} \\
&+ R_3\left\{(\psi_3 - \overline{\psi_3}) - (\psi_5 - \overline{\psi_5})\right\} + R_4\left\{(\psi_4 - \overline{\psi_4}) - (\psi_7 - \overline{\psi_7})\right\} \\
&+ R_5\left\{(\psi_9 - \overline{\psi_9}) - (\psi_6 - \overline{\psi_6})\right\} + R_6\left\{(\psi_{10} - \overline{\psi_{10}}) - (\psi_8 - \overline{\psi_8})\right\} \\
&+ R_7\left\{(f_1 - \overline{f_1}) - (f_3 - \overline{f_3})\right\} + R_8\left\{(f_2 - \overline{f_2}) - (f_3 - \overline{f_3})\right\}.
\end{aligned} \tag{20}
$$

where,

$$f_3 = f(\delta, I, y, t), \qquad \overline{f_3} = f(\delta, I, y, t-1)H,$$

$$\psi_5 = \psi(\delta, I, y, t), \qquad \overline{\psi_5} = \psi(\delta, I, y, t-1)H$$

$$\psi_7 = e^{-\lambda_5 t}\ \psi(\delta, I - \lambda_5, y, t),$$

$$\overline{\psi_7} = e^{-\lambda_5(t-1)}\ \psi(\delta, I - \lambda_5, y, t-1)H,$$

$$\psi_8 = e^{-\lambda_{10} t}\ \psi(\delta, I - \lambda_{10}, y, t), \quad \overline{\psi_8} = e^{-\lambda_{10}(t-1)}\ \psi(\delta, I - \lambda_{10}, y, t-1)H,$$

$$\psi_9 = e^{-\lambda_8 t}\ \psi(\lambda_2, \beta - \lambda_8, y, t), \quad \overline{\psi_9} = e^{-\lambda_8(t-1)}\ \psi(\lambda_2, \beta - \lambda_8, y, t-1)H,$$

$$\psi_{10} = e^{-\lambda_{10} t}\ \psi(\lambda_1, k - \lambda_{10}, y, t), \quad \overline{\psi_{10}} = e^{-\lambda_{10}(t-1)}\ \psi(\lambda_1, k - \lambda_{10}, y, t-1)H.$$

5. SKIN FRICTION

According to Newton's law of viscosity, the viscous drag per unit area at the plate is computed as follows:

$$\tau' = -\mu \frac{\partial u'}{\partial y'}\bigg]_{y=0} = -\mu U_o \frac{\partial u}{\partial y}\frac{\partial y}{\partial y'} = -\mu U_o \frac{\partial u}{\partial y}\frac{\partial}{\partial y'}\left(\frac{U_o y'}{\nu}\right) = -\frac{\mu U_o^2}{\nu}\frac{\partial u}{\partial y}$$

The coefficient of skin friction at the plate is defined as

$$\tau = \frac{\tau'}{\dfrac{\mu U_o^2}{\nu}} = -\frac{\partial u}{\partial y}\bigg]_{y=0}$$

$$\tau = -G - R_1\left\{(\Upsilon_1 - \overline{\Upsilon_1}) - (\Upsilon_5 - \overline{\Upsilon_5})\right\} - R_2\left\{(\Upsilon_2 - \overline{\Upsilon_2}) - (\Upsilon_7 - \overline{\Upsilon_7})\right\}$$
$$-R_3\left\{(\Upsilon_3 - \overline{\Upsilon_3}) - (\Upsilon_5 - \overline{\Upsilon_5})\right\} - R_4\left\{(\Upsilon_4 - \overline{\Upsilon_4}) - (\Upsilon_7 - \overline{\Upsilon_7})\right\}$$
$$-R_5\left\{(\Upsilon_9 - \overline{\Upsilon_9}) - (\Upsilon_6 - \overline{\Upsilon_6})\right\} - R_6\left\{(\Upsilon_{10} - \overline{\Upsilon_{10}}) - (\Upsilon_8 - \overline{\Upsilon_8})\right\}$$
$$-R_7\left\{(\xi_1 - \overline{\xi_1}) - (\xi_3 - \overline{\xi_3})\right\} - R_8\left\{(\xi_2 - \overline{\xi_2}) - (\xi_3 - \overline{\xi_3})\right\}.$$

(21)

where,

$$\Upsilon_1 = \left.\frac{\partial\psi_1}{\partial y}\right]_{y=0} = \Upsilon(\lambda_2, \beta, t), \quad \overline{\Upsilon_1} = \left.\frac{\partial\overline{\psi_1}}{\partial y}\right]_{y=0} = \Upsilon(\lambda_2, \beta, t-1)H,$$

$$\Upsilon_2 = \left.\frac{\partial\psi_2}{\partial y}\right]_{y=0} = e^{-\lambda_5 t}\Upsilon(\lambda_2, \beta - \lambda_5, t), \quad \overline{\Upsilon_2} = \left.\frac{\partial\overline{\psi_2}}{\partial y}\right]_{y=0} = e^{-\lambda_5(t-1)}\Upsilon(\lambda_2, \beta - \lambda_5, t-1)H,$$

$$\Upsilon_3 = \left.\frac{\partial\psi_3}{\partial y}\right]_{y=0} = \Upsilon(\lambda_1, k, t), \quad \overline{\Upsilon_3} = \left.\frac{\partial\overline{\psi_3}}{\partial y}\right]_{y=0} = \Upsilon(\lambda_1, k, t-1)H,$$

$$\Upsilon_4 = \left.\frac{\partial\psi_4}{\partial y}\right]_{y=0} = e^{-\lambda_5 t}\Upsilon(\lambda_1, k - \lambda_5, t), \quad \overline{\Upsilon_4} = \left.\frac{\partial\overline{\psi_4}}{\partial y}\right]_{y=0} = e^{-\lambda_5(t-1)}\Upsilon(\lambda_1, k - \lambda_5, t-1)H,$$

$$\Upsilon_5 = \left.\frac{\partial\psi_5}{\partial y}\right]_{y=0} = \Upsilon(\delta, I, t), \quad \overline{\Upsilon_5} = \left.\frac{\partial\overline{\psi_5}}{\partial y}\right]_{y=0} = \Upsilon(\delta, I, t-1)H,$$

$$\Upsilon_6 = \left.\frac{\partial\psi_6}{\partial y}\right]_{y=0} = e^{-\lambda_8 t}\Upsilon(\delta, I - \lambda_8, t), \quad \overline{\Upsilon_6} = \left.\frac{\partial\overline{\psi_6}}{\partial y}\right]_{y=0} = e^{-\lambda_8(t-1)}\Upsilon(\delta, I - \lambda_8, t-1)H,$$

$$\Upsilon_7 = \left.\frac{\partial\psi_7}{\partial y}\right]_{y=0} = e^{-\lambda_5 t}\Upsilon(\delta, I - \lambda_5, t), \quad \overline{\Upsilon_7} = \left.\frac{\partial\overline{\psi_7}}{\partial y}\right]_{y=0} = e^{-\lambda_5(t-1)}\Upsilon(\delta, I - \lambda_5, t-1)H,$$

$$\Upsilon_8 = \left.\frac{\partial g_8}{\partial y}\right]_{y=0} = e^{-\lambda_{10} t}\Upsilon(\delta, I - \lambda_{10}, t), \quad \overline{\Upsilon_8} = \left.\frac{\partial \overline{g_8}}{\partial y}\right]_{y=0} = e^{-\lambda_{10}(t-1)}\Upsilon(\delta, I - \lambda_{10}, t-1)H,$$

$$\Upsilon_9 = \left.\frac{\partial g_9}{\partial y}\right]_{y=0} = e^{-\lambda_8 t}\Upsilon(\lambda_2, \beta - \lambda_8, t), \quad \overline{\Upsilon_9} = \left.\frac{\partial \overline{g_9}}{\partial y}\right]_{y=0} = e^{-\lambda_8(t-1)}\Upsilon(\lambda_2, \beta - \lambda_8, t-1)H,$$

$$\Upsilon_{10} = \left.\frac{\partial g_{10}}{\partial y}\right]_{y=0} = e^{-\lambda_{10} t}\Upsilon(\lambda_1, k - \lambda_{10}, t), \quad \overline{\Upsilon_{10}} = \left.\frac{\partial \overline{g_{10}}}{\partial y}\right]_{y=0} = e^{-\lambda_{10}(t-1)}\Upsilon(\lambda_1, k - \lambda_{10}, t-1)H,$$

$$V(\delta, I, a, t) = \left.\frac{\partial G}{\partial y}\right]_{y=0}.$$

6. SHERWOOD NUMBER

The calculation of the Sherwood number relies on Fick's law of diffusion and is connected with the rate of mass transfer at the plate.

The mass flux M_w from the plate at y'=0 can be obtained using the following method:

$$M_w = -D_M \left.\frac{\partial C'}{\partial y'}\right]_{y'=0} = -\frac{D_M U_o\left(C'_w - C'_\infty\right)}{v}\left.\frac{\partial C}{\partial y}\right]_{y=0},$$

Thus, the coefficient of rate of mass transport at the plate is,

$$Sh = \frac{M_w}{D_M U_o\left(C'_w - C'_\infty\right)} = -\left.\frac{\partial C}{\partial z}\right]_{z=0},$$

$$Sh = -\left.\frac{\partial C}{\partial y}\right]_{y=0} = -(\xi_1 - \overline{\xi_1}).$$

(22)

where,

$$\xi_1 = \frac{\partial h_1}{\partial y}\bigg]_{y=0} = \xi(\lambda_1, k, t) \text{ and}$$

$$\overline{\xi_1} = \frac{\partial \overline{h_1}}{\partial y}\bigg]_{y=0} = \xi(\lambda_1, k, t-1)H.$$

7. NUSSELT NUMBER

The Nusselt number, which is the ratio of convective to conductive thermal transfer in the fluid across the boundary, is computed by Fourier's conduction law to estimate and comprehend the rate of heat transfer at the plate. The heat flux Q' from the plate $y' = 0$ to the fluid defined by the Fourier's law of conduction can be obtained by

$$Q' = -\kappa \frac{\partial T'}{\partial y'}\bigg]_{y'=0} = -\frac{\kappa U_o \left(T'_w - T'_\infty\right)}{\nu} \frac{\partial T}{\partial y}\bigg]_{y=0},$$

The coefficient of rate of heat transfer at the plate is,

$$Nu = \frac{\nu Q'}{\kappa U_o \left(T'_w - T'_\infty\right)} = -\frac{\partial T}{\partial y}\bigg]_{y=0},$$

$$Nu = -(\lambda_4 A_2 + \lambda_6 B_2)(\xi_1 - \overline{\xi_1})$$
$$-(1 + \lambda_4 A_2 + \lambda_6 B_2)(\xi_2 - \overline{\xi_2})$$
$$-(\lambda_4 A_1 + \lambda_6 B_1)(\Upsilon_1 - \overline{\Upsilon_1}) - (\lambda_4 A_3 + \lambda_6 B_3)(\Upsilon_2 - \overline{\Upsilon_2})$$ \hfill (23)
$$-(\lambda_4 A_1 + \lambda_6 B_1)(\Upsilon_3 - \overline{\Upsilon_3}) - (\lambda_4 A_3 + \lambda_6 B_3)(\Upsilon_4 - \overline{\Upsilon_4}).$$

8. RESULTS AND DISCUSSIONS

In the present investigation it was explored that the impact of Casson parameter (β) reduced the fluid velocity, which is reflected in Figure 2 Moreover, the Casson parameter was found to reduce the momentum boundary layer thickness. Figure 3 exhibits that the fluid motion gets accelerated due to the enhancement of solutal Grashof number *(Gm)*. In other words, it can be said that the fluid velocity upsurges due to the thermal buoyancy force. Further this figure indicates that the fluid velocity first boosts in a very thin layer proximate to the plate and after achieving a peak value it drops down to it's minimum value. This is due to the bouyancy force being more effective in the vicinity of the plate. In addition, this figure demonstrates that the effect of buoyancy force on velocity gets disappeared at the free stream.
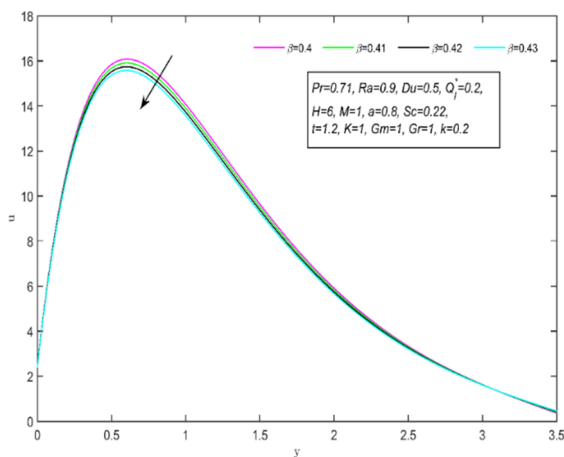

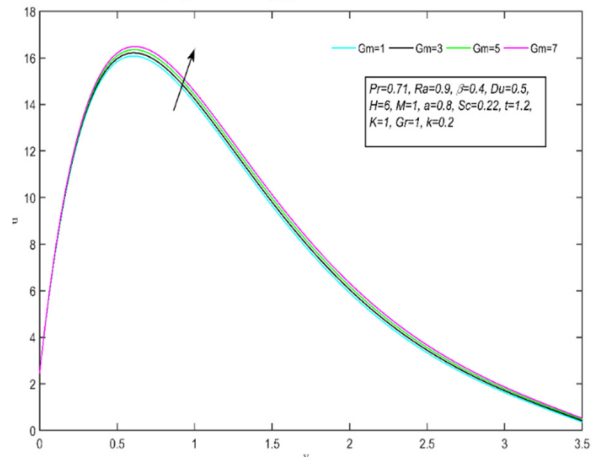**Figure 2.** Velocity versus distinct β   **Figure 3.** Velocity versus distinct Gm

As illustrated in Figure 3, Figure 4 depicts that, the thermal Grashof number *(Gr)* also controls fluid velocity similarly to the solutal Grashof number. Both the figures, i.e Figure 3 and Figure 4 uniquely established the fact that the fluid velocity initially escalates in a very thin layer proximate to the plate and after reaching it's peak value, it asymptotically drops down to its minimum value u=0 at y→∞. From Figure 5 it is evident that the increment of magnetic parameter *(M)* rises the fluid velocity. This is due to the fact that the applied magnetic field produce a force called Lorentz force, which resist the fluid motion.

Figure 6 reveals that the heat generation parameter enhanced the fluid motion. This discloses the physical reality that, as heat generation increases, the temperature of the fluid flow improves and which in turn accelerated the fluid

motion. Figure 7-8 demonstrate the variation of temperature field versus normal co-ordinate y for isothermal and ramped plate condition. In both the figures it is clear that, as the heat generation parameter *(H)* increases, the temperature of the fluid flow improves. Obviously, this is in accordance with the physical reality that as the heat generation of the source increases, the temperature of the surrounding medium improves due to conduction phenomena.
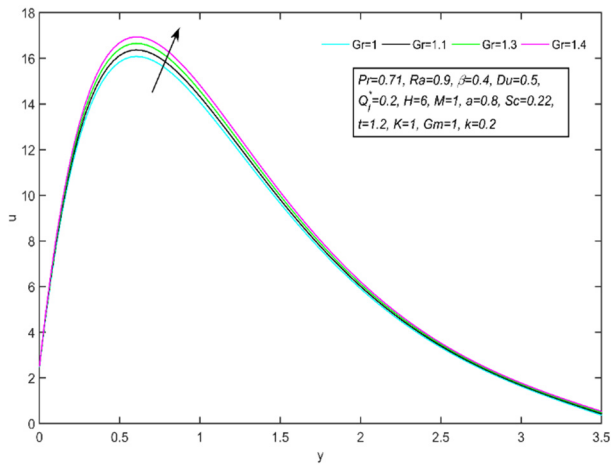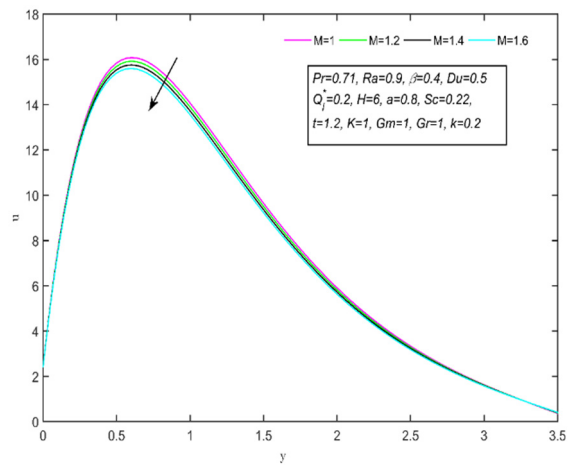

Figure 4. Velocity versus distinct Gr

Figure 5. Velocity versus distinct M
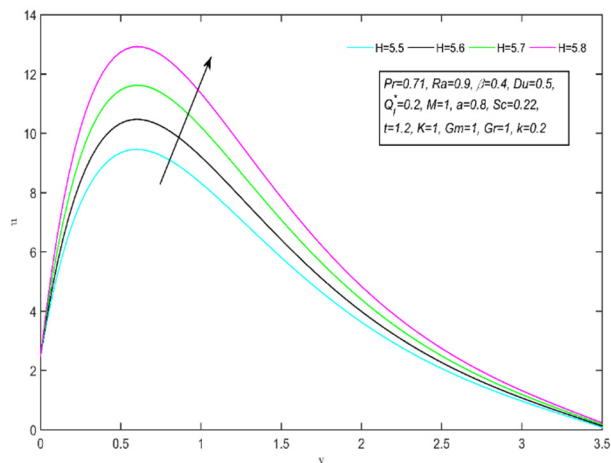
Figure 6. Velocity versus distinct H
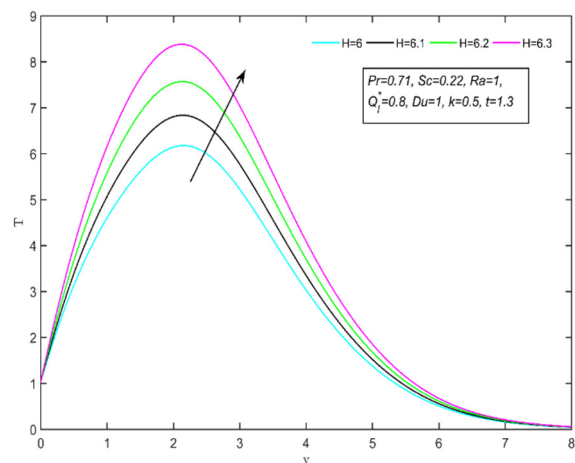
Figure 7. Temperature versus distinct H

Figure 9-10 shows that improving the radiation absorption parameter (Q_l^*) boosts the flow field temperature under both isothermal and ramped plate conditions. The larger the value of the radiation absorption parameter, which implies a significant increase in the dominance of conduction over absorption radiation, resulting in an increase in the buoyancy force and thickness of the thermal and momentum boundary layers.
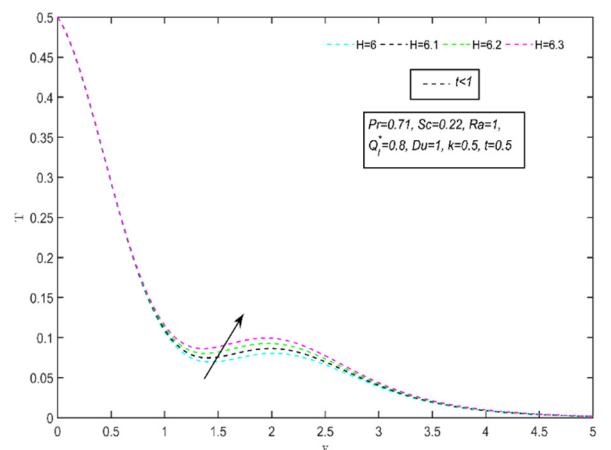
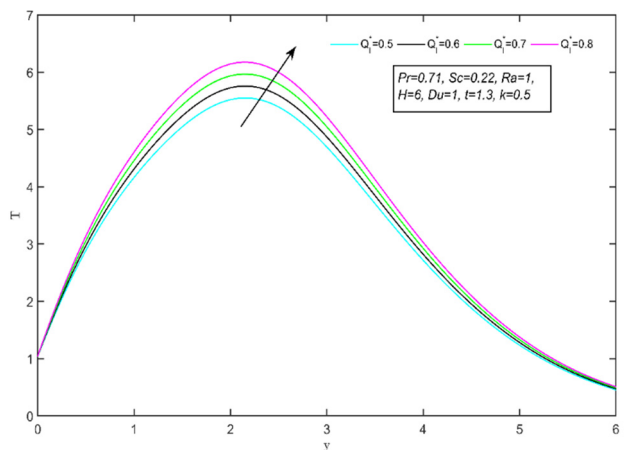**Figure 8.** Temperature versus distinct H for t<1

Figure 9. Temperature versus distinct Q_l^*

The diffusion thermal effect *(Du)* has a great influence on temperature field. Figure 11-12 reflects this impact of thermal diffusion on temperature field and due to which enlargement of temperature field occurs in both the isothermal and ramped plate conditions. Figure 13-14 establishes the relationship between concentration field versus chemical reaction parameter *k*. In both the figures the concentration of the fluid seen to be improved. Physically it divulges the fact that as the consumption of species increases, the fluid becomes thicker and as a result concentration of the fluid drops. In Figure 15-16, it is noticed that as the ramped parameter *(Ra)* increases, the fluid concentration hikes. This implies the fact that the ramped parameter has a tendency to increase fluid concentration.
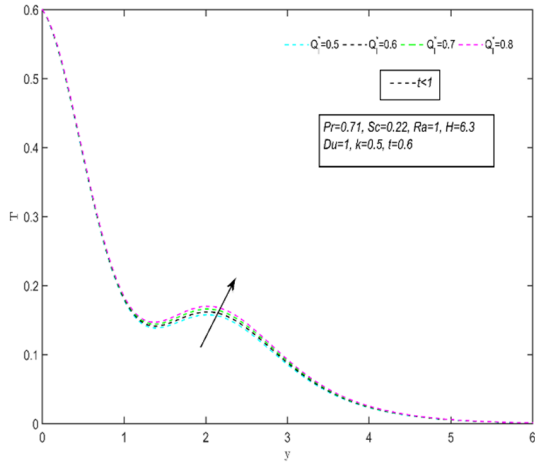
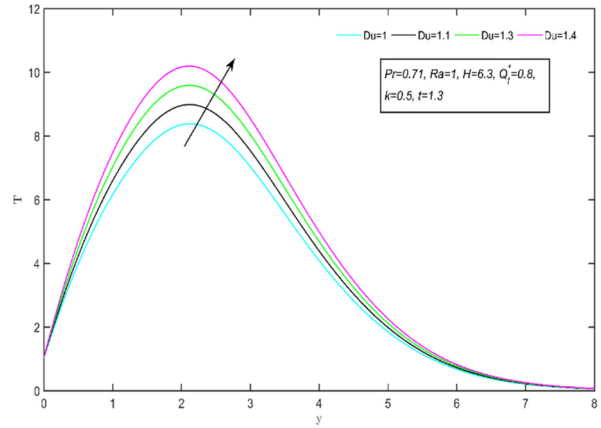**Figure 10.** Temperature versus distinct Q_l^* for t<1

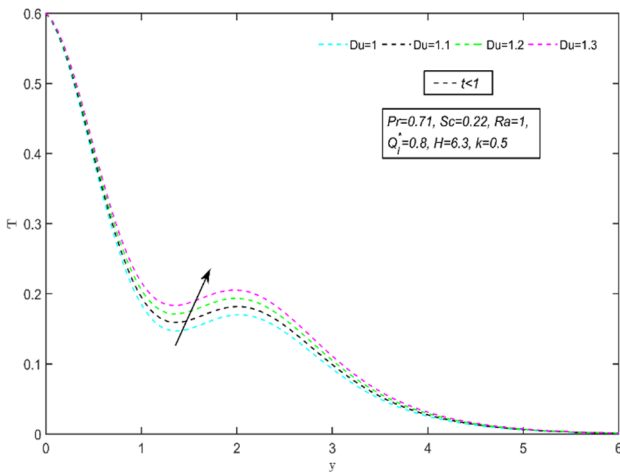**Figure 11.** Temperature versus distinct Du

Figure 12. Temperature versus distinct Du for t< 1
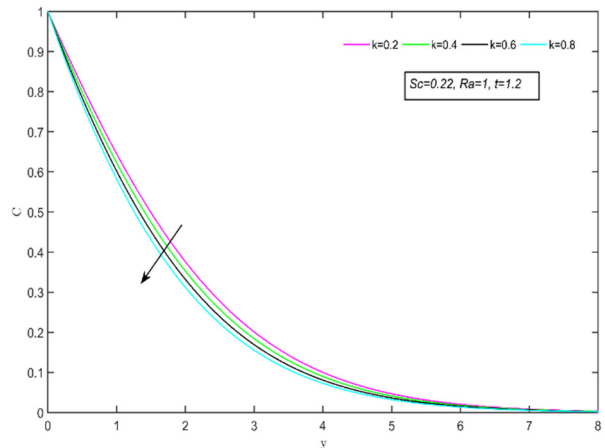

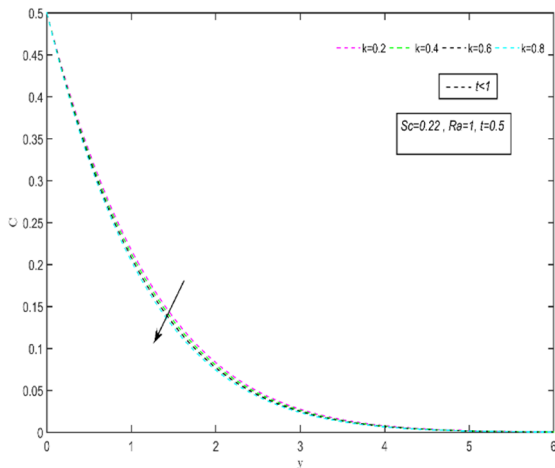**Figure 13.** Concentration versus distinct k

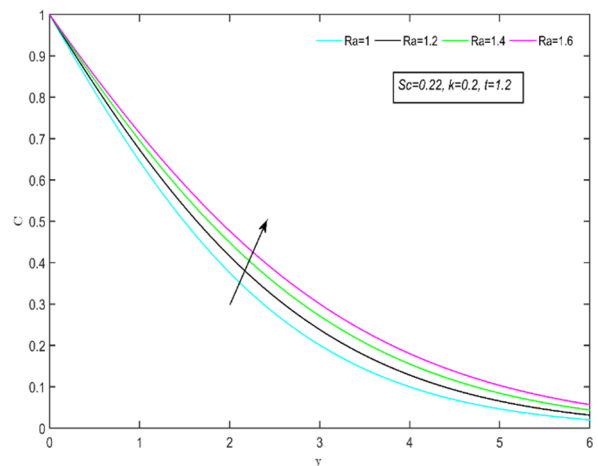**Figure 14.** Concentration versus distinct k for t< 1
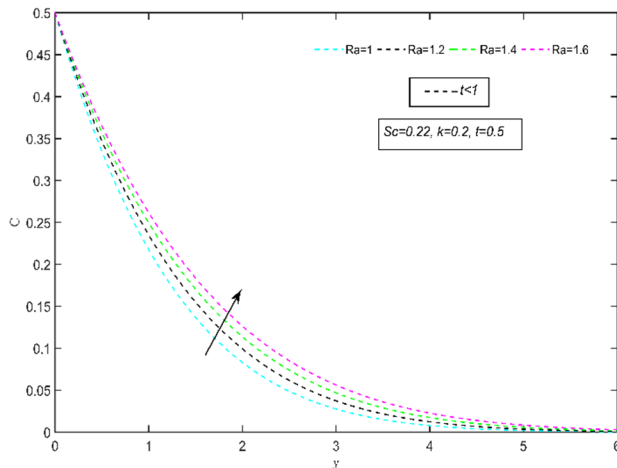

Figure 15. Concentration versus distinct Ra

Figure 16. Concentration versus distinct Ra for t< 1

The variation of skin friction, Nusselt number and Sherwood number for different non dimensional parameters is shown in Table 1, Table 2 and Table 3 respectively. We have also made a comparison between the present study and an earlier study by Kateria and Patel to validate our findings. From Table 1, it is found that the increment of the non-dimensional parameters $Pr, Sc, Gm, k, K, H, t, Q_l^*, Du$ hikes the frictional drag (τ). Moreover, the enhancement of the non-dimensional parameters β, Gr, M diminished the frictional resistance of the fluid flow.

Table 1. Variation of Skin friction

Pr	β	Sc	Gr	Gm	k	M	K	H	t	Q_l^*	Ra	a	Du	Value of skin friction (τ)
2	0.5	0.66	8	5	0.5	1	6	3	1.2	0.4	0.5	0.4	0.5	7.9037
3	0.5	0.66	8	5	0.5	1	6	3	1.2	0.4	0.5	0.4	0.5	11.1574
2	**0.6**	0.66	8	5	0.5	1	6	3	1.2	0.4	0.5	0.4	0.5	7.1107
2	**0.7**	0.66	8	5	0.5	1	6	3	1.2	0.4	0.5	0.4	0.5	6.4600
2	0.5	**0.68**	8	5	0.5	1	6	3	1.2	0.4	0.5	0.4	0.5	8.2617
2	0.5	**0.7**	8	5	0.5	1	6	3	1.2	0.4	0.5	0.4	0.5	8.6495
2	0.5	0.66	**8.2**	5	0.5	1	6	3	1.2	0.4	0.5	0.4	0.5	7.7897
2	0.5	0.66	**8.4**	5	0.5	1	6	3	1.2	0.4	0.5	0.4	0.5	7.6758
2	0.5	0.66	8	**5.2**	0.5	1	6	3	1.2	0.4	0.5	0.4	0.5	7.9313
2	0.5	0.66	8	**5.4**	0.5	1	6	3	1.2	0.4	0.5	0.4	0.5	7.9588
2	0.5	0.66	8	5	**0.6**	1	6	3	1.2	0.4	0.5	0.4	0.5	8.1796
2	0.5	0.66	8	5	**0.7**	1	6	3	1.2	0.4	0.5	0.4	0.5	8.4597
2	0.5	0.66	8	5	0.5	**2**	6	3	1.2	0.4	0.5	0.4	0.5	7.3393
2	0.5	0.66	8	5	0.5	**3**	6	3	1.2	0.4	0.5	0.4	0.5	6.8698
2	0.5	0.66	8	5	0.5	1	**7**	3	1.2	0.4	0.5	0.4	0.5	7.9184
2	0.5	0.66	8	5	0.5	1	**8**	3	1.2	0.4	0.5	0.4	0.5	7.9294
2	0.5	0.66	8	5	0.5	1	6	**3.2**	1.2	0.4	0.5	0.4	0.5	8.6267
2	0.5	0.66	8	5	0.5	1	6	**3.4**	1.2	0.4	0.5	0.4	0.5	9.4493
2	0.5	0.66	8	5	0.5	1	6	3	**1.3**	0.4	0.5	0.4	0.5	10.2623
2	0.5	0.66	8	5	0.5	1	6	3	**1.4**	0.4	0.5	0.4	0.5	13.2560
2	0.5	0.66	8	5	0.5	1	6	3	1.2	**0.5**	0.5	0.4	0.5	8.4221
2	0.5	0.66	8	5	0.5	1	6	3	1.2	**0.6**	0.5	0.4	0.5	8.9404
2	0.5	0.66	8	5	0.5	1	6	3	1.2	0.4	0.5	0.4	**0.6**	8.9032
2	0.5	0.66	8	5	0.5	1	6	3	1.2	0.4	0.5	0.4	**0.7**	9.9026

Table 2 depicts that as the value of the non- dimensional parameters H, t, Q_l^*, Du increases, the rate of heat transfer declines. On the other hand, the increment of the Prandtl number Pr improves the rate of heat transfer. Table 3 shows that the escalating values of the non-dimensional parameters k, Sc, Ra increases the Sherwood number which is associated with rate of mass transfer of the fluid flow.

Table 2. Variation of Nusselt number (Nu)

Pr	**H**	**t**	Q_l^*	Du	Value of Nusselt number
2	3	1.2	0.4	0.5	-14.1252
3	3	1.2	0.4	0.5	-1.8467
2	**3.2**	1.2	0.4	0.5	-16.3795
2	**3.4**	1.2	0.4	0.5	-19.0530
2	3	**1.3**	0.4	0.5	-19.2844

Pr	H	t	Q_l^*	Du	Value of Nusselt number
2	3	**1.4**	0.4	0.5	-26.0778
2	3	1.2	**0.5**	0.5	-15.3553
2	3	1.2	**0.6**	0.5	-16.5854
2	3	1.2	0.4	**0.6**	-17.3255
2	3	1.2	0.4	**0.7**	-20.5258

Table 3. Comparison of Sherwood number values obtained by Kateria and Patel and the current authors

k	Sc	t	Kateria and Patel [8] (Sh)	Ra	Newly finding values of Sherwood number (Sh)	Ra	Newly finding values of Sherwood number (Sh)
5	0.66	0.4	0.9062	1.1	0.8640	1	0.9062
5.1	0.66	0.4	0.9118	1.1	0.8693	1	0.9118
5.2	0.66	0.4	0.9173	1.1	0.8746	1	0.9173
5	**0.7**	0.4	0.9333	1.1	0.8898	1	0.9333
5	**0.8**	0.4	0.9977	1.1	0.9513	1	0.9977
5	0.66	**0.5**	1.0889	1.1	1.0383	1	1.0899
5	0.66	**0.6**	1.2711	1.1	1.2119	1	1.2711

9. COMPARISION OF FINDINGS

In order to validate our findings, we have made a comparison between our current findings of Sherwood number values incorporated with different non-dimensional parameters and the tabulated values for Sherwood number obtained by Kateria and Patel [8] in their research work. Comparing the current values of the Sherwood number with the previously investigated values obtained by Kateria and Patel, we see that when we set the ramped parameter to 1, the previous and current values of the Sherwood number are found identical.

10. CONCLUSIONS

The preeminent findings of this research work are enlisted below:

- The fluid velocity found to be improved asymptotically under the influence of heat generation parameter *H,* solutal Grashof number *Gm,* and thermal Grashof number *Gr.*

- In both the isothermal and ramped plate conditions, the temperature of the flow field spotted to be get enhanced under the influenced heat generation parameter *H*, radiation absorption parameter Q_l^* ,and Dufour effect *Du.*

- The species concentration seen to be reduced under the influenced of chemical reaction parameter *k* in both the isothermal and ramped plate conditions. Moreover, it is evident that, in both the isothermal and ramped plate conditions , the ramped parameter *Ra* has a propensity to hike the fluid concentration.

- The skin friction drag τ upsurges with the increment of non-dimensional parameters *Pr, Sc, Gm, k, K, H, t,* Q_l^**, Du* , while an inverse impact was observed when increasing the value of the non-dimensional parameters β *, Gr, M.*

- It is spotted that the ascending values of time *t*, heat generation parameter *H,* radiation absorption Q_l^* and Dufour effect *Du* dominates the rate of heat transfer. On the other hand, Prandtl number *Pr* increases the rate of heat transfer.

- The Sherwood number observed to be enhanced under the impact of chemical reaction parameter *k* ,Schmidt number *Sc* and time *t*.

Nomenclature

J,	current density vector	t_o	critical time for rampdness
B_o	applied magnetic field strength	*Du*	Dufour number
$\overline{B}$	magnetic flux density	$K^{'}$	permeability of porous medium
k	chemical reaction parameter	*M*	coefficient of viscosity
Pr	Prandtl number	D_M	mass diffusivity
H	heat generation parameter	C_s	concentration susceptibility
Q_l^*	radiation absorption parameter	U_o	characteristic plate velocity
β	Casson parameter	K_T	thermal diffusion ratio
K	non-dimensional permeability parameter	$\beta^{'}$	co-efficient of thermal expansion
g	acceleration due to gravity	ν	kinematic viscosity

APPENDIX

$$G = G(\delta, I+a, y, t) = e^{at} \frac{1}{2}\left[e^{\sqrt{\delta(a+I)}y} erfc\left(\frac{\sqrt{\delta}\,y}{2\sqrt{t}} + \sqrt{(a+I)t} \right) + e^{-\sqrt{\delta(a+I)}y} erfc\left(\frac{\sqrt{\delta}\,y}{2\sqrt{t}} - \sqrt{(a+I)t} \right) \right]$$

$$\psi(\lambda_2, \beta, y, t) = \frac{1}{2}\left[e^{\sqrt{\lambda_2\beta}y} erfc\left(\frac{\sqrt{\lambda_2}\,y}{2\sqrt{t}} + \sqrt{\beta t} \right) + e^{-\sqrt{\lambda_2\beta}y} erfc\left(\frac{\sqrt{\lambda_2}\,y}{2\sqrt{t}} - \sqrt{\beta t} \right) \right]$$

$$\psi(\lambda_2, \beta, y, t-1) = \frac{1}{2}\left[e^{\sqrt{\lambda_2\beta}y} erfc\left(\frac{\sqrt{\lambda_2}\,y}{2\sqrt{(t-1)}} + \sqrt{\beta(t-1)} \right) + e^{-\sqrt{\lambda_2\beta}y} erfc\left(\frac{\sqrt{\lambda_2}\,y}{2\sqrt{(t-1)}} - \sqrt{\beta(t-1)} \right) \right] H$$

$$f(\lambda_1, k, y, t) = \left(\frac{t}{2} + \frac{y}{4}\sqrt{\frac{\lambda_1}{k}} \right) e^{\sqrt{\lambda_1 k}y} erfc\left(\frac{y}{2}\sqrt{\frac{\lambda_1}{t}} + \sqrt{kt} \right) + \left(\frac{t}{2} - \frac{y}{4}\sqrt{\frac{\lambda_1}{k}} \right) e^{-\sqrt{\lambda_1 k}y} erfc\left(\frac{y}{2}\sqrt{\frac{\lambda_1}{t}} - \sqrt{kt} \right)$$

$$f(\lambda_1, k, y, t-1) = \left[\left(\frac{(t-1)}{2} + \frac{y}{4}\sqrt{\frac{\lambda_1}{k}} \right) e^{\sqrt{\lambda_1 k}y} erfc\left(\frac{y}{2}\sqrt{\frac{\lambda_1}{(t-1)}} + \sqrt{k(t-1)} \right) + \left(\frac{(t-1)}{2} - \frac{y}{4}\sqrt{\frac{\lambda_1}{k}} \right) e^{-\sqrt{\lambda_1 k}y} erfc\left(\frac{y}{2}\sqrt{\frac{\lambda_1}{(t-1)}} - \sqrt{k(t-1)} \right) \right] H$$

$$V(\delta, I, a, t) = -e^{at}\left[\sqrt{\frac{\delta}{\pi t}}\, e^{-(I+a)t} + \sqrt{\delta(I+a)}\, erf\left(\sqrt{(I+a)t} \right) \right]$$

$$H = \text{Heaviside(t-1)} = \begin{cases} 1, & t > 1 \\ \dfrac{1}{2}, & t = 0 \\ 0, & t < 1 \end{cases}$$

$$\Upsilon(\lambda_2, \beta, t) = -\left[\sqrt{\frac{\lambda_2}{\pi t}}\, e^{-\beta t} + \sqrt{\lambda_2\beta}\, erf\left(\sqrt{\beta t} \right) \right]$$

$$\Upsilon(\lambda_2, \beta, t-1) = -\left[\sqrt{\frac{\lambda_2}{\pi(t-1)}}\, e^{-\beta(t-1)} + \sqrt{\lambda_2\beta}\, erf\left(\sqrt{\beta(t-1)} \right) \right] H$$

$$\xi(\lambda_1, k, t) = -\left[\sqrt{\frac{\lambda_1}{4k}}\, erf\left(\sqrt{kt} \right) + t\sqrt{\lambda_1 k}\, erf\left(\sqrt{kt} \right) + \sqrt{\frac{t\lambda_1}{\pi}}\, e^{-kt} \right]$$

$$\xi(\lambda_1, k, t-1) = -\left[\sqrt{\frac{\lambda_1}{4k}}\, erf\left(\sqrt{k(t-1)} \right) + (t-1)\sqrt{\lambda_1 k}\, erf\left(\sqrt{k(t-1)} \right) + \sqrt{\frac{(t-1)\lambda_1}{\pi}}\, e^{-k(t-1)} \right] H$$

ORCID
Dibya Jyoti Saikia, https://orcid.org/0000-0001-6067-5390; **Nazibuddin Ahmed,** https://orcid.org/0000-0002-0924-4402

REFERENCES
[1] H. Alfven, "Existence of electromagnetic-hydrodynamic waves," Nature, **150**, 405-406 (1942). https://doi.org/10.1038/150405d0
[2] G.S. Seth, Md.S. Ansari, and R. Nandkeolyar, "MHD natural convection flow with radiative heat transfer past an impulsively moving plate with ramped wall temperature," Heat and mass transfer, **47**, 551-561 (2011). https://doi.org/10.1007/s00231-010-0740-1
[3] B.S. Goud, "Thermal radiation influences on MHD stagnation point stream over a stretching sheet with slip boundary conditions," International Journal of Thermofluid Science and Technology, **7**(2), 070201 (2020). https://doi.org/10.36963/IJTST.2020070201
[4] C. Rath, A. Nayak, and S. Panda, "Impact of viscous dissipation and Dufour on MHD natural convective flow past an accelerated vertical plate with Hall current," Heat Transfer, **51**(6), 5971-5995 (2022). https://doi.org/10.1002/htj.22577
[5] J.K. Singh, G.S. Seth, and P. Rohidas, "Impacts of time varying wall temperature and concentration on MHD free convective flow of a rotating fluid due to moving free-stream with hall and ion-slip currents," International Journal of Thermofluid Science and Technology, **6**(3), 19060301 (2019). https://doi.org/10.36963/IJTST.19060301
[6] M.V. Krishna, N.A. Ahamad, and A.J. Chamkha, "Radiation absorption on MHD convective flow of nanofluids through vertically travelling absorbent plate," Ain Shams Engineering Journal, **12**, 3043-3056 (2021). https://doi.org/10.1016/j.asej.2020.10.028
[7] S.R. Rao, G. Vidyasagar, and G.V.S.R. Deekshitulu, "Unsteady MHD free convection Casson fluid flow past an exponentially accelerated infinite vertical porous plate through porous medium in the presence of radiation absorption with heat generation/absorption," Materials Today: Proceedings, **42**, 1608-1616 (2021). https://doi.org/10.1016/j.matpr.2020.07.554
[8] M.F. Endalew, and A. Nayak, "Thermal radiation and inclined magnetic field effects on MHD flow past a linearly accelerated inclined plate in a porous medium with variable temperature," Heat Transfer - Asian Research, **48**(1), 42-61 (2019). https://doi.org/10.1002/htj.21367
[9] H.R. Kataria, and H.R. Patel, "Effects of chemical reaction and heat generation/absorption on magnetohydrodynamic (MHD) Casson fluid flow over an exponentially accelerated vertical plate embedded in porous medium with ramped wall temperature and ramped surface concentration," Propulsion and power research, **8**, 35-46 (2019). https://doi.org/10.1016/j.jppr.2018.12.001

[10] J.-C. Zhou, A. Abidi, Q.-H. Shi, M.R. Khan, A. Rehman, A. Issakhov, and A.M. Galal, "Unsteady radiative slip flow of MHD Casson fluid over a permeable stretched surface subject to a non-uniform heat source," Case Studies in Thermal Engineering, **26**, 101141 (2021). https://doi.org/10.1016/j.csite.2021.101141

[11] C. Sulochana, S.R. Aparna, and N. Sandeep, "Heat and mass transfer of magnetohydrodynamic Casson fluid flow over a wedge with thermal radiation and chemical reaction," Heat transfer, **50**, 3704-3721 (2021). https://doi.org/10.1002/htj.22049

[12] R. Reyaz, Y.J. Lim, A.Q. Mohamad, M. Saqib, and S. Shafie, "Caputo fractional MHD Casson fluid flow over an oscillating plate with thermal radiation," Journal of Advanced Research in Fluid Mechanics and Thermal Sciences, **85**, 145-158 (2021). https://semarakilmu.com.my/journals/index.php/fluid_mechanics_thermal_sciences/article/view/8087

[13] J. Bodduna, and C.S. Balla, "Bioconvection in a porous square cavity containing gyrotactic microorganisms under the effects of heat generation/absorption," Proceedings of the Institution of Mechanical Engineers, Part E: Journal of Process Mechanical Engineering, **235**, 1534-1544 (2021). https://doi.org/10.1177/09544089211007326

[14] k. Ali, S. Ahmad, K.S. Nisar, A.A. Faridi, and M. Ashraf, "Simulation analysis of MHD hybrid CuAl₂O₃/H₂O nanofluid flow with heat generation through a porous media," International Journal of Energy Research, **45**, 19165-19179 (2021). https://doi.org/10.1002/er.7016

[15] M.R. Khan, S. Mao, W. Deebani, and A.M.A. Elsiddieg, "Numerical analysis of heat transfer and friction drag relating to the effect of Joule heating, viscous dissipation and heat generation/absorption in aligned MHD slip flow of a nanofluid," International Communications in Heat and Mass Transfer, **131**, 105843 (2022). https://doi.org/10.1016/j.icheatmasstransfer.2021.105843

[16] M.K. Nayak, A.A. Hakeem, and B. Ganga, "Influence of non-uniform heat source/sink and variable viscosity on mixed convection flow of third grade nanofluid over an inclined stretched Riga plate," International Journal of Thermofluid Science and Technology, **6**(4), 19060401 (2019). https://doi.org/10.36963/IJTST.19060401

[17] A. Nayak, S. Panda, and D.K. Phukan, "Soret and Dufour effects on mixed convection unsteady MHD boundary layer flow over stretching sheet in porous medium with chemically reactive species," Applied Mathematics and Mechanics, **35**(7), 849-862 (2014). https://doi.org/10.1007/s10483-014-1830-9

[18] N.A. Ahammad, and M.V. Krishna "Numerical investigation of chemical reaction, Soret and Dufour impacts on MHD free convective gyrating flow through a vertical porous channel," Case Studies in Thermal Engineering, **28**, 101571 (2021). https://doi.org/10.1016/j.csite.2021.101571

[19] M. Jawad, A. Saeed, P. Kumam, Z. Shah, and A. Khan, "Analysis of boundary layer MHD Darcy-Forchheimer radiative nanofluid flow with Soret and DuFour effects by means of Marangoni convection," Case Studies in Thermal Engineering, **23**, 100792 (2021). https://doi.org/10.1016/j.csite.2020.100792

[20] N. Ahmed, and D.J. Saikia, "Unsteady MHD free convective flow past a moving vertical plate in a porous medium with radiation and chemical reaction including arbitrary thermal and solutal ramped condition," Heat Transfer, **51,** 6893-6914 (2022). https://doi.org/10.1002/htj.22629

[21] C. Rath, and A. Nayak, "Transient natural convective flow of a radiative viscous incompressible fluid past an exponentially accelerated porous plate with chemical reaction species," Heat Transfer, **52**(1), 467-494 (2023). https://doi.org/10.1002/htj.22703

[22] D. Gopal, S. Saleem, S. Jagadha, F. Ahmad, A.O. Almatroud, and N. Kishan, "Numerical analysis of higher order chemical reaction on electrically MHD nanofluid under influence of viscous dissipation," Alexandria Engineering Journal, **60**, 1861-1871 (2021). https://doi.org/10.1016/j.aej.2020.11.034

[23] N.G. Reddy, V.S. Rao, and B.R. Reddy, "Chemical reaction impact on MHD natural convection flow through porous medium past an exponentially stretching sheet in presence of heat source/sink and viscous dissipation," Case studies in thermal engineering, **25**, 100879 (2021). https://doi.org/10.1016/j.csite.2021.100879

[24] Sehra, S. Ul Haq, S.I.A. Shah, K.S. Nisar, S.U. Jan, and I. Khan, "Convection heat mass transfer and MHD flow over a vertical plate with chemical reaction, arbitrary shear stress and exponential heating," Scientific Reports, **11**, 1-11 (2021). https://doi.org/10.1038/s41598-021-81615-8

[25] P.S. Reddy, and A.J. Chamkha, "Soret and Dufour effects on MHD convective flow of Al₂O₃–water and TiO₂–water nanofluids past a stretching sheet in porous media with heat generation/absorption," Advanced Powder Technology, **27**(4), 1207-1218 (2016). http://dx.doi.org/10.1016%2Fj.apt.2016.04.005

[26] O. Mopuri, R.K. Madhu, M.R. Peram, C. Ganteda, G. Lorenzini, and N.A. Sidik, "Unsteady MHD on convective flow of a Newtonian fluid past an inclined plate in presence of chemical reaction with radiation absorption and Dufour effects," CFD Letters, **14**(7), 62-76 (2022). https://doi.org/10.37934/cfdl.14.7.6276

ТОЧНИЙ АНАЛІЗ ПОТОКУ МГД КАССОНОВОЇ РІДИНИ ПОВЗ ЕКСПОНЕЦІЙНО ПРИСКОРЕНУ ВЕРТИКАЛЬНУ ПЛАСТИНУ В ПОРИСТОМУ СЕРЕДОВИЩІ З ПОГЛИНАННЯМ, ТЕПЛОВИДІЛЕННЯМ ТА ДИФУЗІЙНО-ТЕРМОЕФЕКТАМИ З ТЕРМІЧНИМИ ТА РОЗЧИННИМИ РАМПОВИМИ УМОВАМИ

Діб'я Джйоті Саікія[a,b], Назібуддін Ахмед[c], Ардхенду Кр. Нанді[b], Діп Джйоті Бора[a]

[a]Департамент математики, Університет Гаухаті, Гувахаті 781014, Індія
[b]Департамент математики, коледж Басугаон, Басугаон-783372 Ассам, Індія
[c]Департамент математики, Університет Котона, Гувахаті 781001, Індія

Поточне дослідження спрямоване на вивчення впливу поглинання випромінювання, виділення тепла та числа Дюфура на МГД-потік рідини Кассона повз експоненційно прискорену вертикальну пластину в пористому середовищі з хімічною реакцією. Основні рівняння для імпульсу, енергії та концентрації розв'язуються за допомогою методу перетворення Лапласа. Вирази для тертя поверхні, швидкості теплообміну та швидкості масообміну також виділені та зображені у вигляді таблиці. Дослідження моделює, що параметр Кассона зменшує швидкість рідини, тоді як потік енергії через градієнт концентрації маси покращує проблему температурного поля потоку. Крім того, спостерігається розвиток температурного поля під впливом поглинання випромінювання та виділення тепла. Додатково графічно показано вплив різних безрозмірних параметрів на поле швидкості, температуру рідини та концентрацію частинок.

Ключові слова: *МГД; поглинання випромінювання; Кассонова рідина; теплогенерація; ефект Дюфура*

FLOW OF MAGNETOHYDRODYNAMIC MAXWELL FLUID IN DARCY – FORCHHEIMER MODEL, WITH CATTANEO – CHRISTOV HEAT FLUX, OVER A STRETCHING SHEET SUBJECTED TO CONVECTIVE BOUNDARY CONDITIONS

D. Dastagiri Babu[a]*, S. Venkateswarlu[a], R. Hanuma Naik[b], D. Manjula[c]

aDepartment of Mathematics, Rajeev Gandhi Memorial College of Engineering and Technology,
Nandyal-518501, Andhra Pradesh, India
bDepartment of Electronics and Communication Engineering, Rajeev Gandhi Memorial College of Engineering and Technology,
Nandyal-518501, Andhra Pradesh, India
cDepartment of Mathematics, Mother Theresa Institute of Engineering and Technology,
Palamaner-517408, Andhra Pradesh, India
*Corresponding Author e-mail: dastagiri478@gmail.com

This research communication explores the Darcy - Forchheimer flow of a chemically reacting non-Newtonian Maxwell fluid over a stretching sheet, incorporating the Cattaneo – Christov heat flux under a convective boundary condition. The fluid flow is described by a set of partial differential equations, which are subsequently transformed into a system of nonlinear ordinary differential equations. To solve these equations numerically, the BVP4C Method was employed after appropriately defining non dimensional variables and implementing similarity transformations. The impacts of diverse active parameters such as Deborah parameter, Darcy-Forchheimer parameter, magnetic parameter, Biot number, and porous parameter are examined on the velocity, temperature, and concentration profiles. In addition, the value of the Skin friction, Nusselt number is calculated and presented through tabular forms.
Keywords: *MHD; Maxwell fluid; Darcy-Forchheimer model; Cattaneo-Christov heat flux; Magnetic parameter*
PACS: 44.05.+e, 44.30.+v, 47.11.-j, 44.40.+a, 47.70.Fw

INTRODUCTION

As Advancements in technology progress, our understanding of fluid dynamics has expanded beyond the limitations of Newtonian models. The emergence of non-Newtonian fluid concepts has proven invaluable in comprehending complex flow behaviors. Of particular interest is the Maxwell fluid, renowned for its remarkable attributes in both technical and industrial applications. Maxwell fluids are employed to enhance the thermal radiation characteristics of conductive fluids. In the polymer manufacturing industry, they are particularly useful for understanding and controlling the flow behavior of polymer melts during processing, as well as for optimizing thermal properties such as heat transfer and radiation. Additionally, Maxwell fluids play a role in modeling the behavior of biological fluids, such as blood flow in arteries, where both elastic and viscous effects are significant.

Khan et al. [1] conducted a study on the mathematical analysis of heat and mass transfer in a Maxwell fluid flowing over a stretching sheet, considering the influence of thermophoretic and stratification effects. The heat transport within a two-dimensional steady radiative boundary layer involving Maxwell fluid flow, while also analyzing the impact of heat generation nd Magnetohydrodynamics (MHD) over a porous inclined plate investigated by Sudarmozhi *et al*. [2]. Zhao *et al*. [3] reported the study of unsteady natural convection heat and mass transfer in a porous medium involving a fractional MHD Maxwell fluid, considering the presence of Soret and Dufour effects. Hayat *et al*. [4] analyzed the heat and mass transfer analysis in the stagnation region of Maxwell fluid with chemical reaction over stretched surface. In their study, Riaz *et al*. [5] focused on the combined effects of heat and mass transfer on MHD free convective flow of Maxwell fluid with variable temperature and concentration. The numerical analysis of absorbing boundary condition for the Maxwell fluid flow over a semi-infinite plate with considering the magnetic field was studied by Bao *et al*. [6]. Yasin *et al*. [7] discussed a contemporary investigation on peristatically induced flow of Maxwell fluid, incorporating the modified Darcy's law and Hall effect alongside slip conditions. Babu *et al*. [8] focused on numerical investigation of Thermophorosis and activation energy effects of Maxwell nano fluid over an inclined magnetic field applied to a disk. The authors [9,10,11,12] have instigated the MHD flow and Heat transfer for Maxwell fluid over an exponentially stretching sheet with variable thermal conductivity in porous medium.

Darcy-Forchheimer flow characterizes the movement of fluid through a porous substance, combining the principles of Darcy's law and Forchheimer's quadratic resistance law. This phenomenon finds widespread application in engineering and geophysics, including scenarios like ground water percolation through soil, oil seepage in porous rock formations, and fluid passage within packed beds in chemical reactors. Darcy's law fundamentally states that the flows rate of a fluid through a porous material is directly proportional to the pressure gradient. This principle serves as a cornerstone in understanding fluid movement in porous media.

In their study, Waqas et al. [13] delved into the properties of Magneto-Maxwell nano lquid towards moving radiated surface. Flow analysis subject to Darcy-Forchheimer concept is studied. Newtonian heat/mass conditions and

heat source aspects are taken into account for modeling. Rashid et al. [14] explored the Darcy-Forchheimer flow of Maxwell fluid with activation energy and thermal radiation over an exponential surface. Upreti et al. [15] analyzed the computational study on MHD Darcy-Forchheimer flow and double-diffusive modeling of Maxwell fluid over rotating stretchable surface. Das et al. [16] and Ganesh et al. [17] studied on the Darcy Forchheimer flow of hydromagnetic fluid flow over a stretching surface in a thermally stratified porous medium with second order slip, viscous and ohmic dissipation effects. Cui et al. [18] developed the thermal analysis of radiative Darcy-Forchheimer nano fluid flow across an inclined stretching surface.

The Cattaneo-Christov heat flux model improves upon Fourier's law of heat conduction by incorporating a finite thermal relaxation time, enhancing accuracy for systems with notable thermal inertia or fast temperature variations. This model, when coupled with MHD Maxwell fluids, characterizes visco-elastic fluids affected by magnetic fields and transient heat transfer. Its application extends to analyzing phenomena such as the flow of electrically conducting fluid in magnetic confinement fusion, behavior of magnetorheological fluids in magnetic fields, and heat transfer in systems experiencing rapid temperature changes or possessing high conductivity. Jawad and Nisar [19] studied the upper convected flow of Maxwell fluid near stagnation point through porous surface using heat flux model. Khan et al. [20] developed the numerical investigation of MHD Cattaneo-Christov thermal flux frame work for Maxwell fluid over a steady extending surface with thermal generation in a porous medium. Rubab and Mustafa [21] conducted a study on the MHD three-dimensional upper-convected Maxwell fluid over a bi-directional stretching surface by considering the Cattaneo-Christov heat flux model. The numerical study of radiative Maxwell viscoelastic magnetized flow from a stretching permeable sheet with a Cattaneo-Christov heat flux was developed by Sahid et al. [22]. Islam et al. [23] studied the Cattaneo-Christov theory for a time-dependent magnetohydrodynamics Maxwell fluid through a stretching cylinder. Salmi et al. [24] explained the numerical study of heat and mass transfer enhancement in Prandtl fluid MHD flow using Cattaneo-Christov heat flux theory.

The current study delves into the investigation of steady, two-dimensional flow of a Darcy-Forchheimer Maxwell fluid through a stretchable surface. Additionally, the analysis incorporates heat and mass transfer phenomena, employing the Cattaneo-Christov theory with chemical reactions. The novelty of this work lies in its examination of the Darcy-Forchheimer Maxwell fluid within the framework of the Cattaneo-Christov theory, considering convective boundary conditions, a combination not explored in existing literature. To address this gap, the authors undertake an examination of such effects on Maxwell fluid flow. To normalize the system, similarity variables are introduced. Numerical solutions are obtained using the Matlab bvp4c technique. The study discusses the graphical representation of the evolving parameters along the velocity profile, temperature profile, and concentration profile.

FORMULATION

Figure 1 illustrates a MHD steady Darcy – Forchheimer flow of Maxwell fluid. An incompressible fluid saturates the porous plate. Flow is caused due to a linear stretching surface. Cattaneo-Christov heat flux model instead of conventional Fourier's law of heat conduction is applied to study the heat transfer characteristics. The Cartesian coordinate system is adopted in such a way that x-axis is taken along the stretching sheet and y-axis is orthogonal to it.

Let $U_w(x) = ax$ denotes the surface stretching velocity along the x-axis direction. We also consider the effect of constant magnetic field of strength B_0 which is applied normally to the sheet. With these assumptions, the governing equations for continuity, velocity, temperature, and concentration in a steady two dimensional flow of a Maxwell fluid are given by
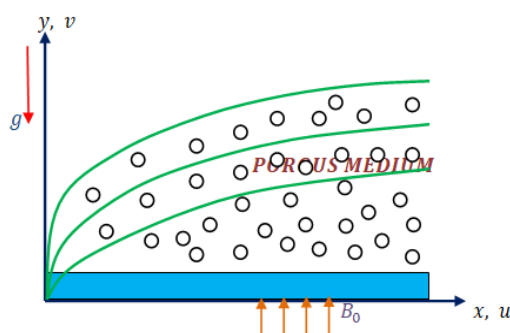

Figure 1. Schematic diagram

$$\frac{\partial u}{\partial x} + \frac{\partial u}{\partial y} = 0 \tag{1}$$

$$u\frac{\partial u}{\partial x} + v\frac{\partial u}{\partial y} + \lambda_1\left[u^2\frac{\partial^2 u}{\partial x^2} + v^2\frac{\partial^2 u}{\partial x^2} + 2uv\frac{\partial^2 u}{\partial x \partial y}\right] = v\frac{\partial^2 u}{\partial y^2} - \frac{v}{k}u - Fu^2 - \frac{\sigma B_0^2}{\rho}u \tag{2}$$

$$u\frac{\partial T}{\partial x}+v\frac{\partial T}{\partial y}+\lambda_2\begin{bmatrix}u\frac{\partial u}{\partial x}\frac{\partial T}{\partial x}+v\frac{\partial v}{\partial y}\frac{\partial T}{\partial y}+u\frac{\partial v}{\partial x}\frac{\partial T}{\partial y}\\+v\frac{\partial u}{\partial y}\frac{\partial T}{\partial x}+2uv\frac{\partial^2 T}{\partial x\partial y}\\+u^2\frac{\partial^2 T}{\partial x^2}+v^2\frac{\partial^2 T}{\partial y^2}\end{bmatrix}=\alpha\frac{\partial^2 T}{\partial y^2}+\frac{\sigma B_0^{\,2}}{\rho c_p}u^2+\tau\begin{bmatrix}D_B\frac{\partial C}{\partial y}\frac{\partial T}{\partial y}\\+\left(\frac{D_m}{T_\infty}\right)\left(\frac{\partial T}{\partial y}\right)^2\end{bmatrix} \quad (3)$$

$$u\frac{\partial C}{\partial x}+v\frac{\partial C}{\partial y}=D_B\frac{\partial^2 C}{\partial y^2}+\left(\frac{D_m}{T_\infty}\right)\frac{\partial^2 T}{\partial y^2}-K_r\left(C-C_\infty\right) \quad (4)$$

With boundary conditions

$$\left.\begin{aligned}u=u_w(x)=ax,\ \ v=0,\ \ -k\frac{\partial T}{\partial y}=h_f\left(T_f-T\right),\ C=C_w\ at\ \ y=0\\u\to 0,\ T\to T_\infty,\ C\to C_\infty\ \ as\ \ y\to\infty\end{aligned}\right\} \quad (5)$$

Invoking the following similarity transformations

$$u=axf'(\eta);\ \ v=-\sqrt{ax}f(\eta);\ \ \theta(\eta)=\frac{T-T_\infty}{T_f-T_\infty};\ \ \eta=y\sqrt{\frac{a}{\upsilon}};\ \ \phi(\eta)=\frac{C-C_\infty}{C_f-C_\infty}; \quad (6)$$

Equation (1) is identically satisfied and Equations (2), (3), (4), and (5) with the help of Equation (6) take the following forms:

$$f'''+f f''+\beta\left(2f f'f''-f^2 f'''\right)-\lambda f'-F_r\left(f'\right)^2-M f'=0 \quad (7)$$

$$\theta''+EcPrM\left(f'\right)^2+\Pr Nb\theta'\phi'+PrNt\left(\theta'\right)^2-Prf\theta'-\Gamma Pr\left(f f'\theta'+f^2\theta''\right)=0 \quad (8)$$

$$\phi''+f Sc\,\phi'+\left(\frac{Nt}{Nb}\right)\theta''-Kc\,Sc\,\phi=0 \quad (9)$$

The transformed boundary conditions are

$$\left.\begin{aligned}At\ \eta=0,\ f=0,\ f'=1,\ \theta'=-Bi\left[1-\theta\right],\ \phi'=1\\As\ \eta\to\infty,\ f'\to0,\ \theta'\to0,\ \phi\to0\end{aligned}\right\} \quad (10)$$

Where β is the Deborah number, $\Gamma=\lambda_2 a$ is the non-dimensional thermal relaxation time, $\lambda=\dfrac{v}{ka}$ denotes the porosity parameter, $Fr=\dfrac{Cb}{\sqrt{k}}$ represents the inertia coefficient, Cb represents drag coefficient, $Pr=\dfrac{v}{\alpha}$ stands for Prandtl number, $M=\dfrac{\sigma B_0^{\,2}}{\rho a}$ is the magnetic parameter, $Sc=\dfrac{v}{D_B}$ denotes Schmidt number, $Kc=\dfrac{Kr}{a}$ represents the chemical reaction parameter, $Nt=\dfrac{\tau D_B\left(T_f-T_\infty\right)}{vT_\infty}$ is the Thermophoretic parameter, $Nb=\dfrac{\tau D_B\left(C_f-C_\infty\right)}{v}$ denotes Brownian motion parameter, $Bi=\sqrt{\dfrac{v}{a}}\left(\dfrac{h_f}{k}\right)$ represents the Biot number, λ_2 denotes Relaxation time for heat flux.

The expression for the Local Skin friction, the Local Nusselt number, and the Sherwood number are defined as:

$$C_f Re_r^{1/2}=f''(0);\ \ NuRe_r^{-1/2}=-\theta'(0);\ \ ShRe_r^{-1/2}=-\phi'(0);$$

METHODOLOGY

The reduced ODE models (7), (8), and (9) are solved numerically by applying the MATLAB bvp4c algorithm. In this regard, initially we convert the higher order equations to first order equations. Let us

take $f_1 = f, f_2 = f', f_3 = f'', f_4 = \theta, f_5 = \theta', f_6 = \phi, f_7 = \phi'$. Then the reduced equations are written as in the following form:

$$f_1' = f_2 \tag{11}$$

$$f_2' = f_3 \tag{12}$$

$$f_3' = \frac{1}{\left(1 - \beta f_1^2\right)}\left(\lambda f_2 + Fr f_2^2 + M f_2 - f_1 f_3 - 2\beta f_1 f_2 f_3\right) \tag{14}$$

$$f_4' = f_5 \tag{15}$$

$$f_5' = \frac{1}{\left(1 - \Gamma \Pr f_1^2\right)}\left(\Gamma \Pr f_1 f_2 f_5 + \Pr f_1 f_5 - Ec \Pr M f_2^2 - \Pr Nb f_5 f_7 - \Pr Nt f_5^2\right) \tag{16}$$

$$f_6' = f_7 \tag{17}$$

$$f_7' = Kc Sc f_6 - Sc f_1 f_7 - \frac{Nt}{Nb}\left(\Gamma \Pr f_1 f_2 f_5 + \Pr f_1 f_5 - Ec \Pr M f_2^2 - \Pr Nb f_5 f_7 - \Pr Nt f_5^2\right) \tag{18}$$

The transformed boundary conditions are

$$\left.\begin{array}{l} At\ \eta = 0,\ f_1 = 0,\ f_2 = 1,\ f_5 = -Bi\left[1 - f_4\right],\ f_7 = 1 \\ As\ \eta \to \infty,\ f_2 \to 0,\ f_5 \to 0,\ f_6 \to 0 \end{array}\right\} \tag{19}$$

RESULTS AND DISCUSSIONS

In this study, a system of nonlinear ordinary differential equations represented by the equations (7), (8), and (9), subject to the constraints specified in equation (10), is solved numerically. The numerical solution is obtained using the shooting process with the bvp4c MATLAB Package. This computational approach allows for the investigation of the influence of various non-dimensional parameters on the profiles of velocity, temperature, and concentration within the system.

Specially, the study explores the impact of non-dimensional parameters such as Deborah number, inertia coefficient, and Biot number, and others on the velocity, temperature and concentration profiles. Additionally, the effects of these parameters on skin friction coefficient, Nusselt number are examined. The study maintains certain non-dimensional parameter values throughout its analysis, setting M to 0.5, Pr to 0.62, Bi to 0.7, Ec to 1, Nt to 0.3, Nb to 0.3, Fr to 0.5, and β to 0.2, λ to 0.2. These values remain constant through the study, except when varying parameters are explicitly depicted in the figures. Overall, the study provides valuable insights into the behavior of the system under different parameter combinations, facilitating a deeper understanding of the underlying physical phenomena and aiding in the optimization of system performance.

Figures 2-4 illustrates the impact of the local Forchheimer number (inertia coefficient) Fr. It is evident from the figures that fluid velocity diminishes with enhancing Fr, as the inertia coefficient is directly related to the porosity of the medium and drag coefficient Cb. Thus, with higher values of Cb, both the porosity of the medium and drag coefficient enhances. Consequently, the resistance force on the liquid is enhanced, resulting in lower velocity corresponding to larger Forchheimer numbers. An enhancing in inertia coefficient (Fr) leads to stronger temperature and concentration profiles and more thickness of boundary layers.
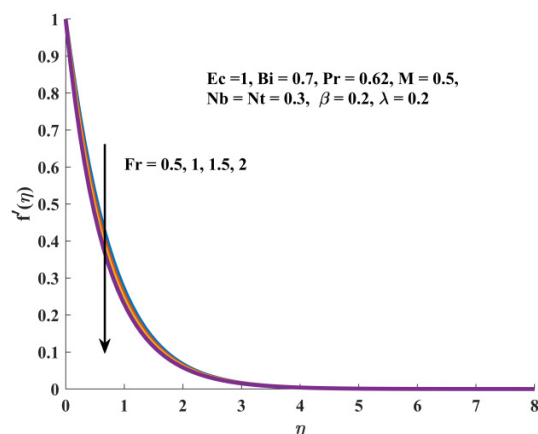
Figure 2. Sketch of Fr on f'
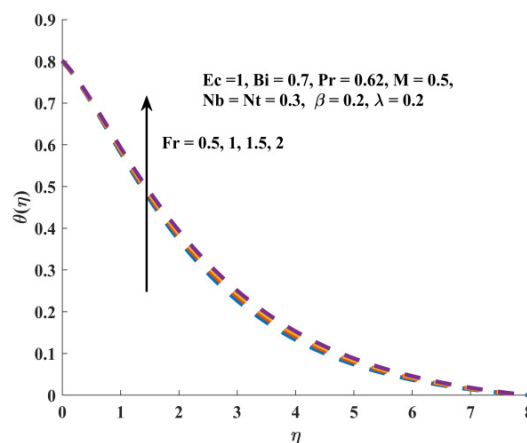
Figure 3. Sketch of Fr on θ

Figures 5–7 depicts the change in velocity, concentration, and temperature profiles for different values of the porosity parameter λ. As porous media tends to increase resistance to fluid motion, the fluid velocity diminishes accordingly. Conversely, an opposite trend is observed in the concentration profile and temperature profile with an increase in the porosity parameter.
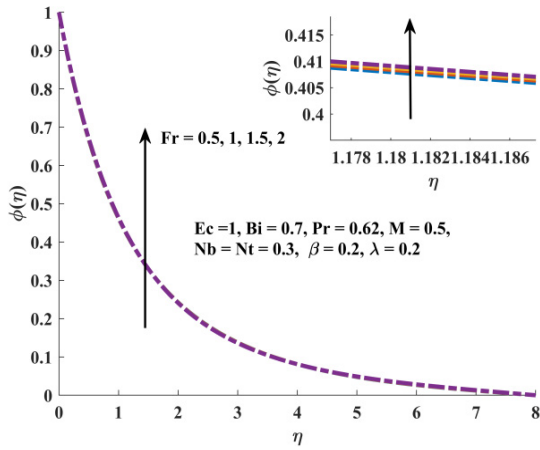
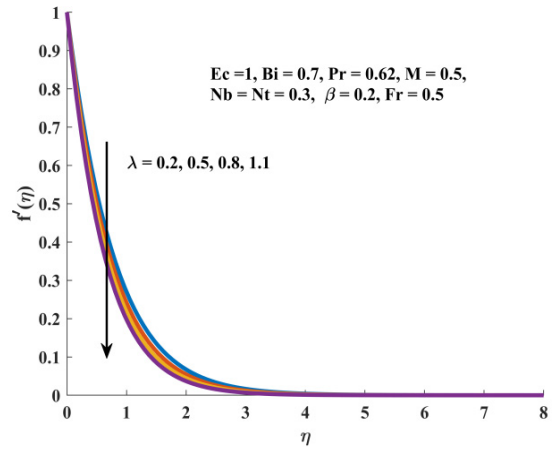
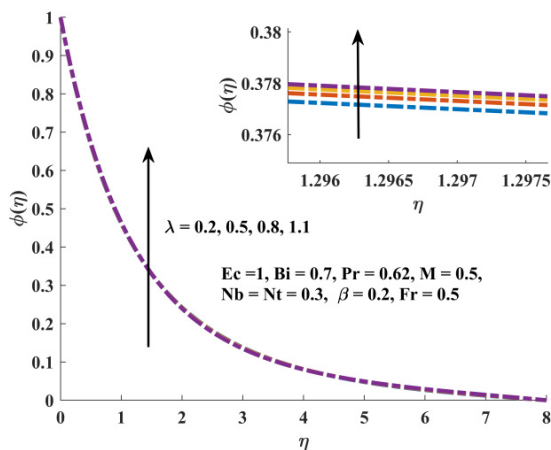
Figure 4. Sketch of Fr on ϕ

Figure 5. Sketch of λ on f'

Figure 6. Sketch of λ on ϕ
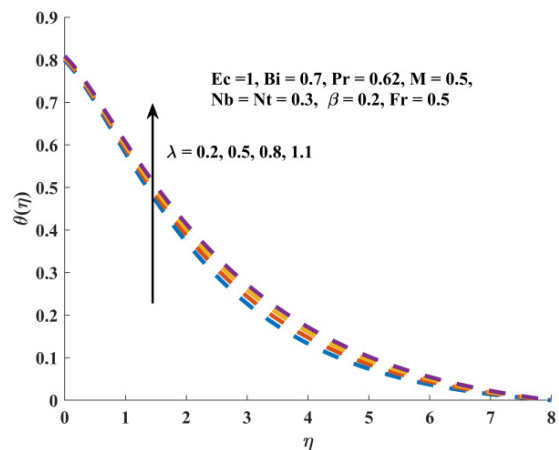
Figure 7. Sketch of λ on θ

Figures 8-10 elucidate how the imposition of magnetic constraints (M) impacts velocity, temperature, and concentration fields. Analysis of these figures led us to anticipate a flattening of fluid velocity with enhancing M. Physically, the magnetic field induces a drag force that opposes fluid motion, thereby reducing velocity. Conversely, temperature and species concentration profiles intensify with changes in the magnetic parameter.
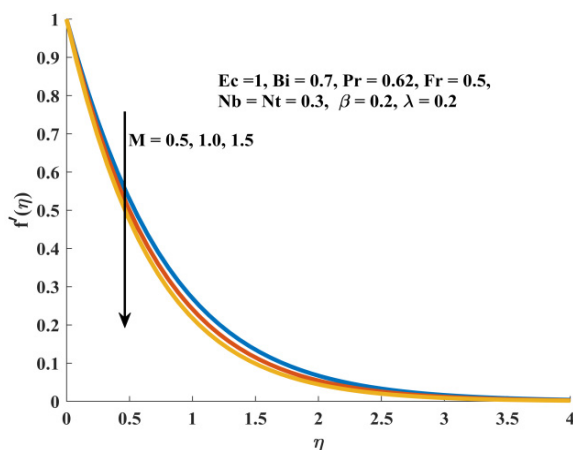
Figure 8. Sketch of M on f'
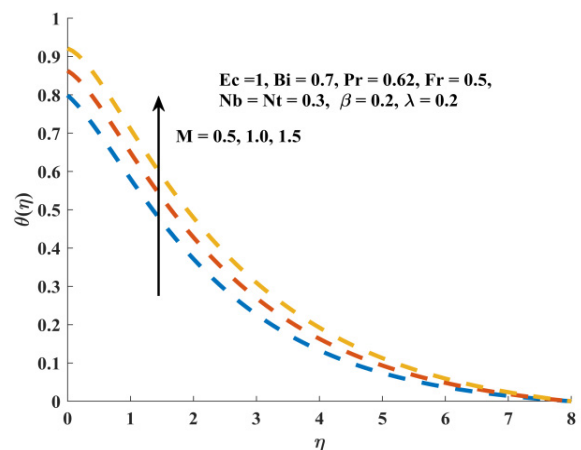
Figure 9. Sketch of M on θ
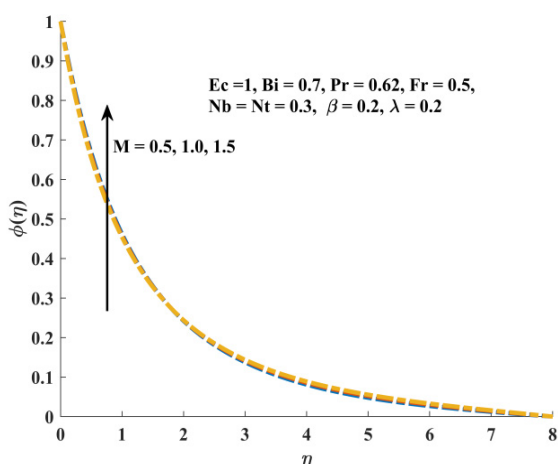
Figure 10. Sketch of M on ϕ
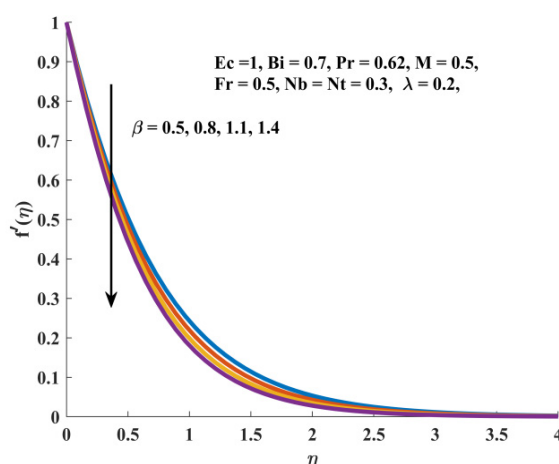
Figure 11. Sketch of β on f'

Figure 11 illustrates how the velocity distribution $f'(\eta)$ is influenced by the Deborah number. As the Deborah number (β) enhances, resulting that the velocity diminishes. In Figure 12, it is shown that higher values of the Deborah number lead to an augmentation in the temperature field (θ) and thickness of the thermal boundary layer. Physically, the Deborah number is associated with relaxation time, which is greater for higher Deborah numbers. Consequently, a larger relaxation time correlates with higher temperatures and thicker thermal boundary layers. The impact of Deborah number (β) on the concentration profile is depicted in Figure 13. Here we observed that the concentration profile is higher when we enhance the values of Deborah number (β).
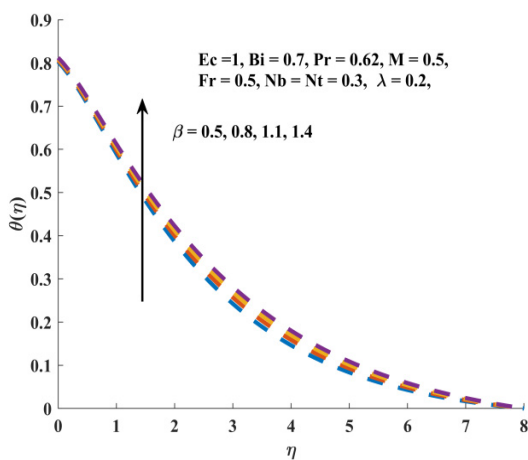
Figure 12. Sketch of β on ϕ
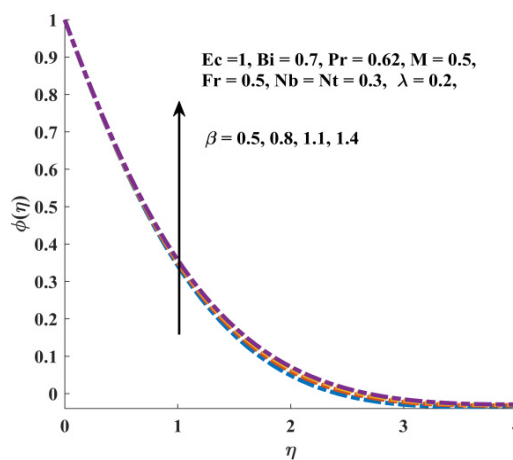
Figure 13. Sketch of β on θ

Observing the Figure 14, it becomes apparent that the temperature profile of the fluid diminishes as the thermal relaxation parameter (Γ) enhances. This phenomenon occurs because, as the parameter (Γ) rises, material particles require more time to transfer heat to adjacent particles. In essence, for higher values of the thermal relaxation parameter (Γ), the material exhibits characteristics akin to non-conductivity, leading to decrease in the temperature profile. Consequently, it can be concluded that the temperature profile is lower in the case of the Cattaneo-Christov heat flux model compared to Fourier's Law. Figure 15 describes the impact of thermal relaxation parameter (Γ) on concentration profile. It shows an increase in the thermal relaxation parameter, the concentration distribution also enhances.

Figures 16-17 showcase the influence of the Prandtl number (Pr) on temperature and concentration distribution. The Prandtl number varies depending on the material and is unique to each fluid. The figures indicate that as Pr increases, the fluid temperature decreases. A high Pr implies that momentum diffusivity surpasses thermal diffusivity, resulting in a reduction in energy boundary layer thickness. Typically, in heat transfer problems, Pr is employed to decrease the relative thickness of both thermal and momentum boundary layers. Similarly, this behavior is observed in concentration profiles.
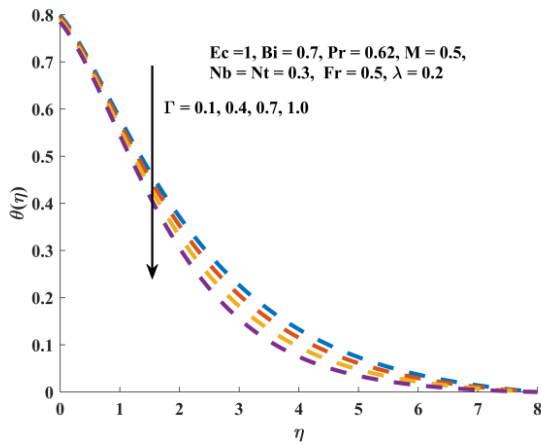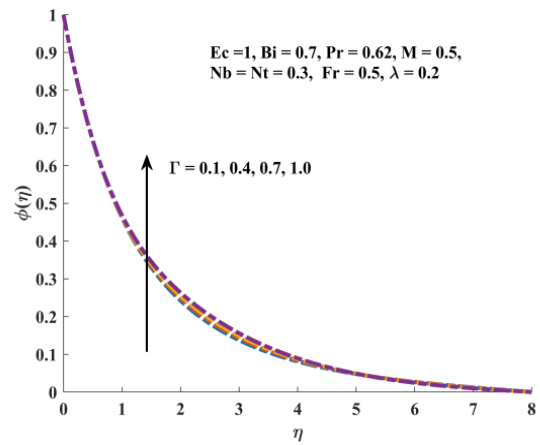
Figure 14. Sketch of Γ on θ

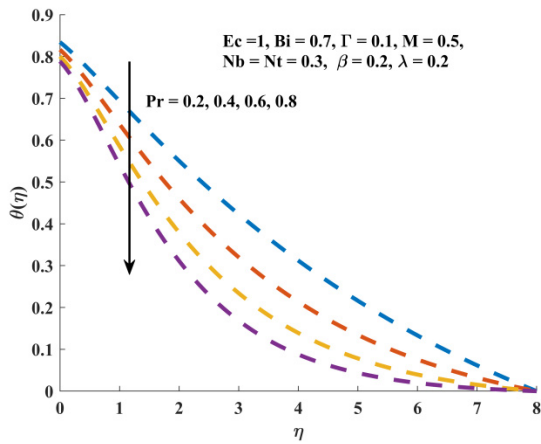**Figure 15.** Sketch of Γ on ϕ
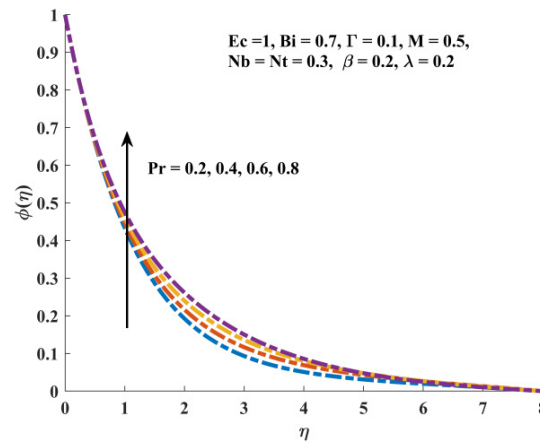
Figure 16. Sketch of Pr on θ

Figure 17. Sketch of Pr on ϕ

Figures 18-19 depict the impact of the thermophoresis parameter (Nt) on the both temperature profiles and concentration profiles. These figures depict that $\theta(\eta), \phi(\eta)$ are the increasing function of thermophoresis parameter for escalating values of Nt. As Nt increases, the thermal conductivity of liquid also enhances. A higher thermal conductivity liquid leads to more advanced temperature and concentration fields.
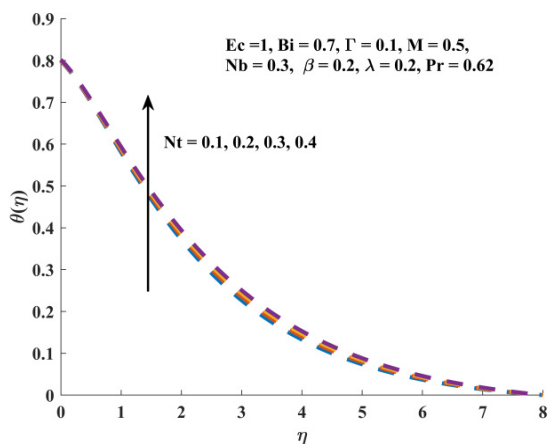
Figure 18. Sketch of Nt on θ
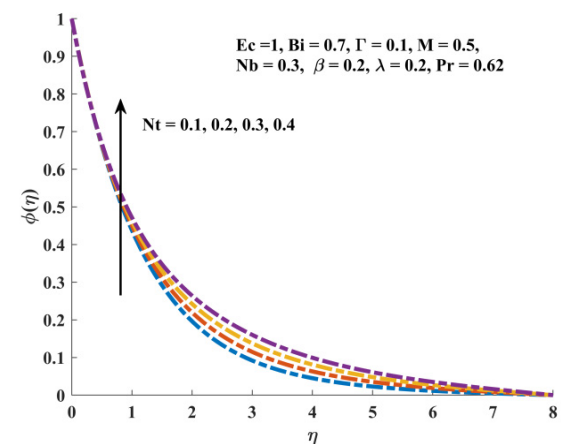
Figure 19. Sketch of Nt on ϕ

Figures 20-21 depict the impact of the Brownian motion parameter (Nb) on the both temperature and concentration profiles. In Figure 20, as enhancing in the Brownian motion parameter (Nb) the temperature profile enhances. Figure

21 illustrates how Nb impacts concentration profiles. Increasing Nb leads to reduced concentration profiles due to enhanced Brownian motion. This parameter signifies diffusion at a microscopic level, causing particles to spread out over time. Higher Nb values indicate more energetic motion, accelerating diffusion and resulting in a more uniform concentration profile. Boundary conditions, like container size and surface presence, influence particle behavior, affecting concentration profiles, particularly near solid boundaries.
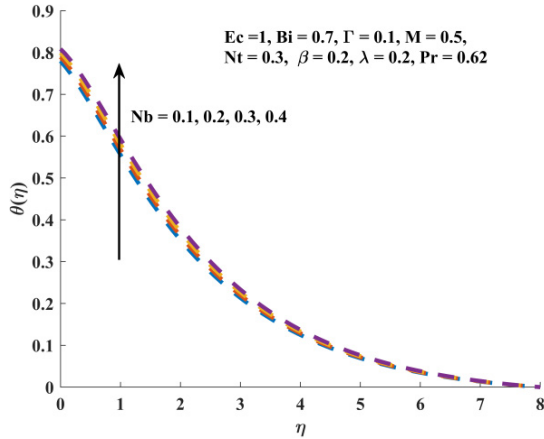
Figure 20. Sketch of Nb on θ
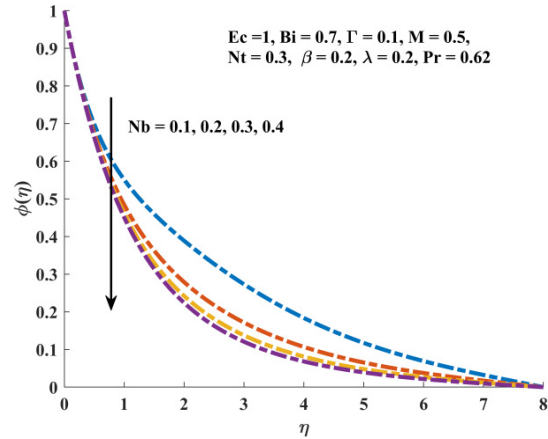
Figure 21. Sketch of Nb on ϕ

Table 1. In this section, we have to elaborate the numerical result against the different prominent factor like, $\beta = 0.2$, $\lambda = 0.2$, $Fr = 0.5$, $M = 0.5$ are the fixed values for the local skin friction coefficient. It is seemed to be as enhance in the values of Deborah number, Porosity parameter, local Forchheimer number (inertia coefficient), and Magnetic parameter, there is a decreasing nature in the skin friction coefficient.

β	λ	Fr	M	C_f
0.2				-0.217955
0.3				-0.239688
0.4				-0.261130
	0.3			-0.257903
	0.4			-0.296672
	0.5			-0.334356
		0.6		-0.243860
		0.7		-0.269300
		0.8		-0.294298
			1	-0.406792
			2	-0.724761
			3	-0.993166

Table 2. In this section, we have to elaborate the numerical result against the different prominent factor like, $\beta = 0.2$, $\lambda = 0.2$, $Fr = 0.5$, $M = 0.5$ are the fixed values for the Nusselt number. It is noticed that the Nusselt number diminishes gradually, an escalating in the values of Deborah number, Porosity parameter, local Forchheimer number (inertia coefficient), and Magnetic parameter.

β	λ	Fr	M	Nu
0.2				0.140714
0.3				0.139823
0.4				0.138949
	0.3			0.139880
	0.4			0.139062
	0.5			0.138263
		0.6		0.140584
		0.7		0.140452
		0.8		0.140318
			1	0.068228
			2	-0.049182
			3	-0.144519

CONCLUSIONS

Key findings of the study are summarized as follows.

- The velocity field diminishes for escalating the values of inertia coefficient, Magnetic parameter, Porosity Parameter, Deborah number, and also thermal relaxation parameter.
- By enhancing the values of inertia coefficient, Magnetic parameter, Porosity Parameter, Deborah number, and thermal relaxation parameter one can escalating the temperature field, but the opposite tend seen with Prandtl number.
- The concentration field increases for larger values of inertia coefficient, Magnetic parameter, Porosity Parameter, Deborah number, thermal relaxation parameter, and also for Prandtl number.
- An increment in the values of thermophoresis parameter, the temperature and concentration profiles corresponding boundary layers are upsurges gradually.
- By increasing the values of Brownian motion parameter, the temperature profile upsurges, but the reverse tend seen in the concentration profile.
- The local skin friction coefficient and Nusselt number diminishes with escalating the values of Deborah number, Inertia coefficient, Porosity, and Magnetic parameter.

ORCID

D. Dastagiri Babu, https://orcid.org/0000-0001-8114-3860; **S. Venkateswarlu,** https://orcid.org/0009-0004-8224-374X
R. Hanuma Naik, https://orcid.org/0000-0002-9817-6594

REFERENCES

[1] M.N. Khan, S. Nadeem, S. Ahmad, and A. Saleem, "Mathematical analysis of heat and mass transfer in a Maxwell fluid," Pro. I. Mech. E. Part C: J. Mech. Eng. Sci. **235**(20), 4967-4976 (2021). https://doi.org/10.1177/0954406220976704

[2] K. Sudarmozhi, D. Iranian, I. Khan, A.S. Al-johani, and S.M. Eldin, "Magneto radiative and heat convective flow boundary layer in Maxwell fluid across a porous inclined vertical plate," Sci. Rep. **13**(1), 6253 (2023). https://doi.org/10.1038/s41598-023-33477-5

[3] J. Zhao, L. Zheng, X. Zhang, and F. Liu, "Convection heat and mass transfer of fractional MHD Maxwell fluid in a porous medium with Soret and Dufour effects," Int. J. Heat Mass Tranf. **103**, 203-210 (2016). https://doi.org/10.1016/j.ijheatmasstransfer.2016.07.057

[4] T. Hayat, M. Ijaz Khan, M. Imtiaz, and A. Alsaedi, "Heat and mass transfer analysis in the stagnation region of Maxwell fluid with chemical reaction over a stretched surface," J. Therm. Sci. Eng. Appl. **10**(1), 011002 (2018). https://doi.org/10.1115/1.4024386

[5] M.B. Riaz, M. Asgir, A.A. Zafar, and S. Yao, "Combined effects of heat and mass transfer on MHD free convective flow of Maxwell fluid with variable temperature and concentration," Math. Probl. Eng. **2021**, 1-36 (2021). https://doi.org/10.1155/2021/6641835

[6] C. Bao, L. Liu, C. Xie, J. Zhu, Y. Quan, S. Chen, L. Feng, and L. Zheng, "Analysis of the absorbing boundary condition for the Maxwell fluid flow over a semi-infinite plate with considering the magnetic field," Comput Math Appl. **154**, 212-223 (2024). https://doi.org/10.1016/j.camwa.2023.11.043

[7] M. Yasin, S. Hina, and R. Naz, "A modern study on peristaltically induced flow of Maxwell fluid considering modified Darcy's law and Hall effect with slip condition," Alex. Eng. J. **76**, 835-850 (2023). https://doi.org/10.1016/j.aej.2023.06.074

[8] D. D. Babu, S. Venkateswarlu, and E. K. Reddy, "Numerical Investigation of Thermophoresis and Activation Energy Effects on Maxwell Nano Fluid Over an Inclined Magnetic Field Applied to a Disk," East Eur. J. Phys. (**4**), 326-335 (2023). https://doi.org/10.26565/2312-4334-2023-4-43

[9] Z. Abbas, T. Javed, N. Ali, and M. Sajid, "Flow and heat transfer of Maxwell fluid over an exponentially stretching sheet: A non-similar solution," Heat Transf-Asian Re. **43**(3), 233-242 (2014). https://doi.org/10.1002/htj.21074

[10] V. Singh, and S. Agarwal, "MHD flow and heat transfer for Maxwell fluid over an exponentially stretching sheet with variable thermal conductivity in porous medium," Therm. Sci. **18**(2), 599-615 (2014). https://doi.org/10.2298/TSCI120530120S

[11] S. Mukhopadhyay, "Heat transfer analysis of the unsteady flow of a Maxwell fluid over a stretching surface in the presence of a heat source/sink," Chin. Phys. Lett. **29**(5), 054703 (2012). https://dx.doi.org/10.1088/0256-307X/29/5/054703

[12] H. Sehra, N. Sadia, A. Z. Gul, and Z.A. Khan, "Convection heat–mass transfer of generalized Maxwell fluid with radiation effect, exponential heating, and chemical reaction using fractional Caputo–Fabrizio derivatives," Open Phys. **20**(1), 1250-1266 (2022). https://doi.org/10.1515/phys-2022-0215

[13] M. Waqas, M.M. Gulzar, W.A. Khan, M.I. Khan, and N.B. Khan, "Newtonian heat and mass conditions impact in thermally radiated Maxwell nanofluid Darcy–Forchheimer flow with heat generation," Int. J. Numer. Meth. Heat & Fluid Flow, **29**(8), 2809-2821 (2019). https://doi.org/10.1108/HFF-11-2018-0695

[14] S. Rashid, M.I. Khan, T. Hayat, M. Ayub, and A. Alsaedi, "Darcy–Forchheimer flow of Maxwell fluid with activation energy and thermal radiation over an exponential surface.," Appl. Nanosci. **10**, 2965-2975 (2020). https://doi.org/10.1007/s13204-019-01008-2

[15] H. Upreti, A. Bisht, and N. Joshi, "MHD Darcy–Forchheimer flow and double-diffusive modeling of Maxwell fluid over rotating stretchable surface: A computational study," Mod. Phys. Lett. B, **38**(27), 2450227, (2024). https://doi.org/10.1142/S0217984924502270

[16] S. Das, A. Ali, and R.N. Jana, "Darcy–Forchheimer flow of a magneto-radiated couple stress fluid over an inclined exponentially stretching surface with Ohmic dissipation," World J. Eng. **18**(2), 345-360 (2021). https://doi.org/10.1108/WJE-07-2020-0258

[17] N.V. Ganesh, A.A. Hakeem, and B. Ganga, "Darcy–Forchheimer flow of hydromagnetic nanofluid over a stretching/shrinking sheet in a thermally stratified porous medium with second order slip, viscous and Ohmic dissipations effects," Ain Shams Eng. J. **9**(4), 939-951 (2018). https://doi.org/10.1016/j.asej.2016.04.019

[18] J. Cui, A. Jan, U. Farooq, M. Hussain, and W.A. Khan, "Thermal analysis of radiative Darcy–Forchheimer nanofluid flow across an inclined stretching surface. Nanomaterials," **12**(23), 4291 (2022). https://doi.org/10.3390/nano12234291

[19] M. Jawad, and K.S. Nisar, "Upper-convected flow of Maxwell fluid near stagnation point through porous surface using Cattaneo-Christov heat flux model," Case Stud. Therm. Eng. **48**, 103155 (2023). https://doi.org/10.1016/j.csite.2023.103155

[20] A. Khan, I.A. Shah, A. Khan, I. Khan, and W.A. Khan, "Numerical investigation of MHD Cattaneo–Christov thermal flux frame work for Maxwell fluid flow over a steady extending surface with thermal generation in a porous medium," Int. J. Thermofluids, **20**, 100418 (2023). https://doi.org/10.1016/j.ijft.2023.100418

[21] K. Rubab, and M. Mustafa, "Cattaneo-Christov heat flux model for MHD three-dimensional flow of Maxwell fluid over a stretching sheet," PLoS One, **11**(4), e0153481 (2016). https://doi.org/10.1371/journal.pone.0153481

[22] A. Shahid, M.M. Bhatti, O.A. Bég, and A. Kadir, "Numerical study of radiative Maxwell viscoelastic magnetized flow from a stretching permeable sheet with the Cattaneo–Christov heat flux model," Neural Comput. Appl. **30**, 3467-3478 (2018). https://doi.org/10.1007/s00521-017-2933-8

[23] S. Islam, A. Dawar, Z. Shah, and A. Tariq, "Cattaneo–Christov theory for a time-dependent magnetohydrodynamic Maxwell fluid flow through a stretching cylinder," Adv. Mech. Eng. **13**(7), (2021). https://doi.org/10.1177/16878140211030152

[24] A. Salmi, H. A. Madkhali, B. Ali, M. Nawaz, S. O. Alharbi, and A. S. Alqahtani, "Numerical study of heat and mass transfer enhancement in Prandtl fluid MHD flow using Cattaneo-Christov heat flux theory," Case Stud. Therm. Eng. **33**, 101949 (2022). https://doi.org/10.1016/j.csite.2022.101949

ПОТІК МАГНІТОГІДРОДИНАМІЧНОЇ РІДИНИ МАКСВЕЛЛА В МОДЕЛІ ДАРСІ – ФОРХГЕЙМЕРА З ТЕПЛОВИМ ПОТОКОМ КАТТАНЕО – КРІСТОВА НАД ЛИСТОМ, ЩО РОЗТЯГУЄТЬСЯ, ЗА КОНВЕКТИВНИХ ГРАНИЧНИХ УМОВ

Д. Дастагірі Бабу[a], С. Венкатешварлу[a], Р. Ханума Наїк[b], Д. Манджула[c]

[a]Кафедра математики, Меморіальний коледж інженерії та технології Раджива Ганді, Нандьял-518501, Андхра-Прадеш, Індія

[b]Кафедра електроніки та комунікаційної техніки, Меморіальний коледж інженерії та технології Раджива Ганді, Нандьял-518501, Андхра-Прадеш, Індія

[c]Кафедра математики, Інститут інженерії та технології матері Терези, Паламанер-517408, Андхра-Прадеш, Індія

У цьому дослідницькому повідомленні досліджується потік Дарсі-Форхгеймера неньютонівської рідини Максвелла, яка хімічно реагує, над розтягнутим листом, включаючи тепловий потік Каттанео-Крістова за конвективних граничних умов. Потік рідини описується системою диференціальних рівнянь у частинних похідних, які згодом перетворюються на систему нелінійних звичайних диференціальних рівнянь. Для чисельного вирішення цих рівнянь було використано метод BVP4C після належного визначення безрозмірних змінних і реалізації перетворень подібності. Вплив різноманітних активних параметрів, таких як параметр Дебори, параметр Дарсі Форхгеймера, магнітний параметр, число Біо та параметр пористості, досліджується на профілі швидкості, температури та концентрації. Крім того, розраховані значення поверхневого тертя, та число Нуссельта представлені в табличній формі.

Ключові слова: *МГД; рідина Максвелла; модель Дарсі-Форхгеймера; тепловий потік Каттанео-Крістова; магнітний параметр*

MHD STEFAN FLOW OF CASSON NANOFLUID COMPLETES A POROUS MEDIUM IN THE PRESENCE OF CHEMICAL REACTION WITH THE EFFECT OF THOMPSON AS WELL AS - TROIAN SLIP OVER A PLATE IN THE COMPANY OF RADIATION

Anitha Deevi Reddy[a], Prabhakara Reddy Deevi Reddy[a], Bhagya Lakshmi Kuntumalla[b], Sneha Latha Madhura[c,d], ⬤Parandhama Areti[e]*

[a]*Mathematics and Computing skills unit, Preparatory Studies Centre, University of Technology and Applied Sciences – Nizwa, Sultanate of Oman – 611*
[b]*Department of Mathematics, CMR Technical Campus, Medchal, Hyderabad, Telangana -501401, India*
[c]*Department of Mathematics, Sambhram Academy of Management Studies, Bangalore-560097, India*
[d]*Sambhram University, Jizzax, Uzbekistan-130100*
[e]*Department of Mathematics, Institute of Aeronautical Engineering, Hyderabad, Telangana-500043, India*
Corresponding Author e-mail: a.parandhama@iare.ac.in
Received May 22, 2024; revised July 9, 2024; accepted July 12, 2024

In this work, we report the effects of Thompson, Troian slip, and Stefan blowing on the magnetohydrodynamic (MHD) Cassonnanofluid behavior via a porous media while a chemical reaction is taking place. We also examine the effects of radiation parameters, Joel heat, and velocity distribution using a two-phase model for nanofluids. Similarity transformations may be used to convert the primary Partial Differential Equations (PDEs) into Ordinary Differential Equations (ODEs). MATLAB Shooting and Runge-Kutta algorithms may be used to solve nonlinear equations. The variations in non-dimensional parameters show the effects on mass transfer, heat, and fluid flow properties. It is shown that the skin friction coefficient falls as the Stefan blowing parameter S increases. As the values of the Thompson and Troian slip parameters increase, the fluid concentration decreases. With an increase in Nt, Nb, and k, the fluid's heat rises but its concentration falls. The results of this analysis provide several enticing aspects that are going to give merits for further study of the problems.
Keywords: *Casson; Chemical reaction; MHD; Porous; Radiation; Thompson and Troian slip*
PACS: 52.30.Cv, 61.30.Pq, 83.10.Bb

1. INTRODUCTION

For the past few decades, the study of nanofluids has been a desirous investigation. Nanofluids are used in a wide range of fields, including research, geophysics, biomedicine, chemical engineering, and electronic cooling. The first to propose the concept of "nanofluid" was Choi [1]. A "nanofluid" is a liquid that contains ultrafine particles having a diameter of less than 50 nm, often metal or metal oxide. Applications for the combination of chemical reactions and heat and mass transfer issues may be found in many different sectors, and engineering domains, including nuclear power plants, gas turbines, various aircraft propulsion systems, missiles, satellites, spacecraft, biological domains, and medicinal procedures. At high operating temperatures, the radiation effect can be quite significant, making the effects of radiation on MHD flow and heat transfer problems more important in industries. (challenges related to the effects of radiation on MHD flow and heat transfer find its significance at high temperatures). Several features of mass transfer, heat transfer, and nanofluid flow with MHD radiation have been examined by several researchers. In their description of heat flow and transport, Wu as well as Zhao [2] laid forth the fundamentals of nanofluid use in engineering research. The impact of heat transmission on nanofluid flow and the consequences of double stratification on boundary layer flow in the context of a vertical plate was discussed by Ibrahim and Makinde [3]. The MHD alumina water nanofluid flow as well as mass transfer across a flat plate with certain slip conditions were examined by Singh and Kumar [4]. Sheikholeslami and Rokni [5] used the transverse magnetic field to investigate the review of MHD and heat transmission of nanofluid. The two-dimensional movement and heat transmission of Casson nanofluid across a cylinder or plate, as well as the effects of thermophoresis as well Brownian motion phenomena, are examined by Farooq *et al.* [6]. Additionally, the impacts of bioconvection, exponential thermal sink/source, and motile microorganisms are taken into account. A numerical analysis of the MHD radiative motion of the near-stagnation point over an exponentially stretchable Cross nanofluid surface with a variable heat source/sink was addressed by Srinivasa Babu *et al.* [7].

Ramesh Babu et al. [8] have not paid much attention to unsteady MHD Non-Newtonian free convective flow through a porous media via a semi-infinite vertical permeable moving plate under the presence of radiation absorption. They researched the flow properties of the visco-elastic fluid and analyzed how radiation absorption is taken into account in the energy equation. A mixed convective magnetohydrodynamically responding two-dimensional non-Newtonian fluid via a vertical exponentially stretchable impermeable barrier was reported by Srinivasa Babu et al. [9] together with temperature and concentration distributions. The mixed convective MHD 2D Williamson fluid is numerically explored under suitable circumstances, including both masses and heat transport rates, via an exponentially

vertical stretching surface. The MHD boundary layer flow of an exponentially expanding sheet with a thermally stratified medium in the presence of suction was examined by Reddappa et al. [10]. The precise solutions for the propulsion of Ree-Eyring liquid under different effects, including Joule heating, MHD, and Hall currents, have been provided by Bhatti and Rashidi [11].

Newtonian fluids have a major part in many biological applications, flow processes in natural occurrences, and mechanical systems, which has led to a lengthy history of study in this area. Numerous models, including the Ellis, Carreau, Williamson, Jeffrey, Eyring-Powell, and Casson fluids, have been presented based on their rheological results. The Casson fluid model is among the models that people use the most often. Thick fruit juices, tomato catchup, and plasma are associated with Casson fluid. Red blood's characteristics match those of Casson fluid as well. When certain important components, such as protein, fibrinogen, and globulin, are present Human red blood cells (RBCs) can create connected formations called aggregates or rouleaux in plasma. The yield stress resulting from Rouleaux's plastic solid state is related to the fixed initial stress of Casson's fluid. The non-linear quantitative description of Casson's model has been used to formulate printing solutions [12], silicon solvents [13], and polymers [14]. Ali et al. [15] performed a computer investigation on the pulsatile pushing of Casson liquid in a porous channel using a finite difference method. Majeed et al. [16] investigate the effects of slip and MHD 2D bioconvection non-Newtonian Casson nanofluid flow towards a nonlinear stretchable surface in the presence of nanoparticles and motile gyrotactic microorganisms. The Optimal Homotopy Analysis Method (OHAM) has been used by Sohail et al. [17] to address the boundary layer Casson liquid flow on a linearly elongating surface. They examined the Casson fluid motion taking into account Joule heating, MHD, and stretching surface using the RK45 technique as outlined by Kumar and Srinivas [18], and Sreenivasulu et al. [19]. Kataria and Patel [20] have provided MATLAB simulations for the MHD Casson liquid propulsion past an oscillating vertical plate. A small number of further studies in the Casson fluid with effects from magnetic fields are presented. Along with others, RajuVenkateswara [21] In the presence of a chemical reaction, the effects of slip and produced magnetic field on a non-linear convective Casson fluid in a vertical past plate with an embedded porous medium are studied theoretically. The no-slip boundary requirements are flawed because fluid flow near a container's walls often differs from the surface velocity of the container. Because of this actual feature of the flow, many slip boundary conditions have been suggested by researchers. Thermal radiation is more common in engineering domains when temperatures are high, especially in tiny convective thermal transfer systems. Moreover, thermal radiation is crucial for regulating thermal transfer schemes and preserving the temperature throughout polymer synthesis operations. As a result, studies on the effects of radiation on fluid flow systems have begun. Mandal and Mukhopadhyay [22] have shown, for example, the thermal investigation of micropolar liquid past a stretching surface under the measurements of radiated environment impacts using a shot scheme. The free convective flow of a non-Newtonian fluid in a vertical deformable porous stratum with the influence of Darcy law was studied by Sreenadh et al. [23]. They noticed that both viscous and Darcy dissipations produce heat inside the fluid.

One may derive the blowing effect from Stefan\Prime's issue, and Stefan's blowing effects are practically significant in many scenarios. The effects of Stefan blowing on a movement involving the transfer of nanofluid on stretched plates were described by Fang and Jing [24]. They observed that the blowing improves the flow's velocity. The potential significance of Stefan blowing was noted by Hamid et al. [25], who also outlined the characteristics of Stefan blowing on species movement for stagnation point flow. The effect of Stefan blowing on the movement of Casson micro fluid due to a stretched part was examined by Lund et al. [26]. Mass conveys oscillated during the flow due to mass blowing at the partition. The effects of Stefan blowing over a bio-convective caused by a stretched cylinder were documented by Rana et al. [27]. Ellahi and his coauthors [28] were able to precisely solve critical flows when nonlinear slip was present in 2010. This issue also takes into account the more general slip condition at the border that Thompson and Troian [29] presented. The effects of the Thompson-Troian slip condition and Cattaneo-Christov heat flow across a stretched sheet were investigated by Ahmad and Nadeem [30]. The effects of a chemical reaction and Thompson and Troian slip on nanofluid flow via a stretching/shrinking sheet on a stagnation zone were described by Ramzan et al. [31]. The effects of the Riga surface and Thompson and Troian slip conditions on mixed convection nanofluid flow were covered by Nadeem et al. [32]. In conjunction with the first-order compound response, Dey et al. [33] recently examined the combined effects of Stefan blowing and Thompson and Troian slip on the forced convective motion of nano liquid across a nonabsorbent plate. They found that when the levels of the Stefan blowing parameter S increase, the skin friction coefficient decreases, and as the slip parameter δ and critical shear rate β rise, the mass transfer rate decreases. The precise nature of the link between these characteristics is not well understood. Further investigation is necessary in the field of existing research about the impact of the Thompson and Troian slip condition. There isn't a single published work that discusses the Stefan flow of nanofluid when uniform shear is present.

The purpose of this paper is to examine the effects of Thompson-Troian slip and Stefan blowing on the Casson nanofluid flow. In a uniform shear, we additionally take into account the impacts of radiation, chemical reactions, Joel heat, and MHD porous media. Appropriate transformations lead to a self-similar version of the leading equations. The R-K shooting technique is then used to solve these equations. When the produced findings and the available data are compared, they demonstrate perfect agreement. The impacts of several factors on the fields of hotness, nanoparticle concentration, velocity slope, and velocity are investigated. Visual representations are used to aid in comprehending these impacts.

2. FORMULATION OF THE PROBLEM

Consider a forced convection Casson micro-liquid flow across a fixed plate in the medium that has a very tiny width and a large span (see Fig. 1). The axis is normal relative to the axis's upward-directed plate. The magnetic field that is generated is assumed to be perpendicular to the plate. The transverse magnetic field's intensity is increased by the magnetic field. Considering that the velocity apparatuses are, respectively, running parallel and normal to the plate. Given the circumstances stated above, the rheological formulas are [33] provided by

$$\tau_{ij} = \begin{cases} 2\left(\mu_B + \frac{p_y}{\sqrt{2\pi}}\right)e_{ij}, & \pi > \pi_c, \\ 2\left(\mu_B + \frac{p_y}{\sqrt{2\pi_c}}\right)e_{ij}, & \pi < \pi_c, \end{cases}$$

in which, P_y is the Casson's yield stress, the scientific expression preordained for the yield stress possibly will be articulated as $P_y = \frac{\mu_B \sqrt{2\pi}}{\beta}$ where μ_B is the Casson fluid's lively viscosity, π signifies the product of the deformation rate's constituent finished themself $\left(\pi = e_{ij}\, e_{ij}\right)$, as well π_c symbolizes the critical value created on the Casson fluid model. In the occasion $\left(\pi > \pi_c\right)$ of Casson fluid motion, the aforementioned is feasible in the case of $\mu = \mu_B + \frac{P_y}{\sqrt{2\pi}}$, By supernumerary, the Casson fluid viscosity remains now (which depends on) contingent on the Casson parameter β, in addition dynamic viscosity μ_B, and it (delete) can be inscribed as: $\mu = \mu_B\left(1 + \frac{1}{\beta}\right)$
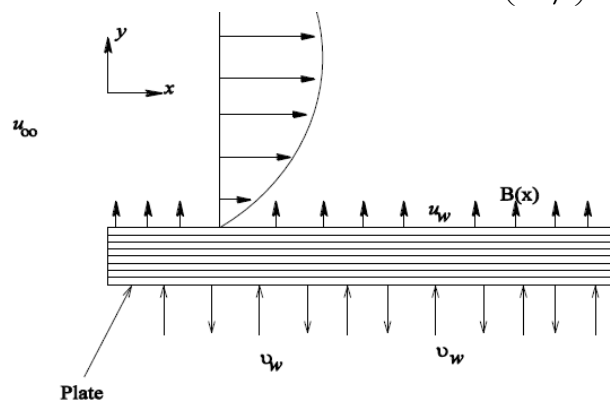
Figure 1. Sketch of the physical flow problem

$$\frac{\partial u}{\partial x} + \frac{\partial v}{\partial y} = 0 \tag{1}$$

$$u\frac{\partial u}{\partial x} + v\frac{\partial u}{\partial y} = \upsilon_f\left(1 + \frac{1}{\beta}\right)\frac{\partial^2 u}{\partial y^2} - \frac{\sigma B_0^2}{\rho_f}(u - u_\infty) - \frac{\mu}{k}u \tag{2}$$

$$u\frac{\partial T}{\partial x} + v\frac{\partial T}{\partial y} = \alpha\frac{\partial^2 T}{\partial y^2} + \frac{(\rho c)_p}{(\rho c)_f}\left[D_B\frac{\partial C}{\partial y}\frac{\partial T}{\partial y} + \frac{D_T}{T_\infty}\left(\frac{\partial T}{\partial y}\right)^2\right] - \frac{1}{(\rho c)_f}\frac{\partial q_r}{\partial y} + \frac{v}{(\rho c)_f}\left(1 + \frac{1}{\beta}\right)\left(\frac{\partial u}{\partial y}\right)^2 \tag{3}$$

$$u\frac{\partial C}{\partial x} + v\frac{\partial c}{\partial y} = D_B\frac{\partial^2 C}{\partial y^2} + \frac{D_T}{T_\infty}\frac{\partial^2 T}{\partial y^2} + k_1\left(C - C_\infty\right) \tag{4}$$

Here, u and v is the Casson fluid parameter, indicates the uniform magnetic field, denotes the electrical conductivity, k is the permeability parameter, corresponds to the fluid's specific heat, t is the time, k denotes the thermal conductivity, denotes the radiative heat flux, and are the parts of the velocity in the x and y directions, respectively. The temperature along the free stream is T, and so are the two temperatures. The variables denoted by α are the thermal diffusivity, free stream velocity, effective heat capacity of the nanofluid as well as nanoparticles, as well as Brownian and thermophoretic diffusion coefficients, correspondingly. C represents the volume percentage of nanoparticles, is the free stream focused attention, $k_1 = \frac{k_0}{x^{2/3}}$, ($k_0$ being constant) is the rate of chemical reaction, wherever $k_1 > 0$ and $k_1 < 0$ indicates that there are chemical processes that are both productive and detrimental. There are several scenarios where the response rate may change inversely with distance. Reaction rate has thus been taken (as a) significant variable in this text. The following list contains the suitable boundary circumstances regarding the present problem,

$$u = \gamma\left(1 - \zeta \frac{\partial u}{\partial y}\right)^{-1/2}\frac{\partial u}{\partial y}, \; v = \frac{-D_B}{(1 - C_w)}\frac{\partial C}{\partial y}, \; T = T_\infty, \; C = C_w \text{ at } y = 0 \tag{5a}$$

$$u = u_\infty(y) = \beta_1 y, \; T = T_\infty, \; C = C_\infty \text{ at } y \to \infty \tag{5b}$$

Here, $\gamma = \gamma_0 x^{1/3}$ is the Navier slip length, γ_0 is the slip factor, ζ is the reciprocal of the shear rate and $\beta_1 = v/L^2$ remains constant. In this case, the consistency of The idea of conservation of mass is shown in Equation (1). Equation (2) describes the momentum equation using boundary layer estimations, and it may be applied to any case involving incompressible fluid flow. The left-hand side (l.h.s) of the text represents the inertial phrases that are discussed in each article. Conversely, the first term on the right (r.h.s.) represents the viscosity term, magnetic field, and overall porous media properties found in all of the studies listed in the text. The initial term in the r.h.s. of Eqs. (3) and (4) transmit a diffusive component, while the l.h.s. of those equations indicate the convective term to earn mass transfer and heat transport, respectively. The last two variables in (3)'s r.h.s. stand for the effects of radiation, Brownian motion, thermophoresis, velocity distribution, and Joel heat – all of which have been found in earlier research [12,20,27]. First-order chemical processes are represented by the last item on the r.h.s. of (4) and have been examined by Daniel et al. [12,23], Dey, and Mukhopadhyay [27]. The thermophoresis effect is shown by the second term on r.h.s. of (4) and is seen in [12,20,27]. (5a) has two boundary conditions: [29–30] provides the second boundary condition for Stefan blowing, while [30–33] provides the first boundary condition for slip. One can locate the uniform shear flow in [36–38] that results in the first condition of (5b). In addition to the mass transfer problem over a flat plate, (5b) provides additional free-stream conditions for every flow and heat.

Resemblance examination in addition to the explanation process

The subsequent similarity conversion relations remain now placed for u, v as

$$u = \frac{\partial \psi}{\partial y}, v = -\frac{\partial \psi}{\partial x} \tag{6}$$

Anywhere, ψ is the stream function. Over, let us familiarize the subsequent dimensionless variables,

$$\eta = \frac{y}{L}\left(\frac{x}{L}\right)^{-1/2}, \; \psi = v\left(\frac{x}{L}\right)^{2/3} f(\eta) \text{ and } \theta = \frac{T - T_\infty}{T_w - T_\infty}, \; \phi = \frac{C - C_\infty}{C_w - C_\infty} \tag{7}$$

The enlargement of native thermal energy is

$$-\frac{\partial q_r}{\partial y'} = 4\,\alpha\,\sigma\,(T_\infty'^4 - T'^4) \tag{8}$$

where σ and α are Stefan-Boltzmann constant in addition to the absorption coefficient. Decrease the Eq. (3) through using Eq. (8) we get

Using the relatives (6)–(7) in the border layer Eq. (2), vigor Eq. (3) in addition to attentiveness Eq. (4) the subsequent equations remaingot.

$$\left(1 + \frac{1}{\beta}\right)f''' + \frac{2}{3}f f'' - \frac{1}{3}(f')^2 - \left(M + \frac{1}{K}\right)f' = 0 \tag{9}$$

$$\frac{1}{Pr}\left(1 + \frac{4R}{3}\right)\theta'' + N_b\,\theta'\phi' + N_t(\theta')^2 + \frac{2}{3}f\,\theta' + Ec\left[(f')^2 + (f'')^2\right] = 0 \tag{10}$$

$$\phi'' + \frac{N_t}{N_b}\theta'' + Le\left[\frac{2}{3}f\,\phi' - k\phi\right] = 0 \tag{11}$$

wherever $M = \sqrt{\frac{x\sigma}{LU}}\,B_0$ is the Magnetic parameter, $K = \frac{\mu}{x^{2/3}Lk}$ is the Porous medium parameter, $Pr = \frac{v}{\alpha}$ is the Prandtl number, R is the radiation $Le = \frac{v}{D_B}$ is the Lewis number, $N_b = \frac{(\rho c)_p D_B (C_w - C_\infty)}{(\rho c)_f\,v}$ is the Brownian motion parameter and $N_t = \frac{(\rho c)_p D_T (T_w - T_\infty)}{(\rho c)_f\,v T_\infty}$ is the thermophoresis parameter, $k = k_1 x^{2/3}$ is the rate at which chemicals react parameter; it shows both constructive as well as destructive chemical processes, but it also shows the absence of chemical reactions. In light of this, boundary requirements ultimately turn into

$$f = \frac{3S}{2Le}\phi', \; f' = \delta\left(1 - \beta_1 f''\right), \; \theta = 1, \; \phi = 1 \text{ at } \eta = 0 \tag{12a}$$

$$f'' = 1, \; \theta = 0, \; \phi = 0 \text{ at } \eta \to \infty \tag{12b}$$

where $\delta = \gamma \frac{1}{L}\left(\frac{x}{L}\right)^{-1/3} = \gamma_0 \frac{1}{L^{2/3}}$, is the velocity slip parameter and $\beta_1 = \zeta \frac{v}{L^2}$, is the critical shear rate. $S = \frac{(C_w - C_\infty)}{1 - C_w}$ is

the Stefan blowing parameter. $S > 0$ shows mass movement from fluid to plate (mass suction), but shows mass transfer from plate to fluid (mass blowing) [13,15].

2.2. Physical quantities

Sherwood number, Nusselt number, as well as skin friction coefficient, are the non-dimensional numbers of practical relevance Sh_x, Nu_x, C_f are given:

$$C_f = \frac{\tau_w}{\rho L^2}, \text{ where } \tau_w = \mu\left(1 + \frac{1}{\beta}\right)\left(\frac{\partial u}{\partial y}\right)_{y=0}, \; Nu_x = \frac{xq_w}{k(T_w - T_\infty)}, \text{ and } Sh_x = \frac{xq_m}{D_B(C_w - C_\infty)}$$

Anywhere q_w, q_m suggests the mass and heat fluxes, besides specifying the thermal conductivity of the nanofluid.

$$q_w = \left[-\left(k + \frac{16\sigma^* T_\infty^3}{3k^*}\right)\left(\frac{\partial T}{\partial y}\right)\right]_{y=0}, \; q_m = -D_m\left(\frac{\partial C}{\partial y}\right)_{y=0}$$

Replacing q_w, and q_m in the above equations, we get.

$$\text{Re}_x^{1/2} C_f \sqrt{\frac{\upsilon x}{L}} = \left(1 + \frac{1}{\beta}\right)f''(0), \; \text{Re}_x^{1/2} Nu_x \sqrt{\frac{\upsilon x}{L}} = -\left(1 + \frac{4}{3}R\right)\theta'(0), \; \text{Re}_x^{1/2} Sh_x \sqrt{\frac{\upsilon x}{L}} = -\phi'(0).$$

where $\text{Re}_x^{-1/2} = \frac{U_w}{\upsilon}$ is the local Reynolds number.

3. RESULTS AND DISCUSSION
3.1. Validation of results:

The present findings (for the no-slip border situation in the absence of Stefan blowing) are contrasted with the available published results of Blasius [34], Ishak et al. [35], Verma et al. [36], and Dey et al. [30] to verify the accuracy of the applied numerical scheme. Table 2 highlights an ideal convention alongside the available results.

3.2. Analysis of results

Numerical computations have been performed using the method outlined in the preceding section for various values of dissimilar parameters to provide a clear picture of the current issue. Figures 2 through 34 provide numerical data that illustrate the results.

The effects of the Casson fluid parameter on the profiles of temperature, concentration, and velocity are shown in Figs. 2, 9, and 22. When the critical shear rate and velocity slip parameter are present, the temperature rises while concentration and velocity drop. The effects of the magnetic parameter on the profiles of velocity, temperature, and concentration are shown in Figs. 3, 15, 23, and 4. As velocity and concentration increase, temperature exhibits the opposite behaviors in the presence of the critical shear rate and velocity slip parameter. Figures 4, 16, and 34 illustrate how the Porous medium parameter affects the profiles of temperature, concentration, and velocity. As the parameter increases, so do the profiles of concentration and velocity; however, when the critical shear rate and velocity slip parameters are present, the temperature exhibits the opposite behavior. The effects of critical shear rate parameters on temperature, concentration, and velocity profiles are depicted in Figs. 5, 18, and 29. Increasing the critical shear rate parameter causes an increase in concentration and velocity, while the presence of the Stefan blowing parameter causes the temperature profile to exhibit the opposite behaviors. The temperature drops for various velocity Thompson-Troian slip parameter values in Figures 6 and 21, respectively, although concentration oscillates in the presence of in Figure 28. The Lewis number's effects on velocity, temperature, and concentration profiles are shown in Figs. 7, 19, and 26. As, temperature and velocity dropped, the concentration profile displayed the opposite behaviors when the Stefan blowing parameter was present. Figure 8 illustrates the reduction in velocity, whereas Figure 20 displays a rise in temperature for varying values of the Stefan blowing parameter. However, Figure 30 displays concentration oscillations when certain values are present. For increasing values, the temperature results are shown in Figs. 12, 13, and 14 together with the impacts of the Brownian motion parameter, the thermophoresis parameter, and the Eckert number. For the values of, there is a temperature rise. The concentration findings with the impacts of the Eckert number, Thermophoresis parameter, and Brownian motion parameter are shown in Figs. 24, 25, and 33. As the concentration profile increases, it oscillates in the presence of. The findings of temperature in relation to the radiation parameter and Prandtl number are shown in Fig. 10, and 11. As and increases,

the fluid's temperature fluctuates in their presence. In the presence of, the concentration profiles from Figs. 31 and 32 show the same performance. We can see from Figures 17 and 27 that, in the presence of, the temperature and concentration are falling as the chemical reaction parameter increases.
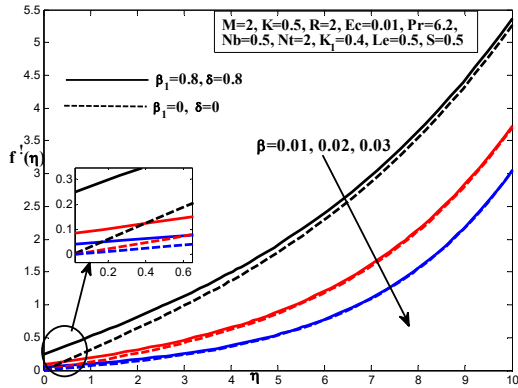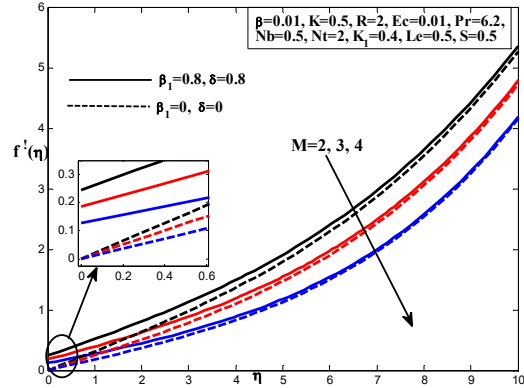
Figure 2. Velocity outline for different values of β
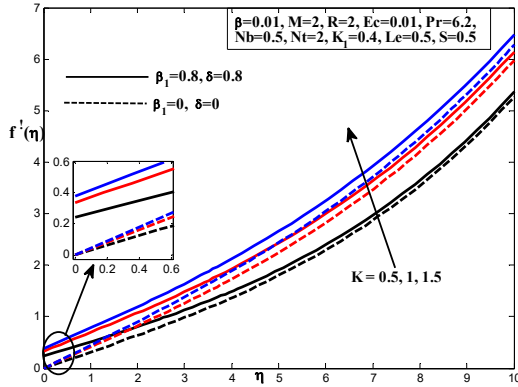
Figure 3. Velocity outline for different values of M
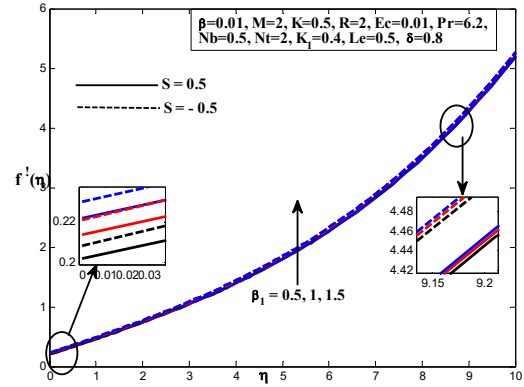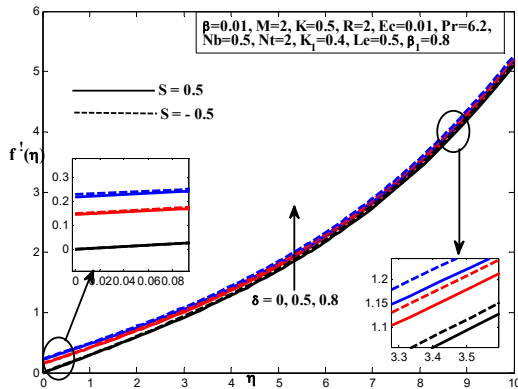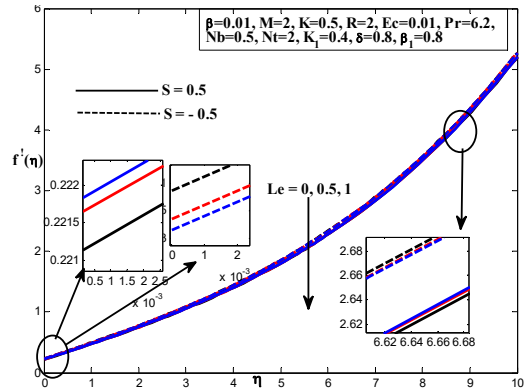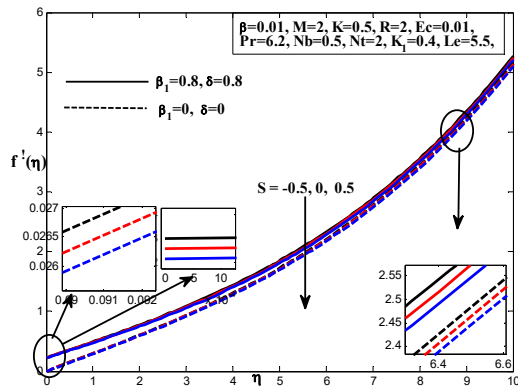
Figure 4. Velocity outline for different values of K

Figure 5. Velocity outline for different values of β_1

Figure 6. Velocity outline for different values of δ

Figure 7. Velocity outline for different values of Le

Figure 8. Velocity outline for different values of S
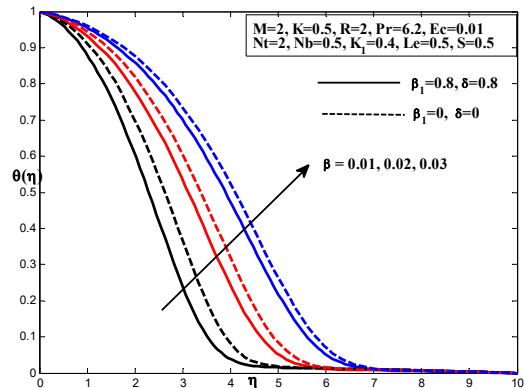
Figure 9. Temperature outline for various values of β
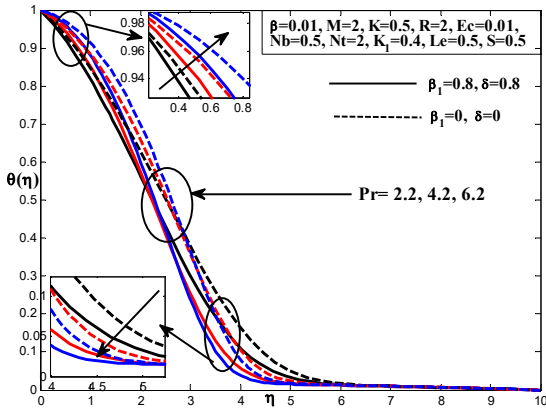
Figure 10. Temperature outline for various values of Pr
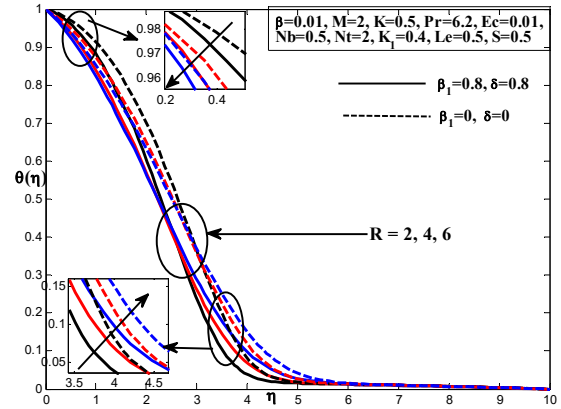
Figure 11. Temperature outline for various values of R
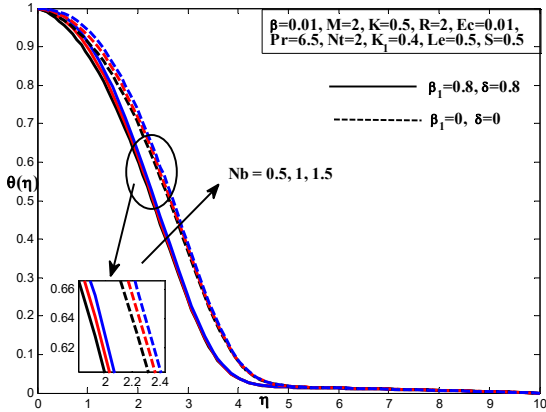
Figure 12. Temperature outline for various values of N_b
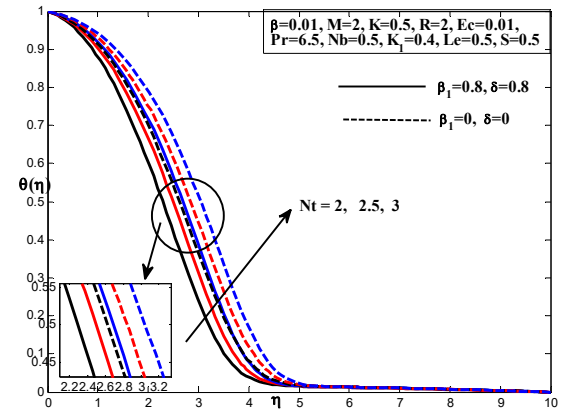
Figure 13. Temperature outline for various values of N_t
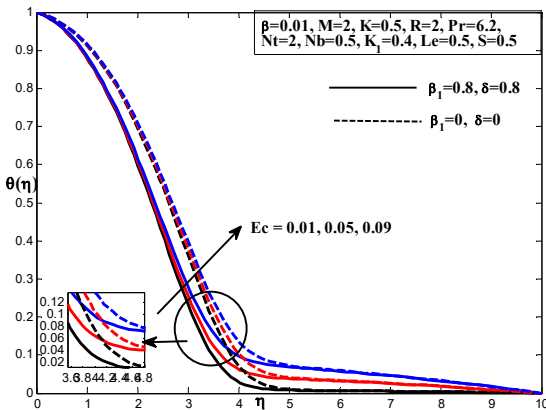
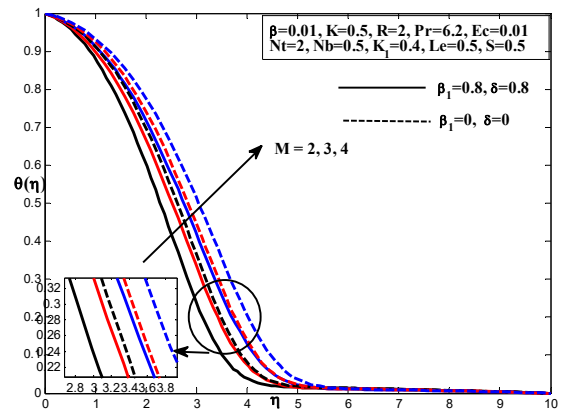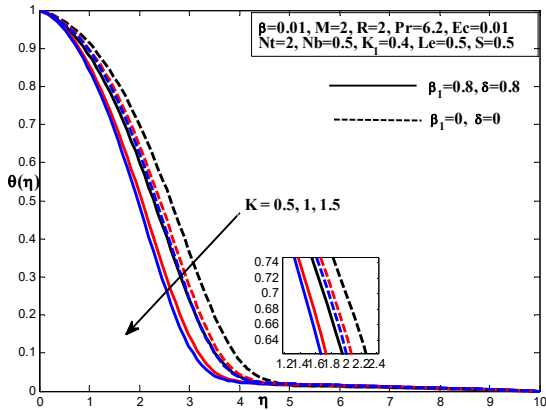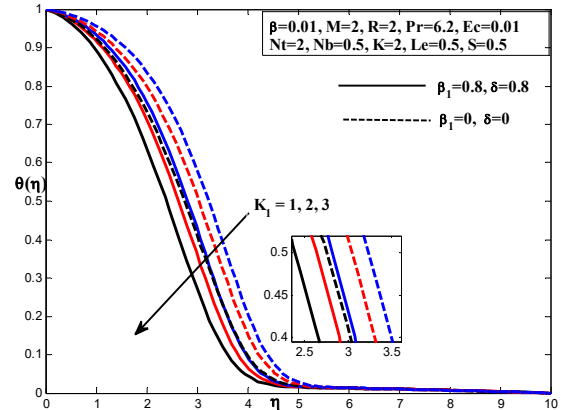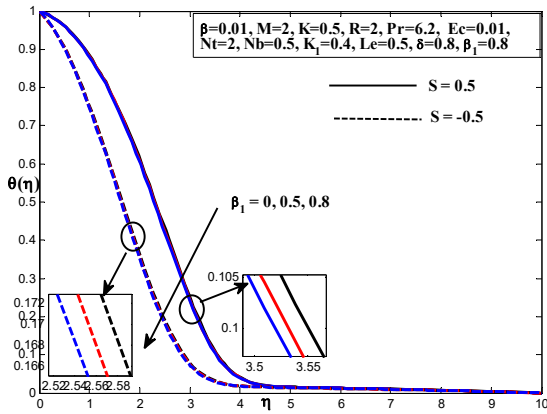**Figure 14.** Temperature outline for various values of Ec

Figure 15. Temperature outline for various values of M

Figure 16. Temperature outline for various values of K

Figure 17. Temperature outline for various values of K_1

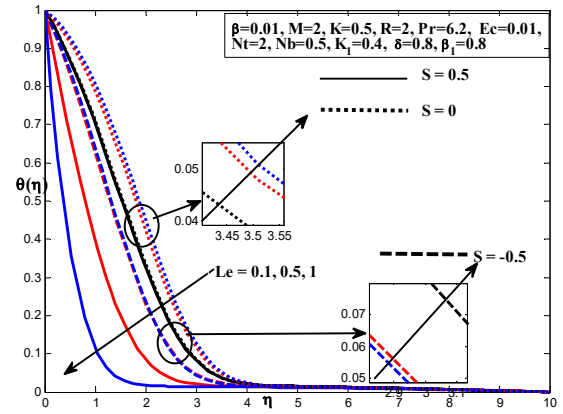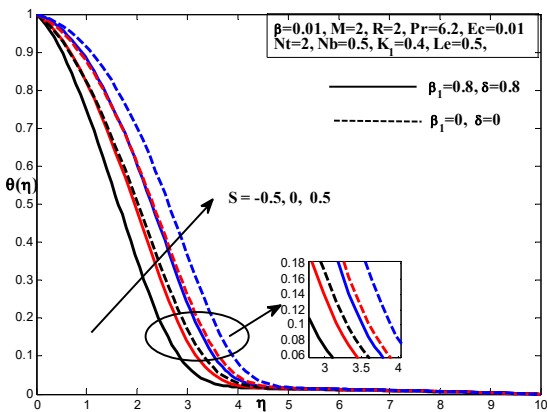**Figure 18.** Temperature outline for various values of β_1

Figure 19. Temperature outline for various values of Le

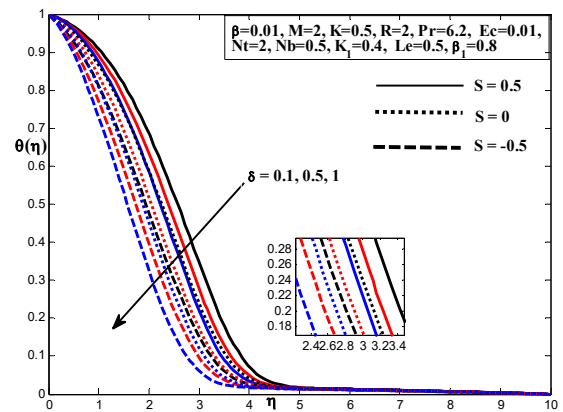**Figure 20.** Temperature outline for various values of S

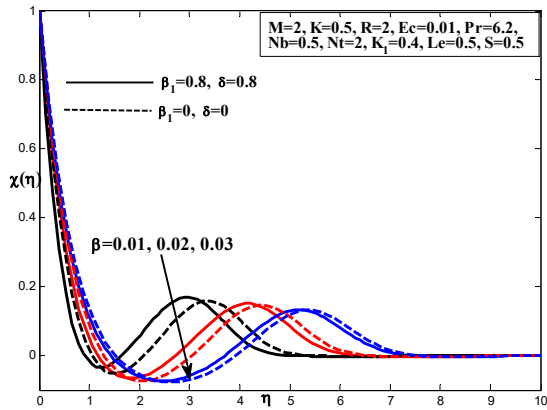**Figure 21.** Temperature outline for various values of δ

Figure 22. Concentration outline for various values of β
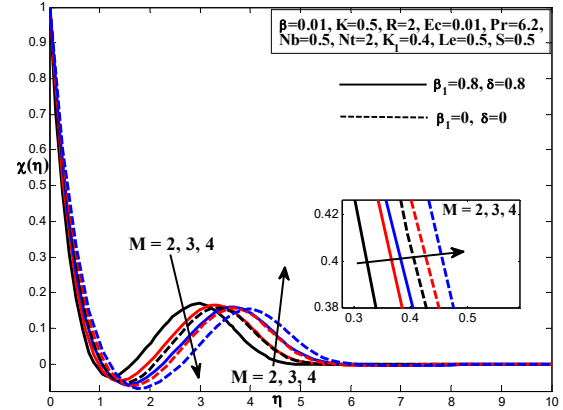

Figure 23. Concentration outline for various values of M
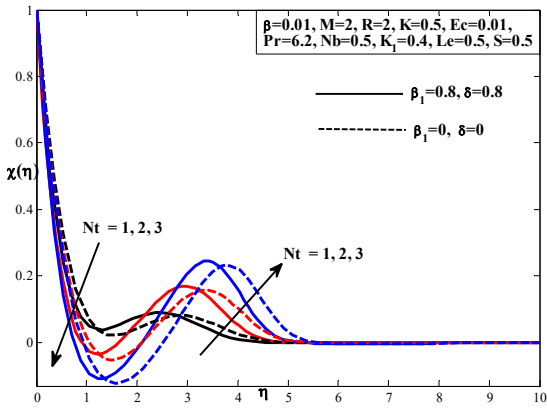

Figure 24. Concentration outline for various values of N_t
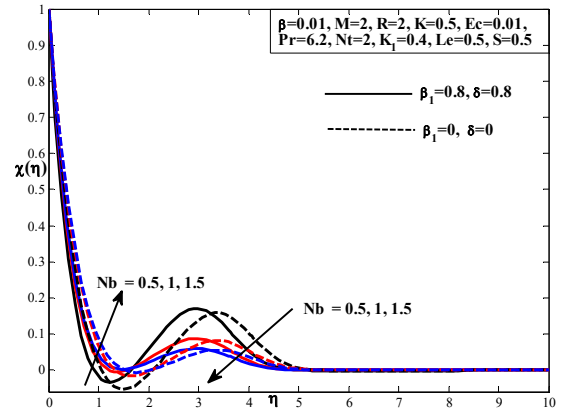

Figure 25. Concentration profile for various values of N_b

Figure 26. Concentration profile for various values of Le

Figure 27. Concentration profile for various values of K_1

Figure 28. Concentration profile for various values of δ

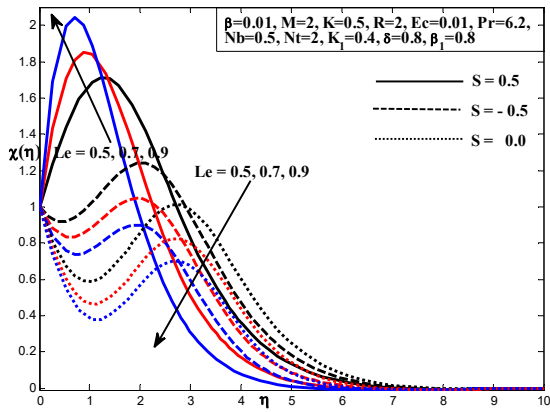**Figure 29.** Concentration profile for various values of β_1

Figure 30. Concentration profile for various values of S

Figure 31. Concentration profile for various values of Pr

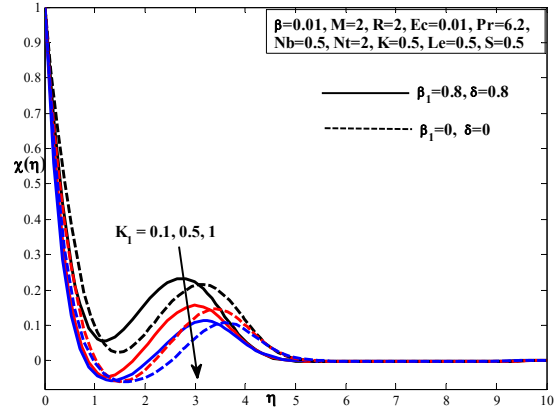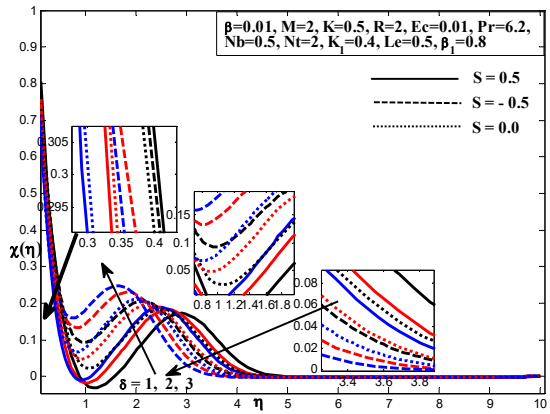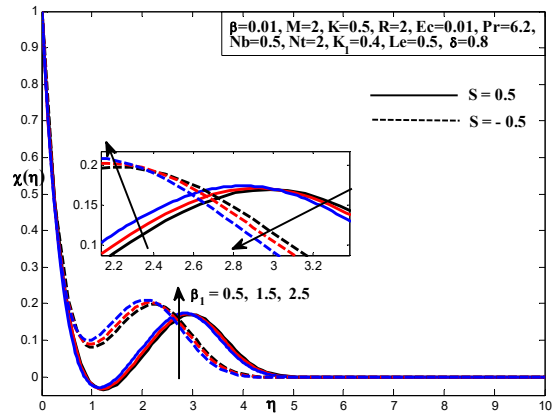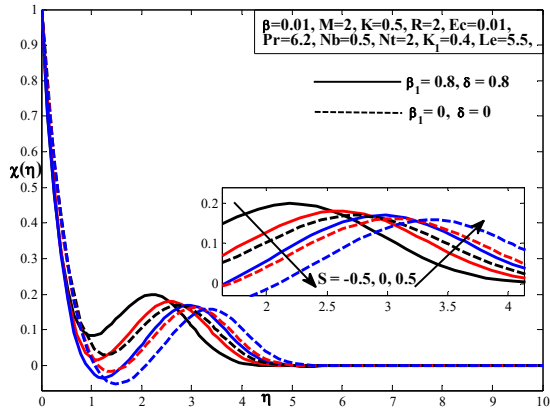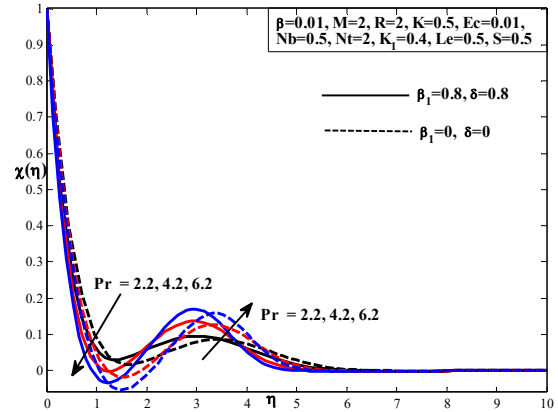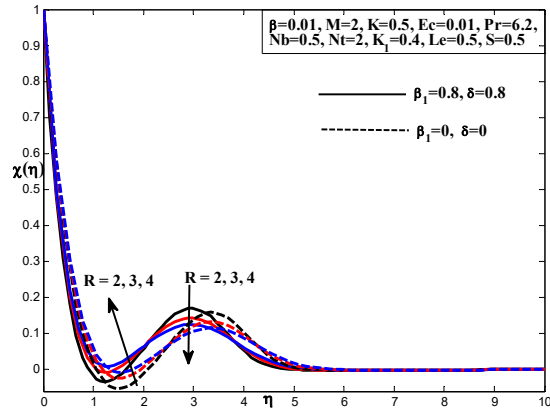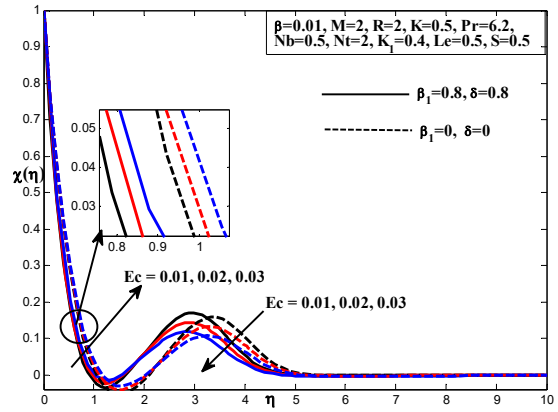**Figure 32.** Concentration profile for various values of R

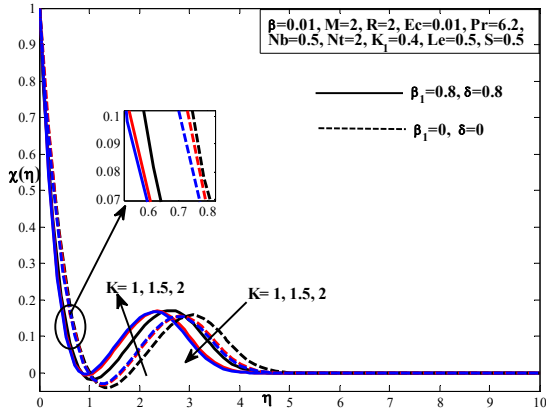**Figure 33.** Concentration profile for various values of Ec

Figure 34. Concentration profile for various values of K

Table 1 displays skin friction, Nusselt number, and shear wood number, which are consistent with earlier research. The skin friction coefficient decreases when development occurs, whereas the parameters show the opposite trend (Table 2). When the parameters are included, the Nusselt number rises, and when the parameters are excluded, the Nusselt number decreases (Table 2). For the parameters, the opposite result is seen when the mass transfer rate decreases. Pr, Ec (Table 2).

Table 1. Values of $f''(0)$, $-\theta'(0)$, $-\phi'(0)$ for $N_t = \beta_1 = \delta = S = 0$ and non-dimensional parameters.

β	M	Pr	R	Ec	K	N_t	K_1	β_1	δ	S	$f''(0)$	$-\theta'(0)$	$-\phi'(0)$
0	0	0	0	0	0	0	0	0	0	0	0.759875	0.0615431	1.4957
								0.1			0.759775	0.0699181	1.53978
								0.2			0.753338	0.0779771	1.58098
								0.3			0.741848	0.0855734	1.61892
									0.1		0.740226	0.0864321	1.62315
									0.2		0.738348	0.087386	1.62785
									0.3		0.736152	0.0884532	1.63309
						0.1					0.752703	0.159365	1.50014
						0.2					0.743802	0.117561	1.57161
						0.3					0.729837	0.0679804	1.6839
										0.1	0.717368	0.0620508	1.78433
										0.2	0.7057	0.0570051	1.87847
										0.3	0.694696	0.052655	1.9674
0.01											1.256512	0.1547812	1.254874
0.02											1.325413	0.1454217	1.225487
	1										0.785213	1.2154784	1.254784
	2										0.795846	1.3524781	1.226487
		2.2									0.759875	1.2345478	0.984577
		4.2									0.745412	1.2254784	0.995841
			2								0.859875	1.5414784	1.024578
			4								0.959875	1.6457841	0.985689
				0.01							0.689875	0.2514782	1.02548
				0.02							0.659875	0.3215478	1.032659
					0.5						0.541741	0.2154784	1.312154
					1						0.442156	0.2165478	1.301215

Table 2. $f''(0)$ for flow over a plate when $\delta = 0 = \beta = S = k$.

Verma et al. [33] $\lambda = e = \delta = s = K = 0$	Ishak et al. [32] $\lambda = 0$	Blasius [31]	Dey et al. [30]	Present work $\beta = M = R = K = 0$
0.33206	0.3321	0.332	0.332566	0.3321265

4. CONCLUDING REMARKS

The flow of a Stefan-Cassonnanofluid across a plate has been studied considering radiation, magnetohydrodynamics (MHD), shear flow, and porous material. The consequences of the Thompson-Troian slide at

the border were also investigated. When the research compared the numerical answers to the existing data, it discovered a very good match. The findings led to the following observations being made.

(i) As the thermophoresis parameter values increase and decrease, the temperature rises. For increasing values of the Brownian motion parameter, concentration is seen.

(ii) As the chemical reaction values rise, the temperature drops and the concentration fluctuates parameter (k).

(iii) The liquid absorbs heat from the plate.

(iv) The skin friction coefficient decreases as the Stefan blowing parameter S increases.

(v) As slip parameter δ and critical shear rate β increase, the mass transfer rate decreases.

ORCID

🆔**Parandhama Areti,** https://orcid.org/0000-0002-7242-895X

REFERENCES

[1]   S.U.S. Choi, "Enhancing thermal conductivity of fluids with nanoparticles," in: *Developments and Applications of Non-Newtonian Flows*, edited by D.A. Siginer, and H.P. Wang, (ASME, New York, 1995), pp. 99–105.

[2]   J.M. Wu, and J. Zhao, "A review of nanofluid heat transfer and critical heat flux enhancement research gap to engineering application," Progr. Nuclear Energy, **66**, 13–24 (2013). https://doi.org/10.1016/j.pnucene.2013.03.009

[3]   W. Ibrahim, and O.D. Makinde, The effect of double stratification on boundary-layer flow and heat transfer of nanofluid over a vertical plate, Comput. Fluids, **86**, 433–441 (2013). https://doi.org/10.1016/j.compfluid.2013.07.029

[4]   P. Singh, and M. Kumar, Mass transfer in MHD flow of alumina water nanofluid over a flat plate under slip conditions, Alex. Eng. J. **54**, 383–387 (2015). https://doi.org/10.1016/j.aej.2015.04.005

[5]   M. Sheikholeslami, and H.B. Rokni, Simulation of nanofluid heat transfer in the presence of magnetic field: a review, Int. J. Heat Mass Transf. **115**, 1203–1233 (2017). https://doi.org/10.1016/j.ijheatmasstransfer.2017.08.108

[6]   U. Farooq, H. Waqas, S.E. Alhazmi, A. Alhushaybari, M. Imran, R. Sadat, T. Muhammad, *et al.*, "Numerical treatment of CassonnanofluidBio convectional flow with heat transfer due to stretching cylinder/plate: Variable physical properties," Arabian Journal of Chemistry, **16**(4), (2023). https://doi.org/10.1016/j.arabjc.2023.104589

[7]   K.S.S. Babu, A. Parandhama, and R.B. Vijaya, "Significance of heat source/sink on the radiative flow of Cross nanofluid across an exponentially stretching surface towards a stagnation point with chemical reaction," Heat Transfer, **51**(4), 2885–2904 (2021). https://doi.org/10.1002/htj.22428

[8]   K.R. Babu, A. Parandhama, K.V. Raju, M.C. Raju, and P.V.S. Narayana, "Unsteady MHD Free Convective Flow of a Visco-Elastic Fluid Past an Infinite Vertical Porous Moving Plate with Variable Temperature and Concentration," Int. J. Appl. Comput. Math. **3**, 3411–3431 (2017). https://doi.org/10.1007/s40819-017-0306-8

[9]   K.S.S. Babu, A. Parandhama, and R.B. Vijaya, "A Numerical Investigation of chemically reacting 2D Williamson fluid over a vertical exponentially stretching surface," South East Asian J. of Mathematics and Mathematical Sciences, **16**(3), 295-310 (2020).

[10]   B. Reddappa, A. Parandhama, K. Venkateswara Raju, and S. Sreenadh, "Analysis of the Boundary Layer Flow of Thermally Conducting Jeffrey Fluid over a Stratified Exponentially Stretching Sheet," Turkish Journal of Computer and Mathematics Education, **12**(13), 730-739 (2021). https://doi.org/10.17762/turcomat.v12i13.8469

[11]   M.M. Bhatti, and M.M. Rashidi, "Study of heat and mass transfer with Joule heating on magnetohydrodynamic (MHD) peristaltic blood flow under the influence of Hall effect," Propulsion and Power Research, **6**(3), 177-185 (2017). https://doi.org/10.1016/j.jppr.2017.07.006

[12]   N. Casson, and C.C. Mill, *Rheology of Dispersed System*, vol. 84, (Pergamon Press, Oxford, 1959).

[13]   W.P. Walwander, T.Y. Chen, and D.F. Cala, "Biorheology, An approximate Casson fluid model for tube flow of blood," Biorheology, **12**, 111-119 (1975). https://doi.org/10.3233/BIR-1975-12202

[14]   G.V. Vinogradov, and A.Y. Malkin, *Rheology of Polymers*, (Mir Publisher, Moscow, 1979). (in Russian)

[15]   A. Ali, H. Farooq, Z. Abbas, Z. Bukhari, and A. Fatima, "Impact of Lorentz force on the pulsatile flow of a non-Newtonian Casson fluid in a constricted channel using Darcy's law: a numerical study," Sci. Rep. **10**(1), 10629 (2020). https://doi.org/10.1038/s41598-020-67685-0

[16]   A. Majeed, N. Golsanami, B. Gong, Q.A. Ahmad, S. Rifaqat, A. Zeeshan, and F.M. Noori, "Analysis of thermal radiation in magnetohydrodynamic motile gyrotactic micro-organisms flow comprising tiny nanoparticle towards a nonlinear surface with velocity slip," Alexandria Engineering Journal, **66**, 543–553 (2023). https://doi.org/10.1016/j.aej.2022.11.012

[17]   M. Sohail, Z. Shah, A. Tassaddiq, P. Kumam, and P. Roy, "Entropy generation in MHD Casson fluid flow with variable heat conductance and thermal conductivity over a non-linear bi-directional stretching surface," Sci. Rep. **10**(1), 12530 (2020). https://doi.org/10.1038/s41598-020-69411-2

[18]   C.K. Kumar, and S. Srinivas, "Influence of Joule heating and thermal radiation on unsteady hydromagnetic flow of chemically reacting Casson fluid over an inclined porous stretching sheet," Spec. Top Rev. Porous Media Int. J. **10**(4), 385-400 (2019). https://doi.org/10.1615/SpecialTopicsRevPorousMedia.2019026908

[19]   P. Sreenivasulu, T. Poornima, and N.B. Reddy, "Influence of Joule heating and non-linear radiation on MHD 3D dissipating flow of Casson nanofluid past a non-linear stretching sheet," Nonlinear Eng. **8**(1), 661-672 (2019). https://doi.org/10.1515/nleng-2017-0143

[20]   H. Kataria, and H. Patel, "Heat and mass transfer in magnetohydrodynamic (MHD) Casson fluid flow past over an oscillating vertical plate embedded in porous medium with ramped wall temperature," Propulsion and Power Research, **7**(3), 257-267 (2018). https://doi.org/10.1016/j.jppr.2018.07.003

[21]   K.V. Raju, A. Parandhama, and M. Changalraju, "Induced Magnetic Field And Slip Effects on Non-Linear Convective Casson Fluid Flow Past a Porous Plate Embedded in Porous Medium," Journal of Xidian University, **14**(5), 1334-1343 (2020). http://dx.doi.org/10.37896/jxu14.5/148

[22] I.C. Mandal, and S. Mukhopadhyay, "Nonlinear convection in micropolar fluid flow past an exponentially stretching sheet in an exponentially moving stream with thermal radiation," Mech. Adv. Mater. Struct. **26**(24), 2040-2046 (2019). https://doi.org/10.1080/15376494.2018.1472325

[23] S. Sreenadh, M.M. Rashidi, K.K.S. Naidu, and A. Parandhama, "Free Convection Flow of a Jeffrey Fluid through a Vertical Deformable Porous Stratum," Journal of Applied Fluid Mechanics, **9**(5), 2391-2401 (2016). https://doi.org/10.18869/acadpub.jafm.68.236.25549

[24] T. Fang, and W. Jing, "Flow heat and species transfer over a stretching plate considering coupled Stefan blowing effects from species transfer," Commun. Nonlinear Sci. Numer. Simul. **19**, 3086–3097 (2014). https://doi.org/10.1016/j. cnsns.2014.02.009

[25] R.A. Hamid, R. Nazar, and I. Pop, "Stagnation point flow, heat transfer, and species transfer over a shrinking sheet with coupled Stefan blowing effects from species transfer," AIP Conf. Proc. **1784**, 050005 (2016), https://doi.org/10.1063/1.4966824

[26] L.A. Lund, Z. Omar, J. Raza, I. Khan, and E.S.M. Sherif, "Effects of Stefan blowing and slip conditions on unsteady MHD Casson nanofluid flow over an unsteady shrinking sheet: dual solutions," Symmetry, **12**(3) 487 (2020). https://doi.org/10.3390/sym12030487

[27] P. Rana, V. Makkar, and G. Gupta, "Finite element study of bio-convective Stefan blowing Ag-MgO/water hybrid nanofluid induced by stretching cylinder utilizing non-Fourier and Non-Fick's Laws," Nanomaterials, **11**, 1735 (2021). https://doi.org/10.3390/nano11071735

[28] R. Ellahi, T. Hayat, F.M. Mahomed, and A. Zeeshan, "Fundamental flows with nonlinear slip conditions: exact solutions," Z. Angew. Math. Phys. **61**, 877–888 (2010). https://doi.org/10.1007/s00033-010-0079-y

[29] P.A. Thompson, and S.M. Troian, "A general boundary condition for liquid flow at solid surfaces," Nature, **389**, 360–362 (1997). https://doi.org/10.1038/38686

[30] S. Ahmad, and S. Nadeem, "Flow analysis by Cattaneo–Christov heat flux in the presence of Thompson and Troian slip condition," Appl. Nanosci. **10**, 4673–4687 (2020). https://doi.org/10.1007/s13204-020-01267-4

[31] M. Ramzan, J.D. Chung, S. Kadry, Y.M. Chu, and M. Akhtar, "Nanofluid flow containing carbon nanotubes with quartic autocatalytic chemical reaction and Thompson and Troian slip at the boundary," Scient. Rep. **10**, 18710 (2020). https://doi.org/10.1038/s41598-020-74855-7

[32] S. Nadeem, S. Ahmad, and M.N. Khan, "Mixed convection flow of hybrid nanoparticle along a Riga surface with Thompson and Troian slip condition," J. Thermal Anal. Calorim. **143**, 2099–2109 (2020). https://doi.org/10.1007/s10973-020-09747-z

[33] S. Dey, S. Mukhopadhyay, and M. Begum, "Stefan flow of nanofluid and heat transport over a plate in company of Thompson and Troian slip and uniform shear flow," Forces in Mechanics, **9**, 100129 (2022). https://doi.org/10.1016/j.finmec.2022.100129

[34] H. Blasius, "Grenzschichten in FlussigkeitenmitkleinerReibung," Z. Math. Phys. **56**, 1–37 (1908).

[35] A. Ishak, R. Nazar, and I. Pop, "Flow and heat transfer characteristics on a moving flat plate in a parallel stream with constant surface heat flux," Heat Mass Transf. **45**, 563–567 (2009). https://doi.org/10.1007/s00231-008-0462-9

[36] A.K. Verma, A.K. Gautam, K. Bhattacharyya, A. Banerjee, and A.J. Chamkha, "Boundary layer flow of non-Newtonian Eyring–Powell nanofluid over a moving flat plate in Darcy porous medium with a parallel free-stream: Multiple solutions and stability analysis," Pramana J. Phys. **173**, 95 (2021). https://doi.org/10.1007/s12043-021-02215-9

ПОВНИЙ МГД ПОТІК СТЕФАНА НАНОРІДИНИ КАСОНА У ПОРИСТОМУ СЕРЕДОВИЩІ ЗА НАЯВНОСТІ ХІМІЧНОЇ РЕАКЦІЇ З ЕФЕКТОМ ТОМПСОНА, А ТАКОЖ ТРОЙАН-КОВЗАННЯ ПО ПЛАСТИНІ ЗА НАЯВНОСТІ ВИПРОМІНЮВАННЯ

Аніта Діві Редді[a], Прабхакара Редді Діві Редді[a], Бхаг'я Лакшмі Кунтумалла[b], Снеха Латха Мадхура[c,d], Парандхама Ареті[e]

[a]Департамент математики та комп'ютерних навичок, Центр підготовчого навчання, Університет технології та прикладних наук, Нізва, Султанат Оман – 611

[b]Факультет математики, Технічний кампус CMR, Медчал, Хайдерабад, Телангана-501401, Індія

[c]Департамент математики Академії менеджменту Самбхрам, Бангалор-560097, Індія

[d]Університет Самбхрам, Джизак, Узбекистан-130100

[e]Кафедра математики, Інститут аеронавігаційної техніки, Хайдарабад, Телангана-500043, Індія

У цій роботі ми повідомляємо про вплив ефекта Томпсона, ковзання Трояна та Стефана на поведінку магнітогідродинамічної (МГД) кассонового нанофлюїду через пористе середовище під час хімічної реакції. Ми також досліджуємо вплив параметрів випромінювання, Джоулевого тепла та розподілу швидкості за допомогою двофазної моделі для нанофлюїдів. Перетворення подібності можна використовувати для перетворення первинних диференціальних рівнянь із частинними похідними (PDE) у звичайні диференціальні рівняння (ODE). Для вирішення нелінійних рівнянь використано алгоритми MATLAB Shooting і Runge-Kutta. Варіації безрозмірних параметрів показують вплив на масообмін, тепло та властивості потоку рідини. Показано, що коефіцієнт поверхневого тертя зменшується зі збільшенням параметра S видування Стефана. Із збільшенням значень параметрів ковзання Томпсона і Трояна концентрація рідини зменшується. Зі збільшенням i k теплота рідини зростає, але її концентрація падає. Результати цього аналізу надають кілька привабливих аспектів, які дадуть можливості для подальшого вивчення проблем.

Ключові слова: *Кассон; хімічна реакція; МГД; пористий; випромінювання; Томпсон і Троян ковзання*

INFLUENCE OF HEAT AND MASS TRANSMISSION ON THE MHD FLUID CIRCULATION IN CONJUNCTION WITH AN UPRIGHT SURFACE IN THE EMERGENCE OF RADIATION THERMOPHORESIS AND THE DUFOUR REPERCUSSIONS

Ashik Hussain Mirza[a], Bamdeb Dey[b*], Rita Choudhury[c]

[a]Department of Mathematics, D.R. College, Golaghat - 785621, Assam, India
[b]Department of Mathematics, Assam Don Bosco University, Guwahati-781017, Assam, India
[c]Department of Mathematics, Gauhati University, Guwahati- 781014, Assam, India
*Corresponding Author e-mail: bamdebdey88@gmail.com

The current research simulates the mass and heat energy transmission model on MHD fluid flow under concentration and temperature deviations on a two-dimensional viscous fluid along an upright facet. Following boundary layer estimations, mathematical simulations for the movement of fluids, the conveyance of heat and mass exposed to radiation, thermophoresis, and Dufour consequences are generated as a set of partial differential equations. The surface's resilient suction was assessed. The built-in solver bvp4c in MATLAB is used for numerically debugging the aforementioned models. Through the inclusion of visualizations and tables, the detrimental effects of influencing variables are examined on the velocity, temperature as well as concentration gradients in conjunction with on the skin friction, Nusselt number, and Sherwood number. Excellent coherence may be shown when comparing between the most present findings and those that have previously been made available in the literature in specific limited circumstances. The Dufour effect, radiation, thermophoresis, and the Grashof number are all factors that influence fluid motion and heat transmission at the interface layer of dirt. Moreover, developments in the Shearing stress, Nusselt number, and Sherwood number coefficient are calculated. The findings are crucial for optimizing a variety of fluid-based technologies and systems, allowing developments in a number of industries including energy-effectiveness, electronics cooling, pursued medicine administration, and many more.
Keywords: *Chemical reaction; Dufour effect; Heat transfer; Mass transfer; Radiation; Thermophoresis*
PACS: 44.05.+e, 44.20.+b, 44.40.+a, 47.50.+d, 47.50.Cd

INTRODUCTION

The concomitant transpiration of both heat and mass remains an extremely important procedure that it has drawn a lot of interest because of its widespread use in STEM fields, including nuclear power facilities, crude oil processing, heat insulation, biological waste control, airflow, plasma analyses, geomagnetic turbines, subterranean industries, and thermal exchangers and many more. There is now a resurgence intriguing in the research of fluid flow, in tandem with the transmission of heat and mass, as an out-turn of these utilitarian processes' expanding uses. In this vein, M.B. Riaz et al. [1] conducted a thorough investigation on the consequences of mass transport along with the amalgamated heat displacement regarding convective fluid circulation with attribute concentration and temperature. R.D. Ene et al. [2] analyze the mass and heat transmission issue in a sticky substance flow to determine that the thickness of the boundary layer is dwindling. I. H. Qureshi et al. [3] performed a numerical simulation of the distribution of heat and mass caused by the infiltration of nanofluid into an impermeable medium to demonstrate that the ambient temperature rose when the frictional impact generated heat while heat is dispersed to the fluid's particle's surface. E.O. Fatunmbi and A. Adeniyan [4] examined heat and mass transition in Micropolar fluid movement across a prolong surface with velocity and thermal friction ambience and found that increasing the thickness attribute improved the exchange of thermal energy effect simultaneously. By using chaotic forced convection, J. E Salhi et al. [5] examined the heat and mass exchange of fluid carried over an even conduit. Some related works [6-10] are also found in the literature survey. Some other significant studies on heat and mass transmission with a variety of tangible characteristics are listed in [6–10].

Numerous important applications of magnetohydrodynamic (MHD) flow phenomena can be found in the fields of natural science, technology, and biomedicine. These applications include MHD power plants, MHD catalysts, blood flow extent, electrolytes, ionized substances, wave propagation tubes, propulsion systems. As a result, a lot of academics [11-15] are now paying more emphasis to how the magnetic field affects the movement of fluids and the conveyance of heat and mass. The adverse impacts of hesitant thermal emission on MHD convective slip propagation of viscoelastic fluid via a porous substrate encased within an opaque medium were explored by Choudhury and Dey [11]. Raju and Venkataramana [12] reviewed MHD and demonstrated viscous evaporation and thermal expansion when the convective flow was carried along permeable material in an elongated conduit with shielded and insurmountable bottom walls. The MHD boundary layer flow across a flat surface with diffuse dissipation has been elucidated by Kalita et al. [13]. It was quite well-explained by Das et al. [14] how magnetohydrodynamics affected entwined evaporative slip flow across an elevated perforated disc with diffuse viscosity and Joule radiation heating. Mahanthesh et al. [15] looked into the magnetohydrodynamic impact on a stochastic elastic sheet and the 3-dimensional propagation of nanofluids involving drift and thermal exposure.

The least amount of energy required by reactants to initiate a chemical process is termed as energy for activation. Fluid motion combined with chemical processes and energy of activation encounters an enormous variety of applications, including crop damage arising from cooling, paper manufacture, food fabrication, porcelain, evaporation, crude oil, fluid emulsion, and so on. Magnetohydrodynamics (MHD), which is used in this work, is a phenomenon that deals with electrically stimulated flows of fluids that have enticing characteristics, which in turn govern the trajectory of flow and polarize the field's magnetism. Y.P. Lv [16] investigated the effect of chemical processes on the behavior of nanofluid motion in a twirling tube with a Hall current. A. M. Sedki [17] explored the consequences of chemical alteration on MHD-infused radiative conveyance of heat dissipation in tiny fluid flows owing to a stochastic lengthen interface via a permeable medium. N.N.W Khalili et al. [18] discuss the chemical retaliation impacts on MHD flow through an incrementally stretched surface with an insulation layer. Samuel and Fayemi [19] analyzed the effects of chemical reactions on harmonic dissipative fluid motion in an opaque medium over a stretched sheet combined with thermal radiation. Shah et al. [20] inquired about the detrimental impact of electromagnetic radiation on progressive heat transport in an MHD boundary region Carreau fluid involving a compound's reaction.

During the exchange of heat happens in a flowing fluid, as in chemical processing and geological mechanisms, it leads to a cross-diffusion phenomenon known as the Dufour effect. The Dufour effect is commonly seen in situations with both heat and concentration gradients, particularly multi-component fuel mixes or unifying mixtures of fluids. Such an effect is insurmountable in fluid flows with strong gradients of concentration and temperature in operations involving chemical manufacture, material acoustic, and numerous engineering projects. Extra variables in both the heat and transportation of mass equations define the Dufour effect numerically. Realizing this, numerous researchers were eager to explore the Dufour effect in diverse fluid movement situations. To mention a few, E. Seid et al. [21] inquired about various slips and Dufour consequences in fluid movement near an upright stretching surface in addition to the presence of magnetized nanoparticles. M. Hasanuzzaman et al. [22] assessed the significance of Dufour as well as thermal dispersion on erratic MHD natural convection and momentum flow over a perpetual stacked accessible surface. Ismail Filahi et al. [23] performed an empirical and quantitative analysis of the Dufour impact on thermosolutal flow in an axial brinkman translucent stack using a serene upper threshold.

Thermophoresis, commonly referred to as the Soret impact, is a physical phenomenon that occurs when tiny molecules or particles move through a fluid media in response to an alteration in temperature. In simple terms, throughout the action, substances in the hot atmosphere travel to a cooler one. In this regard, N. A. Shah et al. [24] performed a quantitative simulation of thermophoretic second-grade fluid motion across an upward slope with varying fluid properties and progressive scorching and shown that increased temperature-sensitive viscous factors improve velocity patterns. F. Mabooda et al. [25] discovered that having a combination of thermophoresis and Brownian motion in a fluid improves the transmission of heat. J. V. Tawade et al. [26] encountered that raising the amount of the Brownian motion attribute causes an increase in the thermal persona, and enhancing the magnitude of the Thermophoresis coefficient causes an increase in the thermal energy circulation. According to B. K. Jha and H. N. Sani [27] whenever thermophoretic readings escalate, it's possible to observe an accumulation of Sherwood number readings at the cooler plate. Furthermore, intriguing development concerning this [28-34] has developed some well-established models.

The contributors meticulously reviewed the existing literature and spotted multiple investigations on the implications of MHD on the transmission of heat and mass transport in the emergence of innumerable flow characteristics, but to their knowledge, there is no investigation regarding the inclusion of chemical reaction, thermophoresis, and the Dufour repercussions in conjunction with the amalgamated transfer of heat as well as mass effect on MHD fluid flow for the plate that is vertical. The inclusion of Thermophoresis and the Dufour effect, in tandem with additional significant flow characteristics, enhances the problem's originality. The proposed model is streamlined using boundary layer estimation and dimensionless transformations. The Numeric scheduling of bvp4c in MATLAB is then worn to solve the underlying combined nonlinear system of equations. The MATLAB quantitative analyzer of bvp4c provides a superb setting for dealing with entangled sets of conventional simultaneous equations. The mentioned approach has been utilized successfully to handle a range of issues pertaining to fluid flow. The aforementioned quantitative approach was most recently applied in the investigation of Dey et al. [35, 36] and Mirza et al. [37]. The insights gained from the results of the investigation will aid its designers in improving the efficacy of unifying mixtures of fluids and Particle Filtration, the combustion process and Burning Propagation, cooling techniques utilized in Bioprocessing and Biotechnology, and food extraction processes that incorporate Thermophoresis and Dufour effects.

MATHEMATICAL FORMULATION

In the instance of heat transmission, considering two-dimensional devoid convective incompressible fluid motion through a vertical plate. A homogenous magnetic gradient B is provided to the plate in the direction of transverse motion. The current investigation looks at the governing fluid's simultaneous heat and mass transmission approach when combined with chemical reactions, the Dufour effect, and thermophoresis. The x-axis advances upwards relative to the sheet, while the y-axis moves parallel to it. In the aforementioned scenario, the effect of the generated electromagnetic-field is neglected. Also, the Renolds number is considered to be very small. In the beginning, the plate and the fluid are kept at identical temperature and concentration. Suddenly, they rise to a temperature of $\overline{T}_w\,(> T_\infty)$ and concentration of $\overline{C}_w (> C_\infty)$ Applying the boundary surface estimation, the governing equations are outlined in the following order
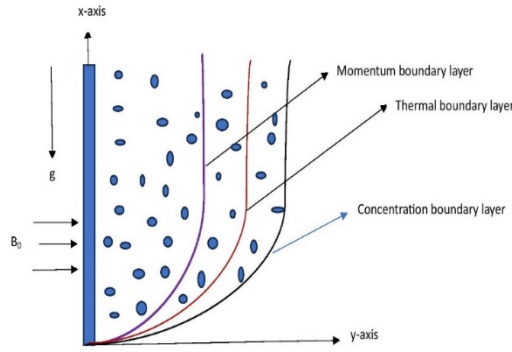
Figure1. Physical model of the flow scheme

Mass flow modeling:

$$\frac{\partial \bar{v}}{\partial \bar{y}} = 0 \tag{1}$$

$$\bar{v}\frac{\partial \bar{u}}{\partial \bar{y}} = \nu \frac{\partial^2 \bar{u}}{\partial \bar{y}^2} - \frac{\sigma}{\rho} B_0^2 \bar{u} + g\beta(\bar{T} - T_\infty) + g\bar{\beta}(\bar{C} - C_\infty) \tag{2}$$

$$\bar{v}\frac{\partial \bar{T}}{\partial \bar{y}} = \frac{\kappa}{\rho C_p}\frac{\partial^2 \bar{T}}{\partial \bar{y}^2} - \frac{1}{\rho C_p}\frac{\partial q_r}{\partial \bar{y}} + \frac{1}{\rho C_p}\left[\frac{\rho D_m K_T}{C_s}\frac{\partial^2 \bar{C}}{\partial \bar{y}^2}\right] \tag{3}$$

$$\bar{v}\frac{\partial \bar{C}}{\partial \bar{y}} = D\frac{\partial^2 \bar{C}}{\partial \bar{y}^2} - k_r(\bar{C} - C_\infty) - \frac{\partial}{\partial \bar{y}}[V_T(\bar{C} - C_\infty)] \tag{4}$$

$$V_T = -\frac{k\nu}{T_r}\frac{\partial \bar{T}}{\partial \bar{y}}, \text{ stands for thermophoretic velocity,} \tag{5}$$

where k is the thermophoretic amount, T_r represents reference temperature.
Relevant boundary situations are:

$$\bar{y} = 0 : \bar{u} = U, \bar{v} = -v_0; \ \bar{T} = \bar{T}_w ; \bar{C} = \bar{C}_w \tag{6}$$

$$\bar{y} \to \infty : \bar{u} \to 0 ; \ \bar{T} \to \bar{T}_\infty ; \bar{C} = \bar{C}_\infty$$

Dimensionless parameters are:

$$f = \frac{\bar{u}}{U}, y = \frac{\bar{y}U}{\nu}, \theta = \frac{\bar{T} - T_\infty}{\bar{T}_w - T_\infty}, C = \frac{\bar{C} - C_\infty}{\bar{C}_w - C_\infty},$$

$$\lambda = \frac{v_0}{U}, \quad M = \frac{\sigma B_0^2 \nu}{\rho U^2}, \quad K = \frac{\nu K_r}{U^2}, \quad Sc = \frac{\nu}{D},$$

$$Gr = \frac{\nu g\beta(\bar{T}_w - T_\infty)}{U^3}, \quad Gm = \frac{\nu g\beta^*(\bar{C}_w - C_\infty)}{U^3}, \quad Pr = \frac{\mu C_p}{\kappa}, \tag{7}$$

$$Ra = \frac{16a^*\nu^2\sigma T_\infty^3}{\kappa U^2}, \quad Du = \frac{D_m k_T(\bar{C}_w - \bar{C}_\infty)}{C_S C_p(\bar{T}_w - T_\infty)}, \quad \tau = -k\frac{(\bar{T}_w - T_\infty)}{\bar{T}_r}$$

Where f is dimensionless velocity, θ is dimensionless temperature, C is dimensionless concentration, y is dimensionless co-ordinate, λ is suction parameter, Gr is thermal Grashof number, Gm is solutalGrashof number, M is magnetic field limitations, Pr is Prandtl number, K is Chemical reaction specification, Sc is Schmidt number, Du is the amount of mass diffusivity (Dufour number), Ra is the radiation specification, τ is the thermophoretic constant.

Non-dimensional governing equation are

$$\frac{d^2f}{dy^2} + \lambda\frac{df}{dy} - Mf + Gr\theta + GmC = 0 \tag{8}$$

$$\frac{d^2\theta}{dy^2} + Pr\lambda\frac{d\theta}{dy} - Ra\theta + PrDu\frac{d^2C}{dy^2} = 0 \tag{9}$$

$$\frac{d^2C}{dy^2} + \lambda Sc\left(1 - \tau\frac{d\theta}{dy}\right)\frac{dC}{dy} - KScC - \tau ScC\frac{d^2\theta}{dy^2} = 0 \tag{10}$$

with Modified boundary conditions

$$y = 0: f = 1; \ \theta = 1, C = 1$$

$$y \to \infty: f \to 0; \ \theta \to 0, C \to 0 \tag{11}$$

METHODOLOGY

The bvp4c quantitative algorithm in MATLAB is applied to the equations (8) to (10) due to the limitations (11). This bvp4c problem-solver is one of MATLAB's most recent extensions and produces excellent outcomes. Three crucial

types of information are needed for this solver to function: the equation that needs to be solved, the given equation's boundary condition, and the initial estimate of the solution. Shampine et al. [38] was the first who initially presented the bvp4c methodology. In the present study, equations (8) to (10) along with the boundary condition (11) are transform into differential equation of first order applying MATLAB built in solver bvp4c as stated below:

Let, $f = y(1), \frac{df}{dx} = y(2), \theta = y(3), \frac{d\theta}{dx} = y(4), C = y(5), \frac{dC}{dx} = y(6)$ gives

dydx = [y(2)

-λ*y(2)+M*y(1)-Gr*y(3)-Gm*y(5)

y(4)

-Pr* λ *y(4)+Ra*y(3)-{Pr*Du*{- λ *Sc*(1 - τ *y(4))*y(6)+K*Sc*y(5)- τ *Sc*y(5)*(Pr* λ *y(4)-Ra*y(3))}/(Pr*Du* τ*Sc*y(5))

y(6)

- λ*Sc*(1 - τ *y(4))*y(6)+K*Sc*y(5)* -Pr* λ*y(4)+Ra*y(3)*{-{Pr*Du*{- λ*Sc*(1 - τ *y(4))*y(6)+K*Sc*y(5)-τ*Sc*y(5)*(Pr* λ*y(4)-Ra*y(3))}/(Pr*Du* τ*Sc*y(5))}]

VALIDATION OF THE CODE

The validity of the strategies adopted for this study is supported by Table. A comparison of Shearing stress (σ) and Nusselts'(Nu) number for radiation parameter (Ra) have been conducted with S. Ahmed [39].

Ra	Sahin et al. [39]		Present study	
	Shearing stress (σ)	Nusselts' number (Nu)	Shearing stress (σ)	Nusselts' number (Nu)
1	1.82981	1.52803	1.4857	1.3838
2	1.77918	1.82209	1.4851	1.3885
3	1.73423	2.17803	1.4845	1.3932

RESULTS AND DISCUSSION

In this survey, we looked at the influence of thermophoresis in viscous fluids, as well as chemical reactions and the Dufour effect. To assess the physical condition, for diverse fluid specifications, we examined the distinctive patterns for flow rate, temperature, and concentration. To begin, take a collection of arbitrary parameters with values, such as the Magnetic flux specification, M=1, Grashof number Gr=8, Solutal Grashof number Gm=3, Chemical reaction constant K=0.1, Radiation Parameter Ra=7, Thermophoresis parameter τ=2, Schimdt number Sc=0.6, Prandtl number Pr=0.71, Coefficient of mass diffusivity Du=0.75 unless otherwise stated. Figures 2–9 illustrate velocity curves tailored to different fluid properties. Figure 2 portray the velocity contour for different consequences of M. The graph shows that enhancing the magnetic value M mitigates the fluid velocity. The drop in fluid velocity is caused by the magnetic pull acting in the regular course of the flow of the fluid, creating aversion amongst fluid particles. For a conductive fluid, such aversion or resistance works as a drag or a form of "magnetic stiffness" that hinders fluid movement. As it turns out, fluid particles are subjected to extra constraints which tend to impede their trajectory along the pathway of how it flows. This drop in velocity results in antagonism in the entire flow rate of the fluid. Figure 3 depicts the unique velocity trends for various values of Du. We found a decrease in the velocity gradient as Du was enriched. It happens because an upsurge in Du can modify the temperature and intensity domains of the fluid, producing disturbances in a fluid's density and viscosity pattern and, as a result, variations in the velocity descent.
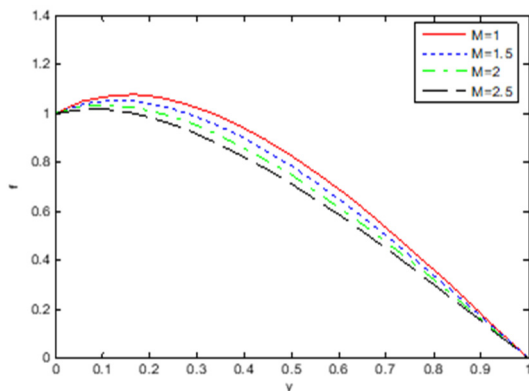

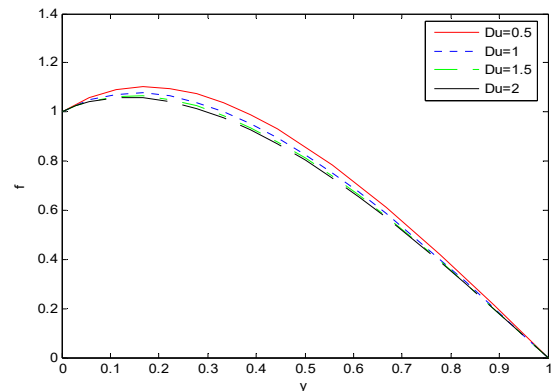**Figure 2.** Velocity outline for varied values of M

Figure 3. Velocity outline for varied values of Du

Figure 4 portrayed the attenuation character of the velocity curve with the growth of τ. The adverse impact of thermophoresis grows more corpulent as the thermophoretic coefficient elevates. As it turns out, the movement of the suspended objects in reaction to its temperature differential might impact the entire fluid motion and modify the velocity profile. This influence can cause changes in the velocity profile, resulting in higher velocities at certain regions within

the fluid. The influence of radiation heat exchange on fluid properties rises as the radiation attribute Ra grows. This can cause variations in the fluid's variation in temperature, which influences its density and fluidity. Changes in the two parameters can influence the fluid's behaviour and, as a result, the velocity distribution. Figure 5 evokes the manner in which the velocity pattern lessened as Ra climbed.

However, Figure 6 depicts the rising character of the velocity depiction when Gr is increased. While the Grashof number escalates, the fluid's motion shifts from being regulated due to viscous pressure to having prevailed by buoyant factors. It culminates in an enormous boost in velocity portrayal. Figure 7 illustrates the developing nature of velocity portrait with the growth of solutal Grashof number (Gm).
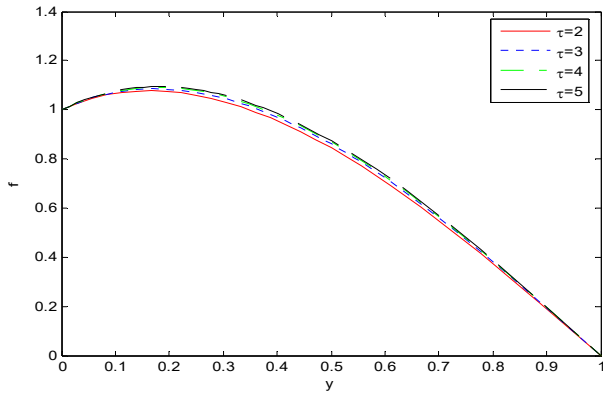
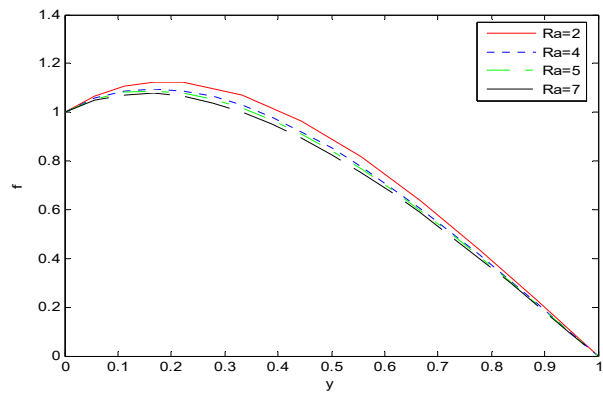

Figure 4. Velocity outline for varied values of τ

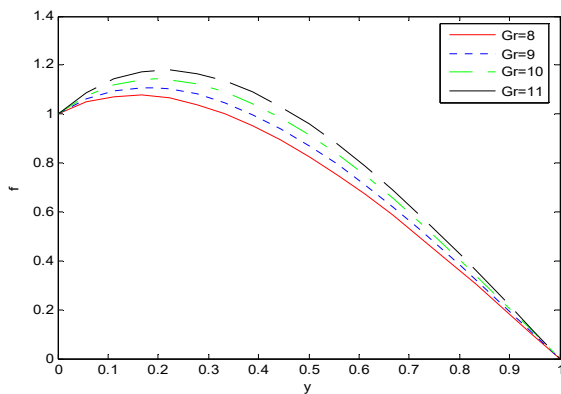**Figure 5.** Velocity outline for varied values of Ra

Figure 6. Velocity outline for varied values of Gr
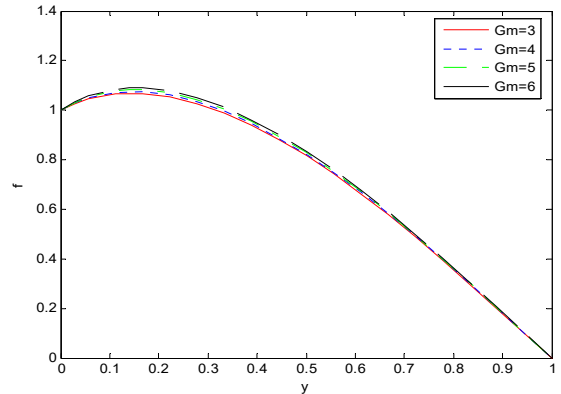

Figure 7. Velocity outline for varied values of Gm

Figure 8 delineates the velocity profile with the variation of Chemical reaction parameter (K). It has been seen that with the increasing of K, velocity decline. Figure 9 shows decreasing profile of velocity for increasing values of Prandtl number (Pr). It is displayed that high Prandtl number (Pr) values prompt the momentum boundary layer size to shrink, which minimizes velocity. Figure 10 demonstrates that with the hike of Schmidt number (Sc), velocity declined. Since the Schmidt number (Sc) indicates the relationship between molecular diffusivity and kinematic viscosity, velocity decreases as a result of this characteristic.
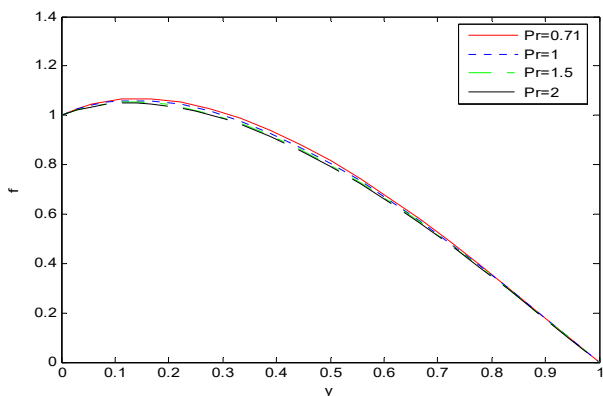

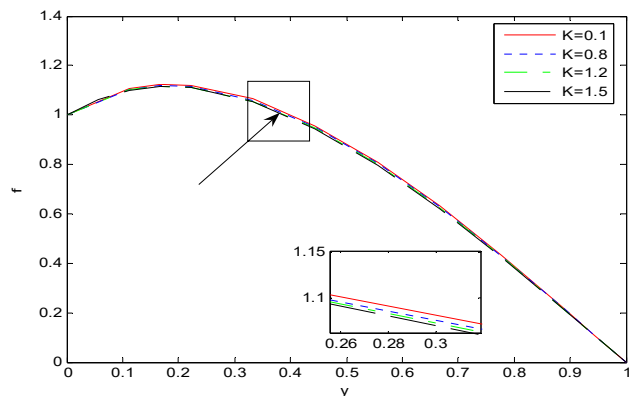**Figure 8.** Velocity outline for varied values of Pr

Figure 9. Velocity outline for varied values of K

Figures 11-16 depict a variety of temperature applicants suited to different characteristics of fluids. A rise through the thermophoretic coefficient τ promotes the motion of particles down the temperature variation. This transfer of energy

can cause particles to accumulate in colder areas inside the fluid, thereby pulling heat aside from such regions. As this happens, the entire temperature gradient in locations where the particle buildup occurs is susceptible to decreases as seen in Figure 11.

The importance of radiation conveyance of heat grows with Ra. The impact of radiation exchange entails the transmission of energy by waves of electromagnetic radiation. The moment radiation develops more prevalent in all aspects of the heat transfer mechanism, the temperature gradient may fall, and this can be seen in Figure 12. The Dufour phenomenon is related to mass dispersion caused by a temperature distinctive in a fluid. In other acronyms, it encompasses an occurrence in which variations in temperature affect. The moment the Dufour effect gets large, it potentially impacts the whole heat transmission process as well. Figure 13 explains that phenomenon.
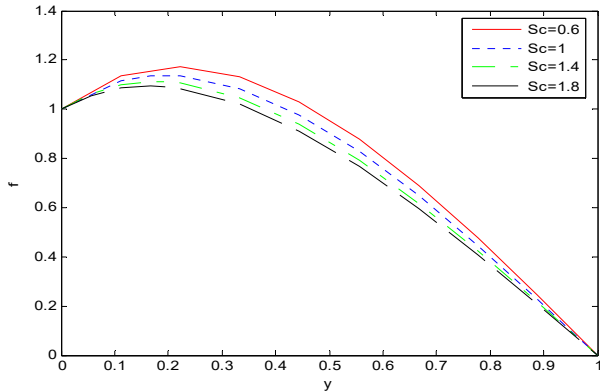

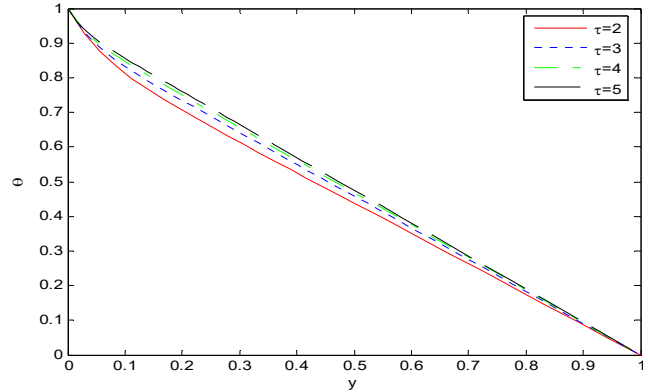**Figure 10.** Velocity outline for varied values of Sc

Figure 11. Temperature outline for varied values of τ
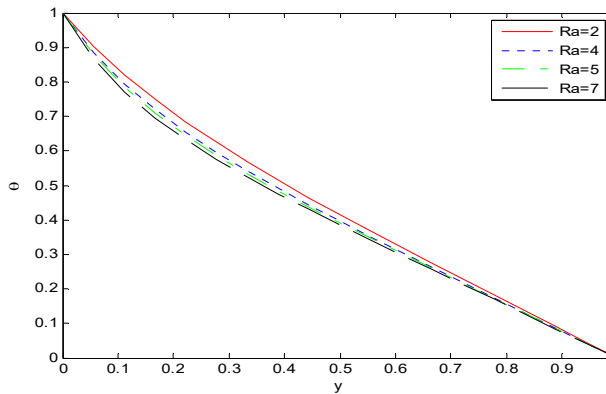
Figure 12. Temperature outline for varied values of Ra
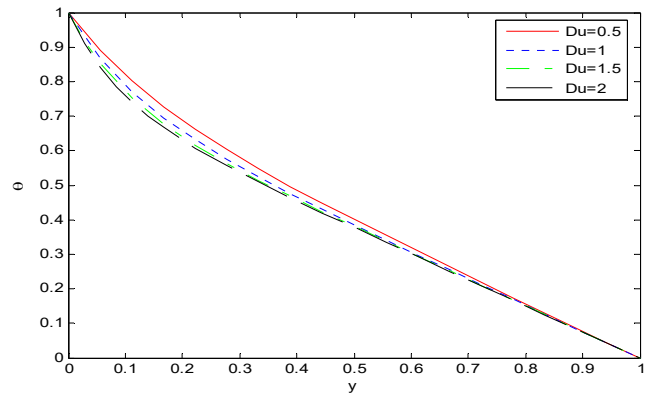
Figure 13. Temperature outline for varied values of Du

The Prandtl number serves as an unrestricted one that describes the relationship between a fluid's viscosity during motion to its thermal diffusion coefficient. It denotes the magnitude of the difference between the momentum propagation vs thermal propagation in a fluid's flow. When weighed against thermal diffusion, a greater Prandtl value suggests that momentum propagation is less important. In fluid motion conditions, especially through an opaque surface's interface layer, a greater Prandtl number might result in a lower temperature gradient as shown in Figure 14 owing to higher diffusion of heat than Momentum diffusion. It has also notice that with the enhanced of Chemical reaction parameter (K), temperature profile declined (Figure 15).

Figure 14. Temperature outline for varied values of Pr

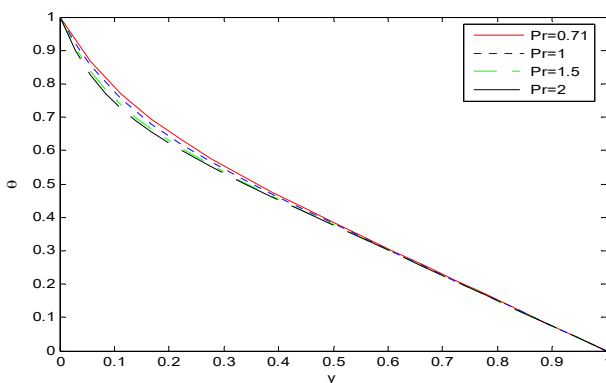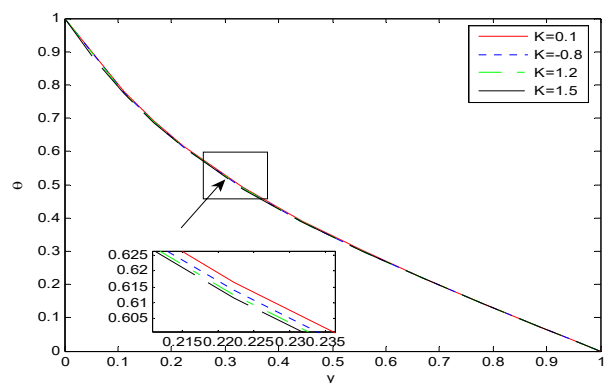**Figure 15.** Temperature outline for varied values of K

A diminishing profile of temperature profile has been seen for the enhancement of Schmidt number (Sc) which is described in Figure 16. Figures 17–21 depict varying concentration patterns. The figure demonstrates that as, τ, K, and Du increase, the concentration profiles decrease in rates. The variation in temperature reduces owing to the reduced effectiveness of the wall's heat source, and this brings the concentration of the separation layer adjacent to the surface of the wall and so causes the distribution of concentration to diminish.

The acquisition of a chemical reaction factor is capable of having a considerable impact on the profile of concentration in a fluid motion. Figure 18 exhibits a downward shift in the concentration profile when the chemical reaction factor is increased. When the thermophoretic coefficient is increased, the thermophoretic pressure grows, forcing particles to disperse more forcefully toward cooler places. As a consequence, the distribution of concentrations falls as the thermophoretic characteristics increase, as particles aggregate in the cooler parts of the fluid flow, as seen in Figure 17.
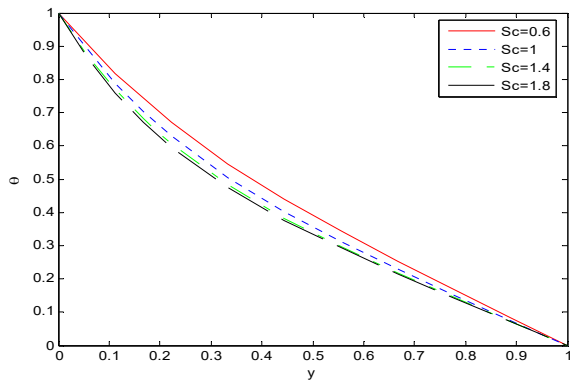
Figure 16. Temperature outline for varied values of Sc
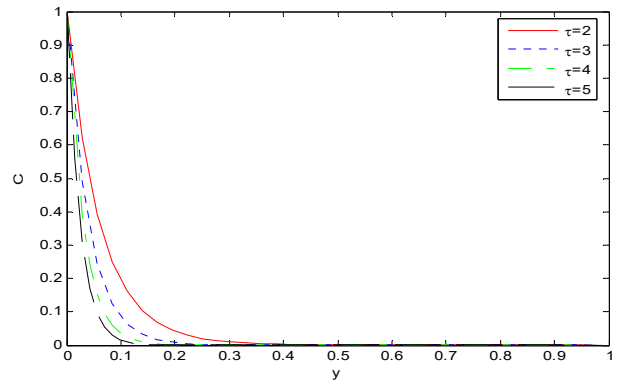
Figure 17. Concentration outline for varied values of τ

Figure 19 makes it apparent that as the Dufour number (Du) rises, the concentration falls. Whenever the Dufour number increases, there is a reduction in the temperature disparity between the fluid and the boundary layer. This ends up resulting in an increases transport of heat if the fluid, which in turn influences its viscosity. As a result, the concentration profile gets flatter.
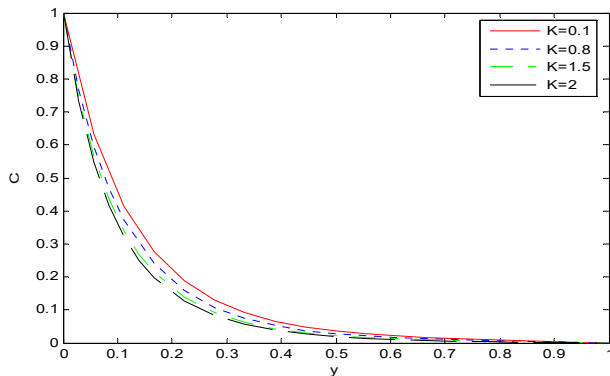
Figure 18. Concentration outline for varied values of K
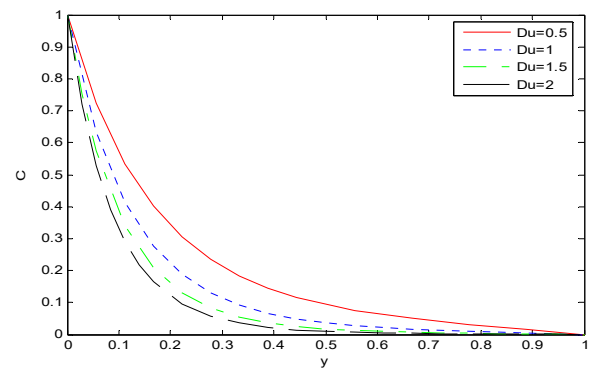
Figure 19. Concentration outline for varied values of Du

Figure 20 shows with the rise of radiation parameter (Ra), Concentration decline. Figure 21 reveals that as Schmidt number (Sc) grows the fluid concentration declines. In actually, the mass diffusivity of the fluid diminishes with increasing Sc, which in consequence lessens in fluid particle concentration.
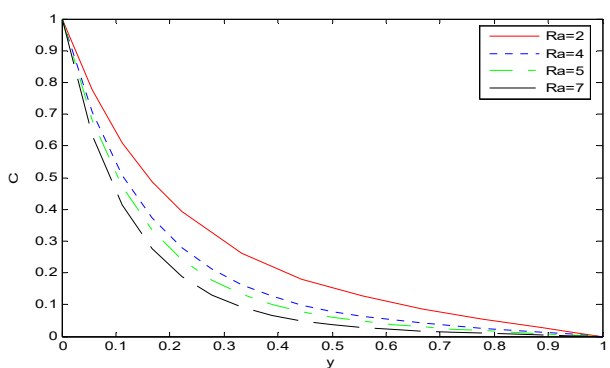
Figure 20. Concentration outline for varied values of Ra

Figure 21. Concentration outline for varied values of Sc

Tables 2,3, and 4 highlight different values of Shearing stress, Nusselt number, and Sherwood number based on various flow attributes. Table 2 shows that shearing stress decreases with increasing magnetic field number, radiation parameter, Prandtl number, Schmidt number and chemical reaction factor but increases with increasing thermophoresis number, Thermal Grashof number and Solutal Grashof number respectively. Table 3 illustrates that the Nusselt number lowers with radiation, Prandtl number and the Dufour effect, but it enhanced for Thermophoretic parameter, Chemical reaction parameter and Schmidt number. Similarly, the Sherwood number enhances with thermophoresis parameter, Grashof number for heat transfer, Prandtl number, chemical reaction parameter and Schmidt number, as seen in Table 4.
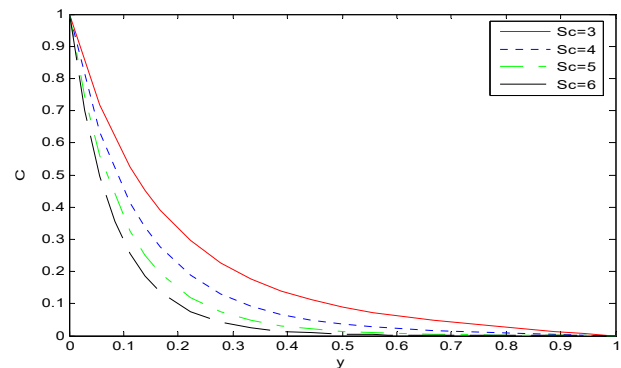
Table 2. Shearing stress for different flow parameters

Gr	Gm	M	Pr	K	Sc	Ra	Du	τ	Shearing stress(σ)	
8	3	1	0.71	0.1	0.6	7	0.75	2	1.1036	
		1.5							0.8963	↓
		2							0.706	
		2.5							0.579	
8	3	1	0.71	0.1	0.6	7	0.75	2	1.1036	
								3	1.1408	↑
								4	1.1844	
								5	1.2343	
8	3	1	0.71	0.1	0.6	7	0.75	2	1.2656	
				0.8					1.1622	↓
				1.2					1.0939	
				1.5					1.0285	
8	3	1	0.71	0.1	0.6	2	0.75	2	1.3710	
						4			1.1885	↓
						5			1.1331	
						7			1.0555	
8	3	1	0.71	0.1	0.6	7	0.75	2	1.0555	
9									1.3150	↑
10									1.5745	
11									1.8341	
8	3	1	0.71	0.1	0.6	7	0.75	2	1.0555	
			1						0.9845	↓
			1.5						0.9131	
			2						0.8704	
8	3	1	0.71	0.1	0.6	7	0.75	2	1.0555	
	4								1.1530	↑
	5								1.2506	
	6								1.3481	
8	3	1	0.71	0.1	0.6	7	0.75	2	1.7413	
					1				1.5361	↓
					1.4				1.3781	
					1.8				1.2622	

Table 3. Nusselt Number for different flow Parameters

Gr	Gm	M	Pr	K	Sc	Ra	Du	τ	Nusselt no. (Nu)	
8	3	1	0.71	0.1	0.6	2	0.75	2	1.4581	
						4			1.2702	↓
						5			1.2108	
						7			1.1258	
8	3	1	0.71	0.1	0.6	7	0.5	2	1.1909	
							0.75		1.1365	↓
							1		1.1036	
							1.35		1.0739	
8	3	1	0.71	0.1	0.6	7	0.75	2	2.3758	
				0.8					2.4179	↑
				1.2					2.4409	
				1.5					2.4576	
8	3	1	0.71	0.1	0.6	7	0.75	2	1.5299	
			1						1.5098	↓
			1.5						1.4642	
			2						1.4138	

Gr	Gm	M	Pr	K	Sc	Ra	Du	τ	Nusselt no. (Nu)	
8	3	1	0.71	0.1	0.6	7	0.75	2	1.8423	↑
					1				2.2295	
					1.4				2.2514	
					1.8				2.7164	
8	3	1	0.71	0.1	0.6	7	0.75	2	2.3758	↑
								3	2.7037	
								4	2.9071	
								5	3.0374	

Table 4. Sherwood number for different flow Parameters

Gr	Gm	M	Pr	K	Sc	Ra	Du	τ	Sherwood no. (Sh)	
8	3	1	0.71	0.1	0.6	7	0.75	2	1.2036	↑
								3	1.308	
								4	1.4544	
								5	1.5443	
8	3	1	0.71	0.1	0.6	7	0.75	2	1.1036	↑
9									1.3846	
10									1.6657	
11									1.9467	
8	3	1	0.71	0.1	0.6	7	0.75	2	1.1258	↑
			1						1.6664	
			1.5						1.9856	
			2						2.1549	
8	3	1	0.71	0.1	0.6	7	0.75	2	1.1258	↑
				0.8					2.1599	
				1.2					2.1707	
				1.5					2.2435	
8	3	1	0.71	0.1	0.6	7	0.75	2	1.5245	↑
					1				1.6492	
					1.4				2.5037	
					1.8				3.0886	

CONCLUSIONS

The effects of both concentration and temperature variations, thermophoresis along with a chemical reaction, and the significance of an applied extraneous electromagnetic field on the transmission of heat and mass over a heat-generating fluid are modeled as combined nonlinear situations with optimal boundary constraints. The aforementioned key points emerge based on the foregoing inquiry:

- Oscillating motions of the flow specifications cause the motion, temperature, and concentration domains in the motion of the fluid area to resemble radiation.
- Fluid mobility is slowed by the magnetic field influence, Dufour number, radiation, Chemical reaction parameter, Prandtl number and Schmidt number parameter applications, but it is accelerated by thermophoretic effect, thermal Grashof number and solutal Grashof number.
- The thermophoretic factor slows down the fluid's temperature, although the Prandtl number, the chemical reaction component, and mass diffusivity accelerate it.
- Fluid concentration diminishes with the growth of thermophoretic parameter, Chemical reaction parameter, Dufour number, radiation parameter and Schmidt number accordingly.
- The intensity of the drag force against a specific flow parameter has an effectible impression under the constraints of the various fluid specifications.
- The Sherwood number shows an increasing pattern under the repercussion of thermophoretic parameter, Thermal Grashof number, Prandtl number, chemical reaction parameter and Schmidt number respectively, but the Nusselt number slows down with elevated radiation parameter, Dufour effect and Prandtl number. Also, the Nusselt's number has increasing trend with the rises of chemical reaction parameter, Schmidt number and thermophoretic parameter.
- Shearing stress diminishes with rising magnetic, Chemical reaction, radiation and chemical reaction variation. Also, it diminishes with the enhancement of Prandtl and Schmidt number. But reverse nature is observed in the cases of thermophoretic parameter and both for Grashof number for heat as well as mass transfer.

FUTURE SCOPE

Other numerical techniques have also been used to solve this problem. The strategy for solving this problem can be employing to other complex geometrical arrangements. One could extend this problem to cover a wide range of non-

Newtonian models. Several important physical properties can be undertaken and their repercussions on the flow fluid spotted. There is an abundance of unrealized research potential as a result.

Nomenclature

$\bar{u}$ and $\bar{v}$ are the corresponding velocity of the fluid motion indices toward and tangential to the plate

g	acceleration due to gravity	k_T	thermal conductivity
β	heat transmission amount of volume growth	C_p	specific heat at persistent pressure
$\bar{\beta}$	amount of extension with species heat at persistent pressure	ν	kinematic viscosity
$\bar{T}$	fluid temperature	σ	thermal conductivity
T_∞	far field temperature	C_s	amount mass diffusivity
$\bar{C}$	species concentration	κ	is the thermal conductivity
C_∞	far field concentration	D	chemical molecular diffusivity
ρ	fluid density	D_m	concentration susceptibility
		k_r	rate of chemical reaction

ORCID

Ashik Hussain Mirza, https://orcid.org/0009-0001-2767-2777; **Bamdeb Dey,** https://orcid.org/0000-0002-9002-676X

REFERENCES

[1] M.B. Riaz, M. Asgir, A.A. Zafar, and S. Yao, "Combined effects of heat and mass transfer on MHD free convective flow of Maxwell fluid with variable temperature and concentration," Mathematical Problems in Engineering, **2021**, 1-36, (2021). https://doi.org/10.1155/2021/6641835

[2] R.D. Ene, N. Pop, and R. Badarau, "Heat and Mass Transfer Analysis for the Viscous Fluid Flow: Dual Approximate Solutions," Mathematics, **11**(7), 16-48 (2023). https://doi.org/10.3390/math11071648

[3] I.H. Qureshi, M. Nawaz, M.A. Abdel-Sattar, S. Aly, and M. Awais, "Numerical study of heat and mass transfer in MHD flow of nanofluid in a porous medium with Soret and Dufour effects," Heat Transfer, **50**(5), 4501-4515 (2021). https://doi.org/10.1002/htj.22085

[4] E.O. Fatunmbi, and A. Adeniyan, "Heat and mass transfer in MHD micropolar fluid flow over a stretching sheet with velocity and thermal slip conditions," Open Journal of Fluid Dynamics, **8**, 195-215 (2018). https://doi.org/10.4236/ojfd.2018.82014

[5] J.E. Salhi, K. Amghar, H. Bouali, and N. Salhi, "Combined heat and mass transfer of fluid flowing through horizontal channel by turbulent forced convection," Modelling and Simulation in Engineering, **2020**, 1-11 (2020). https://doi.org/10.1155/2020/1453893

[6] B.G. Agaie, S. Isa, A.S.A. Mai'anguwa, and A.S. Magaji, "Heat and mass transfer of MHD for an unsteady viscous oscillatory flow," Science World Journal, 16(2), 138-144 (2021). https://www.ajol.info/index.php/swj/article/view/212378/200285

[7] G.P. Vanitha, U.S. Mahabaleshwar, M. Hatami, and X. Yang, "Heat and mass transfer of micropolar liquid flow due to porous stretching/shrinking surface with ternary nanoparticles," Sci. Rep. **13**(1), 3011 (2023). https://doi.org/10.1038/s41598-023-29469-0

[8] B. Dey, J.M. Nath, T.K. Das, and D. Kalita, "Simulation of transmission of heat on viscous fluid flow with varying temperatures over a flat plate," JP Journal of Heat and Mass Transfer, **30**, 1-18 (2022). https://doi.org/10.17654/0973576322052

[9] B. Dey, and R. Choudhury, "Slip Effects on Heat and Mass Transfer in MHD Visco-Elastic Fluid Flow Through a Porous Channel," in: *Emerging Technologies in Data Mining and Information Security: Proceedings of IEMIS 2018*, vol. 1, (Springer Singapore, 2019). pp. 553-564. https://doi.org/10.1007/978-981-13-1951-8_50

[10] R. Kandasamy, K.K.S. Prabhu, and R. Periasamy, "Effects of chemical reaction, heat and mass transfer along a wedge with heat source and concentration in the presence of suction or injection," Int. J. Heat Mass Transfer, **48**, 1388-1396 (2005). https://doi.org/10.1016/j.ijheatmasstransfer.2004.10.008

[11] R. Choudhury, and B. Dey, "Unsteady Thermal Radiation Effects on MHD Convective Slip Flow of Visco-Elastic Fluid Past a Porous Plate Embedded in Porous Medium," International journal of applied mathematics and statistics, **57**(2), 215-226 (2018). http://www.ceser.in/ceserp/index.php/ijamas/article/view/5384/5439

[12] K.V.S. Raju, T.S. Reddy, M.C. Raju, P.V.S. Narayana, and S. Venkataramana, "MHD Convective flow through porous medium in a horizontal channel with insulated and impermeable bottom Walls in the presence of viscous dissipation and joule heating," Ain Shams Engineering Journal, **5**, 543-551 (2014). https://doi.org/10.1016/j.asej.2013.10.007

[13] B.K. Kalita, R. Choudhury, and P. Dhar, "Elucidation of MHD Boundary Layer Flow past a plate with Viscous Dissipation," International Journal of Engineering Research and Technology, **13**, 3321-3327 (2020). https://dx.doi.org/10.37624/IJERT/13.11.2020.3321-3327

[14] S. Das, R.N. Jana, and O.D. Makinde, "Magnetohydrodynamic mixed convective slip flow over an inclined porous plate with viscous dissipation and Joule heating," Alexandria Engineering Journal, **54**(2), 251-261 (2015). https://doi.org/10.1016/j.aej.2015.03.003

[15] B. Mahanthesh, B.J. Gireesha, R.S. Gorla, and O.D. Makinde, "Magnetohydrodynamic three-dimensional flow of nanofluids with slip and thermal radiation over a nonlinear stretching sheet: a numerical study," Neural Computing and Applications, **30**, 1557-1567 (2018). https://doi.org/10.1007/s00521-016-2742-5

[16] Y.P. Lv, N. Shaheen, M. Ramzan, M. Mursaleen, K.S. Nisar, and M.Y. Malik, "Chemical reaction and thermal radiation impact on a nanofluid flow in a rotating channel with Hall current," Scientific Reports, **11**(1), 19-47 (2021). https://doi.org/10.1038/s41598-021-99214-y

[17] A.M. Sedki, "Effect of thermal radiation and chemical reaction on MHD mixed convective heat and mass transfer in nanofluid flow due to nonlinear stretching surface," Results in Materials, **16**, 100334 (2022). https://doi.org/10.1016/j.rinma.2022.100334

[18] N.N.W. Khalili, A.A. Samson, A.S.A. Aziz, and Z.M. Ali, "Chemical reaction and radiation effects on MHD flow past an exponentially stretching sheet with heat sink," Journal of Physics: Conference Series, **890**(1), 12-25 (2017). https://doi.org/10.1088/1742-6596/890/1/012025

[19] D.J. Samuel, and I.A. Fayemi, "Impacts of variable viscosity and chemical reaction on Ohmic dissipative fluid flow in a porous medium over a stretching sheet with thermal radiation," Heat Transfer, **52**, 5022-5040 (2023). https://doi.org/10.1002/htj.22915

[20] S.A.G. A. Shah, A. Hassan, H. Karamti, A. Alhushaybari, S.M. Eldin, and A. M. Galal, "Effect of thermal radiation on convective heat transfer in MHD boundary layer Carreau fluid with chemical reaction," Scientific Reports, **13**(1), 4117 (2023). https://doi.org/10.1038/s41598-023-31151-4

[21] E. Seid, E. Haile, and T. Walelign, "Multiple slip, Soret and Dufour effects in fluid flow near a vertical stretching sheet in the presence of magnetic nanoparticles," International Journal of Thermofluids, **13**, 100136 (2022). https://doi.org/10.1016/j.ijft.2022.100136

[22] M. Hasanuzzaman, M.A.K. Azad, and M.M. Hossain, "Effects of Dufour and thermal diffusion on unsteady MHD free convection and mass transfer flow through an infinite vertical permeable sheet," SN Applied Sciences, **3**(12), 882 (2021). https://doi.org/10.1007/s42452-021-04842-8

[23] I. Filahi, M. Bourich, M. Hasnaoui, and A. Amahmid, "Analytical and numerical study of Soret and Dufour effects on thermosolutal convection in a horizontal Brinkman porous layer with a stress-free upper boundary," Mathematical Problems in Engineering, **2020**, 1-17 (2020). https://doi.org/10.1155/2020/4046570

[24] N.A. Shah, S.J. Yook, and O. Tosin, "Analytic simulation of thermophoretic second grade fluid flow past a vertical surface with variable fluid characteristics and convective heating," Scientific Reports, **12**(1), 5445 (2022). https://doi.org/10.1038/s41598-022-09301-x

[25] F. Mabood, M. D. Shamshuddin, and S. R. Mishra, "Characteristics of thermophoresis and Brownian motion on radiative reactive micropolar fluid flow towards continuously moving flat plate: HAM solution," Mathematics and Computers in Simulation, **191**, 187-202 (2022). https://doi.org/10.1016/j.matcom.2021.08.004

[26] J.V. Tawade, C.N. Guled, S. Noeiaghdam, U. Fernandez-Gamiz, V. Govindan, and S. Balamuralitharan, "Effects of thermophoresis and Brownian motion for thermal and chemically reacting Casson nanofluid flow over a linearly stretching sheet," Results in Engineering, **15**, 100448 (2022). https://doi.org/10.1016/j.rineng.2022.100448

[27] B.K. Jha, and H.N. Sani, "Role of thermophoresis on unsteady/steady mixed convective flow in a vertical channel having convective boundary conditions," SN Applied Sciences, **4**(4), 131 (2022). https://doi.org/10.1007/s42452-022-04971-8

[28] H.P. Mondal, and D.S. Chatterjee, "Thermophoresis and Soret-Dufour on MHD mixed convection mass transfer over an inclined plate with non-uniform heat source/sink and chemical reaction," Ain Shams Engineering Journal, **9**, 2111-2121 (2018). https://doi.org/10.1016/j.asej.2016.10.015

[29] P.S. Reddy, and J.C. Ali, "Soret and Dufour effects on MHD heat and mass transfer flow of micropolar fluid with thermophoresis," Journal of Naval Architecture and Marine Engineering, **13**(1), 39–50 (2016). https://doi.org/10.3329/jname.v13i1.23974

[30] F. Hussain, A. Hussain, and S. Nadeem, "Thermophoresis and Brownian model of pseudo-plastic nanofluid flow over a vertical slender cylinder," Mathematical Problems in Engineering, **2020**, 1-10 (2020). https://doi.org/10.1155/2020/8428762

[31] B. Deka, and R. Choudhury, "Impact of thermophoretic MHD Visco-elastic fluid flow past a wedge with heat source and chemical reaction," in: *Proceedings of IEMIS*, vol. 1, edited by A. Abraham, P. Dutta, J. Mandal, A. Bhattacharya, and S. Dutta, (Springer, Singapore, 2018), pp. 541-552. https://doi.org/10.1007/978-981-13-1951-8_49;

[32] R. Choudhury, and P. Dhar, "Diffusion Thermo effects of visco-elastic fluid past a porous surface in presence of magnetic field and radiation," International Journal of Innovative Research in Science, Engineering and Technology, **2**(3), (2013). https://www.ijirset.com/upload/march/45_DIFFUSION%20THERMO.pdf

[33] H. Upreti, A.K. Pandey, S.K. Rawat, and M. Kumar, "Modified Arrhenius and thermal radiation effects on three-dimensional magnetohydrodynamic flow of carbon nanotubes over bi-directional stretchable surface," Journal of Nanofluids, **10**(4), 538-551 (2021). https://doi.org/10.1166/jon.2021.1804

[34] J.B. Young, "Thermophoresis of a spherical particle: reassessment, clarification, and new analysis," Aerosol Science and Technology, **45**(8), 927-948 (2011). https://doi.org/10.1080/02786826.2011.569777

[35] Dey, B., Dukru, D., Das, T. K., & Nath, J. M. (2024). Modelling and Simulating the Heat Transference in Casson EMHD Fluid Motion Exacerbated by A Flat Plate with Radiant Heat and Ohmic Heating. East European Journal of Physics, (2), 172-180. https://doi.org/10.26565/2312-4334-2024-2-16

[36] B. Dey, B. Kalita, and R. Choudhury, "Radiation and Chemical reaction effects on unsteady viscoelastic fluid flow through porous medium," Frontiers in Heat and Mass Transfer (FHMT), **18**, 1-8 (2022). https://doi.org/10.5098/hmt.18.32

[37] A.H. Mirza, B. Dey, and R. Choudhury, "The detrimental effect of thermal exposure and thermophoresis on MHD flow with combined mass and heat transmission employing permeability," International Journal of Applied Mechanics and Engineering, **29**(1), 90-104 (2024). https://doi.org/10.59441/ijame/181556

[38] Shampine, Lawrence F., Jacek Kierzenka, and Mark W. Reichelt. "Solving boundary value problems for ordinary differential equations in MATLAB with bvp4c." Tutorial notes 2000 (2000): 1-27.

[39] S. Ahmed, "Study of thermal radiation and ohmic heating for steady magnetohydrodynamics natural convection boundary layer flow in a saturated porous regime," International Journal on Recent and Innovation Trends in Computing and Communication, **2**(9), 2796-2801 (2014). https://core.ac.uk/download/pdf/539907531.pdf

ВПЛИВ ТЕПЛОМАСОПЕРЕНОСУ НА МГД ЦИРКУЛЯЦІЮ РІДИНИ В ПОЄДНАННІ З ВЕРТИКАЛЬНОЮ ПОВЕРХНЕЮ ПРИ ВИНИКНЕННІ РАДІАЦІЙНОГО ТЕРМОФОРЕЗУ ТА РЕПЕРКУСІЇ ДЮФУРА

Ашик Хуссейн Мірза[a], Бамдеб Дей[b], Ріта Чоудхарі[c]
[a]Кафедра математики, Д.Р. Коледж, Голагат - 785621, Ассам, Індія
[b]Департамент математики, Університет Дона Боско в Ассамі, Гувахаті-781017, Ассам, Індія
[c]Департамент математики, Університет Гаухаті, Гувахаті- 781014, Ассам, Індія

Поточне дослідження моделює модель передачі маси та теплової енергії на МГД-потоці рідини за умов відхилення концентрації та температури на двовимірній в'язкій рідині вздовж вертикальної грані. Після оцінки граничного шару, математичного моделювання руху рідин, перенесення тепла та маси під дією випромінювання, термофорезу та реперкусії Дюфура генерується як набір диференціальних рівнянь у похідних. Було оцінено пружне всмоктування поверхні. Вбудований вирішувач bvp4c в MATLAB використовується для чисельного налагодження вищезгаданих моделей. За допомогою візуалізації та таблиць досліджується шкідливий вплив змінних на швидкість, температуру, а також градієнти концентрації в поєднанні з тертям шкіри, числом Нуссельта та числом Шервуда. Чудова узгодженість може бути продемонстрована при порівнянні між найсучаснішими висновками та тими, які раніше були доступні в літературі за конкретних обмежених обставин. Ефект Дюфура, випромінювання, термофорез і число Грасгофа – це всі фактори, які впливають на рух рідини та передачу тепла на межовому шарі бруду. Крім того, розраховуються зміни напруги зсуву, числа Нуссельта та коефіцієнта числа Шервуда. Отримані результати мають вирішальне значення для оптимізації різноманітних технологій і систем на основі рідини, що дозволяє розвивати низку галузей, включаючи енергоефективність, охолодження електроніки, медичне управління та багато іншого.
Ключові слова: *хімічна реакція; ефект Дюфура; теплопередача; масообмін; випромінювання; термофорез*

EFFECTS OF THERMAL AND MASS STRATIFICATION ON UNSTEADY MHD FLOW PAST AN OSCILLATING VERTICAL PLATE EMBEDDED IN A POROUS MEDIUM WITH VARIABLE SURFACE CONDITIONS

[ID] **Pappu Das**[*], [ID] **Rudra Kanta Deka**

Department of Mathematics, Gauhati University, Guwahati-781014, Assam, India
[*]Corresponding Author e-mail: pappudas751@gmail.com

Investigations have been made into how thermal and mass stratification affect the magnetohydrodynamic flow past a plate which is oscillating vertically in its own axis in which it is embedded in a porous medium with variable heat and mass diffusion. For concentration, temperature and velocity fields, the non-dimensional governing equations are solved using the Laplace transform method for the unitary Prandtl and Schmidt numbers, when the plate is oscillating in its own plane harmonically. Numerical computations are carried out and presented in graphs for different physical parameters like thermal Grashof number, phase angle, mass Grashof number, stratification parameter and time on concentration, velocity, temperature, plate heat flux, mass flux and skin friction. The findings of this study can be utilized to enhance comprehension of MHD flow on vertical oscillating plate in combined stratified environments. Significant findings arising from the mass and thermal stratification are compared to the scenario in which stratification is absent.

Keywords: *MHD flow; Oscillating plate; Electrically conducting fluid; Unsteady flow; Thermal stratification; Mass stratification; Porous medium*

PACS: 44.05.+e, 47.11.-j, 47.55.P-, 47.56.+r, 47.65.-d

1. INTRODUCTION

When two types of stream with different temperatures come into contact, thermal stratification happens. A colder, denser layer is covered by a warmer, less dense layer in a process known as thermal stratification of fluid, which occurs naturally at higher temperatures. It happens mostly as a result of changes in temperature, concentration, or the presence of various fluids with differing densities. Between cold and hot fluid zones, this natural mechanism produces a temperature gradient transition zone. Because of its numerous widespread applications in a variety of industrial, engineering, and environmental applications, the dynamics of thermally stratified fluid has recently caught the attention of researchers and emerged as an important area for scientific inquiry. Engineering problems like electromagnetic casting, liquid-metal cooling of nuclear reactors, and plasma confinement are all related to magnetohydrodynamic flow.

MHD flow under thermal and mass stratification effects have been a topic of great interest for the last three decades. Many authors have been studied MHD flow past vertical plates and cylinders with stratification effects. Some of the authors are Soundalgekar *et. al.* [1], Park and Hyun [2], Das *et. al.* [3]. Natural convection of a viscous stratified fluid in one dimension was studied by Park and Hyun [2] and Park [4]. Shapiro and Fedorovich [5] studied thermally stratified fluid flows through vertical plates and cylinders under various surface conditions and by include the stratification parameter in the energy equation, they have recently improved the classical theory of one-dimensional flow. In contrast with using the similarity transformation method, Magyari *et. al.* [6] investigated the unstable free convection flow along an infinite vertical flat plate embedded in a stably stratified fluid-saturated porous media. [7] and [9] investigated the effects of thermal and mass stratification in non-Newtonian fluid saturated porous media along a vertical wavy truncated cone and a vertical wavy surface respectively. [8] came up with an analytical solution of MHD heat and mass diffusion flow by natural convection past a surface embedded in a porous medium. Analytical solution for unsteady natural convection flow past an accelerated vertical plate in a thermally stratified fluid was given by [10]. Under MHD conditions, the impact of a thermally stratified ambient fluid along a moving non-isothermal vertical plate was examined by [11]. [12] studied how a transverse magnetic field effects the flow of a convectively driven flow immersed in a fluid with stable stratification along an infinite vertical plate. [13] investigated the radiative flow past an exponentially accelerated vertical plate with variable temperature and mass diffusion. Under MHD free convection the effects of chemical reaction and and radiation was studied by [14] when the flow past an exponentially accelerated vertical plate with variable temperature and variable mass diffusion. Effects of thermal and mass stratification on convectively driven flow past an infinite moving vertical cylinder was studied by [15]. [16] came up with the closed form solution of thermal and mass stratification effects on unsteady flow past an accelerated infinite vertical plate with variable temperature and exponential mass diffusion in porous medium. The effects of thermal and mass stratification on unsteady parabolic flow past an infinite vertical plate with exponential decaying temperature and variable mass diffusion in porous medium was studied by [17]. [18] conducted research on thermal and mass stratification effects on MHD nanofluid past an exponentially accelerated vertical plate through a porous medium

with thermal radiation and heat source. Theoretical study of thermal and mass stratification effects on MHD nanofluid past an exponentially accelerated vertical plate in a porous medium in presence of heat source, thermal radiation and chemical reaction were done by [19]. [20] and [21] came up with the solutions of thermal and mass stratification impacts on unsteady MHD flow with different conditions. [22] looked at the influences of thermal stratification and chemical reaction on MHD free convective flow along an accelerated vertical plate with variable temperature and exponential mass diffusion in a porous medium.

In this article, we investigate the impacts of thermal and mass stratification on MHD flow through a plate which is oscillating vertically in its own axis and is embedded in a porous medium with variable surface conditions. In this case, the term known as pressure work is included in the thermodynamic energy equation, the consideration of thermal and mass stratification. For the unit Prandtl and Schmidt numbers the solutions are then obtained. The investigation on velocity, temperature and concentration profiles are made under the impacts of variables and displayed on graphs. These variables include the thermal Grashof number Gr, mass Grashof number Gc, magnetic parameter M, time t, permeability of the porous medium K and stratification parameters γ and ξ. On other physical phenomena including the rate of heat and mass transfer and skin friction, the effects of M, Gr, Gc, γ, ξ and t are also studied.
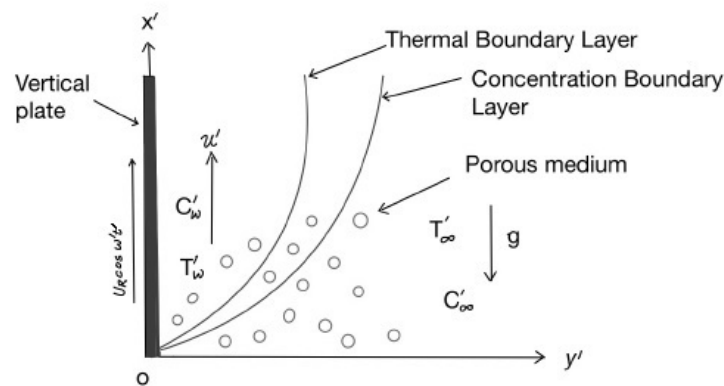

Figure 1. Physical Model and Coordinate System

2. MATHEMATICAL ANALYSIS

In our study an incompressible, viscous and electrically conducting fluid along an oscillating vertical plate that is embedded in a porous medium with variable surface conditions in two dimensional flow is examined. The plate is taken along the x'-axis, and the y'-axis is taken normal to it. At the beginning, the fluid and the plate have the same temperature T'_∞ and concentration C'_∞ throughout. The plate begins oscillating in its own plane at time t', moving with a velocity $U_R \cos \omega' t'$, the concentration level at the plate is raised to C'_w and the plate temperature is raised to T'_w. In order to ignore the induced magnetic field, a uniformly strong magnetic field is applied perpendicular to the plate with a modest magnetic Reynolds number. Following these conditions, the equations for motion, energy and concentration are represented using the Boussinesq's approximation as follows:

$$\frac{\partial u'}{\partial t'} = \nu \frac{\partial^2 u'}{\partial y'^2} + \left[g\beta(T' - T'_\infty) + g\beta_c(C' - C'_\infty) \right] - \frac{\sigma B_0^2 u'}{\rho} - \frac{\nu u'}{k'} \tag{1}$$

$$\frac{\partial T'}{\partial t'} = \frac{k}{\rho C_P} \frac{\partial^2 T'}{\partial y'^2} - \gamma' u' \tag{2}$$

$$\frac{\partial C'}{\partial t'} = D \frac{\partial^2 C'}{\partial y'^2} - \xi' u' \tag{3}$$

Considering the initial and boundary conditions as:

$$u' = 0, \quad T' = T'_\infty, \qquad C' = C'_\infty \qquad \forall \, y', t' \leq 0$$

$$u' = U_R \cos \omega' t', \qquad T' = T'_\infty + (T'_w - T'_\infty)At',$$

$$C' = C'_\infty + (C'_w - C'_\infty)At' \quad \text{at} \quad y' = 0, \quad t' > 0 \tag{4}$$

$$u' \to 0, \qquad T' \to T'_\infty, \qquad C' \to C'_\infty \quad \text{as} \quad y' \to \infty, \, t' > 0$$

Now, we introduce the following non-dimensional quantities:

$$y = \frac{y'}{L_R}, \quad t = \frac{t'}{t_R}, \quad u = \frac{u'}{U_R}, \quad Da = \frac{U_R^2 k'}{v^2}, \quad \omega = \omega' t_R, \quad Pr = \frac{\mu C_P}{k}$$

$$M = \frac{\sigma B_0^2 v}{\rho U_R^2}, \quad Sc = \frac{v}{D}, \quad \theta = \frac{T' - T'_\infty}{T'_w - T'_\infty}, \quad C = \frac{C' - C'_\infty}{C'_w - C'_\infty}, \quad \Delta T = T'_w - T'_\infty \tag{5}$$

$$Gc = \frac{v g \beta_c (C'_w - C'_\infty)}{U_R^3}, \quad U_R = (v g \beta \Delta T)^{1/3}, \quad L_R = \left(\frac{g \beta \Delta T}{v^2}\right)^{-1/3}, \quad A = \frac{1}{t_R},$$

$$t_R = (g \beta \Delta T)^{-2/3} v^{1/3}, \quad Gr = \frac{v g \beta (T'_w - T'_\infty)}{U_R^3}, \quad \gamma = \frac{\gamma' L_R}{\Delta T}, \quad \xi = \frac{\xi' L_R}{C' - C'_\infty}$$

The following forms are taken by equations (1), (2) and (3) when the non-dimensional quantities defined in (5) above are used,

$$\frac{\partial u}{\partial t} = \frac{\partial^2 u}{\partial y^2} + Gr\theta + GcC - \left(M + \frac{1}{Da}\right)u \tag{6}$$

$$\frac{\partial \theta}{\partial t} = \frac{1}{Pr}\frac{\partial^2 \theta}{\partial y^2} - \gamma u \tag{7}$$

$$\frac{\partial C}{\partial t} = \frac{1}{Sc}\frac{\partial^2 C}{\partial y^2} - \xi u \tag{8}$$

And the corresponding initial and boundary conditions (4) then reduce to,

$$u = 0, \quad \theta = 0, \quad C = 0 \quad \forall \, y, \, t \le 0$$

$$u = \cos \omega t, \quad \theta = t, \quad C = t \quad \text{at } y = 0, \, t > 0 \tag{9}$$

$$u \to 0, \quad \theta \to 0, \quad C \to 0 \quad \text{as } y \to \infty, \, t > 0$$

2.1. Method of Solution

With respect to the boundary conditions (9), the non-dimensional governing equations (6), (7), and (8) are solved using the Laplace transform technique for the tractable cases $Pr = 1$ and $Sc = 1$. The expression for velocity, temperature and concentration profiles are obtained with the help of [23] are as follows,

$$u = C_1\left[f_1(A, -i\omega) + f_1(A, i\omega)\right] - C_2\left[f_1(B, -i\omega) + f_1(B, i\omega)\right] - C_3\left[f_2(A) + f_2(B)\right] \tag{10}$$

$$\theta = t(1 + D_1 - D_2)\left\{\left(1 + \frac{y^2}{2t}\right)erfc\left(\frac{y}{2\sqrt{t}}\right) - \frac{ye^{-\frac{y^2}{4t}}}{\sqrt{\pi t}}\right\}$$

$$+ \frac{\gamma}{2(A-B)} \big[f_1(A,-i\omega) + f_1(A,i\omega) - f_1(B,-i\omega) - f_1(B,i\omega) \big] - \frac{D_1}{A} \big[B f_2(A) - A f_2(B) \big] \quad (11)$$

$$C = t\big(1 + E_1 - E_2\big) \left\{ \left(1 + \frac{y^2}{2t}\right) erfc\left(\frac{y}{2\sqrt{t}}\right) - \frac{y e^{-\frac{y^2}{4t}}}{\sqrt{\pi t}} \right\}$$

$$+ \frac{\xi}{2(A-B)} \big[f_1(A,-i\omega) + f_1(A,i\omega) - f_1(B,-i\omega) - f_1(B,i\omega) \big] - \frac{E_1}{A} \big[B f_2(A) - A f_2(B) \big] \quad (12)$$

For the sake of succinctness, our study refers to the situation where pressure work is omitted and the environment is isothermal ($\gamma = 0$, $\xi = 0$) as the classical scenario. The velocity (u^*), temperature (θ^*) and concentration (C^*) profiles for classical case are obtained as,

$$u^* \quad = \quad \frac{1}{2}\big[f_1(N,-i\omega) \quad + \quad f_1(N,i\omega) \big] \quad - \quad D_3 f_2(N) \quad + \quad tD_3 \left[\left(1 \quad + \quad \frac{y^2}{2t}\right) erfc\left(\frac{y}{2\sqrt{t}}\right) \quad - \quad \frac{y e^{-\frac{y^2}{4t}}}{\sqrt{\pi t}} \right] \quad (13)$$

$$\theta^* = t \left[\left(1 + \frac{y^2}{2t}\right) erfc\left(\frac{y}{2\sqrt{t}}\right) - \frac{y e^{-\frac{y^2}{4t}}}{\sqrt{\pi t}} \right] \quad (14)$$

$$C^* = t \left[\left(1 + \frac{y^2}{2t}\right) erfc\left(\frac{y}{2\sqrt{t}}\right) - \frac{y e^{-\frac{y^2}{4t}}}{\sqrt{\pi t}} \right] \quad (15)$$

where

$$N = M + \frac{1}{Da}, \quad A = \frac{N + \sqrt{N^2 - 4\gamma Gr - 4\xi Gc}}{2}, \quad B = \frac{N - \sqrt{N^2 - 4\gamma Gr - 4\xi Gc}}{2}, \quad C_1 = \frac{A}{2(A-B)},$$

$$C_2 = \frac{B}{2(A-B)}, \quad C_3 = \frac{Gr + Gc}{A - B}, \quad D_1 = \frac{\gamma(Gr + Gc)}{A(A-B)}, \quad D_2 = \frac{\gamma(Gr + Gc)}{B(A-B)}, \quad D_3 = \frac{Gr + Gc}{N},$$

$$E_1 = \frac{\xi(Gr + Gc)}{A(A-B)}, \quad E_2 = \frac{\xi(Gr + Gc)}{B(A-B)}, \quad E_3 = \frac{\gamma}{2(A-B)}, \quad E_4 = \frac{\xi}{2(A-B)}.$$

And f_i's are inverse Laplace transforms and are given by

$$f_1(A,i\omega) = L^{-1}\left\{ \frac{e^{-y\sqrt{s+A}}}{s + i\omega} \right\} \text{ and } f_2(A) = L^{-1}\left\{ \frac{e^{-y\sqrt{s+A}}}{s^2} \right\}$$

Using the formulas given by [19], we separate the complex arguments of the error function that were present in the preceding expressions into real and imaginary components.

2.2. Skin-Friction
The following provides non-dimensional computation of skin-friction of the plate:

$$\tau = -\frac{du}{dy}\bigg|_{y=0} \quad (16)$$

Now from equation (10) we get the expression for skin-friction as,

$$\tau = C_1 \left[e^{i\omega t}\left(\sqrt{A + i\omega}\right) erf\left(\sqrt{(A + i\omega)t}\right) + e^{-i\omega t}\left(\sqrt{A - i\omega}\right) erf\left(\sqrt{(A - i\omega)t}\right) + \frac{2e^{-At}}{\sqrt{\pi t}} \right] -$$

$$C_2\left[e^{i\omega t}\left(\sqrt{B+i\omega}\right)erf\left(\sqrt{(B+i\omega)t}\right) + e^{-i\omega t}\left(\sqrt{B-i\omega}\right)erf\left(\sqrt{(B-i\omega)t}\right) + \frac{2e^{-Bt}}{\sqrt{\pi t}}\right]-$$

$$C_3\left[t\sqrt{A}erf\left(\sqrt{At}\right) - t\sqrt{B}erf\left(\sqrt{Bt}\right) + \sqrt{\frac{t}{\pi}}\left(e^{-At} - e^{-Bt}\right) + \frac{erf\left(\sqrt{At}\right)}{2\sqrt{A}} - \frac{erf\left(\sqrt{Bt}\right)}{2\sqrt{B}}\right] \quad (17)$$

Skin-friction in classical scenario is obtained as,

$$\tau^* = \frac{1}{2}\left[e^{i\omega t}\left(\sqrt{N+i\omega}\right)erf\left(\sqrt{(N+i\omega)t}\right) + e^{-i\omega t}\left(\sqrt{N-i\omega}\right)erf\left(\sqrt{(N-i\omega)t}\right) + \frac{2e^{-Nt}}{\sqrt{\pi t}}\right]-$$

$$D_3\left[t\sqrt{N}erf\left(\sqrt{Nt}\right) - \sqrt{\frac{t}{\pi}}e^{-Nt} - \frac{erf\left(\sqrt{Nt}\right)}{\sqrt{N}}\right] \quad (18)$$

2.3. Plate Heat Flux (Nusselt Number)

The non-dimensional form of rate of heat transfer (Nusselt Number) is given by,

$$Nu = -\frac{d\theta}{dy}\bigg|_{y=0} \quad (19)$$

Now from equation (11) we get the expression for Nusselt number as,

$$Nu = 2\sqrt{\frac{t}{\pi}}(1 + D_1 - D_2) + E_3\left[e^{i\omega t}\left(\sqrt{A+i\omega}\right)erf\left(\sqrt{(A+i\omega)t}\right) + e^{-i\omega t}\left(\sqrt{A-i\omega}\right)erf\left(\sqrt{(A-i\omega)t}\right)\right.$$

$$\left. + \frac{2e^{-At}}{\sqrt{\pi t}} - e^{i\omega t}\left(\sqrt{B+i\omega}\right)erf\left(\sqrt{(B+i\omega)t}\right) - e^{-i\omega t}\left(\sqrt{B-i\omega}\right)erf\left(\sqrt{(B-i\omega)t}\right) - \frac{2e^{-Bt}}{\sqrt{\pi t}}\right]-$$

$$D_1\left[t\sqrt{A}erf\left(\sqrt{At}\right) + \sqrt{\frac{t}{\pi}}e^{-At} + \frac{erf\left(\sqrt{At}\right)}{2\sqrt{A}}\right] + D_2\left[t\sqrt{B}erf\left(\sqrt{Bt}\right) + \sqrt{\frac{t}{\pi}}e^{-Bt} + \frac{erf\left(\sqrt{Bt}\right)}{2\sqrt{B}}\right] \quad (20)$$

For classical case, Nusselt number is derived as,

$$Nu^* = 2\sqrt{\frac{t}{\pi}} \quad (21)$$

2.4. Sherwood Number

The non-dimensional form of rate of mass transfer (Sherwood Number) is given by,

$$Sh = -\frac{dC}{dy}\bigg|_{y=0} \quad (22)$$

Now from equation (12) we get the expression for Sherwood number as,

$$Sh = 2\sqrt{\frac{t}{\pi}}(1 + E_1 - E_2) + E_4\left[e^{i\omega t}\left(\sqrt{A+i\omega}\right)erf\left(\sqrt{(A+i\omega)t}\right) + e^{-i\omega t}\left(\sqrt{A-i\omega}\right)erf\left(\sqrt{(A-i\omega)t}\right)\right.$$

$$\left. + \frac{2e^{-At}}{\sqrt{\pi t}} - e^{i\omega t}\left(\sqrt{B+i\omega}\right)erf\left(\sqrt{(B+i\omega)t}\right) - e^{-i\omega t}\left(\sqrt{B-i\omega}\right)erf\left(\sqrt{(B-i\omega)t}\right) - \frac{2e^{-Bt}}{\sqrt{\pi t}}\right]-$$

$$E_1\left[t\sqrt{A}erf\left(\sqrt{At}\right) + \sqrt{\frac{t}{\pi}}e^{-At} + \frac{erf\left(\sqrt{At}\right)}{2\sqrt{A}}\right] + E_2\left[t\sqrt{B}erf\left(\sqrt{Bt}\right) + \sqrt{\frac{t}{\pi}}e^{-Bt} + \frac{erf\left(\sqrt{Bt}\right)}{2\sqrt{B}}\right] \quad (23)$$

For classical case, Sherwood number is derived as,

$$Sh^* = 2\sqrt{\frac{t}{\pi}}$$ (24)

3. RESULTS AND DISCUSSIONS

The solutions from the preceding section are shown in Figures from 2 to 18 after being numerically computed to talk about how the temperature, velocity, concentration fields, skin-friction, Nusselt number and Sherwood number are influenced by different physical parameters. This provides us with better understanding of the problem in case of physical significance. It has been found that a stratified fluid moves more slowly than an equivalent volume of an unstratified fluid. For various values of magnetic parameter M, Darcy number Da, thermal Grashof number Gr, mass Grashof number Gc, Figures 2 to 9 represent the velocity profiles. It has been observed that while increasing the magnetic parameter M, velocity profile decreases due to a resistive type of force (Lorentz force) occurs which lowers the flow velocity. While velocity increases as Darcy number Da, thermal Grashof number Gr and mass Grashof number Gc are increased in both the cases ($\gamma = 0$, $\xi = 0$) and ($\gamma \neq 0$, $\xi \neq 0$). The classical velocity increases over time (t), but it stabilizes when stratification is present.
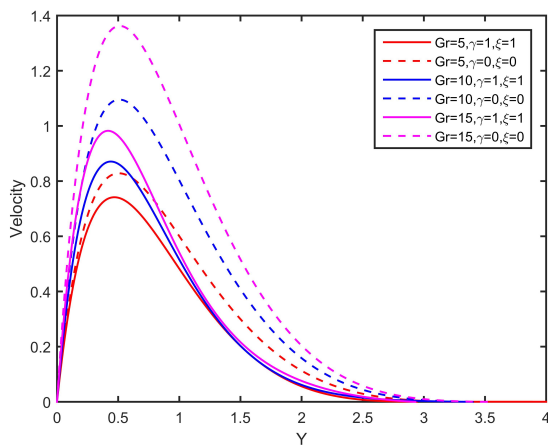
Figure 2. Effects of Gr on Velocity Profile for $t = 1$, $M = 1$, $Gc = 10$, $Da = 0.5$, $\omega = \frac{\pi}{4}$.
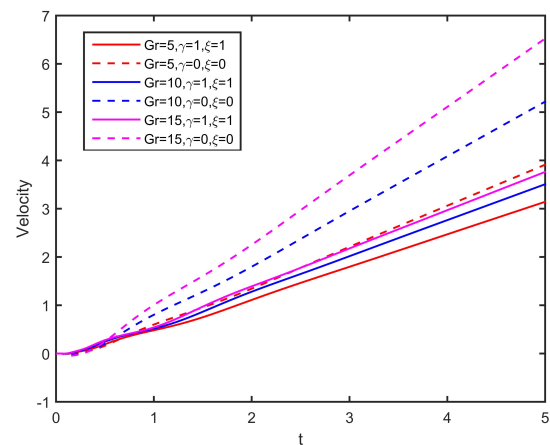

Figure 3. Effects of Gr on Velocity Profile for $y = 1$, $M = 1$, $Gc = 10$, $Da = 0.5$, $\omega = \frac{\pi}{4}$.
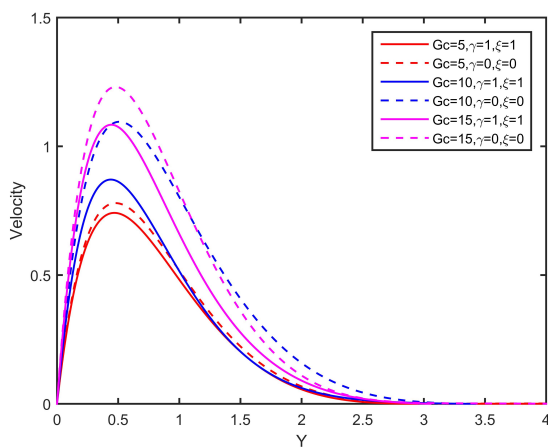

Figure 4. Effects of Gc on Velocity Profile for $t = 1$, $M = 1$, $Gr = 10$, $Da = 0.5$, $\omega = \frac{\pi}{4}$.
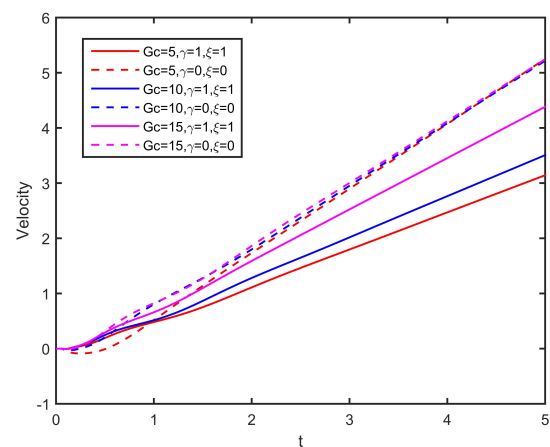

Figure 5. Effects of Gc on Velocity Profile for $y = 1$, $M = 1$, $Gr = 10$, $Da = 0.5$, $\omega = \frac{\pi}{4}$.

The effects of Gr and Gc on temperature profile are seen in Figures (10) and (11). Temperature increases as Gr and Gc increase and decreases as Gr and Gc decrease simultaneously. The effects of magnetic parameter M on temperature profile are depicted in the Figures 12 and 13. Temperature increases as M increases and decreases with decreasing the
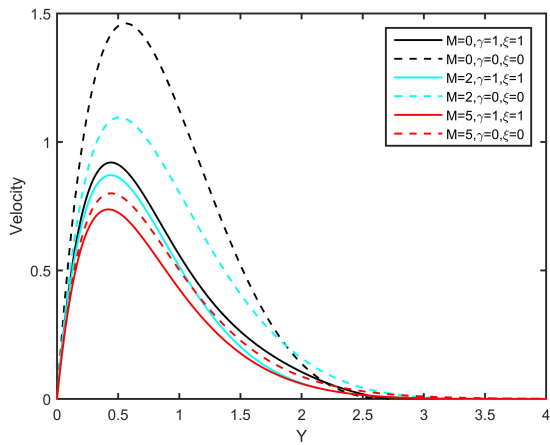
Figure 6. Effects of M on Velocity Profile for $t = 1$, $Gr = 10$, $Gc = 10$, $Da = 0.5$, $\omega = \frac{\pi}{4}$.
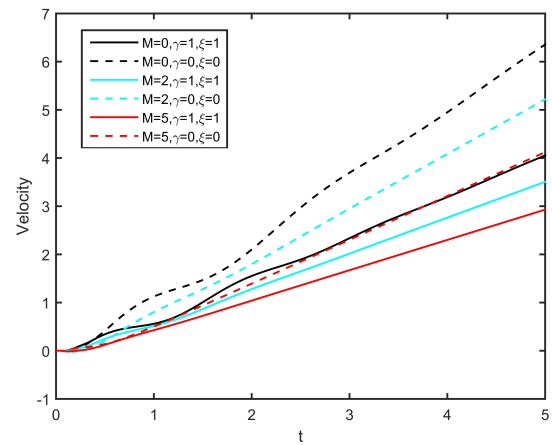

Figure 7. Effects of M on Velocity Profile for $y = 1$, $Gr = 10$, $Gc = 10$, $Da = 0.5$, $\omega = \frac{\pi}{4}$.
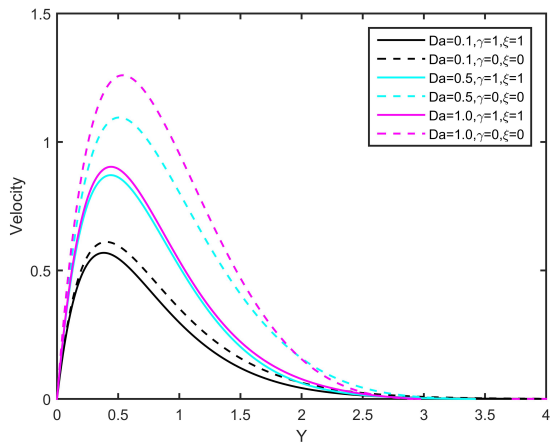

Figure 8. Effects of Da on Velocity Profile for $t = 1$, $Gr = 10$, $Gc = 10$, $M = 1$, $\omega = \frac{\pi}{4}$.
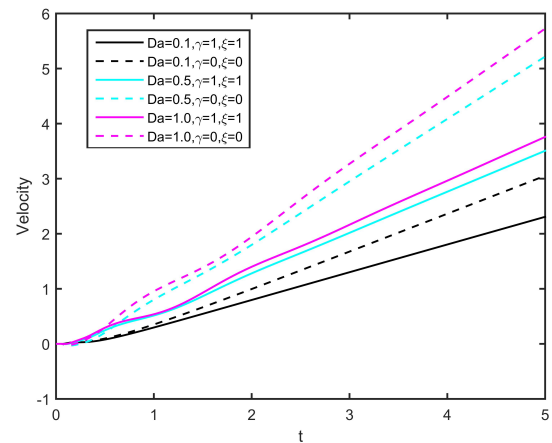

Figure 9. Effects of Da on Velocity Profile for $y = 1$, $Gr = 10$, $Gc = 10$, $M = 1$, $\omega = \frac{\pi}{4}$.

magnetic parameter M. In our study it has been found that temperature is more in classical case as compared to the case
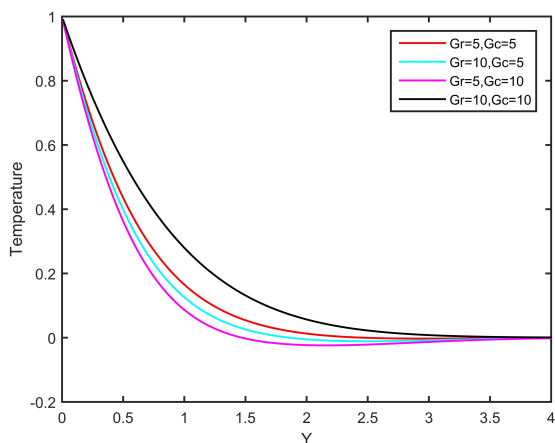

Figure 10. Effects of Gr and Gc on Temperature Profile for $t = 1$, $\gamma = 1$, $\xi = 1$, $M = 1$, $Da = 0.5$, $\omega = \frac{\pi}{4}$.
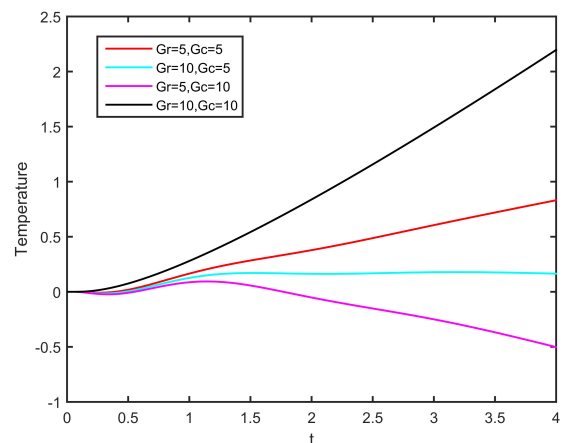

Figure 11. Effects of Gr and Gc on Temperature Profile for $y = 1$, $\gamma = 1$, $\xi = 1$, $M = 1$, $Da = 0.5$, $\omega = \frac{\pi}{4}$.
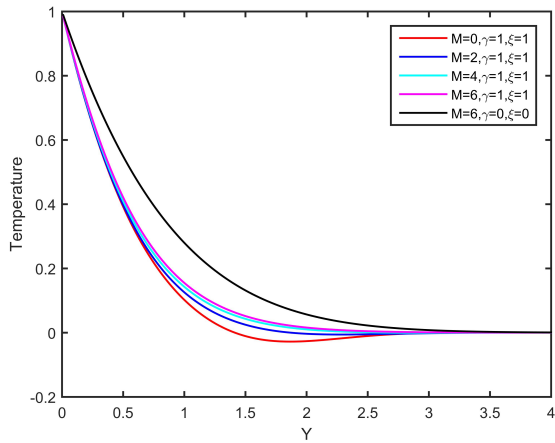
Figure 12. Effects of M on Temperature Profile for $t = 1$, $Gr = 10$, $Gc = 10$, $M = 1$, $Da = 0.5$, $\omega = \frac{\pi}{4}$.
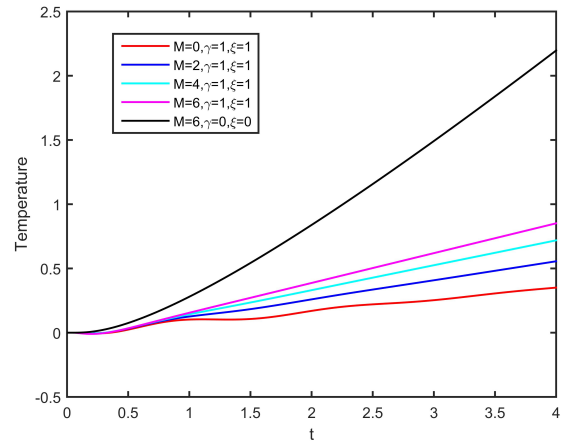

Figure 13. Effects of M on Temperature Profile for $y = 1$, $Gr = 10$, $Gc = 10$, $M = 1$, $Da = 0.5$, $\omega = \frac{\pi}{4}$.
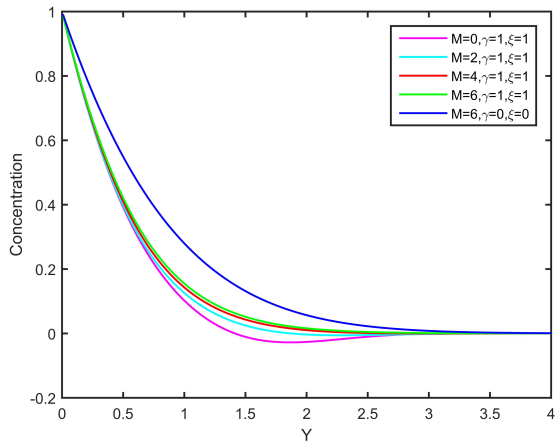

Figure 14. Effects of M on Concentration Profile for $t = 1$, $Gr = 10$, $Gc = 10$, $Da = 0.5$, $\omega = \frac{\pi}{4}$.
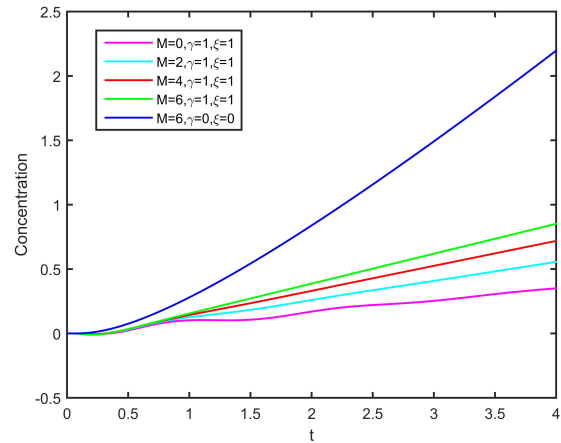

Figure 15. Effects of M on Concentration Profile for $y = 1$, $Gr = 10$, $Gc = 10$, $Da = 0.5$, $\omega = \frac{\pi}{4}$.

Figure 16. Effects of Gr on Skin-Friction Profile for $y = 1$, $Gc = 10$, $Da = 0.5$, $\omega = \frac{\pi}{4}$.

Figure 17. Effects of Gc on Skin-Friction Profile for $y = 1$, $Gr = 10$, $Da = 0.5$, $\omega = \frac{\pi}{4}$.

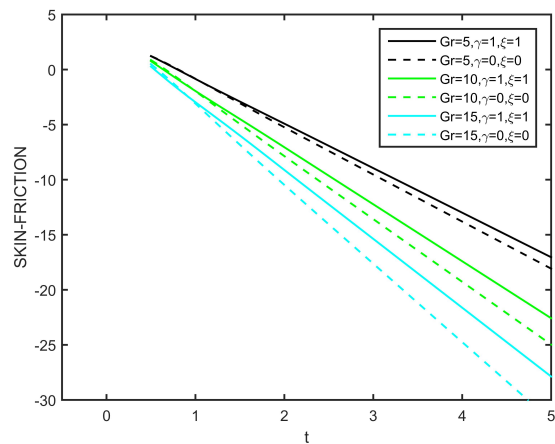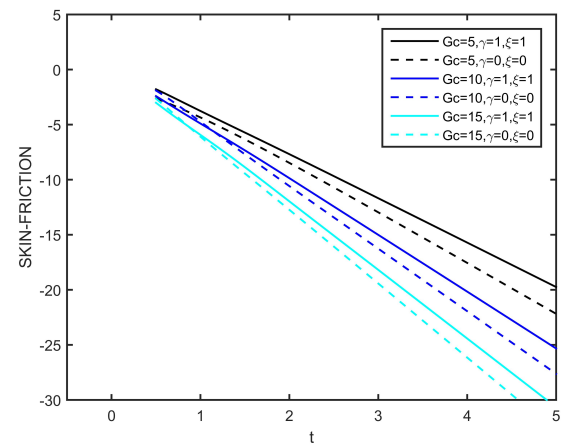of stratification. This happens due to the fluid velocity decreases with increase in magnetic parameter M, therefore heat will not easily be convected, as a result this in turn increases the temperature of the fluid. Figure (14) and 15 depicted the

effects of magnetic parameter M on concentration profile. Concentration increases as M increases but in classical case M has no influence on concentration profile.

In contrast to the stratified scenario, our study indicates that the classical instance exhibits more concentration. Figures (16) to (18) illustrated the effects of Gr, Gc and M on skin-friction profile. It has been observed that skin-friction increases with increase in magnetic parameter M while decreases as Gr and Gc are increased in both the cases ($\gamma \neq 0$, $\xi \neq 0$) and ($\gamma = 0$, $\xi = 0$). From 2 we can conclude that Nusselt number rise in proportion to increase in Gr and Gc but as M rises, Nusselt number decreases. While increasing the Darcy number, Nusselt number also increases. Sherwood number increases in direct proportion to Gr and Gc declines. In proportion to increase in M and Da, Sherwood number grows.
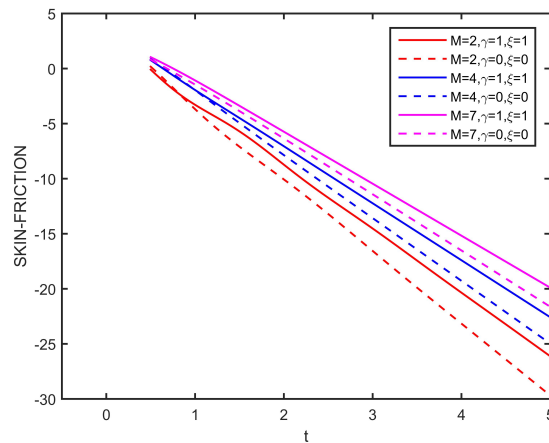

Figure 18. Effects of M on Skin-Friction Profile for $y = 1$,
$Gr = 10$, $Gc = 10$, $Da = 0.5$, $\omega = \frac{\pi}{4}$.

Table 1. The impact of different parameters on Sherwood number with $t = 1$, $\omega = \frac{\pi}{4}$.

γ	ξ	Gr	Gc	M	Da	Sh
1	1	10	10	1	0.5	1.4732
0	0	10	10	1	0.5	1.1227
1	1	5	5	1	0.5	1.5896
1	1	10	10	2	0.5	1.6458
1	1	10	10	1	1	1.6593

Table 2. The impact of different parameters on Nusselt number with $t = 1$, $\omega = \frac{\pi}{4}$.

γ	ξ	Gr	Gc	M	Da	Nu
1	1	10	10	1	0.5	1.6544
0	0	10	10	1	0.5	1.1227
1	1	5	5	1	0.5	1.6011
1	1	10	10	2	0.5	1.6466
1	1	10	10	1	1	1.6597

4. CONCLUSION

We have studied the impact of thermal and mass stratification on MHD flow past an oscillating vertical plate embedded in a porous medium with variable surface conditions. The results of our investigation are contrasted with the scenario in which stratification does not exist. The following are the findings of our investigation:

- For both ($\gamma = 0$, $\xi = 0$) and ($\gamma \neq 0$, $\xi \neq 0$), velocity falls as magnetic parameter M increases. In contrast to the stratified scenario, velocity is higher in the classical instance.

- For both the situation of ($\gamma = 0$, $\xi = 0$) and ($\gamma \neq 0$, $\xi \neq 0$), velocity grows with increasing Darcy number Da. Nonetheless, in contrast to the stratified situation, velocity is higher in the classical case.

- In the cases of ($\gamma = 0$, $\xi = 0$) and ($\gamma \neq 0$, $\xi \neq 0$), velocity increases with increase in the thermal (Gr) and mass Grashof (Gc) numbers. But in the classical scenario, velocity is higher than in the stratified case.

- Temperature grows as the magnetic parameter (M) increases and while increasing Gr and Gc, temperature rises. Temperature is higher in classical situation than in the combined stratified environment.

- Concentration rises with rising in the magnetic parameter M. In contrast to the stratified instance, the classical situation ($\gamma = 0$, $\xi = 0$) involves more concentration.

- Skin-friction decreases as Gr and Gc increases, but increases as M increases, while skin-friction is more in case of stratification.

- In the presence of stratification, the plate heat flux falls with increasing the magnetic parameter M but it grows while increasing the values of Gr, Gc and Da. In contrast to the stratified situation, heat flux is reduced in the classical case.

- The mass flux increases as M, Da, Gr and Gc increase in presence of stratification. However, in classical case, mass flux decreases as compared to the case of stratification.

ORCID

Pappu Das, https://orcid.org/0009-0007-8006-3659; **Rudra Kanta Deka**, https://orcid.org/0009-0007-1573-4890

REFERENCES

[1] V.M. Soundalgekar, U.N. Das, and R.K. Deka, "Free convection effects on MHD flow past an infinite vertical oscillating plate with constant heat flux," Indian J. Math. **39**, 195-202 (1997).

[2] J.S Park, and J.M. Hyun, "Transient behavior of vertical buoyancy layer in a stratified fluid," Intl. J. Heat Mass Transfer, **41**, 4393-4397 (1998). https://doi.org/10.1016/S0017-9310(98)00175-6

[3] U.N. Das, R.K. Deka, and V.M. Soundalgekar, "Transient free convection flow past an infinite vertical plate with periodic temperature variation," J. Heat Transfer, **121**, 1091-1094 (1999). https://doi.org/10.1115/1.2826063

[4] J.S. Park, "Transient buoyant flows of a stratified fluid in a vertical channel," KSME. Intl. J. **15**, 656-664 (2001). https://doi.org/10.1007/BF03184382

[5] A. Shapiro, and E. Fedorovich, "Unsteady convectively driven flow along a vertical plate immersed in a stably stratified fluid," J. Fluid Mech. **498**, 333-352 (2004). https://doi.org/10.1017/S0022112003006803

[6] E. Magyari, I. Pop, and B. Keller, "Unsteady free convection along an infinite vertical flat plate embedded in a stably stratified fluid- saturated porous medium," Transport in Porous Media, **62**, 233-249 (2006). https://doi.org/10.1007/s11242-005-1292-6

[7] C.Y. Cheng, "Double-diffusive natural convection along a vertical wavy truncated cone in non-newtonian fluid saturated porous media with thermal and mass stratification," Int. Commun. Heat Mass Transf. **35**(8), 985–990 (2008). https://doi.org/10.1016/j.icheatmasstransfer.2008.04.007

[8] R.C. Chaudhary, and A. Jain, "MHD heat and mass diffusion flow by natural convection past a surface embedded in a porous medium," Theoret. Appl. Mech. **36**(1), 1-27 (2009). http://dx.doi.org/10.2298/TAM0901001C

[9] C.Y. Cheng, "Combined heat and mass transfer in natural convection flow from a vertical wavy surface in a power-law fluid saturated porous medium with thermal and mass stratification," Int. Commun. Heat Mass Transf. **36**(4), 351–356 (2009). http://dx.doi.org/10.1016/j.icheatmasstransfer.2009.01.003

[10] B.C. Neog, and R.K. Deka, "Unsteady natural convection flow past an accelerated vertical plate in a thermally stratified fluid," Theoret. Appl. Mech. **6**(4), 261-274 (2009). https://doi.org/10.2298/TAM0904261D

[11] S. Gurminder, P.R. Sharma, and A.J. Chamkha, "Effect of thermally stratified ambient fluid on MHD convective flow along a moving nonisothermal vertical plate, Intl. J. Phy. Sci. **5**(3), 208-215 (2010). https://doi.org/10.5897/IJPS.9000199

[12] R.K. Deka, and A. Bhattacharya, "Magneto-Hydrodynamic (MHD) flow past an infinite vertical plate immersed in a stably stratified fluid," International Journal of the Physical Sciences, **6**(24), 5831-5836 (2011). https://doi.org/10.5897/IJPS11.011

[13] R. Muthucumaraswamy, and V. Visalakshi, "Radiative flow past an exponentially accelerated vertical plate with variable temperature and mass diffusion," Int. J. of Enng. Annals. of Faculty Engineering Hunedoara, 9, 137-140 (2011). https://annals.fih.upt.ro/pdf-full/2011/ANNALS-2011-2-26.pdf

[14] A.G.V. Kumar, S.V.K. Varma, and R. Mohan, "Chemical reaction and radiation effects on MHD free convective flow past an exponentially accelerated vertical plate with variable temperature and variable mass diffusion," Annals of the Faculty of Engineering Hunedoara, 10(2), 195 (2012). https://annals.fih.upt.ro/pdf-full/2012/ANNALS-2012-2-32.pdf

[15] R.K. Deka, and A. Paul, "Convectively driven flow past an infinite moving vertical cylinder with thermal and mass stratification," Pramana, **81**, 641–665 (2013). http://dx.doi.org/10.1007/s12043-013-0604-6

[16] H. Kumar, and R.K. Deka, "Thermal and mass stratification effects on unsteady flow past an accelerated infinite vertical plate with variable temperature and exponential mass diffusion in porous medium," East European Journal of Physics, (4), 87-97 (2023). https://doi.org/10.26565/2312-4334-2023-4-09

[17] R.S. Nath, and R.K. Deka, "Thermal and mass stratification effects on unsteady parabolic flow past an infinite vertical plate with exponential decaying temperature and variable mass diffusion in porous medium," ZAMM-Journal of Applied Mathematics and Mechanics/Zeitschrift für Angewandte Mathematik und Mechanik, **104**(6), e202300475 (2024). http://dx.doi.org/10.1002/zamm.202300475

[18] R.S. Nath, R.K. Deka, "Thermal and mass stratification effects on MHD nanofluid past an exponentially accelerated vertical plate through a porous medium with thermal radiation and heat source," Int J Mod Phys B, 2550045. In press (2024). https://doi.org/10.1142/S0217979225500456

[19] R.S. Nath, R.K. Deka, "Theoretical study of thermal and mass stratification effects on MHD nanofluid past an exponentially accelerated vertical plate in a porous medium in presence of heat source, thermal radiation and chemical reaction," Int J Appl Comput Math, **10**(2): 92 (2024). https://doi.org/10.1007/s40819-024-01721-9

[20] P. Das, R.K. Deka, "Thermal and mass stratification effects on unsteady MHD parabolic flow past an infinite vertical plate with variable temperature and mass diffusion through porous medium," East European Journal of Physics, 2: 181-191 (2024). https://doi.org/10.26565/2312-4334-2024-2-17

[21] D. Sahu, R.K. Deka, "Thermal and mass stratification effects on MHD flow past an accelerated vertical plate with variable temperature and exponential mass diffusion embedded in a porous medium," East European Journal of Physics, 2: 161-171 (2024). https://doi.org/10.26565/2312-4334-2024-2-15

[22] D. Sahu, R.K. Deka, "Influences of thermal stratification and chemical reaction on MHD free convective flow along an accelerated vertical plate with variable temperature and exponential mass diffusion in a porous medium," Heat Transfer, 2024; 1-24 (2024). https://doi.org/10.1002/htj.23106

[23] R.B. Hetnarski, "An algorithm for generating some inverse Laplace transforms of exponential form," ZAMP, **26**, 249-253 (1975). https://doi.org/10.1007/BF01591514

[24] M. Abramowitz, I.A. Stegun, and R.H. Romer, "Handbook of mathematical functions with formulas, graphs, and mathematical tables," American Journal of Physics, **56**(10), 958 (1988). https://doi.org/10.1119/1.15378

ВПЛИВ ТЕРМІЧНОЇ ТА МАСОВОЇ СТРАТИФІКАЦІЇ НА НЕСТАЦІОНАРНИЙ МГД-ПОТІК ПОВЗ ОСЦИЛЮЮЧУ ВЕРТИКАЛЬНУ ПЛАСТИНУ, ВМОНТОВАНУ В ПОРИСТЕ СЕРЕДОВИЩЕ ЗІ ЗМІННИМИ УМОВАМИ ПОВЕРХНІ

Паппу Дас, **Рудра Канта Дека**

Факультет математики, Університет Гаухаті, Гувахаті-781014, Ассам, Індія

Було проведено дослідження того, як теплова та масова стратифікація впливає на магнітогідродинамічний потік повз пластину, яка коливається вертикально навколо своєї власної осі, в яку вона занурена в пористе середовище зі змінною дифузією тепла та маси. Для полів концентрації, температури та швидкості безрозмірні керівні рівняння розв'язуються за допомогою методу перетворення Лапласа для унітарних чисел Прандтля та Шмідта, коли пластина гармонійно коливається у власній площині. Числові обчислення проводяться та представлені у вигляді графіків для різних фізичних параметрів, таких як теплове число Грасгофа, фазовий кут, масове число Грасгофа, параметр стратифікації та час на концентрацію, швидкість, температуру, тепловий потік пластини, потік маси та тертя шкіри. Результати цього дослідження можуть бути використані для покращення розуміння потоку МГД на вертикальній коливальній пластині в комбінованих стратифікованих середовищах. Значні висновки, що випливають із масової та термічної стратифікації, порівнюються зі сценарієм, у якому стратифікація відсутня.

Ключові слова: *МГД потік; коливальна пластина; електропровідна рідина; нестабільний потік; термічна стратифікація; масове розшарування; пористе середовище*